Rune Halseid

Ammonia as Hydrogen Carrier

Effects of Ammonia on Polymer Electrolyte Membrane Fuel Cells

Thesis submitted in partial fulfilment of
the requirements for the degree of
Doktor Ingeniør

Department of Materials Technology
Norwegian University of
Science and Technology (NTNU)

Dissertation nr. 2004:25 - March 2004

Ammonia as Hydrogen Carrier
Effects of Ammonia on
Polymer Electrolyte Membrane Fuel Cells

Rune Halseid
Institutt for materialteknologi
Norges teknisk-naturvitenskapelige universitet (NTNU)
Trondheim, Norway
ISBN 82-471-6252-0 (electronic version)
ISBN 82-471-6253-9 (printed version)
ISSN 0809-103X
Doktoringeniøravhandling 2004:25
IMT-rapport 2004:59

Acknowledgements

First of all I wish to thank Prof. Reidar Tunold for inspiration, motivation and help throughout my PhD study. He also put me in contact with Prof. Robert F. Savinell and Dr. Jesse S. Wainright of Case Western Reserve University in Cleveland, OH, where I spent altogether eight months. This gave me the opportunity to use equipment not available at NTNU, but more importantly, insight into a different approach of testing fuel cells. This gave me new ideas for experiments which I made back home in Norway. I also very much appreciated the discussions every Friday in the group meetings of Drs. Savinell, Wainright and Litt, although I must admit that my knowledge of polymer chemistry was put to the test in some of the meetings.

The people at NTNU and SINTEF working with hydrogen technology and fuel cells, along with the rest of the people at Group of Electrochemistry, also made important contributions to my research work as well as making my time at NTNU very enjoyable. Martha Bjerknes and Kjell Røkke both took care of many of the practicalities allowing me to focus on my research.

In experimental work, it is of paramount importance to have access to highly skilled precision mechanics and glass blowers. Ketil Joner and Astrid Salvesen provided me with these services at NTNU. Wayne Schmidt at CWRU helped me out during my stay there. I also got invaluable help with design of the electronic control systems from Trygve Knag and Jan Ole Sundli. Not all of my ideas for new experiments turned out to be successful, but that was not because of the equipment.

Dr. Preben Vie and Torstein Lange, who both shared office with me, were very supportive. They also had to put up with a lot of discussions; I love to argue. Preben was also part of the "Ammonia as Hydrogen Carrier for PEMFCs" project for most of my stay at NTNU, and contributed with his experience when we designed and built the test stations and other equipment as well as proofreading parts of this Thesis.

We have had the pleasure to have several students working in our project over the years. Agata Zbyszyńska, Tomáš Bystroň, Ole-Erich Haas and Trivo Jelisavac all contributed to the experimental work. It was a pleasure to have them working with the project. Fellow PhD students also helped with some of the experiments. Anne-Kristine Meland operated the test stations during parts

of my stay at CWRU. Frode Seland helped me out with some experimental work towards the end and also did some proofreading. All these contributions are highly appreciated.

Norsk Hydro ASA and the Research Council of Norway funded my work at NTNU. The project I was a part of had sufficient funding to perform efficient research work. Dr. Rolf Jarle Aaberg, Associate Prof. Børre Børresen and Prof. Reidar Tunold deserves recognition together with representatives from Hydro and NFR for initiating and starting the project. Norsk Hydro also contributed with valuable input in the technical discussions throughout the project. Further, I was granted a permission of leave from Norsk Hydro for my PhD study.

Finally, I want to thank to my parents for always letting me do what I wanted to and supporting my choices.

Summary

Several aspects of ammonia as a hydrogen carrier and ammonia poisoning of Polymer Electrolyte Fuel Cells (PEMFCs) are discussed in this Thesis. The most important findings in the different parts of this Thesis are presented here.

- Ammonia is a hydrogen carrier that has relatively high energy density, it is a well known chemical commodity product, and the energy efficiency of the production process is the same as f. ex. for methanol. The major drawback is the toxicity. Presently production is based on fossil fuels and natural gas in particular. Carbon capture from fossil fuel based ammonia production is highly feasible; it is actually a vital part of the synthesis process. The major draw-back with any hydrogen carrier is the cost, both economical and energetic, of synthesizing it from either fossil or renewable energy sources with subsequent splitting or reforming to hydrogen at the point of use.

- Ion exchange equilibria of ammonium between an aqueous phase and Nafion® 117 were measured at 10, 25, 40, and 60 °C by equilibrating the membrane in 0.1 M chloride electrolytes of known cationic composition. The water content in the membrane phase was found to decrease linearly with increasing cation fraction of ammonium in the membrane phase ($y_{NH_4^+}$) from $\lambda_{H_2O} = 21.2$ (mols of water per mol sufonic acid groups) in proton form Nafion® in pure water to $\lambda_{H_2O} = 13.2$ in ammonium form Nafion® in a 0.1 M chloride solution. The conductivity was also found to decrease linearly with increasing $y_{NH_4^+}$ from 97 mS/cm to 25 mS/cm at 25.0 °C. The activation energy for ionic conductivity was found to depend on membrane composition and hence water content.

- Different cell geometries used for ac impedance measurements on PEMFCs were evaluated. Artifacts in impedance measurements may arise from small deviations from the ideal cell geometry. These deviations are very difficult to avoid. Our calculations show that a planar cell design with a thin electrolyte is not suited for three-electrode ac impedance measurements. A two-electrode set-up performs equally well and in some cases even better than the three-electrode set-up.

- The mechanism for Hydrogen Oxidation Reduction (HOR) on the PtRu anode catalyst has been investigated. Polarization curves of hydrogen mixed with N_2, Ar, He and CO_2 have been measured, both in fuel cells ($H_2|O_2$) and in symmetrical cells ($H_2|H_2$). HOR on the PtRu anode catalyst seems to follow the Tafel-Volmer mechanism based the on observation of limiting currents that were not due to mass transfer but rather due to reaction limitations. The conclusion is also supported by the observation of higher HOR rates after the electrodes had been electrochemically cleaned. The mass transfer limiting currents in the Gas Diffusion Layer was found to be very high. We further found that the influence of CO_2 on the performance of the PtRu anode was significant, especially in cells with hydrogen on either electrode (symmetrical cells). The contamination species formed on the anode and on platinized Pt by CO_2 and CO respectively were different. The adsorbed contaminants formed from CO displaced the contaminants formed by CO_2. Nitrogen did not seem to have any effect on anode performance other than dilution. Dilution of hydrogen with the noble gases Ar and He gave very similar results compared to dilution with nitrogen.

- We have found that ammonium is electrochemically active in acidic solutions at room temperature. Oxidation of ammonium to form nitrogen or nitric oxide species is however slow, at least at room temperature. Formation of N_2 has been found using Differential Electrochemical Mass Spectroscopy (DEMS), and also NO was detected at electrode potentials higher than 1.2 V_{RHE}. Cyclic Voltammetry and Electrochemical Quartz Crystal Microbalance (EQCM) data show that presence of ammonium affects the formation and reduction of Pt oxide at high potentials. This seems to involve the formation of very stable nitrogen or nitrogen-oxygen species on the surface of the electrode. Some of these species seem to be removed from the electrode only at very low potentials in the hydrogen adsorption region. The hydrogen adsorption region is also strongly affected by presence of ammonium, in particular the most strongly bond hydrogen which is shifted to lower potentials. The hydrogen desorption region is virtually unaffected by ammonium. The moderate oxidation activity of ammonium can be critical to understand state state tolerance of of PEMFCs towards ammonium poisoning. Recovery after contamination will also be influenced by the rate of ammonium oxidation.

- The Oxygen Reduction Reaction (ORR) rate was studied using a Rotating Disk Electrode. The effect of ammonium in moderate concentrations on ORR in a sulfuric acid electrolyte is significant. The oxide-free Pt surface is more affected by ammonium than the oxide covered. The Tafel slope at low current density (c.d.) on oxide-free Pt is about 90 mV/dec. in the presence of ammonium compared to about 60 mV/dec. in pure acid. The Tafel slope of ORR on oxide-free Pt at high c.d. is the same in pure acid as with ammonium present. Also the exchange c.d. is lower in the presence of ammonium. The Tafel slope of ORR on oxidized Pt is not significantly affected by ammonium. The exhange c.d. is lower for the ammonium containing electrolyte also in this case. The apparent reaction order of ammonium in the ORR is -0.4 to -0.5 on the oxide-free Pt and -0.15 to -0.2 on the oxide covered Pt. The origin of the loss of ORR activity has not been identified.

- The effect of ammonia on PEMFC was tested by addition of 10 ppm NH_3 to the hydrogen fed to PEMFCs based on GORE™ PRIMEA® MEAs. There was a very significant loss in performance of the FCs. The poisoning process was slow taking 24 hours or more to reach a steady state. In some cases no steady state was reached during the experiment. The performance loss was in most cases reversible, but only after operation on neat hydrogen for several days. Additions of 1 ppm NH_3 for one week also resulted in significant performance losses. An MEA based on carbon supported Pt catalyst did not differ from the GORE™ MEA which used a PtRu based anode catalyst.

  The performance losses were higher than could be explained by the observed increase in ohmic resistance in the cell. There was also a significant decay in performance in a symmetrical $H_2|H_2$ cell especially at high c.d. where a reaction limiting current was observed. The limiting current is consistent with the Tafel step in a Tafel-Volmer HOR mechanism. There is also a significant effect of ammonium on the ORR of the cathode. The effect on the ORR is dominant at lower c.d., but at higher c.d. the reaction limiting current of the HOR becomes the most important limitation of the cell.

Contents

List of Tables

List of Figures

Nomenclature

Roman Letters

A	Area	m^2
a_i	Activity of component i	Pa or M
c_i	Concentration of i	mol/m^3
D_{AB}	Binary diffusion coefficient for A in B (and B in A)	m^2/s
E	Potential	V
E_a	Activation energy in Arrhenius equation	kJ/mol
F	Faraday's constant	96485 C/mol
f	F/RT	
f_0	Fundamental resonance frequency of quartz crystal	Hz
G	Gibbs energy	J
H	Enthalpy	J
I	Current	A
I	Ionic strength	M
i	Current density	A/cm^2
i_0	Exchange current density	A/cm^2
k	Reaction rate constant	various
k_d	Mass transfer coefficient	mol/cm^2s bar
$k_{H,i}$	Henry's law constant	bar/M
K_p	Ideal gas contribution to equilibrium constant for ammonia splitting	-

K_ϕ	Non-ideal contribution to equilibrium constant for ammonia splitting	-
K_y	Equilibrium constant for ammonia splitting excluding pressure effects	-
l	Membrane thickness	m
M	Molecular or Equivalent weight	g/mol
n	n^{th} overtone of quartz crystal	-
n	Number of electrons involved in the total reaction	-
n	Number of membranes in stack	-
p	Pressure	Pa
p_i	Partial pressure of component i	Pa
p_i	Reaction order of i	-
Q	Charge	C/m^2
q	Heat supplied to the system	J
R	Area specific resistance	Ωcm^2
R	Resistance	Ω
R	Universal gas constant	8.314 J/mol K
R^2	Coefficient of determination in linear regression	-
S	Entropy	J/K
T	Temperature	K
U	Internal energy	J
V	Volume	m^3
w	Work supplied to the system	J
x_i	Cation fraction of i in the aqueous solution	-
y	Function defined in Equation 5.29	
y_i	Cation fraction of i in the membrane phase	-
y_i	Molar fraction of i in gas	-
z	Number of electrons involved in the rate determining step	-
z_i	Valency of species i	-

Greek Letters

α_i	Symmetry factor for charge transfer	-
β_i	Parameter in regression model	various
$\widehat{\beta_i}$	Estimator for parameter in regression model	various
δ	Thickness of GDL	m
Δf	Frequency change	Hz
ΔH	Change in enthalpy	J/mol
Δm	Mass change	g/m^2
ΔQ_{ox}	Difference in net oxidation charge between ammonium containing electrolyte and pure acid	C/m^2
ΔG	Gibbs energy change	J/mol
ΔS	Entropy change	J/mol K
ϵ	Porosity	-
η	Efficiency	-
η	Overpotential	V
κ	Conductivity	S/m
Λ_i	Molar conductivity of i	mS m^2 mol^{-1}
λ_i	Mols of i per mol of sulfonic groups in the membrane	-
μ	Shear modulus of quarts	kg/ms^2
ν	Kinematic viscosity	m^2/s
ν	Sweep rate	V/s
ω	Rotation rate	rad/s
Φ	Galvani potential	V
φ_i	Fugacity coefficient of component i	-
ρ	Density	kg/m^3
τ	Tortuosity	-
θ_i	Surface coverage of species i	-
ξ_i	Conversion of component $_i$	-

Sub- and Superscripts

0	Standard state
a	Anode/anodic
ad	Adiabatic (flame temperature)
ads	Adsorbed
amb	Ambient (temperature)
b	Bulk
b	Reverse direction of reaction as written
C	Carnot
c	Cathode/cathodic
c	Combustion (temperature)
$cell$	Cell (cell potential)
$cond$	Condensation
ct	Charge transfer
d	Diffusion
$elec$	Electrolyte
ext	Contact between Pt electrode and outer membranes in stack
f	Forward direction of reaction as written
$film$	Liquid film between each membrane in the stack
gap	Gap between conductivity cell and membrane stack
H	Heyrowsky step
h	High
k	Kinetic (current)
l	Limiting
l	Low
lm	Log mean value, defined in Equation 5.9
mem	Membrane
$non-pV$	Work other than pV work

ox	Oxidation
p	Peak, used for E_p; peak potential in CV
p	Polarization (used for polarization resistance)
pV	Pressure-Volume work
r	Reaction
rev	Reversible
s	Surface
T	Tafel step
tot	Total
V	Volmer step
$water$	Water

Acronyms

ac	Alternating Current
ACCEPT	Ammonia Cracking for Clean Electric Power Technology
AFC	Alkaline Fuel Cell
AIP	Air-Independent Propulsion
ATR	AutoThermal Reforming
BAT	Best Available Technique
c.d.	Current density
CNG	Compressed Natural Gas
CUTE	Clean Urban Transport for Europe
CV	Cyclic Voltammetry
DAFC	Direct Ammonia Fuel Cell
dc	Direct Current
DEG	Di-ethyleneglycol
DEMS	Differential Electrochemical Mass Sectroscopy
DMFC	Direct Methanol Fuel Cell

EIPH2	European Integrated Hydrogen Project – Phase 2 `www.eihp.org`
ePTFE	Expanded PolyTetraFluoroEtylene
EQCM	Electrochemical Quartz Micro Balance
EU	European Union
FC	Fuel Cell
FP	Framework Program
GDL	Gas Diffusion Layer
GHG	GreenHouse Gases
GT	Gas Turbine
HHV	Higher Heating Value, HHV = ΔH
HOR	Hydrogen Oxidation Reaction
IAFC	Indirect Ammonia Fuel Cell
ICE	Internal Combustion Engine
IDLH	Concentration Immediately Dangerous to Life or Health
IPCC	Intergovernmental Panel on Climate Change `http://www.ipcc.ch/`
IRAS	Infra-Red Reflection Spectroscopy
JHFC	Japan Hydrogen & Fuel Cell Demonstration Project `www.jhfc.jp`
LHV	Lower Heating Value, LHV = $\Delta H - \Delta H^{cond}_{water}$
LNG	Liquefied Natural Gas
LSV	Linear Sweep Voltammetry
MCFC	Molten Carbonate Fuel Cell
MEA	Membrane Electrode Assembly
MH	Metal Hydride
N/A	Not Applicable
OCV	Open Circuit Voltage
ORR	Oxygen Reduction Reaction

PAFC	Phosphoric Acid Fuel Cell
PEMFC	Polmer Electrolyte Membrane Fuel Cell *or* Proton Exchange Membrane Fuel Cells
PFSA	PerFluorSulfonic Acid
POX	Partial OXidation
RDE	Rotating Disk Electrode
RRDE	Rotating Ring-Disk Electrode
rds	Rate determining step
RE	Reference Electrode
RHE	The potential of a Reversible Hydrogen Electrode in the electrolyte in question
SEM	Secondary Electron Multiplier
SERS	Surface Enhanced Raman Spectroscopy
Sm^3	Standard cubic meters of gas at 15 ^oC and 1 atma pressure
SOFC	Solid Oxide Fuel Cell
SOFC-μGT	Hybride of SOFC and micro Gas Turbine
STEL	Short-Time Exposure Limit
TBA	Tetrabutylammonium
TMP	Turbo Molecular Pump
toe	Tonn oil equivalent
TWA	Time-Weighted Average
UHP	Ultra High Purity
WE	Working Electrode

Chapter 1

Introduction

1.1 Background

Energy is one of the most important commodities in modern society, and the industrialized world is today totally dependent on affordable fossil fuels. At the same time it is clear that human activity influences global climate as comprehensively documented in reports from, amongst others, the Intergovernmental Panel on Climate Change (IPCC). Thus, a transition from fossil to renewable energy sources is required in a not too distant future. Fossil fuels, but with carbon capture, may be essential in a transitional period. Hydrogen has been suggested as the ultimate energy carrier in the future. Extraction of renewable energy often requires capability to store and transport energy due to the irregular availability and scattered occurrence of renewable energy. Mobile applications also require a way to store energy. One technology to convert hydrogen back to energy when needed is *Fuel Cells* (FC).

1.1.1 History of Fuel Cells

The *fuel cell effect* was first reported in January 1839 by Christian Friedrich Schönbein in the paper *"On the Voltaic Polarization of certain Solid and Fluid Substances"* and also reported by Sir William Robert Grove in February 1839 in the note *"On Voltaic Series and the Combination of Gases by Platinum"* [1]. Sir Grove later constructed an FC generator, or the *"Gaseous Voltaic Battery"*, which was described in several papers in the period 1842–1845 [1]. FCs were studied in the following years, but the steam engine and later the

Internal Combustion Engine (ICE) proved to be more successful technologies impeding the development of FCs.

The direct coal FC, which in many aspects is the predecessor of the Molten Carbonate Fuel Cell (MCFC), was studied at the start of the last century [2]. There was also some interest in Solid Oxide Fuel Cells (SOFC) in the 1930ties based on work on solid oxide conductors performed by Nernst late in the 19^{th} century [2].

A renewed interest in FCs in the 1950ties and 1960ties resulted in development of most of the FC types still being studied. The Alkaline Fuel Cell (AFC) was developed by Francis T. Bacon starting in 1932. AFCs were introduced in the Apollo space program and later used in the Space Shuttle. The Polymer Electrolyte Membrane Fuel Cell (PEMFC) was developed by General Electric also for space travel in the 1960ties. It was used for on-board electric power generation in the Gemini Earth-orbiting Mission in 1962-1966 [3]. However, material problems with the membrane hindered use of this technology in the Apollo program. Later, PerFluorSulfonic Acid (PFSA) based polymers (like Nafion®) were developed making the PEMFC more attractive. FCs based on direct oxidation of the fuel (methanol, ammonia and hydrazin) were investigated in the late 1960ties. The Direct Methanol Fuel Cell (DMFC) has gained the most attention, especially in recent years for use in portable electronics. A more comprehensive overview of direct ammonia and hydrazine FCs will be given in Section 2.5.1. SOFC technology was also studied in the 1960ties by researchers at Westinghouse Electric Corporation. MCFC technology was also further developed [2]. The Phosphoric Acid Fuel Cell (PAFC) was also developed in the late 1960ties [3], and relatively large power generation units based on this technology have been made, f. ex an 11 MW PAFC plant installed in Japan [2].

1.1.2 Recent Interest for Fuel Cells

Recent interest in FCs is partly motivated by efficiency considerations. The fact that chemical energy may be transformed directly into electrical energy without going via combustion processes, which transform the chemical energy into heat and then into mechanical energy which in turn may be transformed to electrical energy, makes FCs more efficient[1] than practical combustion processes.

[1] However, it is not correct to say that this is because the ICE is restricted by the Carnot cycle efficiency whereas the FC is not. This is further discussed in Section 2.6.1

Further, emissions of local pollutants are strongly reduced if not eliminated when using FCs as compared to ICEs.

Transportation

Road transportation. One application that has received much attention is transportation, especially for use in cars and buses. Local pollution in urban areas is an important factor in this respect. Legislative initiatives like the U.S. Clean Air Act and similar initiatives in California have brought about more focus on low-emissions vehicles from the car manufacturers. Nearly all major car manufacturers have programs in place for development of FC vehicles, see for example `www.fuelcells.org/charts.htm` for an excellent summary of all projects up to date on both buses and cars equipped with FCs. Recently also the FreedomCAR initiative put focus on hydrogen for transportation. More fuel efficient cars are also of interest as stated in the press release when the FreedomCAR initiative was launched: *"America's transportation sector is 95 % dependent on petroleum, with transportation consuming 67 % of the petroleum used in the U.S. The Federal government and its industry partners recognize the steady growth of imported oil needed to meet U.S. requirements – today about 10 million barrels of foreign oil each day – cannot continue."* [4]. There are also many other initiatives like the California Fuel Cell Partnership (`www.fuelcellpartnership.org`) consisting of car companies, FC manufacturers, oil companies and governmental organizations, and Japan Hydrogen & Fuel Cell Demonstration Project (JHFC) (`www.jhfc.jp`) with several car manufacturers and gas companies involved. JHFC also evaluates several different concepts for hydrogen fuelling stations (different technologies and hydrocarbons as hydrogen source). The European Union (EU) also has programs in place for development of sustainable energy systems and road transportation under the 6^{th} Framework Program (FP). EU have also had similar programs under the 5^{th} FP like the European Integrated Hydrogen Project – Phase 2 (EIHP2), which focuses on development and harmonization of rules and regulations for hydrogen fuelled road vehicles, and the Clean Urban Transport for Europe (CUTE) program.

Many researchers and companies are very optimistic regarding how quickly large scale introduction of affordable and viable FC based cars may be introduced. As an example, General Motors claim that FC cars should be in regular production by 2010. However, it is still much debated when this will actually happen. In the history of hydrogen energy and FCs, predictions that

the technology will be commercialized "in 10 years time" have often been made but not yet fulfilled.

Further, the actual gain in reduced emissions of GreenHouse Gases (GHGs) by introduction of FCs may not be as large as one often can get the impression of. Recent studies performed at Massachusetts Institute of Technology indicate that hybrid cars based on diesel engines and batteries will be very comparable to FC based cars both with respect to energy efficiency and emissions of GHGs, even in 2020. This conclusion holds even when allowing for an optimistic scenario for development of the FC technology [5]. Recently, L-B-Systemtechnik together with General Motors, supported by Shell, BP, ExxonMobil, and TotalFinaElf, performed a study of many different fuel chains and vehicle drive options. They concluded that the *well-to-wheel* efficiency of hybrid cars (Opel Zaphira size) based on diesel ICE was comparable to FCs based on reforming gasoline on-board. FC concepts based on other fuels were less energy efficient. Only hydrogen production based on renewable energy sources gave lower emissions of GHGs [6]. Other studies have indicated that hydrogen generated from natural gas in central facilities may give a lower GHG emission than diesel ICE hybrids [7].

One obstacle for large scale market penetration of FCs is efficient distribution of an appropriate fuel for FCs in cars. Several strategies for introduction of FCs and transition to hydrogen based FCs are foreseeable [7]. One could base the first FC applications on reformed gasoline/diesel for which a distribution grid is in place. Mass production of FC components for this market would pave the way for cheaper FC components. However, reforming technology for these fuels is less developed, especially for diesel [7], and the gain relative to ICE hybrids is marginal if not negative in terms of GHG emissions [5–7]. The second scenario is introduction of alternative fuels, in particular methanol. Distribution is a problem, so there is a need for enormous investments in fuel infrastructure (production, transportation and filling facilities). If methanol is only a temporary solution, it may be difficult to defend the enormous investments in infrastructure. Also, introduction of methanol may impede the development of pure hydrogen based fuel cycles. The gain in terms of GHG emissions for FCs running on methanol is also marginal compared to hybrid ICE systems [5–7]. The third scenario is that hydrogen (in the start based on natural gas reforming) is used for fleet-operation vehicles (*i.e.* buses, taxies, delivery cars and trucks etc.) because fewer filling stations would be required. The question is if this market segment is large enough to achieve price reduction of FC components due to large production volumes.

Maritime transportation. Marine application has the advantage that they can carry relatively large and heavy power generation systems. Recently, the first vessel in a new submarine class (U212A) was produced in Germany with nine 30-50 kW PEMFC systems for Air-Independent Propulsion (AIP). The first submarine of this class was launched in March 2002, and is presently under testing. It is scheduled for commissioning in March 2004 [8]. The submarines are also equipped with diesel engines and lead-acid batteries for high-speed operation, but the PEMFC provide up to two weeks of silent cruising running on pure hydrogen and oxygen. Further, due to the low noise level and no emissions of exhaust, the submarine has very good signature characteristics. Four class 212A submarines have been ordered by the German Navy and two by the Italian Navy. The class 214 is a new version of the class 212A with two 120 kW PEMFC modules increasing the possible time-span of AIP. The Greek Navy have ordered three class 214 as has the South-Korean Navy [8]. Three 25 years old class 209 greek submarines will also have PEMFC based AIP systems retrofitted [9].

FCs are also interesting for civilian ships, and there are several projects considering this. One problem often faced is the lack of approved codes and standards for hydrogen as a fuel and FCs as power sources for propulsion. There have been several problem to get acceptance for FCs as the main propulsion machinery in ships. The EU sponsored FCSHIP program is one of the initiatives to get codes and regulations in place in Europe.

Distributed Power Generation

The power crisis in California in 2001 boosted interest in distributed power generation which would make consumers less dependent on power from a central distribution grid. Recently similar events in Italy and North-Eastern US have further attracted attention to the vulnerability of the electric grid. Distributed power generation also have the inherent advantage that less investments are required in the grid. Further, upgrades of the grid are not necessarily required to overcome bottlenecks and peak demand. An interesting case study from New York City illustrates this; deferral benefits from not installing a new transformer in the 13 kV grid for two years could justify an investment of 5500 USD/kW in an FC system [10]. Peak load on the electrical grid in summer is not concurrent with peak load on the natural gas grid. Thus, distributed FC generators based on natural gas would be an interesting alternative to installation of new transmission lines and power generation capacity.

Power generation puts less strict demands on weight and volume the FC may occupy compared to transportation applications making it easier to adopt the technology. However, durability is of greater concern in power generation applications than in mobile applications. Combined heat and power generation also has the advantage that heat is generated close to the point of use eliminating the requirement for a separate distribution net for heat.

Combined Fuel Cell and Turbine Concepts.

One has also considered centralized power generation plants based on SOFC often combined with turbines to increase electrical efficiency (often called SOFC-μGT). Competition from Gas Turbine (GT) based power plants is fierce, especially for large power plants (>100 MW). Attainable electrical efficiency from advanced GT power plants combined with steam cycles is typically 58%(LHV). The attainable power efficiency from SOFC-μGT systems may be as high as 60% even for systems as small as 100 kW, and also the efficiency on partial load is very high [11]. Testing of a demonstration unit at University of California at Irvine achived 53 % efficiency for a 220 kW system [12].

The Gibbs energy of hydrogen, CO and methanol decreases with increasing temperature ($\Delta S < 0$ [13]) so that the maximum extractable energy in an FC from a given quantity of fuel decreases with increasing temperature. However, if the FC is combined with a bottoming cycle (either a gas turbine or a steam turbine), the energy lost by the FC in form of reaction entropy can be recovered in the bottoming cycle. Thus, the theoretical efficiency of a combined FC and turbine is unaffected by the operating temperature of the FC assuming that the bottoming cycle expels heat at ambient temperature [14].

Recent research on SOFC technology has focused on systems that captures the CO_2 generated from chemical combustion of fossile fuel so that the power plant is close to neutral in terms of emissions of GHGs. Use of so-called mixed conductors, textiti.e. ceramic materials that transport both oxygen and electrons which are spin-offs from SOFC research, is another interesting technology for production of nearly GHG neutral energy.

Premium Power Applications

Premium power applications for powering portable electronics and power back-up for large computer systems may also be interesting applications for FCs. The attainable price for energy in this market is relatively high. Therefore, the

present relatively high cost for FCs is not inhibitive for market penetration. FCs may also offer higher energy densities and easier recharging procedures than present battery technology which would make FCs even more competitive for portable applications.

1.1.3 Hydrogen Carriers

One of the main challenges for a successful introduction of FC technology to the consumer market besides cost and durability, is to establish safe, convenient and economical ways to transport and store fuel suited for use in FCs. Several possible solutions have been proposed, such as storage of compressed hydrogen, liquid hydrogen, hydrogen in metal hydrides or hydrogen containing fuels like natural gas (Liquefied Natural Gas (LNG), Compressed Natural Gas (CNG)) or alcohols (methanol, ethanol etc.). It is also possible to use gasoline and diesel as hydrogen sources for FCs. Fuels other than pure hydrogen require conversion/reforming to hydrogen rich gas before the energy can be utilized in low temperature FCs except for DMFC. Some of the reasons for using liquid fuels are:

- Liquid fuels make it easier to transport energy from the source to the consumer. This is especially interesting for so-called "stranded gas", or natural gas being co-produced with oil far from any market that may make use of this natural gas. Presently a large fraction of this gas is flared at the production site

- Codes and regulations for large scale handling are already in place for most of these liquid fuels. However, codes and regulations are needed for use on a consumer level

- An industrial distribution system is in place for some of the fuels mentioned above. However, most of these fuels would require investment in new consumer distribution systems

- Consumers are used to liquid fuels

- The operating conditions for storage are less severe (temperature and/or pressure) compared to storage of compressed/liquid hydrogen. Compression or liquification of hydrogen are expensive processes both in terms of energy and cost. Further, the pressure energy contained in high pressure gas bottles is a safety risk

- High volumetric energy density is attainable with liquid fuels

One common property of the liquid fuels mentioned above is that they all contain carbon. Presently all these chemicals are based on fossil fuels, and therefore releases "new" CO_2 when used.

1.2 Motivation for the Thesis

If release of CO_2 originating from fossil fuels is to be significantly reduced, CO_2 has to be captured and disposed. This is very difficult to do if carbon containing fuels are reformed locally. Central facilities for carbon capture are likely to be much more cost-efficient than distributed carbon capture. If carbon capture is of interest, carboneous, liquid fuels as mentioned above can not be used to carry energy to the end user. Ammonia offers the advantage that splitting of ammonia results in hydrogen and nitrogen, and does not carry carbon to the end user. It is also possible to synthesize ammonia from renewable energy sources[2], which would make ammonia a viable fuel also in a post-fossil fuel society.

Ammonia may be present in hydrogen produced by thermal splitting of ammonia. Further, ammonia as such is an interesting contaminant in PEMFC even if ammonia is not used as a hydrogen carrier. Ammonia may be formed in fuel reforming processes at levels up to 150 ppm [15], especially if the reforming involves homogeneous precombustion with air, or the fuel itself contains nitrogen containing components [16]. Ammonia may also be present as a trace component in ambient air as such. There has also been reports in the literature that metal hydride alloys has a catalytic effect on the formation of ammonia from hydrogen and nitrogen mixtures [17] so that ammonia may be present also in hydrogen from metal hydride storages if nitrogen is present.

Only a few papers on how ammonia affects the operation of PEMFC are available. To our knowledge, three different research groups have published papers and proceedings regarding ammonia in PEMFC [18–21], but no details are available from Chellappa *et al.* [18]. The focus of Uribe *et al.* [19, 20] and Soto *et al.* [21] was to study poisoning of cells and recovery after exposure to ammonia. The poisoning mechanism has only partly been identified. Further, detailed studies of oxidation of ammonia in acidic solutions have not

[2]Other fuels, like alcohols and methane, may also be produced from renewable energy sources. These are then often called *biofuels*

been reported in the literature. Oxidation of ammonia in alkaline solutions has been studied in more detail, and different reaction mechanisms have been suggested [22–24]. However, much remains to be done also in the alkaline system as nitrogen has a very complex chemistry with many different oxidation states possible in (adsorbed) intermediates and reaction products. Oxidation numbers of nitrogen may vary from -III (NH_3 or NH_4^+) to +VII (NO_4^-). This is discussed in more detail in Chapter 6.

The Thesis work has been performed as a part of a larger project at NTNU which looked at ammonia as hydrogen carrier for PEMFC. The scope of the total project included testing of a stack, testing of single cells as well as energetic modelling of ammonia as a hydrogen carrier. The focus of the Thesis work has been the more fundamental aspects of ammonia as a hydrogen carrier and effects of ammonia on PEMFC.

1.3 Problem Statement

The main objective of the Thesis work was to separate different effects of ammonia on PEMFCs, see Figure 1.1.

1.3.1 Conductivity Effects

Ammonia is alkaline. It is thus readily absorbed by the acidic membranes used in PEMFCs forming ammonium in the membrane phase. The ionic conductivity is an important factor determining the performance of PEMFCs. Ammonium reduces the conductivity of Nafion®[3] as pointed out by Uribe *et al.* [20]. Reduced conductivity can be important both as a bulk membrane effect increasing the ohmic drop in the cell, as well as in the active layer on either anode or cathode. Soto *et al.* [21] found that only 10% of the observed performance loss could be assign to ohmic losses in the bulk membrane. It is therefore of interest to study the effect of ammonia on PEMFC membranes in terms of conductivity, but also in terms of other physical properties.

1.3.2 Dilution of Hydrogen Fuel

The resulting fuel gas contains only 75 vol% hydrogen when splitting ammonia. The high content of nitrogen poses a potential problem to stable operation

[3] **Nafion®** is a DuPont registered trademark by E. I. du Pont de Nemours and Company.

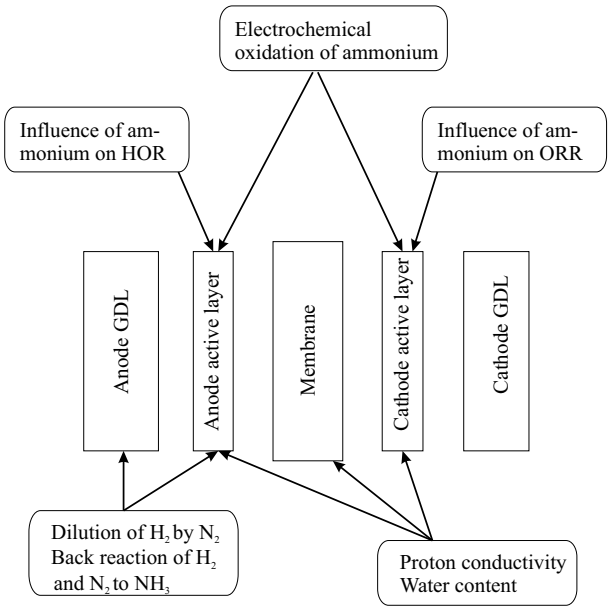

Figure 1.1: Different effects of ammonia on PEMFC performance considered in this Thesis.

of the FC, and will also slightly reduce the Nernstian potential of the cell. It was also of some concern that hydrogen and nitrogen might recombine to ammonium at low temperatures (typical PEMFC operating temperature).

1.3.3 Oxidation and Removal of Ammonia

Oxidation of ammonium on either the anode, or probably more likely, the cathode, is also important for steady state tolerance and for recovery of the FC performance once the cell has been exposed to ammonia. Volatility of ammonium in the membrane phase is also of interest for the same reasons.

1.3.4 Effects on Electrode Kintics

Earlier work by Szymanski *et al.* [25] on PAFC showed that ammonia had an effect on performance, and cathode performance in particular. It is therefore of interest to assess if similar effects are present in PEMFCs, that is, if the

Oxygen Reduction Reaction (ORR) or Hydrogen Oxydation Reaction (HOR) is affected by the presence of ammonium in the FC.

1.4 Methodology

An FC is a complex system even if we only look at the active parts shown in Figure 1.1. In addition, there are many supporting systems and operational parameters like gas supply, humidification of gases, water balance, potential/current control, temperature control, operation under elevated pressure and pressure gradients, manufacture and assembly techniques for Membrane-Electrode Assemblies (MEAs[4]), flow-field design etc. to be controlled. It is thus challenging to make FC measurements that are reproducible and stable, and where we have good control over *all* the operational parameters simultaneously. We have therefore tried to measure the effect of ammonia on the different components of the FC in simplified systems where we more easily can control and reproduce the operational parameters. In addition, testing of single cells is required in order to evaluate the total effect of ammonia.

1.4.1 Single Cell Testing

The test station is designed to perform long term testing of complete FCs with supporting systems. Typical measurements include polarization curves at different intervals, monitoring of internal cell resistance, exposure to ammonia at different concentrations and times etc. One of the cells is fitted with a Reference Electrode (RE), but this RE was, in our experience, not reliable, see also Chapter 4 for a further discussion. It is thus not possible to separate effects on the two electrodes by use of this RE.

1.4.2 Testing of Symmetrical Cells

Overpotentials associated with the cathode are large compared to normal overpotentials observed on the anode. It is therefore difficult to identify effects of ammonia on the anode when making measurements on a complete FC ($H_2|O_2$).

[4]The concept of MEA and GDL is not always clearly distinguished, and use of the terms vary from source to source. In our experiments the active catalyst containing layer was applied to the membrane, hence the membrane with active layers on either side is denoted as MEA. The GDL is a porous carbon cloth through which reactants and products diffuse (gases, water and electrons).

By feeding pure hydrogen to the cathode side of the FC, anode effects due to ammonia and dilution of hydrogen on the anode side are more easily studied. It is possible to determine the polarization of the cathode by running on neat hydrogen on both electrodes assuming that both HOR on the anode and HER on the cathode are associated with the same magnitude of overvoltage at any given current density.

1.4.3 Effect of Ammonium on Membrane Properties

The conductivity of the membrane containing different fractions of ammonium compared to protons was measured in a special conductivity cell. Equilibrium uptake of water and ammonium fraction was also determined in separate studies. Further, we studied the volatility of ammonia in membranes, that is, if ammonium is released from the membrane.

1.4.4 Electrochemical Oxidation of Ammonium

The oxidation of ammonium was studied by Differential Electrochemical Mass Sectroscopy (DEMS), Cyclic Voltammetry (CV), Electrochemical Quartz Micro Balance (EQCM) and Rotating Disk Electrodes (RDE). In DEMS, volatile intermediates and products from the oxidation process may be studied on-line as the potential of the Working Electrode (WE) is swept in a slow CV. In EQCM, the resonant frequency of a quartz crystal is monitored as the potential of the WE is swept. The *net* mass of the species adsorbing and desorbing on the electrode can then be determined. DEMS and EQCM are complimentary methods as they are designed to identify volatile and adsorbed species respectively. The RDE method was used to evaluate if soluble species were formed.

1.4.5 Effect of Ammonium on HOR and ORR

To more clearly identify the effect of ammonium on ORR, measurements with an RDE were made in acidic aqueous solutions. Typical techniques include variation of rotation speed and Linear Sweep Voltammetry (LSV). The effect of ammonium on HOR was studied in a symmetrical cell discussed above.

1.5 Outline of Thesis

This Thesis is organized as a collection of individual Chapters dedicated to the different topics covered in this Thesis. This format is chosen because some of the work has already been published and some will be published later. It is therefore easier to divide the Thesis into separate Chapters. This format unavoidably leads to some repetition of background information, but this has hopefully been kept to a minimum. Appendices are used to elaborate on issues that are not essential for the understanding of the results.

Chapter 1. Introduction. Gives a short summary of the history of FCs. Some present and future applications for FCs are also reviewed. The motivation for the project as well as problem statement and methodology is presented

Chapter 2. Ammonia as Energy Carrier. Summarizes available literature on use of ammonia as a hydrogen carrier. Synthesis, splitting, health related issues as well as energetic efficiency of ammonia as hydrogen carrier are discussed. Parts of this chapter has been presented at the 4^{th} Nordic Symposium on Hydrogen and Fuel Cells for Energy Storage in Helsinki, Finland, December 2000

Chapter 3. Influence of Ammonium on conductivity and water content of Nafion® 117 Membranes. In this chapter we discuss how ammonia affects conductivity, including activation energy for ionic conduction, water content and swelling effects of the membrane phase. Equilibrium isotherms between the membrane phase and the equilibrating aqueous phase are also measured. The results in this chapter have been presented at the 202^{nd} Meeting of The Electrochemical Society, Third International Symposium on Proton Conducting Membrane Fuel Cells, Salt Lake City, UT, USA October 2002 with a paper in the proceeding volume. A slightly revised paper, which is the same as the one in this Thesis, has been published in Journal of The Electrochemical Society [26]

Chapter 4. Influence of Cell Geometry on ac Impedance Measurements as Applied to PEMFCs. The complications of using a reference electrode in a cell with a thin electrolyte is reviewed, and theoretical calculations presented. A suggestion for a revised cell design is made. The

results presented in this section have been presented as a poster at the 1st European PEFC Forum held in Lucerne, Switzerland [27]

Chapter 5. Effect of Inert Components. The dilution effects of nitrogen in hydrogen were assessed in a single cell test, and compared with the effects of noble gases (He and Ar) as well as CO_2. Some of the results from this chapter have been presented by Preben J. S. Vie as a poster on the 7th Grove Fuel Cell Symposium in London, UK, September 2001

Chapter 6. Electrochemical Oxidation of Ammonium. Reaction mechanisms suggested in the literature for oxidation in alkaline solutions are reviewed and compared to our findings in acidic solutions. Oxidation products and formation of adsorbed species on Pt in acids containing ammonium are studied. Tomáš Bystroň helped out with Cyclic Voltammetry measurements on platinized platinum in perchloric acid. Frode Seland performed the measurements on the RDE. Some of the results in this chapter were presented at the 203rd Meeting of The Electrochemical Society in Paris, France, May 2003

Chapter 7. Influence of Ammonium on ORR. The influence of ammonium on Pt in sulfuric acid has been measured. Tomáš Bystroň performed most of the measurements and also contributed to the interpretation of the results. The results are to be presented at the 55th Meeting of the International Society of Electrochemistry in Thessaloniki, September 2004

Chapter 8. Influence of Ammonium on Fuel Cell Reactions. Both the effects of ammonium on ORR and HOR have been assessed in regular fuel cells ($H_2|O_2$) and in symmetrical cells ($H_2|H_2$) respectively. Anne-Kristine Meland and Ole-Erich Haas performed some of the measurements

Chapter 2

Ammonia as Hydrogen Carrier

2.1 Summary

A comprehensive literature review of ammonia as hydrogen carrier, with emphasis on Fuel Cells (FCs) is presented.

Ammonia is a hydrogen carrier that should be considered for use as hydrogen source for FCs. It has a relatively high energy density, it is a well known chemical commodity product, and the energy efficiency of the production process is the same as f. ex. for methanol. Present production is based on fossil fuels and natural gas in particular, but production based on renewable energy sources is feasible. Economically viable, large scale production of hydrogen and all other hydrogen carriers is presently also based on fossil fuels. Carbon capture from fossil fuel based ammonia production is highly feasible; it is actually a vital part of the synthesis. Ammonia based on natural gas can thus be a nearly "CO_2 -free" fuel. To realize truly CO_2 -free fuels, renewable energy sources are needed. The major draw-back with any hydrogen carrier is the cost, both economical and energetic, of synthesizing it from either fossil or renewable energy sources and subsequent splitting or reforming to hydrogen.

Ammonia has advantages over f. ex. methanol and especially hydrocarbons because splitting of ammonia is a relatively simple process although high temperature is required. The drawback is that acidic FCs have a limited tolerance to ammonia. Alkaline and high temperature FCs have high tolerance to ammonia.

More evaluation is needed to properly assess environmental impact of large scale use of ammonia and to ensure safe handling on a consumer level. Health

hazards connected with ammonia may limit its application to professionally maintained systems. Pre-split ammonia may be the fuel available to the consumer, not ammonia as such.

Introduction of hydrogen carries also poses considerable need for investment in infrastructure. Such investments will not be made for any hydrogen carrier unless the infrastructure is usable for decades to come. In fact, hydrogen carriers may impede the introduction of pure hydrogen, believed by many to be the ultimate fuel of the future.

2.2 Introduction

Ammonia is the most important petrochemical product as measured by sales [28] with a world-wide installed production capacity of 135.7 10^6 metric tons N/annum [29]. About 85 % of the production was used for fertilizers in 1997 [29], either directly or in the form of nitrate salts or urea. The ability to fixate nitrogen from air was probably one of the most important technological achievements of the 20^{th} century. In Norway, Norsk Hydro was founded based on the electric arc technology developed by Kristian Birkeland and Sam Eyde in which nitric oxides are formed at about 3000°C [30]. However, ammonia synthesis with subsequent oxidation, for which Fritz Haber (1918) and Carl Bosch (1931) received the Nobel Prize in chemistry, proved to be a much more efficient and economical process. Today, more than 90 % of the Worlds production of ammonia is based on the Haber-Bosch synthesis [28].

As discussed in Chapter 1.1.3, use of energy carriers, or in the case of low temperature FCs, hydrogen carriers, is a likely scenario, at least in a transition period going from fossil to renewable energy. Some work has been undertaken with ammonia as a hydrogen carrier, both experimental and theoretical. However, the use of ammonia as a hydrogen carrier for FCs has not benefited from as much research efforts as methanol, gasoline or metal hydrides. Ammonia presents many interesting characteristics as a hydrogen carrier:

- High hydrogen content
- Ease of storage
- Ease of hydrogen extraction
- Widely available

- Synthesis can be designed to have low emissions of CO_2, which is an advantage in terms of global warming [31], see also Sec. 2.3.1
- Carbon-free hydrogen carrier, can thus be used in AFCs, which have potential advantages over other fuel cell technologies [32–34]
- Absence of carbon monoxide in the FC hydrogen feed stream, a poison for most electrocatalysts, especially in low-temperature FCs. However, traces of ammonia affect performance of acidic FCs [19–21, 25]
- Production, storage, and transport of ammonia are well understood industrial processes that have been optimized for nearly a century. There are also rules, regulations and procedures in place for safe handling of ammonia on an industrial scale, mainly because of its use as a fertilizer [29, 35, 36]
- The flammability range is relatively narrow with the lower concentration limit for explosive air/ammonia mixes being relatively high
- Strong smell makes detection of small leaks easier. However, in the event of acute emissions, ammonia is toxic and harmful to humans and the environment

In this chapter the following issues will be addressed:

- Physical properties of ammonia, ammonia storage and transportation, and health related properties of ammonia.
- Review of available literature on ammonia used as hydrogen carrier
- Rough estimates on the efficiency of an ammonia fuel cycle
- A brief comparison to other hydrogen carriers

2.3 Properties of Ammonia

2.3.1 Physical Properties of Ammonia

Physical properties of ammonia are readily available from standard chemical engineering sources [29, 37]. Only some of the key properties are given here. Ammonia is a compound of nitrogen and hydrogen (NH_3) with a molecular weight of 17.03 g/mol. The hydrogen content is 17.6 wt%. At ambient temperature and sea-level pressure, ammonia is a colorless, lighter-than-air gas, with a pungent and characteristic odor with a density of 0.7016 kg/m^3. Ammonia can be liquefied, either by compression (1003 kPa at 25 ^{o}C), or cryogenically (-33.43 ^{o}C at 101 kPa). The liquid densities are 603 and 682 kg/m^3 respectively [29]. The LHV of vaporous ammonia is 18.577 MJ/kg, and the HHV is 22.543 MJ/kg at 25 ^{o}C [29]. The heat of vaporization is temperature dependent; 1.370 MJ/kg for the cryogenic liquid and 1.166 MJ/kg for liquid ammonia at 25 ^{o}C.

Synthesis of Ammonia

Production of ammonia is predominantly based on fossil fuels, and especially on production of synthesis gas from natural gas with subsequent synthesis of ammonia based on the Haber-Bosch synthesis. Ammonia production may also be based on water electrolysis as the hydrogen source and air separation as the nitrogen source, followed by the Haber-Bosch synthesis. However, this synthesis route is presently not economical due to the difference in energy price between electricity and natural gas. Norsk Hydro based their production of ammonia on water electrolysis from around 1930 to 1965 [30].

The actual synthesis route is dependent on which feedstock the process is based on. However, all routes have a CO_2 removal step upstream the synthesis step because CO and CO_2 are poisonous to the ammonia synthesis catalyst. In other words, most of the carbon in the feedstock is separated from the synthesis gas and may be disposed. Presently this CO_2 is partly used as a chemical for other chemical industry like urea production and for production of beverages, but mostly released directly to atmosphere [38].

The primary reformer in the conventional steam reformer flow scheme is heated with fuel gas. The CO_2 emissions due to the fuel gas heating are about 30% of the total CO_2 emissions. However, new technology based on more intensive heat integration of the primary and secondary reformer, so-called

Auto-Thermal Reformer (ATR), eliminates the fired furnace. In order to close the heat balance, excess air or oxygen enriched air is required in the reformer. This way, nearly all CO_2 is captured in the CO_2 removal step [39]. Further, emissions of NO_x are reduced by about 50% [39].

Other synthesis routes for ammonia have also been considered, like conversion in homogenous solutions containing organometallic complexes which catalyze ammonia formaion [29], and electrolytic synthesis in molten salts via formation of nitride [40]. Use of bacteria and algae may also be possible [41]. However, none of these processes are presently commercial.

2.3.2 Corrosion Properties

Ammonia corrodes copper, zinc and their alloys with the exception of some cupronickel alloys [35]. Iron, steels and aluminium are suitable construction materials, but it is recommended that the ammonia should contain 0.2-0.5 % water because this acts as an inhibitor protecting against stress corrosion cracking [35, 36]. Rubber and plastics may be affected by ammonia, and are usually avoided in the construction of devices for ammonia handling [35].

2.3.3 Storage and Transportation of Ammonia

Ammonia is usually chilled to -33 ^{o}C (boiling point at ambient pressure) for large scale storage and transportation [39]. Pressurized vessels are more economical for small scale storage [36]. 10 million metric tons of ammonia were shipped by ocean going vessels in 1991. The use of barges and rail cars is also very usual. Dedicated pipelines for ammonia transportation have been built; two in the U.S. (MidAmerica Pipeline System and Gulf Central Pipeline), and one from Russia to Ukraine (2424 km long) [36].

2.3.4 Health Related Properties of Ammonia

The toxicity of ammonia is often underplayed in the technical literature where ammonia is considered as a hydrogen carrier. Use of ammonia is widespread due to its application in agriculture and cooling systems, therefore a lot of experience data exist as to how ammonia affects humans. US poison control centers reported around 6000 cases of ammonia exposure in 1998 alone. 13% of these exposures resulted in serious conditions [42].

Exposure Levels

There are three measures of permissible exposure levels to ammonia [42]:

- Time-Weighted Average (TWA): This is the concentration which workers can be exposed to for 8 hours a day, 5 days a week without harm; **25 ppm for ammonia**
- Short-Time Exposure Limit (STEL): This is the concentration that is dangerous after 15 minutes and can produce immediate or chronic harm; **35 ppm for ammonia**
- Concentration Immediately Dangerous to Life or Health (IDLH); **500 ppm for ammonia**

Effects of different ammonia exposure levels may be found in the literature, but different sources differ somewhat [41]. The data in Table 2.1 are taken from [29].

Table 2.1: Health related effects of exposure to different concentrations of ammonia [29].

Conc. (ppm)	Effect
9-45	Perception limit
50-72	Respiration is not disturbed
100	Irritation of nose and throat is observed. Burning sensation in the eyes
200	Headache and nausea in addition to previous symptoms
250-500	Tachypnoe and tachycardia
700	Immediate onset of burning sensations in the eyes
1000	Immediate coughing
1700	Coughing with laboured breathing, sometimes with momentary inability to breath
2500-4500	May be fatal after short exposure
5000	Death caused by respiratory arrest

Immediate Toxicity

The effects of short-time exposure to high concentrations of ammonia are well known due to the many accident reports available. Yet, it is difficult to match these effects to the precise concentrations that induced them [42]. Damages include (see [41] for a more comprehensive review and further references):

- General symptoms for heavily intoxicated subjects
  - Moderate to severe shock
  - Vomiting sometimes occurs, which may be bloodstained either from the stomach or the larynx
  - Patients may suffer minor delirium
  - Patients suffer migraine and nausea
  - Heart pulse varies from unusually rapid to imperceptible
- Skin damages
  - Thermal burns either due to heat release when absorbed in bodily fluids, or frost bite due to vaporization of liquid ammonia
  - Alkali burns of the skin. Alkali burns due to ammonia are often much more severe than those caused by other alkalis. Alkalis penetrate deeply inside the tissues because they liquefy them
- Respiratory tract damages
- Digestive tract damages
- Eye damages – The eye is very sensitive to ammonia exposure. Eye damages result from thermal and alkali burns
- Internal organs may also be affected
- Patients' fates – Many patients treated for ammonia intoxication recover in 2–3 weeks. Some endure chronic residual affections (loss of eye sight, scars, bronchitis). Mental affections such as anxiety and insomnia may also remain. Yet, several patients died due to the severity of the intoxication, or to impairing initial physical condition. Death occurred within 48 hours and 2 weeks of the exposure to ammonia. In closed spaces, mortality rates approached 75%. Patients that previously suffered lung diseases, especially respiratory disease, are particularly at risk

Environmental Impact

The major source of ammonia emissions today is agriculture. In Canada the total estimated emissions of ammonia in 1990 was 651 000 tonnes. 87% came from agriculture, hereof 82% from animals and 18% from fertilizers [43]. When the total fixation of N is considered (N_2O, NO and NH_3), fertilizers contribute 60%, legume crops about 27% and combustion of fossil fuels 13% [44]. Human caused emissions of the total global emissions are 70% for ammonia, 80% for NO, and 40% for N_2O [44].

Greenhouse Gases Ammonia itself may not be considered a GHG because of its solubility in water [35]. However, ammonia may form nitric oxides of which especially N_2O is a very potent GHG [44]. Production of ammonia itself releases GHGs, CO_2 in particular, when fossil fuels are used as feed stock for the synthesis.

Acidification and Eutrophication Nitrogen (nitric acid, ammonia and ammonium) contributes to the acidification of ecosystems because uptake of ammonium as well as nitrification release protons [44]. Plant growth in freshwater is generally limited by availability of phosphorous, thus nitrogen components are normally not a problem. In costal waters the situation is the reverse [43]. Growth of toxic plankton is highly stimulated, fish die and the diversity of the biotope is greatly reduced.

Smog and Particulate Matter Nitric oxides contribute to smog problems. Ammonia emissions also contribute to smog due to formation of particulate matter when converted to ammonium nitrate and sulfate upon contact with atmospheric acidic emissions. The effects on humans include an aggravation of existing affections, impaired breathing, impairment of the immune system, cardiac system stress and premature death in some cases. Particulate matters also screen the sunlight and reduce visibility [43].

Emissions from Ammonia Synthesis Ammonia synthesis plants emit several chemicals to the environment. The actual emissions depend on age of the plant, feed stock used etc., but emission levels from typical existing plants are available [39]:

- Emissions to air. 1.65–1.8 t CO_2/t NH_3, 0.9 kg NO_x/t NH_3, <0.01 kg SO_2/t NH_3 depending on fuel, <0.03 kg CO/t NH_3
- Emissions to water. NH_3 or NH_4^+ (as N) 0.1 kg N/t NH_3
- Solid wastes. Spent catalyst etc. <0.2 kg/t NH_3

In addition, amine solution in the CO_2 removal process is used at a rate of 0.02–0.04 kg/t NH_3. Methanol and large parts of the ammonia emissions to water have been dramatically reduced in modern plants. No data were available for methanol emissions [39].

2.4 Direct Combustion of Ammonia

Early experiments carried out by Norsk Hydro with ammonia as a fuel for ICE took place as early as 1933, see Figure 2.1. The truck ran on a ammonia/hydrogen mix, but there were problems with emissions of unburnt ammonia as well as NO_x formation. Additions of gasoline were tried, but this resulted in the formation of hydro cyanic acid (HCN) [30].

A group of students and their supervisor at University of Tennesse converted a gasoline engine for running on ammonia [45]. There has also been several other studies, both with ICEs and Gas Turbines, mainly in the 60ties, see Gay and Ehsani [41] for more details and further references.

Due to the low flammability of ammonia, it may be advantageous to partially split the ammonia before entering the ICE [46, 47]. There seems to be disagreement as to which residual levels of ammonia that are acceptable (5% residual ammonia [47] and 1.25 to 2.5% hydrogen in the fuel [46]).

2.5 Ammonia as Fuel for Fuel Cells

In Direct Ammonia Fuel Cells (DAFC), ammonia is fed directly to the FC anode where it is catalytically oxidized in the anode reaction. In Indirect Ammonia Fuel Cells (IAFC), ammonia is first dissociated into nitrogen and hydrogen and then fed to the anode. The dissociation reaction is referred to as *cracking* or *splitting*.

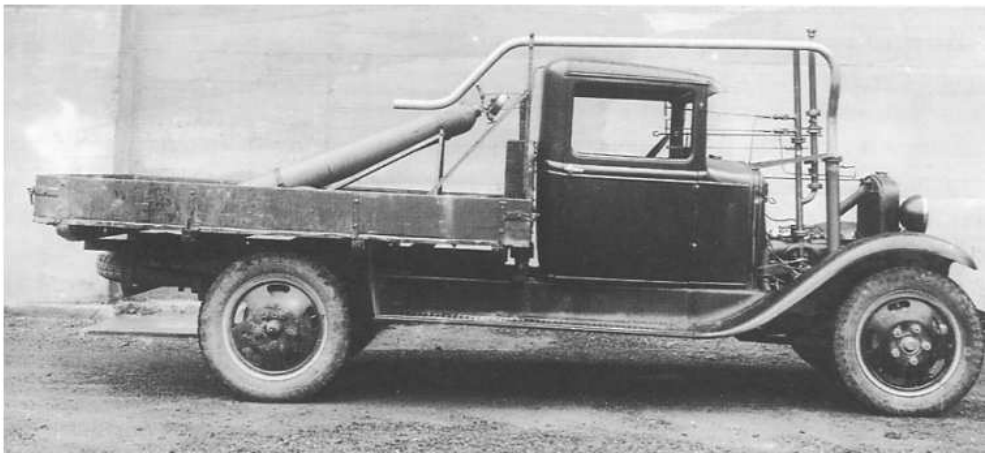

Figure 2.1: Experimental truck used by Norsk Hydro in 1933–1936 for testing ammonia and ammonia/hydrogen mixtures as fuel [30].

2.5.1 Direct Ammonia Fuel Cells

Alkaline Fuel Cells

Direct oxidation of ammonia in alkaline solution for application in FCs was studied particulary in the 1960ties and early 1970ties. We will revert in more detail to the papers dedicated to oxidation mechanism of ammonium on platinum in Chapter 6.

The net reaction for oxidation of ammonia is:

$$2NH_3 + 3/2O_2 \rightarrow N_2 + 3H_2O \tag{2.1}$$

with an E^0 of 1.172 V at standard conditions compared to 1.229 V for hydrogen fuelled FCs. The oxidation rate is significant only in alkaline solutions, and occurs mainly at potentials in the double layer region of platinum [48, 49]. However, even in alkaline solutions the oxidation rate of ammonium is relatively modest, and there is a tendency to self-poisoning of the electrode by formation of N_{ads} species, see Section 6.2.1 and subsequent sections for further details. Recently, it was shown that the oxidation of ammonia on platinum is very sensitive to the surface structure of platinum with Pt(1 0 0) being the most active [50].

Current efficiency Oxidation of ammonia in alkaline solutions was studied as early as in 1905 by Müller and Spitzer [51] by galvanostatic experiments. They found that several oxidation products were formed (N_2, NO_2^- and NO_3^-). In addition, about 23 % of the total passed current could not be accounted for. We did not find any data regarding the potential at which the anode was operated under during these experiments. In 1963, Katan and Galiotto [52] also performed galvanostatic experiments. They found that only N_2 was formed. The anode potential was 0.3 to 0.7 V_{RHE} during these experiments.

Oxidation rate and catalysts In 1961, Wynveen reported experiments with an alkaline DAFC, but with low performance (OCV about 0.5 V depending on temperature, and a maximum current density of 35 mA/cm^2 at 0.2 V and 80 °C [53]). Oswin and Salomon [22] also found that the oxidation rate was low. They also performed mechanistic studies which will be discussed further in Section 6.2.1. McKee *et al.* [54] tried to develop more efficient electrocatalysts based on iridium and Ir-Pt alloys. They found especially pure Ir to be more efficient in the DAFC, reducing the anodic overpotential by 100-120 mV at current densities at least up to 300 mA/cm^2 for unsupported electrocatalysts. The gain was slightly less for supported catalysts. Simons *et al.* [55] developed Teflon®[1] bonded electrodes containing carbon supported Pt catalysts, and obtained power densities of 50 mW/cm^2 at 0.5 V and elevated temperatures (120 °C) in a DAFC/air FC with 2.5 mg/cm^2 catalyst loading.

Effect of pH Frick *et al.* found oxidized platinum to be inactive for ammonia oxidation and that oxidation was very slow at pH$<$ 9.5. Spahrbier and Wolf [56] found that both the maximum quasi-stationary oxidation rate, as well as the potential at which this rate occurred, were dependent on the pH of the solution dropping markedly off between pH=12.8 and 12.2.

Solid Oxide Fuel Cells

There have been some reports on using ammonia as fuel for SOFCs. The high operating temperature probably facilitates splitting of ammonia to nitrogen and hydrogen. The performance of ammonia in an SOFC will thus be relatively good. However, if the ammonia used is produced from natural gas, it would be more fuel efficient to use the natural gas directly. SOFCs have capabilities for

[1] Teflon® is a registered trademarks of E.I. du Pont de Nemours and Company

internal reforming of natural gas, or can easily be thermally integrated with external reformers due to the high operating temperature of the SOFC.

Farr and Vayeans [57] studied the possibility of converting ammonia to nitric oxide in a SOFC to take advantage of the released energy. Oxidation of ammonia is usual in the fertilizer industry to produce nitrate based fertilizers. Gamanovic and Novikov have published several brief communications describing the use of ammonia and ammonia/alcohol mixtures as fuel for SOFC [58–60]. However, the current densities obtained seems to be very low (about 0.1 mA/cm^2). Singhal *et al.* [61] found that addition of 5000 ppm NH_3 to the fuel had no negative effect on the SOFC operation for 2500 hours; ammonia actually acted as a fuel increasing the cell voltage. Wojcik *et al.* [62] incorporated a splitting catalyst (steel wool and finely divided iron oxide) inside a tubular SOFC. The performance of the SOFC was more or less the same as with pure hydrogen fuel when using the iron catalyst for ammonia decomposition.

An ongoing EU-project (ACCEPT, Ammonia Cracking for Clean Electric Power Technology) [63] looks into using ammonia for SOFCs. No detailed results from this project have been found.

Hydrazine as Fuel for Fuel Cells

In the late 1960ties and early 1970ties there was also some activity in making FCs based on hydrazine (N_2H_4) as fuel. Examples here are conversion of a Puch motor cycle and an Austin car to run on hydrazine (Dr. Karl Kordesch of Union Carbide) [49]. There has been much less research on hydrazine lately partly because hydrazine is classified as carcinogenic. However, a direct PEM hydrazine fuelled FC has been reported recently [64], but fuel crossover is a problem. In some cases also chemical decomposition of the fuel to either ammonia or nitrogen and hydrogen occurs. The cell voltage at low currents is however high (OCV 1.2 V, 0.9 V at 50 mA/cm^2).

2.5.2 Splitting of Ammonia

Splitting of ammonia is a well known endothermic reaction [29]:

$$NH_3 \rightleftarrows 1/2N_2 + 3/2H_2 \qquad \Delta H^0 = 46.22\ kJ/mol \tag{2.2}$$

Equilibrium of Ammonia Splitting

Splitting of ammonia is favoured by high temperature and low pressure according to Le Châtelier principle because the reaction is endothermic and has a positive change in stoichiometric coefficients. The equilibrium is given by:

$$K = \sqrt{\frac{a_{N_2} a_{H_2}^3}{a_{NH_3}^2}} = p_{tot} \sqrt{\frac{y_{N_2} y_{H_2}^3}{y_{NH_3}^2}} \sqrt{\frac{\varphi_{N_2} \varphi_{H_2}^3}{\varphi_{NH_3}^2}} = p_{tot} K_y K_\varphi = K_p K_\varphi \tag{2.3}$$

We assume that the fugacity coefficients, φ_i, of the gas species are unity (*i.e.*, $a_i = y_i \varphi_i p_{tot} = y_i p_{tot}$), and thus $K_\varphi = 1$. This assumption is justified at low pressures [65]. If we assume that 1 mol of NH_3 is split with equilibrium conversion ξ_{NH_3}, $1 - \xi_{NH_3}$ mols of NH_3 remains and $1/2\,\xi_{NH_3}$ mol N_2 and $3/2\,\xi_{NH_3}$ mols H_2 is formed, so that the total amount of gas is $1 + \xi_{NH_3}$ mols. Combining this with the relation $K_y = K/p_{tot}$, we get:

$$\xi_{NH_3} = \sqrt{\frac{K_y}{\sqrt{27/16} + K_y}} \approx \sqrt{\frac{K_y}{1.299 + K_y}} \tag{2.4}$$

The equilibrium constant is calculated from

$$\Delta G^0 = -RT \ln K \tag{2.5}$$

Values of ΔG^0 at different temperatures are given by Appl [29] from 300 K to 1000 K. Linear extrapolation was used to estimate ΔG^0 at higher temperatures. The equilibrium composition of ammonia, nitrogen and hydrogen at different temperatures and pressures is shown in Figure 2.2.

Catalysts for Splitting of Ammonia

Different catalysts may be used to promote the splitting reaction. Catalysts used for synthesis of ammonia, like Girdler G-56 (NiO on Al_2O_3) and G-41 (iron oxide on Al_2O_3), are suited [66]. Ni, Co, Cu, Os, Zn and U based catalysts also exhibits activity towards ammonia splitting [47, 67]. Boffito and Baker studied alloys based on $Zr_{1-x}Ti_xM_1M_2$ where M_1, M_2 were selected from Cr, Mn, Fe, Co and Ni mixed with 20-50 wt% Al (either as a mechnical binder and/or an element in the alloy). They found the splitting activities to be 2-3 times higher than the commercially available St 909 alloy (40.5% Zr, 24.5% Mn, 25% Fe and 10% Al binder) [47]. However, the scope of these studies

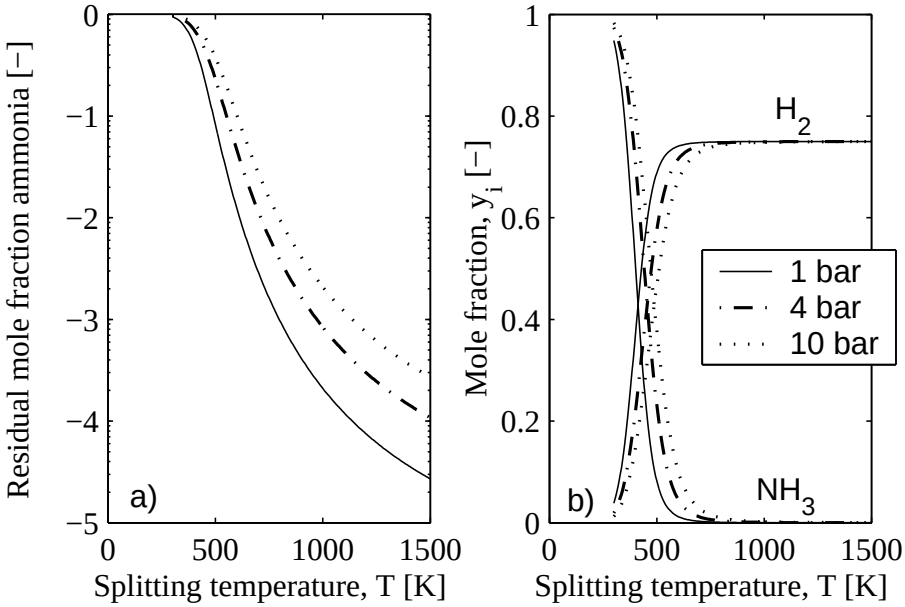

Figure 2.2: Equilibrium for splitting of pure ammonia at different pressures and temperatures. a) residual ammonia in splitted gas (semi-logarithmic plot vs. splitting temperature) and b) mol fractions of hydrogen and ammonia in the splitted gas.

was for use in AFCs or ICEs; hence the residual ammonia in the gas could be relatively high (>1 vol%).

Precious metal based catalysts have been studied in the literature to attain higher conversions at relatively low temperatures and lower catalyst loadings. It is found that the activity for ammonia splitting is higher for Ir wire than for Rh, Pd, and Pt wires, but the catalyst substrate as well as the loading is important [68]. Choudhary *et al.* found that 65% Ni on SiO_2/Al_2O_3 had similar performance as 10% Ir on SiO_2 [68]. They also found supported Ru to be more active than supported Ir in contrast to the finding with metal wires of the precious metals. Faleschini *et al.* [67] also found Ru supported on NiO to be the best performing catalyst of the ones tested (Pt, Rh, Pd, La_2O_3, Ru on either NiO or Al_2O_3).

Ammonia Splitter Designs

The ammonia splitter designs mainly differ in how heat is supplied for the reaction, see [41] for a more comprehensive description. The heat may be supplied from an **external furnace** heating the outside of the splitting reactor by combustion of tail gas from the FC anode[2]. The external furnace design is the only one in which the tail gas may easily be used to split incoming ammonia. To enhance the responce time of the splitter, it has been suggested to burn ammonia directly in the external furnace. Formation of NO_x is then a risk. Alternatively, propane or similar could be used [66], but with added system complexity and need for filling and storing two fuels.

It is also possible to use **electric heating**, but the thermal efficiency of the system is then lower because the efficiency of the FC is lower than that of an external furnace. Further, tail gas from the FC would not be utilized. It is also possible to perform **auto-thermal splitting** where a sufficient amount of air is added to the incoming ammonia so that the combustion of ammonia/hydrogen by oxygen from air provides the required heat for splitting ammonia. The drawback is that the concentration of hydrogen in the fuel is lower due to dilution by nitrogen from air in addition to nitrogen from the splitting reaction. Further, the tail gas from the FC is not used. It is also possible to combine **auto-thermal and external furnace** designs to enhance efficiency by utilizing the tail gas, but simultaneously incorporate the much more efficient heat transfer in auto-thermal designs and thus shorter start-up times and enhanced response times to load changes.

Integration of a hydrogen separation unit in the splitter has also been discussed both for use in ammonia synthesis as well as ammonia splitting [69, 70]. One option would be to use a thin palladium membrane through which hydrogen can permeate. This would reduce problems associated with inert components in the fuel. It would also promote the splitting of ammonia because the partial pressure of hydrogen would be reduced. Lower splitter temperatures could then also be used because the separation would favour the splitting reaction.

[2]The conversion of hydrogen in the FC can not be 100% due to the presence of inert N_2 in the fuel.

2.5.3 Indirect Ammonia Fuel Cells

Alkaline Fuel Cells

Ammonia does not pose a poisoning problem in AFC (ammonia may be used as a fuel directly). Therefore, hydrogen from splitted ammonia would be well suited for AFCs [32–34]. Further, AFCs do not tolerate CO and CO_2 due to formation of carbonates in the electrolyte. Nitrogen containing hydrogen carriers (ammonia and hydrazine) are therefore preferred over carboneous carriers. Indeed, several studies of this application have been published. One of the earliest was a Swedish study on propulsion of a submarine by use of ammonia and air driven FC [49]. However, the project was never realized. Apollo Energy Systems (former Electric Auto Corporation) together with University of Graz still have activities on using hydrogen from ammonia to fuel AFCs [34, 67].

Polymer Electrolyte Membrane Fuel Cells

Studies have shown that ammonia reduces performance of PEMFC even when exposed to concentrations as low as to 13 ppm [20, 21]. It has therefore been suggested that ammonia needs to be removed, f. ex. by adsorption in Nafion® beads [20], highly specific adsorbents [18], or in acid absorbed in silica [71].

Integration of ammonia splitting and a 50 W PEMFC has been demonstrated ([18] and references therein). The ongoing EU-project ACCEPT [63] also looks into using ammonia for PEMFCs, but no results have been found in the open literature. The poisoning mechanisms and tolerance towards ammonia in PEMFC will be discussed in detail later in this Thesis.

Phosphoric Acid Fuel Cells

One example of an IAFC for PAFC was described by Adlhart and Terry [72]. They designed a relatively small system (100 W net effect) based on an electrically heated ammonia splitter. An overall thermal efficiency of 30% was found, even for this small system. No data on long-term performance have been found.

Later, Collins *et al.* [71] developed a 300 W system with an externally fired ammonia splitter operating at about 850 °C using precious metal catalysts. The rest concentration of ammonia was about 100 ppm and reduced to <1 ppm by absorption in sulfuric acid adsorbed on silica gel. They reported the system to be operational for several months. They also reported a system efficiency

of 50% at the design point falling off towards lower loads mainly due to less efficient ammonia splitting.

Szymanski *et al.* [25] studied the effect of ammonia in the fuel gas on PAFC performance. They found that the poisoning lead to formation of $(NH_4)H_2PO_4$, which reduced the performance of the cathode. The FC recovered fully after exposure to ammonia when running on pure hydrogen and air. They concluded that ammonium was oxidized in the cell at the cathode such that the cell had a steady state tolerance towards ammonia in the fuel stream. The tolerance was higher at higher operating voltages of the cell. They did not observe any back reaction of hydrogen and nitrogen to form ammonia (the reverse of reaction 2.2).

Molten Carbonate Fuel Cells

Kawase *et al.* [73, 74] studied the effect of traces of ammonia and NO_x on the performance of an MCFC experimental cell. 500 ppm ammonia had no effect on performance during 1200 hours. NO_x had a slight effect forming NO_2^- and NO_3^- in the electrolyte.

Solid Oxide Fuel Cells

The temperature of the SOFC is relatively high so that internal reforming in the FC itself is probably feasible. This has already been discussed in Section 2.5.1.

2.6 Efficiency of an Ammonia Fuel Chain

2.6.1 Definition of Fuel Cell Efficiency

The basic relations and definitions of the different thermodynamic functions etc. are given in standard textbooks such as Laidler and Meiser [75] and are used here without further references. The general definition of efficiency is

$$\eta = \frac{-w}{q} \tag{2.6}$$

We here use the IUPAC convention that work, w, done on the system and heat, q, supplied to the system both are positive quantities.

Ideal Efficiencies

Electrochemical cell. The attainable electrical work $w_{el} = w_{non-pV}$ from an FC follows from the definition of Gibbs energy, $G = H - TS$, enthalpy, $H = U + pV$, and internal energy, $U = q + w$. Kinetic and potential energy of the control volume are neglected in the further discussion. The change in internal energy, U, may be expressed as:

$$\begin{aligned} \mathrm{d}U &= \mathrm{d}q + \mathrm{d}w \\ &= T\mathrm{d}S + \mathrm{d}w_{pV} + \mathrm{d}w_{non-pV} \\ &= T\mathrm{d}S - p\mathrm{d}V + \mathrm{d}w_{non-pV} \end{aligned} \tag{2.7}$$

$\mathrm{d}q = T\mathrm{d}S$ since the process is reversible, and $\mathrm{d}w_{pV} = -p\mathrm{d}V$ since the volume change of the process is $\mathrm{d}V$. The change in Gibbs energy is given by:

$$\begin{aligned} \mathrm{d}G &= \mathrm{d}H - T\mathrm{d}S - S\mathrm{d}T \\ &= \mathrm{d}U + p\mathrm{d}V + V\mathrm{d}p - T\mathrm{d}S - S\mathrm{d}T \\ &= \mathrm{d}U + p\mathrm{d}V - T\mathrm{d}S \end{aligned} \tag{2.8}$$

We have here assumed that the processes takes place at constant temperature ($\mathrm{d}T = 0$) and constant pressure ($\mathrm{d}p = 0$). Combining Equations 2.7 and 2.8 we get:

$$\mathrm{d}G = \mathrm{d}w_{non-pV} \quad \text{or} \quad \Delta G = w_{non-pV} = w_{el} \tag{2.9}$$

ΔH is the *heat of reaction*, and is therefore normally considered as the energy available from a given (combustion) reaction. The definition of the FC efficiency η_{FC} then becomes:

$$\eta_{FC} = \frac{w_{el}}{\Delta H} = \frac{\Delta G}{\Delta H} \tag{2.10}$$

There is however a problem with this definition of efficiency as pointed out by Lutz *et al.* [76]. Equation 2.10 will give efficiencies greater than unity for reactions which have a positive entropy change ($\Delta S > 0$). This is the case for f. ex. oxidation of carbon and higher alkanes to CO and CO_2, and for oxidation of formic acid [13, 77]. The reason is that the reversible heat, $T\Delta S$, must

be supplied from the surroundings at the operating temperature of the FC to maintain the operating temperature of the FC. Lutz *et al.* therefore suggested an alternate definition of the heat input to be used in efficiency calculations:

$$q = \begin{cases} \Delta H & \text{if} \quad \Delta S < 0 \\ \Delta H - T\Delta S = \Delta G & \text{if} \quad \Delta S \geq 0 \end{cases} \tag{2.11}$$

This definition of q means that the efficiency of an FC is always ≤ 1, which it should be.

Heat engine. An isentropic heat engine can convert heat into work, w, by working between two heat reservoirs. The heat q_h is absorbed at T_h and q_l released at T_l. The work is $-w = q_h - q_l$ because $\mathrm{d}U = \mathrm{d}q + \mathrm{d}w = 0$ for the complete cycle which follows from the 1st law. It follows from the 2nd law of thermodynamics that the Carnot efficiency η_C is given by [75]:

$$\eta_C = \frac{q_h - q_l}{q_h} = \frac{T_h - T_l}{T_h} \tag{2.12}$$

As easily seen from Equation 2.12, the higher T_h or the lower T_l, the higher the Carnot efficiency. T_l is for practical purposes bound by the ambient temperature, T_{amb}. The maximum temperature attainable by combustion is the *adiabatic flame temperature*, T_{ad}, defined by:

$$\Delta H = H(T_{ad}, \text{Products}) - H(T_{ad}, \text{Reactants}) = 0 \tag{2.13}$$

However, the adiabatic flame temperature is, by definition, achieved when there is no heat exchange between the reaction and the surroundings, *i.e.*, there is no available heat to drive a heat engine. The appropriate temperature to be used is the *combustion temperature*, T_c[3], defined by [76, 77]:

$$\Delta G(T_c) = 0 \quad \Leftrightarrow \quad T_c = \left.\frac{\Delta H}{\Delta S}\right|_{T_c} \tag{2.14}$$

[3]There is a complication in the definition of the combustion temperature, namely for reactions where $\Delta S \geq 0$. For reactions with small (neagtive) $\Delta S \to 0^- \quad \Rightarrow \quad T_c \to +\infty \quad \Rightarrow \quad \eta_C \to 1^-$ meaning that all enthalpy released by the reaction may be transformed into work in the heat engine, see [76] for further discussion of this. However, when $\Delta S > 0 \quad \Rightarrow \quad T_c < 0 \quad \Rightarrow \quad \eta_C > 1$ which is the same as observed for FCs. The reason is that heat must be supplied to the reaction chamber from the surroundings at the reaction temperature. The correct heat input to use in the general efficiency expression given in Equation 2.6 is not ΔH, but $\Delta H + T\Delta S = \Delta G$ just as for FCs, see Equation 2.11.

A heat engine can now absorb heat at T_c. The reaction runs at T_c, and because $\Delta G = 0$, the process is reversible. Substituting this into the Carnot efficiency expression:

$$\begin{aligned} \eta_C &= \frac{T_h - T_l}{T_h} = \frac{\frac{\Delta H}{\Delta S} - T_{amb}}{\frac{\Delta H}{\Delta S}} \\ &= \frac{\Delta H - T_{amb}\Delta S}{\Delta H} = \frac{\Delta G(T_{amb})}{\Delta H} = \eta_{FC} \end{aligned} \tag{2.15}$$

where we have assumed that ΔH and ΔS are independent of temperature. The interesting result here is that the theoretical efficiency of a heat engine and an FC *is the same. It is therefore not correct to say that the efficiency of a heat engine is limited by the Carnot efficiency whereas the FC is not.* However, the difference is that a heat engine has to operate at T_c, which for hydrogen-oxygen is about 3800 K, a temperature much too high for ordinary construction materials, in order to extract the maximum work ($\Delta G(T_{amb})$). An FC can, in principle, extract this work operating at ambient temperature. The result is not surprising considering Equation 2.9 which showed that the available *non-pV* work from a reaction is the Gibbs energy change of the reaction making no assumption as to which process (FC, heat engine, ...) that converts chemical reaction energy into work.

Real Efficiencies

Fuel chain efficiencies. In addition to theoretical limitations, there are also many other practical limitations to the achievable efficiency. For an FC these may include electrode overpotentials, ohmic losses, mass transport losses, auxilary losses (fans, pumps, electronics), losses in dc/ac conversion, electrical motor if the energy is to be used for vehicular propulsion etc. There are also losses connected with production, transportation and storage of the fuel. Further, reforming/splitting of the fuel, if required before being used in the FC, is also associated with losses. All these losses should be included to assess the real efficiency of any fuel chain. The key question is how much of the energy in the raw materials that is actually converted into useful energy at the point of use. This is especially important for fossil fuels.

Higher and lower heating value The working definition for efficiency is the ratio of work performed by the system to supplied heat as defined in Equation 2.6. The supplied heat is usually set to the enthalpy change of the reaction (with exceptions shown in Equation 2.11). The enthalpy change is also called the *Higher Heating Value* (HHV). However, traditionally the enthalpy associated with water condensation has been regarded as unattainable by heat engines because the exhaust temperature normally exceeds 100 °C. It has therefore been usual to use the *Lower Heating Value* (LHV) in efficiency calculations (LHV = $\Delta H - \Delta H^{cond}_{water}$). Using methane as an example (HHV_{CH_4} = -912 kJ/mol, LHV_{CH_4} = -826 kJ/mol [78]), η_{LHV} = 58% corresponds to η_{HHV} = 52.5%. For pure hydrogen (HHV_{H_2} = -285 kJ/mol, LHV_{H_2} = -242 kJ/mol), the same η_{LHV} = 58% corresponds to η_{HHV} = 49.2%. In other words, reported efficiencies are quite often misleading because one does not consider *all* the available heat of reaction in the calculation of efficiencies. The condensation energy is actually attainable in low temperature FCs because water may be produced as a liquid.

Gibbs energy as measure of available work from a chemical reaction. It is sometimes argued that the Gibbs energy should be used in calculation of efficiency as the energy input to the FC instead of the enthalpy [14]. This would lead to unity theoretical efficiency for all processes, both FCs and combustion engines, because the Gibbs energy is the available *non-pV* work from a chemical reaction, see Equation 2.9. However, this way of defining efficiency is related to the reversibility of the process and the *exergy* concept [79]. This efficiency shows how much of the ideally available work that is actually converted from chemical energy to work.

2.6.2 The Ammonia Fuel Chain

A schematic of the ammonia fuel chain is shown in Figure 2.3.

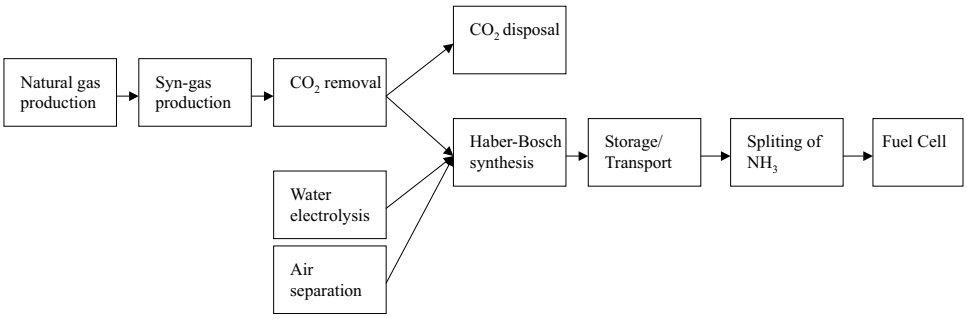

Figure 2.3: Schematic representation of an ammonia fuel chain.

Table 2.2: Energy efficiency of the different links in the ammonia fuel chain. The ammonia production is based on either water electrolysis or natural gas reforming. See also Figure 2.4.

Process	Energy efficiency η_{HHV} %	
	Electrolysis	Natural gas
Production of natural gas	N/A	96
Ammonia production	57	70
Transport and storage	95	95
Ammonia splitting	80	80
Fuel cell energy conversion	47	47
Auxiliaries	95	95
Electrical motor/inverter	95	95
Total "well-to-wheel"	19	22
Total "well-to-tank"	54	64
Total "tank-to-wheel"	34	

A simplified "well-to-wheel" analysis of the ammonia fuel chain is presented here. Typical efficiencies for the different processes involved are used. The background for these efficiencies is given in Appendix A. All efficiencies

are based on Higher Heating Values (HHV). Energies are converted to HHV assuming pure methane feedstock when literature data are given on a LHV basis. The results are summarized in Table 2.2 and Figure 2.4.

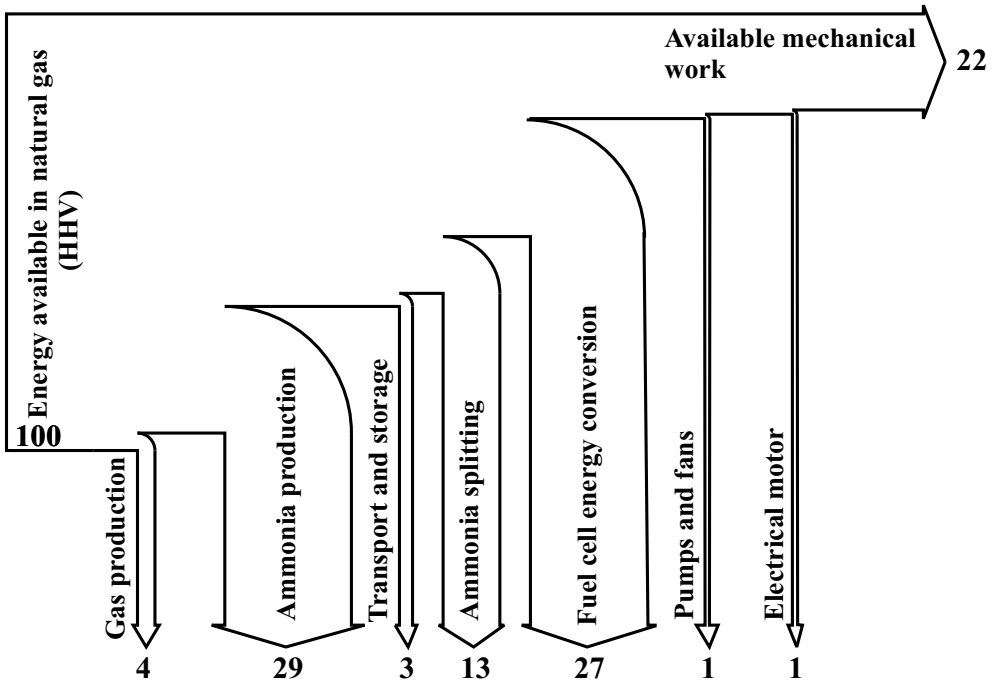

Figure 2.4: Graphical representation of losses in the ammonia fuel fuel chain from well-to-wheel when basing the ammonia production on natural gas.

2.7 Comparison to Other Energy Carriers

This comparison is made primarily to methanol and with emphasis on mobile applications. However, other fuels and applications are also briefly discussed.

2.7.1 Energy Density

The energy density of hydrogen carriers is important, especially for use in the transportation sector. The range of the vehicle is dependent on how much

energy that can be carried on-board in a relatively small volume. The net energy densities for several fuels are given in Table 2.3.

Table 2.3: Hydrogen content and energy density of different hydrogen carriers [46, 78]. Weight and volume of storage vessels etc. are **not** included.

Fuel	H_2 content wt%	Energy density (HHV) gravimetric MJ/kg	volumetric MJ/l
Ammonia (liq)[1]	17.6	22.4	13.5
Methanol	12.5	22.7	17.8
Ethanol	13.0	29.6	23.2
Hydrogen (200 bar)	100.0	142.5	2.1
Hydrogen (liq)	100.0	142.5	10.0
Hydrogen (MH)[2]	2.8	4.0	13.7
Methane (200 bar)	25.0	55.6	8.3
Isooctane (gasoline)	15.8	47.8	33.4

[1] Heat of vaporization is not subtracted.
[2] Hydrogen stored in metal hydride, $FeTi_x$ is used here [46].

In addition, cylinders and tanks are required for storing the fuel. The weights of these are to a large extent an engineering question. Modern cars often have complex shaped tanks to fit available space. This favours truly liquid fuels. Liquid ammonia must be kept at a pressure of 10 bar, which limits the design flexibility. To maximize the hydrogen yield from methanol reforming, a 1:1 mixture of methanol and water has to be used reducing the energy density. Alternatively, water from the FC exhaust must be recycled. This is due to differences in reforming processes, see Sec. 2.7.4

2.7.2 Energy Efficiency

Ammonia and methanol synthesis both have similar energy efficiencies. English *et al.* [80] reports that in the mid-1990s, the energy requirement for production of methanol was about 29.0-30.3 GJ/t(LHV) resulting in an efficiency η_{HHV} of 68-71% when converting LHV to HHV assuming pure methane as feedstock. Ammonia synthesis plants also operates at about 70% efficiency (HHV), see Appendix A, Table A.1. Production of hydrogen, and cryogenic hydrogen in

particular, is less energy efficient than both methanol and ammonia synthesis when compression and/or cooling of the product is included [41, 81].

In an analysis by Metkemeijer and Achard [33], it was concluded that a fuel chain based on ammonia would be more efficient than a fuel chain based on methanol. The reason for this was that AFCs could be used for hydrogen from ammonia (because there is no CO_2 in this gas), but PEMFCs would have to be used for hydrogen from methanol. AFCs have higher operating cell voltage than PEMFC, typically 0.80 vs. 0.70 V, and are hence more efficient than the PEMFC, at least at lower current densities. Ohmic losses, which become more important at higher current densities, are relatively high in AFC because the electrolyte is 10–100 times thicker than in the PEMFC. Metkemeijer and Achard [33] found that the energy efficiency was not very dependent upon reformer temperature. The difference between efficiency of ammonia and methanol was thus not significantly affected by the relatively large difference in reformer/splitter temperature.

2.7.3 Flammability

The flammability properties of ammonia are advantageous as compared to most other fuels. A relatively narrow flammability interval combined with a high lower flammability range, high ignition temperature as well as being a lighter-than-air gas, all contributes to these advantageous property, see Figure 2.5.

2.7.4 Reforming

Major differences between different fuels when it comes to reforming are given below with emphasis on comparison with methanol:

- Both processes are well known in chemical engineering. The challenge is to scale down the technology for small units. Methanol reforming technology for mobile applications has been furthest developed
- Process dynamics remains a challenge for both systems although start-up times for methanol reformers are now acceptable with processes based on Partial OXidation (POX)[14]
- Maximizing hydrogen yield when reforming methanol requires recycling of water or using mixtures of water and methanol as fuel. Ammonia splitting does not require any additional reactant

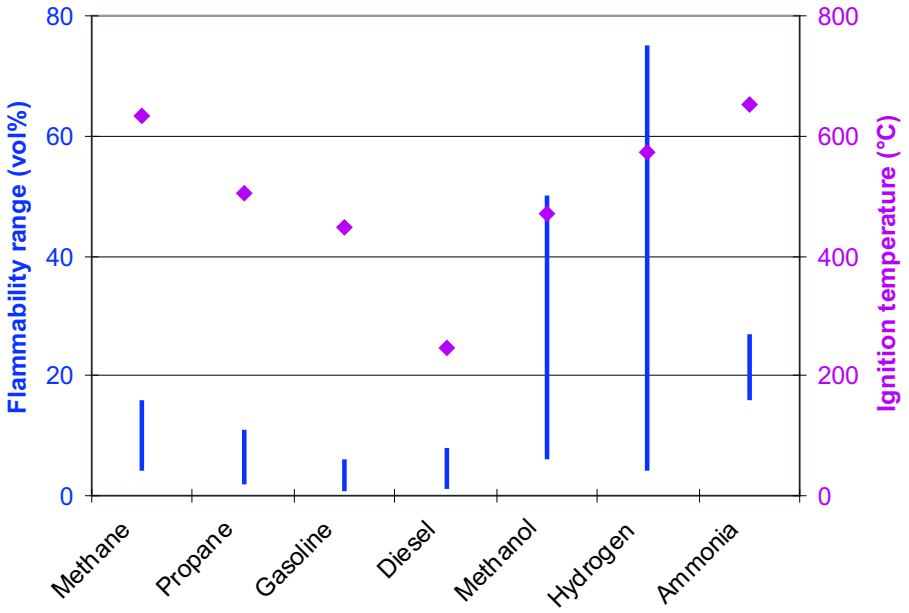

Figure 2.5: Flammability interval and ignition temperature of different fuels (from the Kirk-Othmer Encyclopedia [82] except data for ammonia which are from Appl [29]).

- Hydrogen gas from both ammonia splitting and methanol reforming both requires clean-up for use in PEMFC. Both residual CO and NH_3 affect PEMFC performance. AFCs can not operate on hydrogen produced from methanol or other carbon containing fuels

- Reforming temperatures are much lower for methanol, but more processing is needed when reforming methanol in order to remove CO. The lower required reforming temperature may facilitate internal reforming of methanol in PAFC type cells

- Low temperature DAFCs are not feasible, see Section 2.5.1. Direct Methanol Fuel Cells (DMFC) are feasible in small units, but severe poi-

soning of the anode and methanol crossover presently prevents use of DMFC for use in high power/high efficiency applications

- The concentration of inerts (N_2 and CO_2 respectively) is about the same for externally heated ammonia splitting and steam reforming of methanol (about 75% H_2). In autothermal splitting of ammonia, which is the equivalent of POX for methanol, the hydrogen content in fuel gas based on splitting of ammonia is higher than in hydrogen based on POX of methanol

2.7.5 Costs

The cost of hydrogen production from ammonia has been estimated to be more competitive than cryogenic liquid hydrogen, and also competitive with natural gas reforming in small plants [35, 81]. Ammonia is also more cost effective than methanol according to some sources [67]. However, comparison of the cost of alternative fuels to gasoline or diesel is not always correct. A substantial part of the consumer price of gasoline is due to taxation, especially outside North-America. If alternative fuels should be successful, it is likely that taxes will also be added to these fuels so that revenue effects are neutral. The other factor that has to be considered is that the present utilization of the worlds production capacity of ammonia has only been about 80% [29]. Major restructuring of the ammonia business has recently taken place. The price of ammonia in recent years may thus have been artificially low.

2.8 Conclusions

Ammonia is a hydrogen carrier that should be considered for use as hydrogen source for FCs. It has a relatively high energy density, it is a well known chemical commodity product, and the energy efficiency of the production process is the same as f. ex. for methanol. Present production is based on fossil fuels and natural gas in particular, but production based on renewable energy sources is feasible. Economically viable, large scale production of hydrogen and all other hydrogen carriers is presently based on fossil fuels. Carbon capture from fossil fuel based ammonia production is highly feasible; it is actually a vital part of the synthesis process.

Ammonia has advantages over f. ex. methanol and especially hydrocarbons because the reforming or splitting of ammonia is a relatively simple process. The drawback is that acidic FCs have a limited tolerance to ammonia. However, there may be ways to enhance this tolerance. Alkaline and high temperature FCs have high tolerance to ammonia.

More evaluation is needed to properly assess environmental impact of large scale use of ammonia, and to ensure safe handling on a consumer level. Health hazards connected with ammonia may limit its application to professionally maintained systems.

Chapter 3

Influence of Ammonium on Conductivity and Water Content of Nafion® 117 Membranes

Rune Halseid, Preben J. S. Vie*, and Reidar Tunold

Norwegian University of Science and Technology
Department of Materials Technology
NO–7491 Trondheim, Norway

*Present address: Institute for Energy Technology
P.O. Box 40, NO–2027 Kjeller, Norway

 The archival version of this work was published in *J. Electrochem. Soc.* **151**(3) A381–A388 (2004).

3.1 Summary

Ion exchange equilibria of ammonium between an aqueous phase and Nafion® 117 were measured at 10, 25, 40, and 60 °C by equilibrating the membrane in 0.1 M chloride electrolytes of known cation composition. The water content in the membrane phase was found to decrease linearly with increasing cation fraction of ammonium in the membrane phase ($y_{NH_4^+}$) from $\lambda_{H_2O} = 21.2$ (mols of water per mol sufonic acid groups) in proton form Nafion® in pure water to $\lambda_{H_2O} = 13.2$ in ammonium form Nafion® in a 0.1 M chloride solution. The conductivity was measured by *ac* impedance in a two-electrode set-up using a stack of membranes. The conductivity was also found to decrease linearly with increasing $y_{NH_4^+}$ from 97 mS/cm to 25 mS/cm at 25.0 °C. Our results indicate that the conductivity of Nafion® is isotropic, however, available literature is not conclusive on this matter. The temperature dependence of the conductivity was measured, and the fitted activation energy in an Arrhenius-type equation was found to depend on membrane composition and hence water content.

3.2 Introduction

As resarch on low temperature polymer electrolyte membrane (PEM) fuel cells (FCs) has progressed, increasing focus has been put on how gaseous contaminants, and carbon monoxide in particular, influence the FC performance, and how these effects may be alleviated. Less work has been published on other contaminants present in fuel and air streams, ammonia being one of these components. Ammonia may be formed in fuel reforming processes at levels up to 150 ppm [15] especially if the reforming involves homogeneous precombustion, or if the fuel itself contains nitrogen containing components [16]. Ammonia may also be present as a trace component if ammonia is used as feedstock for hydrogen production by thermal splitting [18], or in ambient air as such. Earlier work by Szymanski *et al.* [25] on phosphoric acid FCs has shown that ammonia has an effect on FC performance, and on cathode performance in particular.

Since ammonia is alkaline, it is expected that it will be readily absorbed by the acidic membranes used in PEM FCs forming ammonium in the membrane phase. An important factor determining the performance of PEM FCs, is

the ionic conductivity. Ammonium reduces the conductivity of Nafion®[1] as pointed out by Uribe *et al.* [20] and Soto *et al.* [21]. Reduced conductivity can be important both as a bulk membrane effect increasing the ohmic drop in the cell, as well as in the active layer(s) on either anode or cathode. Based on High Frequency Resistance (HFR) and other data collected from an FC operating with 13 to 130 ppm ammonia in the fuel, Uribe *et al.* [20] concluded that the most important effect in the short term is reduced conductivity in the anode catalyst layer. When operating the FC for longer times, the bulk conductivity was also affected. Soto *et al.* [21] found that the increased ohmic resistance as measured by current interruption, only accounted for 10% of the observed performance loss. This indicates that other effects, such as reduced conductivity within the electrode layers, are important.

The aim of this work is to quantify the ion exchange equilibrium between Nafion® 117 in an aqueous electrolyte containing different cation fractions of ammonium, $x_{\mathrm{NH_4^+}}$, and the corresponding membrane phase composition, $y_{\mathrm{NH_4^+}}$, and how this influences membrane conductivity, κ_{mem}, membrane water content, λ_{H_2O}, as well as swelling of the membrane. An aqueous phase is used since it is easier to control the membrane phase composition indirectly through an aqueous phase rather than through a vapor phase by addition of ammonia. It should be kept in mind that the parameters studied here (swelling, conductivity, and water content) may be differently influenced when Nafion® is in equilibrium with a vapor phase rather than with a liquid electrolyte, and that other effects, such as catalyst poisoning, may also be important factors influencing PEM fuel cell performance.

3.2.1 Methods Used in the Literature for Membrane Conductivity Measurement

Several different methods to determine membrane conductivity have been described in the literature, and both *ac* and *dc* polarization methods have been used. It has been shown that the conductivity of Nafion® is independent upon frequency in the range 1 Hz to 100 kHz [83, 84], so that the *dc* conductivity of interest in FCs indeed can be measured by impedance spectroscopy provided the cell design used minimizes contact effects. The different methods described in the literature use different ways of contacting the current collectors to the membrane phase, and differ in whether the normal or the in-plane component

[1] **Nafion®** is a DuPont registered trademark by E. I. du Pont de Nemours and Company.

of the conductivity is measured. The normal component has been measured by:

1. Passing *dc* current through an electrolyte filled cell with and without a membrane present separating the two half cells. The difference in cell resistance is then the membrane resistance. The voltage drop is measured by two separate electrodes placed close to the membrane to minimize the electrolyte contribution to the measured resistance [85–92].
2. Contacting the membrane by mercury on either side [92–95].
3. Gold or platinum electrodes evaporated onto the membrane surfaces. The membrane is then clamped between current collectors [83, 96].
4. Clamping the membrane between two bare Pt or Au electrodes [84, 97–99].
5. Use a stack of membranes which is stepwise increased in thickness by adding membranes, thus yielding the membrane resistance as the slope of resistance vs. number of membranes in the stack [100, 101].
6. Using a coaxial probe passing very high frequency *ac* current between the center electrode and the annular electrode [102, 103].
7. Applying fuel cell electrodes to the membrane and measure the resistance in a controlled humidity environment in inert atmosphere [104].
8. Using microelectrodes to contact the membrane [105].

The in-plane component of the conductivity has been measured by:

9. Electrodes mechanically clamping onto the membrane with or without separate voltage probes [84, 96, 106–108].
10. Placing the membrane between two electrolyte reservoirs passing *dc* current in-plane through the membrane, and using separate voltage probes to measure the potential drop in a segment of the membrane strip [109].
11. Gold electrodes evaporated onto the ends of a membrane strip [83].
12. Coaxial probe, the in-plane component of the measurement being dependent on the ratio of the gap between the coaxial contacts and the membrane thickness [102, 103].

3.3 Experimental

3.3.1 Preparation of Membranes and Solutions

Nafion® 117 membranes were purchased from IonPower Inc., and pretreated at 85 °C in purified water produced by a MilliPore Academic water purification system for 15 minutes, thereafter in 5% H_2O_2 (Merck *p.a.*) for 30 minutes, then again in purified water for 15 minutes, then ion-exchanged twice in 0.05 M H_2SO_4 (Merck *p.a.*), each time for 30 minutes, and then finally four times in purified water, each time for about 15 minutes. Membrane disks (20.35 mm ∅) were then punched out for conductivity measurements, and these disks were again purified using the same procedure. Samples used for equilibrium measurements were cut in a rectangular shape (approximately 25 by 30 mm, 0.2 to 0.3 g dry) prior to membrane pretreatment. All samples were stored in purified water at least over night and until used in further experiments.

3.3.2 Equilibration of Membrane Samples

Standard solutions of known molality were prepared using HCl, NH_4Cl (Merck *p.a.*) and purified water. The required amounts of these solutions were weighed into measuring flasks to yield the desired cation compositions with a total chloride concentration of 0.1000 M. All solutions were prepared in glassware calibrated with purified water. The membrane samples were equilibrated with the solutions of interest in water baths at the temperatures of interest (10.0, 25.0, 40.0 and 60.0 °C) within ± 0.1 °C. The equilibrating solutions were changed at least four times during a minimum of six days. One day equilibrating time was allowed in experiments where only the equilibrium temperature was varied and the membranes stayed in the protonic form.

3.3.3 Water Content

The weights of wet membranes were determined by quickly wiping off excess liquid with a lint-free paper before weighing the membrane samples. The samples were then immersed in the solution again for at least 30 seconds to re-equilibrate the membrane with water. This procedure was repeated until at least three readings identical to within ±0.5 mg had been obtained. Zawodzinski *et al.* [106] found that rehydration of even completely dry membranes is rapid in liquid water; in about 15 seconds the membrane is re-hydrated to 90% of its equilibrium hydration level.

The membrane samples were dried in their protonic form under vacuum at room temperature for 24 hours, and then transferred to a dessicator containing Merck SicaPent dessicant (P_2O_5). The membranes were not exposed to elevated temperatures during the drying process as that has been shown to affect the membrane properties [106, 108]. After four to five days the membrane samples were weighed in a glove box (<5 ppm water vapor).

3.3.4 Swelling Properties

A vernier caliper was used to measure the diameter of the samples used in conductivity measurements to determine changes in dimensions of the membranes due to swelling. Membrane thicknesses were measured using a micrometer screw. Dimensional measurements were only performed on membranes equilibrated at 25.0 °C since the sample dimensions had to be measured at room temperature (approximately 23 ± 2 °C).

3.3.5 Equilibrium Isotherm Measurements

The membranes were taken out of the equilibrating solutions, and weighed as described previously to determine the water content at a given temperature and external ammonium cation fraction. The samples were then transferred to flasks containing known volumes of 0.1 M pure hydrochloric acid to ion-exchange ammonium from the membranes. The membranes were kept in these solutions for seven to ten days at room temperature before the samples were transferred to a fresh hydrochloric acid solution for further ion-exchange. The concentrations of ammonium in the exchange solutions were determined by using an Ion Selective Electrode (NH4ISE25 from RadioMeter). The results were compared to analysis performed using Kjeldahl's method, and there was very good agreement between the two methods.

3.3.6 Conductivity Measurements

The apparatus used to measure the conductivity is shown in Fig. 3.1a), and uses the same principle as used by Halim *et al.* and Ottøy [100, 101]. The conductivity cell was made out of glass whereas the electrode pistons were made out of poly(tetrafluoroethylene), PTFE. The cell was thermostated from the same water bath as the membrane samples were kept in. The platinum electrodes were made from Pt foil, and were 20 mm in diameter. The platinum

electrodes were platinized prior to use, and stored short-circuited in 0.1 M HCl between measurements. In our experiments, four membranes were stacked between the two electrodes at the time, and loads added to ensure good contact. The cell was filled with the equilibrating electrolyte. The High Frequency Resistance (HFR) was measured using a Solartron 1287/1255B set-up (25 mV *ac* amplitude applied ,and the imaginary part of the impedance was zero at 2–6 kHz). The HFR as function of the number of membranes in the stack was recorded. The coefficients of determination of the fitted straight lines, R^2, were larger than 0.9998 in all cases.

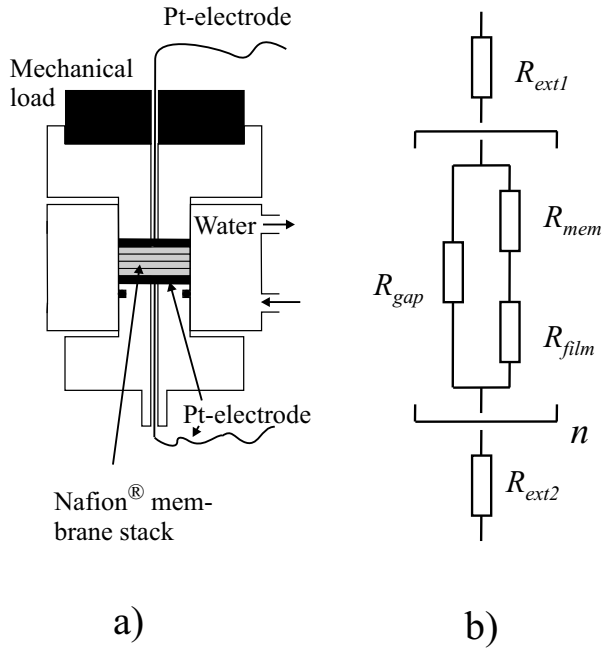

Figure 3.1: a) Conductivity cell used in this work. Not drawn to scale nor proportions. b) Equivalent circuit for the conductivity cell showing only the ohmic components in the circuit for a stack of n membranes: membrane resistance, R_{mem}; contact resistances, R_{ext1} and R_{ext2}; contributions from liquid film between the membranes, R_{film}; and the parallel electrolyte resistance R_{gap} due to incomplete filling of the cross section in the conductivity cell.

The ohmic components in the membrane stack can be represented by the network of resistors as shown in Fig. 3.1 b). The total resistance, R_{tot}, is found from the slope of HFR vs. number of membranes, and contains contributions from liquid layers between the membranes, R_{film}, and resistance due to incomplete filling of the cross section in the conductivity cell, R_{gap}.

Resistances in leads and the electrolyte film between electrodes and the membrane stack, R_{ext1} and R_{ext2}, do not affect the results since only the slope of the curve of HFR vs. number of membranes is used in further calculations. Different loads were also applied to the membrane stack (7.5 to 40 kPa) in order to verify if this influenced the results. It was found that the slope of the line of HFR vs. number of membranes was not affected (and thus not the reported conductivity), whereas there was a slight effect on the intercept of the line with the y-axis as expected since higher applied loads reduces the resistances R_{ext1} and R_{ext2}. Further, the membranes were taken directly from the equilibrating solution to the apparatus to minimize the thermal disturbances the membranes were exposed to.

As shown later, the diameter of the membrane samples was found to depend on $y_{NH_4^+}$. The membranes were cut out from Nafion® in the protonic form, and hence contracted when exposed to ammonium containing external electrolytes. To correct for this we assume that the contraction is a linear function of $y_{NH_4^+}$, see Fig. 3.4 for justification of this, and that the conductivity in the aqueous phase, κ_{elec}, is a linear function of the composition, *i.e.*, $\kappa_{elec} = x_{H^+}\kappa_{HCl} + x_{NH_4^+}\kappa_{NH_4Cl}$. The conductivity of pure 0.1000 M HCl and 0.1000 M NH_4Cl is 39.11 and 12.88 mS/cm respectively at 25 °C [78]. The resistance due to the membrane, R_{mem}, is then calculated from

$$1/R_{mem} = 1/R_{tot} - 1/R_{gap} = 1/R_{tot} - \kappa_{elec}\left(A_{tot} - A_{mem}\right)/l_{mem} \qquad (3.1)$$

where A_{mem} is the actual area of the membrane, l_{mem} is the actual thickness of the membrane, and A_{tot} is the total cross sectional area of the conductivity cell. The measured diameters and thicknesses of the membranes, as shown in Fig. 3.4, were used in these calculations. No corrections were made for R_{film} because it was small compared to R_{mem} as discussed in more detail later. Calculating the membrane conductivity κ_{mem} is then straightforward:

$$\kappa_{mem} = l_{mem}/(A_{mem}R_{mem}) \qquad (3.2)$$

3.4 Results and Discussion

3.4.1 Equilibria between Nafion® and aqueous electrolytes

Membrane Equivalent Weight

The equivalent weight was found to be 1100 ± 40 g/mol SO_3^- by adding 20.00 ml 0.0500 M sodium hydroxide to membrane samples that were in equilibrium with purified water, and then back-titrate with hydrochloric acid using Bromothymol Blue as indicator.

Based on analysis of the ammonium content of Nafion® 117 membranes in equilibrium with 0.1000 M ammonium chloride, we found that the equivalent weight was 1056 ± 20 g/mol SO_3^-. A possible explanation for the observed difference is absorption of chloride into the membrane phase. Jones *et al.* [110] report that the content of chloride in Nafion® 117 in equilibrium with a 0.1 M NaCl solution is about $\lambda_{Cl^-} = 0.05$ (mols chloride per mol sulfonic acid group). The difference in the equivalent weights between membranes in purified water and in 0.1 M chloride solutions reported here corresponds to $\lambda_{Cl^-} = 0.04$.

An equivalent weight of 1100 g/mol SO_3^- is used in further calculations on water content since the reported λ_{H_2O} values are based on the number of sulfonic acid groups in the membrane. Equilibrium isotherms and membrane compositions are based on the total amount of ammonium in the membrane phase, *i. e.* including ammonium found as ammonium chloride in the membrane phase, thus an equivalent weight of 1056 g/mol is used in these calculations.

Equilibrium Isotherms

Equilibrium isotherms at 10.0, 25.0, 40.0, and 60.0 °C were measured in Nafion® 117 in equilibrium with solutions with total chloride concentrations of 0.1000 M. Only the 25.0 °C isotherm is shown here in Fig. 3.2.

Water Content in Nafion®

The water content in Nafion® 117 was determined at room temperature (23 ± 2 °C), and was found to be $\lambda_{H_2O} = 21.2 \pm 0.4$ mols of water per equivalent of sulfonic acid groups in the membrane two days after preparation. This is in good agreement with other results reported ($\lambda_{H_2O} = 21 - 23$ [91, 100, 106, 107, 111, 112]). After leaving the membranes in purified water for one

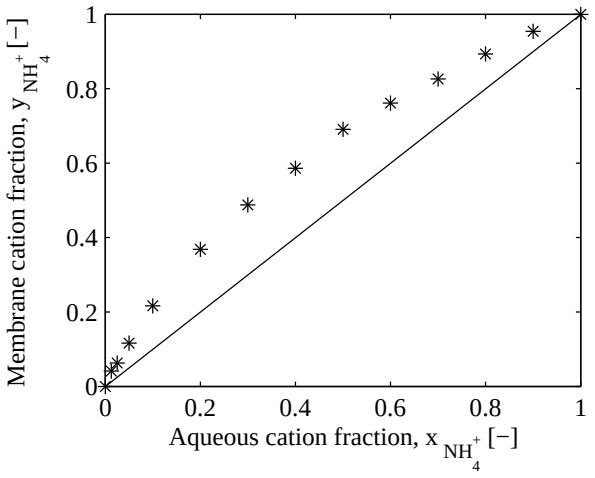

Figure 3.2: Ion exchange equilibrium between proton and ammonium at 25.0 ± 0.1 °C for Nafion® 117. The line $x_{NH_4^+} = y_{NH_4^+}$ is also shown for reference.

month after preparation, the water content had decreased from 21.2 ± 0.4 to 20.5 ± 0.4 as shown in Fig. 3.3a). The water content of Nafion® was slightly dependent on temperature, and was also lower when in equilibrium with 0.1000 M hydrochloric acid as compared to pure water, see Fig. 3.3a). However, none of these observations are statistically significant at the 95% confidence level.

The water content was found to vary significantly with the ammonium content of the membrane phase as shown in Fig. 3.3b). We observed that the water content in pure ammonium form Nafion® is reduced to $\lambda_{H_2O} = 13.2$ at 25.0 °C. Xie and Okada [107] studied the water content in different alkaline and alkaline earth ionic forms of Nafion® in equilibrium with 0.03 M chloride solutions, and found that the water content of sodium form Nafion® 117 was $\lambda_{H_2O} = 16.5$ whereas the potassium form had a $\lambda_{H_2O} = 10.8$ at 25.0 °C.

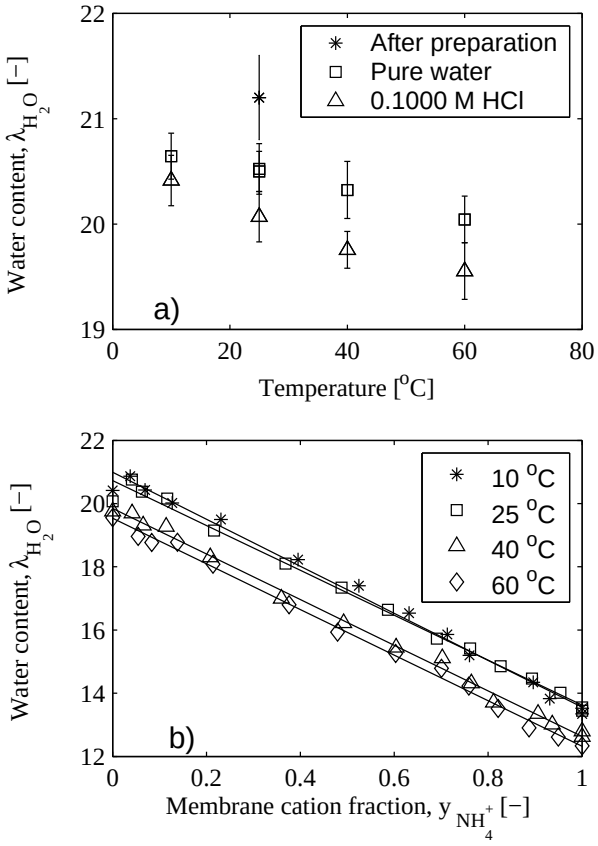

Figure 3.3: Water content in Nafion® 117 at a) different temperatures in pure water and 0.1000 M hydrochloric acid (error bars shown are only one standard deviation, data are averages of four to eight observations) and b) at different ammonium contents in the membrane phase ($y_{NH_4^+}$). The regression lines for the different temperatures are also shown in b). The water content in Nafion® in 0.1000 M at 25.0 °C is estimated by regression to be $\lambda_{H2O} = 20.6 \pm 0.2$.

Dimensions of Nafion® at Various Membrane Composition

The diameters and thicknesses of membrane samples equilibrated at 25.0 ± 0.1 °C were measured at room temperature (23 ± 2 °C). The absolute values when in equilibrium with 0.1000 M HCl were 20.33 ± 0.05 mm and 207 ± 10 μm for diameter and thickness respectively. In Fig. 3.4 the relative changes in diameter and thickness are shown as functions of membrane composition. If we assume that *1)* the total volume of Nafion® is the sum of the partial volumes of Nafion® and water, *2)* the swelling is isotropic, and *3)* that the density of both proton and ammonium form dry Nafion® is 2.05 g/cm^3 [96], we estimate that the relative dimensions in ammonium form Nafion® should be 95.2% of those in proton form Nafion®. This is in good agreement with our findings for the diameter, see Fig. 3.4a, but less good for the thickness. Morris and Sun [96] found that the thickness changed about two times more relatively to the diameter of Nafion® 117 when in equilibrium with different vapor pressures of water. Datasheets for Nafion® provided by DuPont [113] states that the swelling is nearly equal in all directions. In our measurements the uncertainty for the determination of membrane thicknesses was much larger than for the diameter determinations, and even though the observed thicknesses change less than the diameter, this difference is not statistically significant.

3.4.2 Conductivity of Nafion® 117

The conductivity of Nafion® 117 in equilibrium with different electrolytes containing ammonium and protons was then measured at 25.0 ± 0.1 °C. The results were corrected for the fact that the membrane diameter and thickness changed in different electrolytes (Equations 3.1 and 3.2), but was not corrected for a liquid film between the membranes. In pure proton and ammonium forms of Nafion® 117 the conductivities were found to be 97 mS/cm and 25 mS/cm respectively. The results are plotted in Fig. 3.5. There is a linear relationship between membrane cation fraction of ammonium, $y_{NH_4^+}$, and conductivity, κ_{mem}. This is in accordance with the findings of Logette *et al.* [114], and indicates that the ionic mobilities of protons and ammonium are independent of membrane composition. However, in situations involving di- and trivalent cations, the situation has been shown to be more complicated [94, 111, 114, 115].

We used three different ensembles of membranes randomly cut out of the same sheet of Nafion®. However, we measured differences in membrane con-

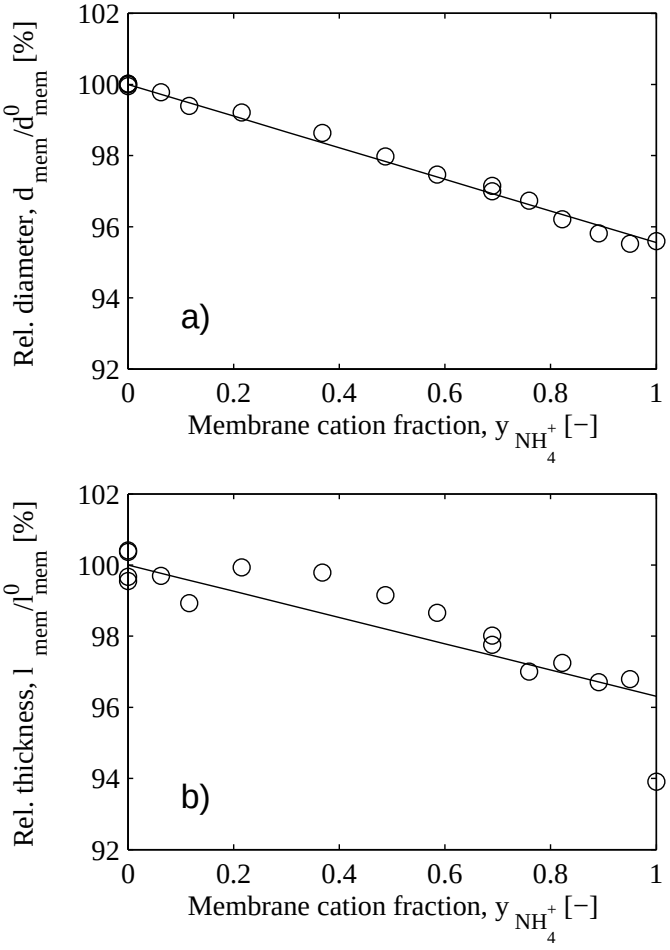

Figure 3.4: a) Relative diameter, and b) relative thickness of Nafion® 117 at 23 ± 2 °C. Also shown is the least square fits with the constraint that the lines shall pass through (0,100). The fitted lines were a) 100 - $(4.47 \pm 0.20) y_{NH_4^+}$ and b) 100 - $(3.69 \pm 1.10) y_{NH_4^+}$. The measured diameter of proton form Nafion® was 20.33 ± 0.05 mm and the thickness 207 ± 10 μm.

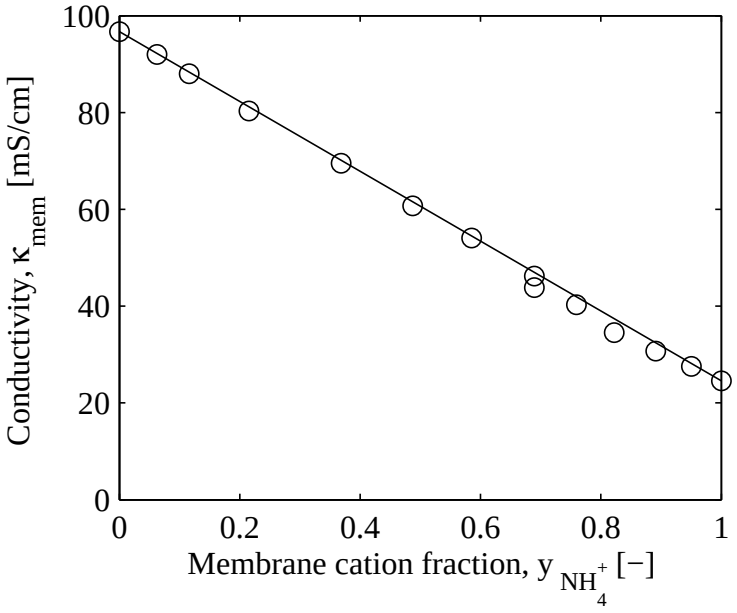

Figure 3.5: Conductivity at 25.0 ± 0.1 °C in Nafion® 117 plotted against ammonium content in the membrane phase ($y_{NH_4^+}$). The linear interpolation between the pure proton and the pure ammonium form Nafion® 117 conductivity is also shown in both plots.

ductivity between the different ensembles. The differences between the ensembles were within 2%. When the conductivity measurements at 25 °C and at different compositions were finished, the membranes were transferred back to their protonic form by ion exchange, and the conductivity measured again. It was noted that the conductivity in the pure protonic form had dropped by about 2% during the experiments. This was not recoverable even when the membranes were treated in hydrogen peroxide and hot, dilute sulfuric acid as described in the preparation procedures. Uribe *et al* [20] found that FC performance was not fully recovered when operating on neat hydrogen after initial exposure to 30 ppm ammonia for 15 hours. More recently Soto *et al.* [21] found full recovery after exposure to 200 ppm ammonia for 10 hours. It is not clear if ammonium reacts irreversibly with the membrane to degrade conductivity.

Influence of External Electrolyte Concentration on Measured Conductivity

If the concentration of chloride in the external solution is high, chloride will penetrate into the ion exchange membrane as measured f. ex. by Jones *et al.* [110]. However, the mobility of the anions is probably low due to the structure of Nafion®, and there are indications that anions are transported in the hydrophobic regions of the membrane [116] which significantly reduces the mobility of the anions. Lteif *et al.* [117] found that the conductivity of Nafion® 117 in equilibrium with LiCl, NaCl and KCl increased slightly going from 0.1 to 0.2 M, and then slowly decreased thereafter (measurements up to 2 M).

The membrane conductivity of Nafion® 117 immersed in HCl solutions of different concentrations was measured to verify that the external solution concentrations did not influence our results significantly. The experimental results are shown in Fig. 3.6. The expected influence of the external electrolyte strength in a liquid film between each membrane in the stack was also calculated. The molar conductivity of HCl solutions is taken from [78], and fitted to $\Lambda_{HCl} = 42.18 - 0.2854\sqrt{c_{HCl}}$ [mS m^2 mol^{-1}], where c_{HCl} is given in [mol/m^3]. Further, the observed membrane thickness in 0.1 M HCl (207 μm) and membrane diameter (20.33 mm) was used in the calculations. The total diameter of the cell was 20.35 mm, and a network of resistors as shown in Fig. 3.1b) used in the calculations. Various thicknesses of a possible electrolyte film between the membranes was used in the calculations as shown in Fig. 3.6, and all lines were forced through the point (0.1 M, 97 mS/cm). It is concluded from Fig. 3.6 that the liquid layer between the membranes is probably <0.1 μm, and thus that the influence of a liquid film is $< 0.1\%$ of the membrane resistance. It is also observed that the experimental conductivity tends to increase at higher electrolyte concentrations, probably due to anion absorption. The chosen electrolyte concentration of 0.1 M thus seems to offer a reasonable trade-off between influence of an electrolyte film and chloride ingress into the membrane.

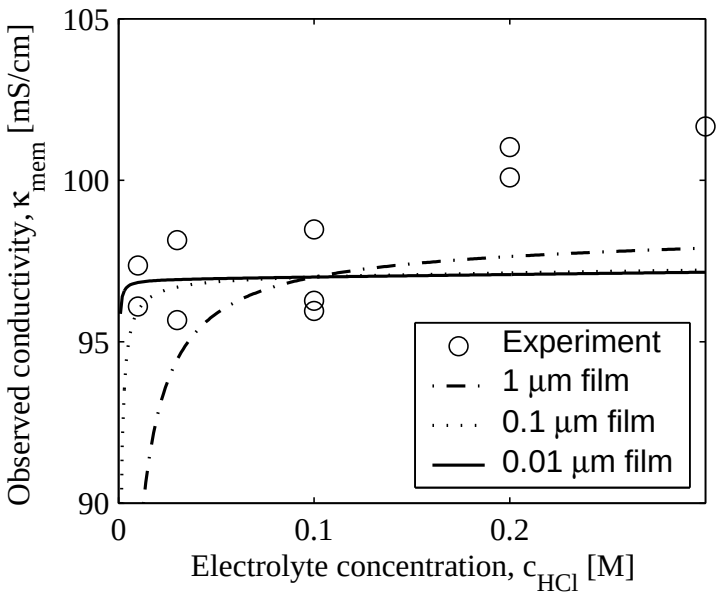

Figure 3.6: Conductivity at 25.0 ± 0.1 °C in Nafion® 117 as function of the external electrolyte strength. Also shown is the calculated dependencies of observed membrane conductivity on electrolyte strength given different thicknesses of a liquid film between the membranes. A network of resistors as shown in Fig. 3.1b) was used in the calculations.

Table 3.1: Conductivity and activation energy data for Nafion® reported in the literature.

Nafion membrane	Electrolyte	Technique[1]	No. of Probes			Pretreat[2]	T [^{o}C]	E_a [kJ/mol]	κ [mS/cm]	Ref.
117	0.1 M HCl	5	2	ac	$\perp$	4	25	10.3	97	This work
117	Water	5	2	ac	$\perp$	4	20	13.5	90	[100]
117	0.03 M HCl	5	2	ac	$\perp$	4	25	-	93	[101]
117	0.3/1/3 M H_2SO_4	1	4	dc	$\perp$	4	Room	-	86/88/73	[87]
111	0.3/1/3 M H_2SO_4	1	4	dc	$\perp$	4	Room	-	53/66/41	[87]
117	1 M H_2SO_4	1	4	dc	$\perp$	4	20	12[3]	89	[88]
112/1135/ 115/117	1 M H_2SO_4	1	4	dc	$\perp$	4	25	-	83/111/ 134/159	[91]
117	0.1M HCl	2	2	ac	$\perp$	3	Room	-	25	[93]
117	0.1 M HNO_3			ac	$\perp$	1	Room	-	62	[114]
117	Water	8	2	ac	$\perp$	0	30	22	40	[105]
112/115/117	Water	4	2	ac	$\perp$	2	15	9[3]	13/43/58	[98,99]
117	1 M H_2SO_4		4		$\perp$	4	25	-	140	[118]
117	Water	6, 12	2	ac	$\perp$ / $\parallel$	3	Room	-	24/67	[102]
117	Water	6, 12	2	ac	$\perp$ / $\parallel$	4	Room	-	23.9/85.6	[103]
117	Water	9	2	ac	$\parallel$	4	25	10[3]	101	[106]
112/117	Water	9	2	ac	$\parallel$	4	25	-	100/100	[118]
117	0.03 M HCl	9	2	ac	$\parallel$	4	25	-	160-200	[107, 111, 115]
115	Water	9	2	ac	$\parallel$		25	14[3]	128	[119]
All	Water	9	2	ac	$\parallel$	2	25	-	83	[113]
117	10^{-5} M H_2SO_4	10	4	dc	$\parallel$	0/2	Room	11	63/79	[109]

1. Numbers refer to the listing of different techniques in the Introduction
2. 0: "as-received", hydrated at room temperature, 1: Ion-exchanged to protonic form, hydrated at room temperature, 2: Hydrated in hot (80-100 ^{o}C) water, 3: Ion-exchanged and hydrated in hot water,4: Hot, oxidizing agent (H_2O_2 or HNO_3), ion-exchanged and rinsed in hot water. Variations occur; these are only generic pretreatment procedures.
3. Fitted to Equation 3.3 based on experimental data given in the references.

Comparison with Available Literature Data on Conductivity of Nafion®

Most data reported in the literature are in relatively good agreement with our findings (97 mS/cm). We see this agreement with literature data both as a confirmation of the accuracy of the method, and an indication that the conductivity in Nafion® is presumably isotropic within the experimental accuracy of our method.

Some of the reported literature data for Nafion® conductivities immersed in water or different electrolytes are summarized in Table 3.1. Some of the lower conductivities reported [105, 114] are probably due to the fact that the membranes were only hydrated at room temperature. It is well known that the conductivity depends on the thermal history of the membrane, especially drying and hydration at elevated temperatures [106]. The reasons for the low observed conductivity reported by Gavach *et al.* [93] and Dimitrova *et al.* [98, 99] have not been clarified.

On the other hand, the relatively high conductivity reported by Okada *et al.* [107, 111, 115] is probably because the voids of the conductivity cell (similar to that used by Zawodzinski *et al.* [106]) were filled with the equilibrating electrolyte solution, and not pure water. Hence, part of the current carried through the cell flowed through the aqueous electrolyte resulting in a higher observed conductivity. There are also some measurements of conductivity in relatively high concentration sulfuric acid that showed higher conductivities [91, 118], and it was assumed that this might be due to ingress of sulfate in the membrane [118]. However, other data reported were lower [87, 88], and in the same range (80-100 mS/cm) as reported in most other studies, see Table 3.1.

Further Discussion of Isotropy of Conductivity in Nafion®

Kolde *et al.* [118] found that the conductivity in a 20 μm Gore-Select membrane was isotropic. In contrast to our and Kolde's findings, Gardner and Anantaraman [102, 103] found that the in-plane component is three times larger than the normal component of the conductivity (85.6 vs. 23.9 mS/cm). Recent data published by Slade *et al.* [91] and Dimitrova *et al.* [99] showed that the conductivity of Nafion® 1100 depends on the membrane thickness; the thinner the membrane, the lower the observed normal component of the conductivity. This observation would most easily be explained by a lower conductivity close to the surface of the membrane [99] which would translate into an anisotropic conductivity. Earlier results reported by Verbrugge

et al.[87] also showed that the conductivity was lower for thinner membranes (both Nafion® and membranes from Dow Chemical Company), although not as much as found by Slade *et al.* and Dimitrova *et al.*. On the other hand, Kolde *et al.* [118] found that the conductivity of Nafion® 115 and 117 was the same. Datasheets available from DuPont [113] also makes no distinction between conductivity of different thicknesses of the membranes. A study by Johnson and Liu [104] concluded that the conductivity of Nafion® is not dependent on thickness. Yoshida *et al.* [119] found that the conductivity of Flemion®[2] R, S, and T is not dependent on the membrane thickness. Available literature data is therefore not conclusive regarding if there is an effect of membrane thickness, which would also indicate anisotropic conductivity of Nafion®.

Effect of Ammonium on Membrane Conductivity

We found that ammonium reduces the conductivity by a factor of 3.8 (Table 3.2) to 3.9 (Fig. 3.5) relative to pure H-form Nafion® 117 at 25.0 °C, which is in good agreement with the findings of Uribe *et al.* [20] who found that the conductivity of Nafion® 1035 decreased from 133 to 32–33 mS/cm, or by a factor of 4.0 to 4.2.

The ratio of conductivities, $\kappa_{HCl}/\kappa_{NH_4Cl}$, in 1.0 M aqueous electrolyte is 3.10 [78]. The higher relative conductivity in proton form Nafion® compared to an aqueous solution can possibly be explained by the fact that ammonium form Nafion® also contains less water thereby reducing the mobility of the ions within the membrane phase. It is well known that conductivity in Nafion® in equilibrium with water vapor depends strongly on water vapor activity, and thus water content in the membrane [96, 108, 120]. If we assume that the same correlation for conductivity as function of water content as used by Springer *et al.* [120] may be used in this case, we estimate that the conductivity ratio due to difference in water content should be 1.47. Multiplied with the relative conductivity ratio in 1.0 M aqueous solutions, a total conductivity ratio of 4.56 is estimated. This is slightly high, suggesting that the effects of ionic form and water content on conductivity are not simply additive.

[2] **Flemion®** is a registered trademark by Asahi Glass Company Ltd.

Temperature Effect on Conductivity

The conductivity of Nafion® 117 was also measured at various temperatures as summarized in Table 3.2. The same membranes were used as in previous measurements, and as noted above, the conductivities are slightly lower than the ones shown in Fig. 3.5. From Table 3.2 we see that a linear relationship between membrane composition and conductivity still holds, and we are able to predict the conductivity at $x_{NH_4^+} = 0.5$ within ±4%.

Table 3.2: Conductivity in Nafion® at different temperatures and ionic forms, equilibrium content of ammonium in membrane phase $y_{NH_4^+}$ at $x_{NH_4^+} = 0.5$, and estimated conductivity, κ_{mem}^{est}, at $x_{NH_4^+} = 0.5$ assuming that a linear combination of conductivity in the two pure membrane forms is valid. Conductivities reported in this table are not corrected for R_{gap}, see Equations 3.1 and 3.2. Further, it is assumed that the dimensions of the membranes are the same at all temperatures as at 25 °C.

T	κ_{mem} at			$y_{NH_4^+}$ at	κ_{mem}^{est}
	$x_{NH_4^+} = 0$	$x_{NH_4^+} = 0.5$	$x_{NH_4^+} = 1.0$	$x_{NH_4^+}$=0.5	$x_{NH_4^+} = 0.5$
[°C]	[mS/cm]	[mS/cm]	[mS/cm]	[-]	[mS/cm]
10	73	**35**	18	0.71	**34**
25	95	**47**	25	0.69	**47**
40	117	**61**	34	0.70	**59**
60	144	**79**	46	0.70	**76**

The temperature effect is also shown in Fig. 3.7. The data for each composition of Nafion® 117 were fitted to an Arrhenius type equation:

$$\kappa_{mem} = \kappa_{mem}^{o} \exp\left(E_a/RT\right) \tag{3.3}$$

The activation energy was found to vary with membrane composition as shown in the insert graph in Fig. 3.7, and we used a linear relation to describe $E_a = 10.3 + 4.2 y_{NH_4^+}$[kJ/mol]. The deviation between experimentally measured conductivities and those calculated using Equation 3.3, is within ±5%.

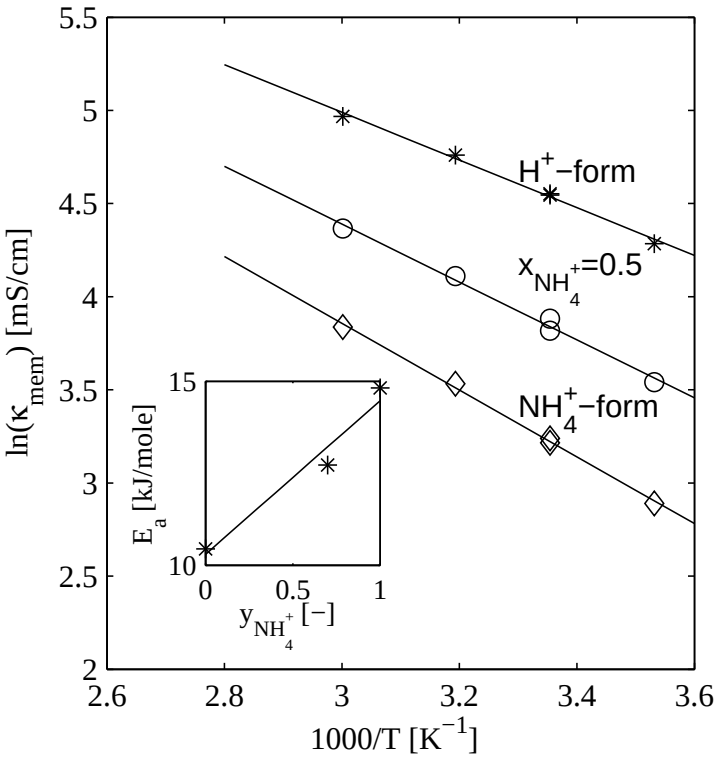

Figure 3.7: Arrhenius plot of conductivity of Nafion® 117 at different membrane compositions. The activation energy E_a for proton transport in Nafion ($E_a = 10.3 + 4.2 y_{NH_4^+}$[kJ/mol]) in Equation 3.3 is also shown as an insert as function of membrane composition.

Comparison to Available Literature Data on Activation Energy for Conductivity in Nafion®

Several authors have reported activation energies for proton form Nafion® as shown in Table 3.1. We see that our findings are in good agreement with the available literature data [88, 98, 100, 109, 121]. Parthasarathy *et al.* [105] reported an activation energy of 20 kJ/mol, but this was correlated with a large increase in water in the membrane as the cell was gradually heated (λ_{H_2O} increased from 13 to 24). This reported activation energy is thus probably a combined effect of water content and temperature.

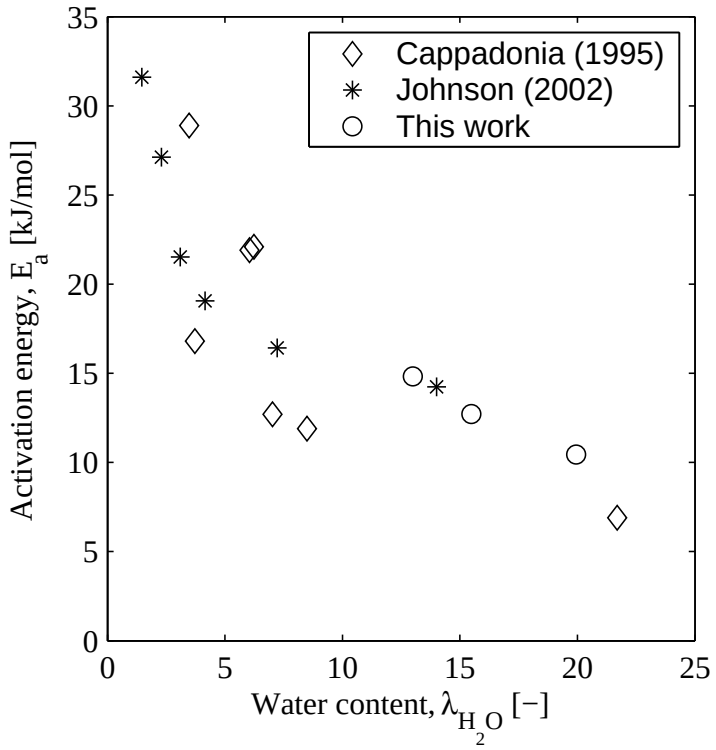

Figure 3.8: Activation energy, E_a, for proton transport in Nafion® as function of membrane water content, λ_{H_2O}. Literature data are from Cappadonia *et al.* and Johnson and Liu [97, 104]

We also found that the activation energy was a function of the membrane composition, and thus the membrane water content. Other researchers have also found that the activation energy varies with water content. Johnson and Liu recently reported that the activation energy was dependent on relative humidity of the gas phase [104]. Cappadonia *et al.* [97] investigated the conductivity from room temperature down to 140 K, and found two activation energies for proton conduction, the transition occurring at 225 to 260 K depending on water content. Dimitrova *et al.* [98, 99] studied the conductivity in the range 15–85 °C, and concluded that the conductivity was not strictly following a modified Arrhenius equation. Cappadonia *et al.* and Dimitrova *et al.* [97–99] used an alternative formulation of Arrhenius equation, $\kappa_{mem}T = A' \exp(E'_a/RT)$, which is consistent with the Nernst-Einstein equation [122]. Since this alternative formulation of the Arrhenius equation generally gives higher activation energies than Equation 3.3, we re-fitted the experimental data from Cappadonia *et al.* and Dimitrova *et al.* to Equation 3.3. Further, the water content reported by Cappadonia *et al.* [97] is given as additional water uptake of *as-received* membranes. We estimate the the water content in these membranes was about λ_{H_2O}=3.5 assuming that the relative humidity was 50% (standard conditions employed by DuPont [113]) then using the correlation by Springer *et al.* [120] to find the corresponding water content. Likewise, the relative humidity reported by Johnson and Liu [104] was converted to a membrane water content using the same correlation. The activation energy data are given in Fig. 3.8 as function of water content, and are in good agreement with our data.

Sone *et al.* [108] performed a comprehensive study of Nafion® conductivity using different pre-treatment procedures, and measured the conductivity in equilibrium with gases at different humidity. They found that the activation energy was very small, only about 1 kJ/mol for membranes pretreated similarly to our procedure. Below 45 °C they observed a slight decrease in conductivity with rising temperature.

3.5 Conclusions

Ion exchange equilibria of ammonium between an aqueous phase and Nafion® 117 were measured at 10.0, 25.0, 40.0, and 60.0 °C. The water content in the membrane phase was found to decrease linearly with increasing cation fraction of ammonium in the membrane phase ($y_{NH_4^+}$) from $\lambda_{H_2O} = 21.2 \pm 0.4$ in proton form Nafion® in pure water to $\lambda_{H_2O} = 13.2$ in pure ammonium form Nafion® in a 0.1 M chloride solution. The conductivity was also found to decrease linearly with increasing $y_{NH_4^+}$ from 97 mS/cm to 25 mS/cm at 25.0 °C. The relative conductivity ratio of proton form Nafion® compared to ammonium form Nafion® is higher than the relative conductivity ratio of pure aqueous 1.0 M HCl and 1.0 M NH_4Cl (a factor of 3.8 – 3.9 vs. 3.10). This difference may be explained by the additional effect of lower water content in the membrane phase when in the ammonium form resulting in a lower conductivity. Our results indicate that the conductivity of Nafion® is isotropic, however, available literature is not conclusive on this matter. The temperature dependence of the conductivity was measured, and the fitted activation energy was found to depend on membrane composition and hence water content, $E_a = 10.3 + 4.2 y_{NH_4^+}$[kJ/mol].

3.6 Acknowledgement

We gratefully acknowledge Norsk Hydro ASA and the Research Council of Norway for support of this work.

Norsk Hydro ASA and the Research Council of Norway assisted in meeting the publication costs of this article.

Chapter 4

Influence of Cell Geometry on ac Impedance Measurements as Applied to PEMFCs

Rune Halseid, Preben J. S. Vie*, Rolf Jarle Aaberg**, and Reidar Tunold

Norwegian University of Science and Technology
Department of Materials Technology
NO–7491 Trondheim, Norway

*Present address: Institute for Energy Technology
P.O. Box 40, NO–2027 Kjeller, Norway
**Present address: Statkraft SF
P.O. Box 200 Lilleaker, NO–0216 Oslo, Norway
Revised version of Proceedings from the 1st European PEFC Forum, Eds. F. Büchi, G. G. Scherer, and A. Wokaun, 119–134 (2001).

4.1 Abstract

Different cell geometries used for ac impedance measurements on Polymer Electrolyte Membrane Fuel Cells (PEMFCs) are evaluated. Artifacts in impedance measurements may arise from small deviations from the ideal planar cell geometry usually employed in these measurements. These deviations are very difficult to avoid. Our calculations show that a planar cell design with a thin electrolyte is not suited for three-electrode ac impedance measurements. A two-electrode set-up performs equally well and in some cases better than the three-electrode set-up.

Three-electrode set-ups are required to study effects of low levels of CO contamination or other contaminants in the hydrogen that result in a slightly higher impedance than for electrodes operating on neat hydrogen. In theory, an improved cell geometry shows promising capabilities for studying such electrodes. The applicability of the cell remains to be demonstrated experimentally.

4.2 Introduction

In situ ac impedance measurements, also referred to as *in situ* Electrochemical Impedance Spectroscopy (EIS), has proven to be a powerful tool for characterization of electrode kinetics in PEMFC including transport properties of the backing material [123], electrode structure and ionomer content [124] and CO contamination of hydrogen fuel gas [125, 126] to mention a few papers.

Geometric effects on EIS measurements have received much attention both theoretically and experimentally, especially in SOFC research [127–130]. The method used by Winkler *et al.* [128] is also used in this paper to study cell geometries commonly used in the PEMFC literature. The implications of Reference Electrode (RE) placement and geometric effects in measurements on PEMFC has recently also been reviewed by Adler [131] using a different numeric method which makes estimation of the full EIS response of the cell possible. Liu *et al.* [132] also used a similar method as Winkler *et al.*, but allowed for non-linear electrode kinetics. He and Nguyen [133] have reported experiments where the relative size and overlapping of the electrodes were intentionally varied to find the effect on the measured overpotential and thus polarization resistance in PEMFC.

4.2.1 Two- *vs.* Three-Electrode Setups in EIS of PEMFC

Two fundamentally different experimental set-ups are used for impedance measurements:

1. Two-electrode EIS set-ups measures the total impedance of the cell, *i.e.*, contributions from the Working Electrode (WE) (which is the one under study), the Counter Electrode (CE) as well as membrane impedance are all included in the observed impedance

2. Three-electrode set-ups where a third electrode, the RE, is used to separate the impedance of the WE from the CE and in part from the membrane resistance.

If the impedance of the WE is much larger than the impedance of the CE, a two-electrode setup may give acceptably accurate results. However, it is required to use a three-electrode setup if the impedance of the WE is only slightly higher than that of the CE.

4.2.2 General Requirements to Electrodes and Cell Geometry

A small ac perturbation signal is used in EIS to obtain the impedance spectrum of the system under study. It is required that the system is stable and causal. Further, most methods used for interpretation of the results require that the system is linear putting a limitation on the amplitude of the perturbation used.

Given that these basic requirements are fulfilled, other recommendations for experimental design are also made in the literature [127–129, 134]:

1. The current distribution and electric potential field in the electrolyte should not shift with the applied frequency of the perturbation signal

2. The RE area should be small to avoid sampling a range of equipotential surfaces

3. A Luggin capillary type RE is preferred. The distance between the tip of the Luggin capillary and the WE should not be smaller than twice the outer diameter of the capillary to avoid shielding effects

4. The impedance of the RE must be small as compared to the impedance of the electrochemical measuring instruments

4.2.3 Some reported EIS measurements on PEMFC

Most of the work reported in the literature has employed two-electrode EIS measurement [123–126, 135], *i.e.*, the CE is also used as RE. It is assumed that the impedance of the CE is negligible as compared to the impedance of the WE. The WE is typically either an oxygen electrode (Fuel Cell (FC) cathode) or a hydrogen electrode where the hydrogen contains relatively high levels of carbon monoxide.

However, it is also of interest to develop geometries that are suited to study kinetics of FC anodes with slightly higher impedance than the standard anode (low levels of CO contamination, other contaminants in the hydrogen fuel etc.). In these cases an RE is required to resolve the contribution from each of the electrodes to the total cell impedance.

Three-electrode EIS, *i.e.*, inclusion of a separate RE, has been used in several papers to assess the reversibility of the CE [123, 125, 126, 135, 136]. However, no impedance data for the three-electrode configurations were reported except in [136] where a relatively large ring electrode was used as RE with the WE in the center in a symmetrical $H_2|H_2$ cell. Different cell designs used in the literature are sketched in Figure 4.1. The electrode configuration shown in Figure 4.1a) was used in [123], configuration *b*) in [125, 126], configuration *e*) in [136] and configuration g) in [133, 137, 138]. Recently, sandwiched cells [131, 139] and microelectrodes have also been suggested [131]. This will be discussed later.

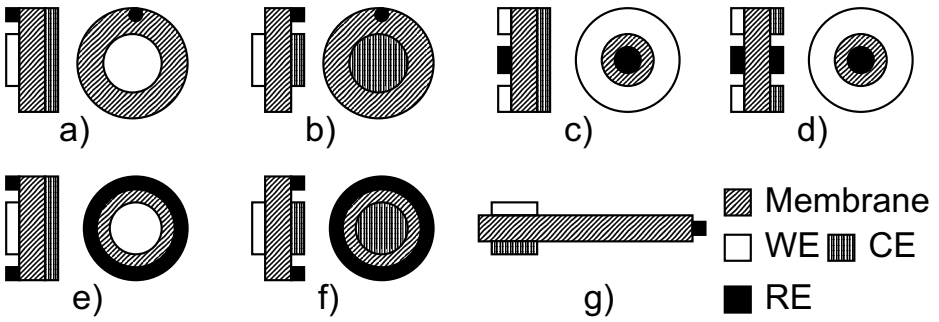

Figure 4.1: Different electrode configurations for planar cells with thin electrolytes (*not drawn to scale*).

4.3 Model

The electric potential, Φ, obeys Laplace's equation

$$\nabla^2 \Phi = 0 \tag{4.1}$$

The following boundary conditions apply:

$$\Phi_{WE} = V \quad \text{at the outer surface of the WE} \tag{4.2}$$
$$\Phi_{CE} = 0 \quad \text{at the outer surface of the CE} \tag{4.3}$$
$$\overrightarrow{n} \cdot (\kappa \nabla \Phi) = 0 \quad \text{at all other surfaces} \tag{4.4}$$

where $\overrightarrow{n}$ is the normal vector to the surface in question and κ is the conductivity of the given layer.

It is assumed that the conductivity, κ, in each layer shown in Figure 4.1 is isotropic and uniform. Further, we assume that a linear polarization resistance is assigned to the electrode layer can represent the electrode behavior at low frequencies ($\omega \to 0$).

The method first employed by Winkler *et al.* [128] is to first calculate $\Phi_{RE}^{\omega \to 0}$ as well as the current $I^{\omega \to 0}$, *i.e.*, the secondary current distribution based on linear kinetics. Then the same calculations are made as $\omega \to \infty$ to determine $\Phi_{RE}^{\omega \to \infty}$ and $I^{\omega \to \infty}$, *i.e.*, the primary current distribution. This is achieved by setting the conductivity in the electrode layers to be very high so that only the membrane resistance is effective. The polarization resistance, R_p^{exp}, may then be found using the following equations:

$$R_{mem} = A_{WE} \frac{\Phi_{WE}^{\omega \to \infty} - \Phi_{RE}^{\omega \to \infty}}{I^{\omega \to \infty}} \tag{4.5}$$
$$R_p = A_{WE} \frac{\Phi_{WE}^{\omega \to 0} - \Phi_{RE}^{\omega \to 0}}{I^{\omega \to 0}} - R_{mem} \tag{4.6}$$

R_{mem} is the membrane resistance and A_{WE} is the WE area. R_p is an input parameter to the model. Therefore we can compare the "experimental" polarization resistance, R_p^{exp}, to the true polarization resistance,R_p, and thus assess the error introduced by RE misalignment [128].

4.4 Model Parameters

The base case parameters used in our model are given in Table 4.1.

Table 4.1: Parameters used in the model for assessment of artifacts of RE in EIS. Data are taken from [123–126, 136]

Layer	κ [S/m]	R_p [Ωcm^2]	l [μm]
Backing materials	>10 000	<0.0002	200
Electrolyte (Nafion® 117)	5	0.36	180
Hydrogen oxidation	1	0.1	10
Oxygen reduction	0.01	10	10

It should be noted that the polarization resistance, being a measure of electrode performance, is strongly dependent upon potential, temperature, catalyst loading and electrode preparation. Especially the cathode impedance is very dependent upon cell potential, that is, the degree of dc polarization of the FC [123–125, 135]. For simplicity we restrict this work to high cell potentials (>0.85 V) where the polarization resistance for the cathode is high compared to the anode. Electrode backings are not included in the models because the conductivity of the backing materials is very high, see Table 4.1.

A commercially available numeric calculation package (FEMLAB 2.0 and MATLAB® 5.3) was used to solve Eqns. 4.1–4.4. FEMLAB includes automatic routines for mesh generation yielding a denser mesh near corners and interfaces in the geometric model. The mesh was refined until no further change was observed in calculated properties. As a further check it was confirmed that the total current is conserved within 0.05%.

4.5 Results and Discussion

As stated in the Introduction, we are interested in hydrogen electrodes with only slightly higher impedance than the standard PEMFC anode thus requiring the use of an RE. All cells considered here are symmetrical $H_2|H_2$ cells if not otherwise stated. We first discuss the positioning of the RE before proceeding with numerical analysis of geometric artifacts encountered in polarization resistance measurements using a three-electrode set-up. At the end we suggest an improved cell design better suited for studying PEMFC anodes.

4.5.1 Position of Reference Electrode

The potential gradient over the RE should be minimized as mentioned above. The potential gradient on the membrane surface is shown in Figure 4.2. Potential gradients are of interest because physical REs are not mathematical points. Figure 4.2 can be used to estimate the minimum separation of RE and WE or CE because the dimension of RE times the gradient is the approximate potential difference over the RE. This potential difference should not exceed 0.1% of the applied voltage [128], which was 0.1 V in this case. As seen from Figure 4.2, this requirement is dependent on the membrane conductivity and also the membrane thickness, but is generally fulfilled for a gap between the RE and WE larger than 1-2 mm when the WE and CE are symmetrical, both geometrically and kinetically.

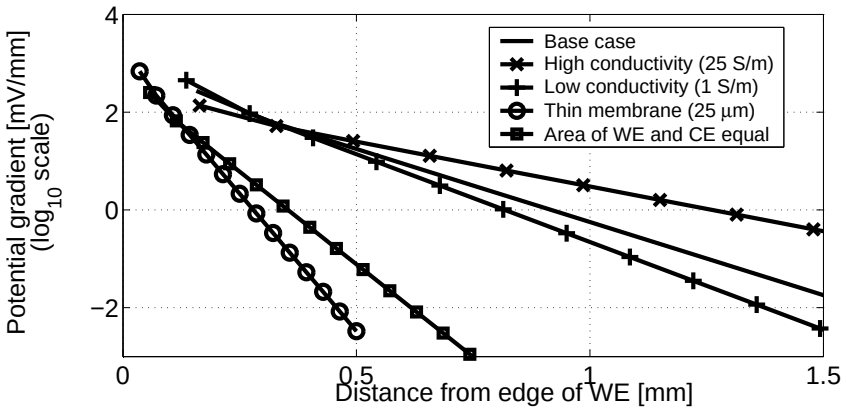

Figure 4.2: Potential gradient on membrane surface as function of distance from WE for different parameter sets. Base case and high/low κ are valid for configurations with a large CE (configuration a, c and e) shown in Figure 4.1. The line with squares is valid for configurations b, d and f in Figure 4.1.

If the WE and CE are the same in shape and size, we observe less sensitivity to the separation of RE and CE *provided the electrodes are perfectly aligned*. Substantial potential gradients on the membrane surface, where the RE shall be placed, are observed if the WE and CE are not perfectly aligned. This is shown in Figures 4.3(a) and 4.3(b). We see that even a slight misalignment results in a large potential gradient (>0.1mV/mm) along the edge

of the membrane. This effect is reduced if the CE is larger than the WE. A ring shaped RE (configurations shown in Figure 4.1e and f) is even more sensitive to misalignment because it samples the potential all along the edge of the membrane.

Our calculations show that it is not important on which side of the membrane the RE is located (WE or CE side). However, for practical reasons, it will in most cases be natural to locate the RE on the CE side because the CE normally operates on neat hydrogen thus eliminating the need for a separate gas supply to the RE.

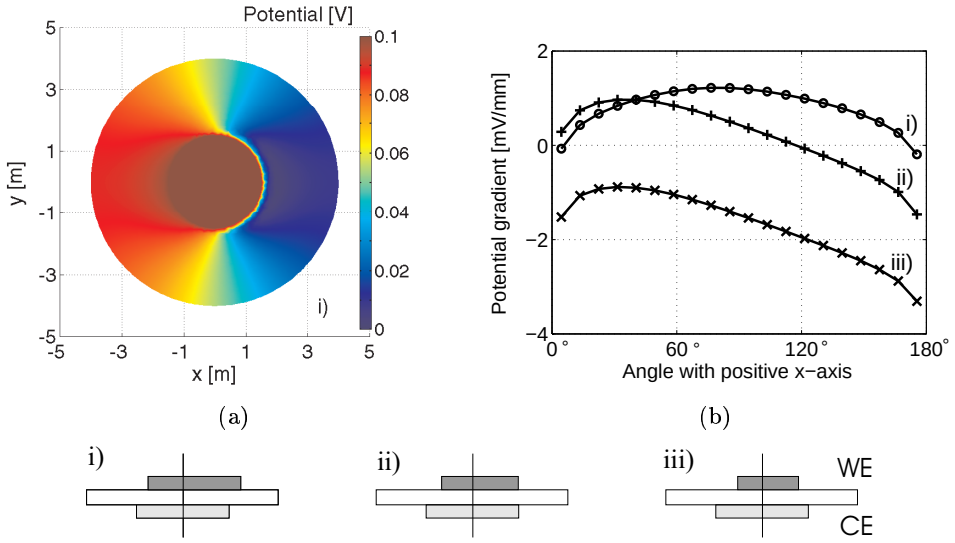

Figure 4.3: Effect of 0.5 mm displacement of WE in the xy-plane for three different cases i) both CE and WE Ø3 mm ii) WE Ø3 mm, CE Ø4 mm iii) WE Ø2 mm, CE Ø4 mm. a) shows the calculated potential, b) shows the calculated calculated potential gradient at the edge of the membrane (Ø8 mm).

The configuration in Figure 4.1g has been used in the study of water electrolyzers [137, 138] with a membrane electrolyte and recently also in a PEMFC [133]. The potential sampled at the end of the membrane strip outside the cell is the same as the potential sampled inside the cell by a RE located say 1-2 mm from the WE/CE, see Figure 4.4.

The RE is located externally to the cell, therefore, one may use Hg|$HgSO_4$ or other REs if desirable. If the cell is operated at elevated temperatures,

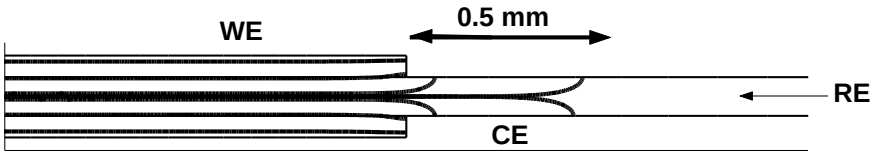

Figure 4.4: Equipotential lines for configuration g) in Figure 1 for perfectly aligned WE/CE electrodes in a $H_2|H_2$ cell as $\omega \to 0$ (*not to scale)*. The lines shown from bottom to top are 0.05V, 0.2V, 0.45V, 0.4999V, 0.5001V, 0.55V, 0.8V, and 0.95V.

thermoelectric potential effects in the membrane have to be accounted for if absolute potentials are required. For a temperature difference of 60 °C between the WE/CE and the RE, the thermoelectric potential is about 40 mV for Nafion® 117 [140]. There may also be contributions from the salt bridge between the membrane strip and the RE.

4.5.2 Influence of Cell Geometry and Kinetic Parameters on WE Polarization Resistance Determination

It is in general very difficult to avoid errors if a planar cell with a thin electrolyte is used. Deviations from symmetry both with respect to geometry and electrode performance give rise to errors in the experimentally determined R_p^{exp} [127–129, 131, 132, 134]. In the following calculations we use the configurations shown in Figure 4.1a and b to demonstrate the potential errors in experimentally determined R_p^{exp}.

In Figure 4.5(a) we see that if the CE is shifted *towards* the RE, or if the CE is larger than the WE, R_p is overestimated. This is because some of the CE layer is included as $\omega \to 0$ as shown in Figure 4.6 (curve iii), and in fact becomes more similar to a two-electrode set-up. The error in R_p^{exp} levels out when the equipotential line from the RE includes the entire CE. The measured polarization resistance is then effectively $R_p^{CE} + R_p^{WE}$, *i.e.*, the same as would be measured in a two-electrode set-up. If the CE is shifted *away* from the RE, R_p is underestimated. The reason is that not all of the WE layer is included as $\omega \to 0$ as shown in Figure 4.6 (curve i). The error does not level out because the equipotential line from the RE includes less and less of the WE as the CE

is shifted away from the RE.

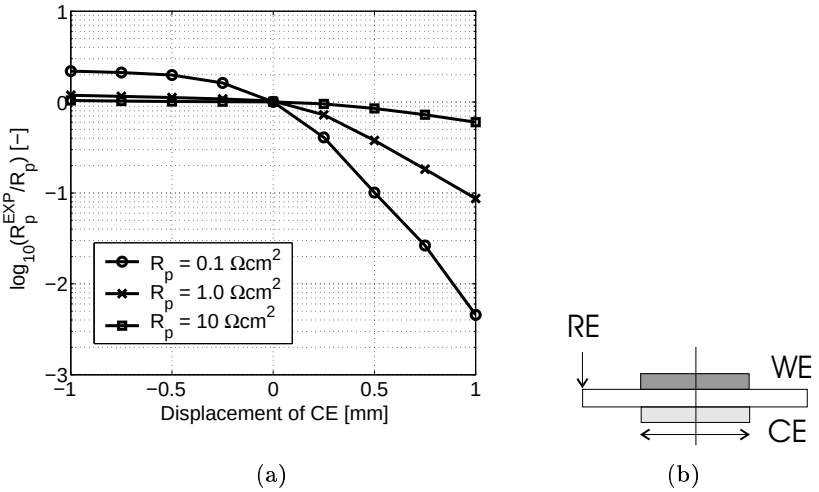

Figure 4.5: Deviation of numerically determined R_p^{exp} from input R_p for a geometry as in Figure 1b as function of relative position of WE and CE. The polarization resistance of the CE is kept constant at 0.1 Ω cm^2 in all cases. The shift of CE relative to WE was modeled with a 2D model, *i.e.*, assuming a rectangular cell. A more correct 3D model was very computationally demanding. A sketch showing the definition of "positive" and "negative" shift in shown in b).

As we have shown in this section, the errors in estimated polarization resistances can be very large when using planar cells with thin electrolytes. It is not possible to separate the impedances from each electrode by the use of an RE. This can also affect the observed impedance spectra. Even inductive behavior can be observed in systems where no such effects should be present due to artifacts related to the RE [131].

A two-electrode EIS set-up is in some cases better than a three-electrode set-up; see Figure 4.5(a) where R_p is grossly underestimated when the CE is shifted away from the RE. If a two-electrode set-up had been used instead, one would be sure that the total impedance, $R_p^{CE} + R_p^{WE}$, of the cell was measured. The problem with the equipotential line from the RE including less and less of the WE as the CE is shifted away from the RE would thus have been avoided.

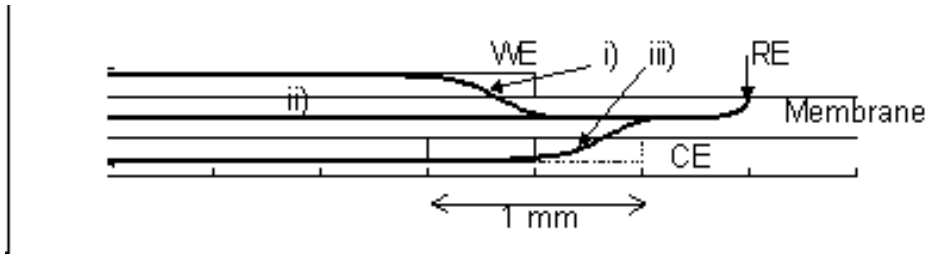

Figure 4.6: Equipotential lines from RE (Φ_{RE}) as $\omega \rightarrow 0$ for i) CE shifted 0.5 mm away from RE ii) perfect alignment of WE and CE iii) CE shifted 0.5 mm towards RE in a symmetric $H_2|H_2$ cell ($R_p = 0.1\ \Omega\ cm^2$ for both WE and CE).

4.5.3 Alternative Cell Design

Several researchers working with SOFCs recommend using a thicker electrolyte to reduce the risk of artifacts due to geometry [127, 128, 131, 134]. At the same time, the resistance of the electrolyte should not be too high as compared to the R_p of the electrode under study. If so, the real part of the impedance would then dominate making the measurement of imaginary parts of the impedance much less accurate. One could increase the electrolyte thickness by using a stack of membranes [131], but this would introduce an uncertainty regarding the contact resistance between each membrane. Also, a membrane stack only reduces the problems with artifacts even if the RE is forced to sense the potential in the middle of the stack. The stack does not eliminate the artifacts [131]. Ohmic heating would also be a potential problem in a thick solid membrane because all dissipated energy in the membrane would have to be carried by heat conduction. The introduction of a metallic quasi-reference sandwiched in a stack has been suggested [139]. This configuration has the same limitations as other membrane stacks in addition to the fact that the reference potential is not thermodynamically well defined. Liu *et al.* [132] suggested to use two RE positioned on the same side of the membrane in the Membrane Electrode Assembly, but at opposing edges. By measuring the potential of both REs, *some* of the error due to misalignment of the electrode may be eliminated provided the electrodes are of the same size and shape.

We propose an improved design, see Figure 4.7 below which in principle is similar to the Risø pellet used for SOFC research [128]. The CE compartment is filled with a liquid electrolyte (e.g. a sulfuric acid solution) that can be

circulated to prevent excessive heating.

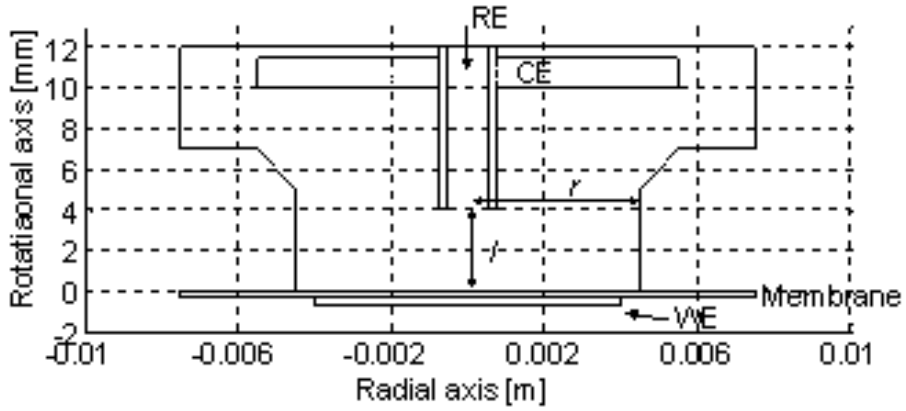

Figure 4.7: Cross section of the alternative cell design.

Table 4.2: Influence of different parameters on accuracy of determination of R_p^{exp} for the improved cell design. Refer to Figure 4.7 for a definition of symbols used.

Parameter	R_p^{exp}/R_p
Base case, as shown in Figure 4.7	1.05
$r = 4$ mm	1.003
$r = 5$ mm	1.1
RE closer to WE, $l = 3$mm	1.03
WE R_p 1/10th of base case R_p	1.07
WE R_p 10 times base case R_p	1.02

We see from Table 4.2 that the improved design is much less sensitive to geometry thereby yielding results that are more reliable. This improved cell design also allows one to more freely vary the area and type of CE in order to assure that the kinetic properties of the CE are favorable compared to the WE. Further, this alternative configuration makes it possible to use other REs than the RHE, e.g. $Hg|HgSO_4$, if desirable. The liquid electrolyte will ensure that the water saturation of the membrane is stable and may ease thermal

control of the cell due to higher heat capacity and the possibility of circulating the electrolyte. The water content of a membrane in contact with a liquid is higher than in contact with a gas resulting in higher membrane conductivity than in a real FC. The higher water content may influence the kinetics of the WE particularly if studying the oxygen reduction reaction [123]. It also makes it impossible to measure kinetic parameters as function of humidity. However, the external electrolyte makes it easier to control the level of ammonium contamination of the membrane than in a conventional FC. On the other side, anions from the electrolyte may penetrate the membrane affecting the electrode process under study at the WE. Finally, the interface between the membrane and the liquid electrolyte will make a contribution to the total impedance of the cell. All these effects have to be evaluated experimentally.

4.6 Conclusions

Our calculations show that a planar cell design with a thin electrolyte is not suited for three-electrode ac impedance measurements. A two-electrode set-up using a symmetrical cell performs equally well and in some cases better than the three-electrode set-up. Three-electrode set-ups are required to study effects of low levels of CO contamination or other contaminants on the hydrogen anode that result in only a slightly higher impedance than for the standard anode. An improved cell geometry with a liquid electrolyte as CE compartment shows promising capabilities for the study of such electrodes.

4.7 Acknowledgement

Norsk Hydro ASA and the Research Council of Norway supported this work.

Chapter 5

Effects of N_2 and CO_2 on PEMFC Performance

5.1 Summary

The mechanism for Hydrogen Oxidation Reduction (HOR) on the PtRu anode catalyst has been investigated. Polarization curves of hydrogen mixed with N_2, Ar, He and CO_2 have been measured, both in fuel cells ($H_2|O_2$) and in symmetrical cells ($H_2|H_2$). Experiments with poisoning of platinized Pt in sulfuric acid by CO and CO_2 have been made. Theoretical relations for both the Tafel-Volmer and the Herowsky-Volmer mechanisms are also presented.

HOR on the PtRu anode catalyst follows the Tafel-Volmer mechanism based on the observation of limiting currents that were not due to mass transfer. The conclusion is also supported by the observation of higher HOR rates after the electrodes had been electrochemically cleaned. The mass transfer limiting current in the Gas Diffusion Layer (GDL) was found to be very high based on the observation of a small difference in limiting current for H_2 diluted with N_2 or He. Transport through the ionomer in the catalyst layer covering the active catalyst also contributed to the limiting current. It was not possible to accurately estimate the relative importance of the mass transfer resistance in the ionomer compared to the reaction limiting current due to the Tafel step.

We further found that the influence of CO_2 on the performance of the PtRu anode was significant, especially in symmetrical cells. Nitrogen did not seem to have any effect on anode performance other than dilution. Dilution of hydrogen with the noble gases Ar and He gave very similar results as dilution with nitrogen.

The contamination species formed on platinized Pt by CO_2 and CO respectively were different as observed by CV. The contamination coverage of the catalyst when exposed to CO was higher than for CO_2. The adsorbed contaminants formed from CO also displaced the contaminants formed by CO_2. The poisoning mechanism for CO_2 can not be explained by formation of CO_{ads} through the reverse water-gas shift reaction alone. Other species, such as $COOH_{ads}$ and COH_{ads}, may be involved.

Recovery of the symmetrical $H_2|H_2$ cell after exposure to CO_2 was quite slow and not complete. To achieve complete recovery, it was required to electrochemically activate electrodes by oxidation of contaminants. Recovery of the $H_2|O_2$ cell was complete after some time without electrochemical activation of the electrodes.

5.2 Introduction

Inert[1] components are formed when reforming or splitting liquid fuels and dilutes the hydrogen fuel stream as discussed in Section 2.7.4. The hydrogen typically contains 25-50 vol% inert components (CO_2 and N_2) depending on which reforming process that is used. It is usually uneconomical to remove these components, therefore, it is of interest to study how these components affect FCs. CO_2 is present in hydrogen based on carbonous fuels. Several studies on CO_2 influence have been reported both in the context of FCs, but also in more general studies of adsorption of species originating from CO_2 on Pt in acidic solutions. There is some divergence in the literature as to which species that are involved in CO_2 poisoning as further discussed below.

5.2.1 Effects of CO_2

Reduction of CO_2 on Pt in Acidic Solutions

Giner [141] found that CO_2 reacts with electrochemically adsorbed hydrogen in the potential region 0–250 mV_{RHE} forming a reduced specie (r-CO_2). Giner found this reaction to be slow at room temperature, but much faster at higher temperatures. The oxidation peak for r-CO_2 was larger at higher temperature and occurred at a lower potential. CO_{ads} and $COOH_{ads}$ were suggested as probable products of CO_2 reduction.

[1] The term "inert" may be somewhat imprecise because some of these components may interactions with the electrocatalyst.

Vassiliev *et al.* [142] studied adsorption of CO_2 on various metals including platinum metals. They found that reduction of CO_2 only occurred at Pt and Rh, and concluded that presence of H_{ads} is required, but not sufficient, to reduce CO_2. This was concluded based on the observation that Pd, Ir, Ru and Os did not show activity for reduction of CO_2. They also found that the species formed on Pt were similar to intermediates produced during dehydrogenation of methanol. The species differed from those produced by CO adsorption on Pt. No solution species were observed at positive electrode potentials *vs.* RHE. Vassiliev *et al.* proposed that triply bond COH_{ads} was the most important species formed with $COOH_{ads}$ and CO_{ads} as possible intermediate steps. The coverage of Pt by reduced CO_2 species was about 70–80% in the potential range 0 – 250 mV_{RHE} as also confirmed by Papageorgopoulos and de Brujin [143]. The coverage was about 98% in the case of CO induced species. Thus, effects of CO_2 poisoning in FCs are expected to be much less severe than CO poisoning.

Brisard *et al.* [144] found in a DEMS study that formaldehyde, formic acid, methanol and traces of methane were formed by reduction of CO_2 on Pt in perchloric acid at *negative* potentials vs. RHE. Both methanol and formaldehyde were also detected in experiments where CO was used, but no formic acid was detected. This lead the authors to conclude that there is a parallel pathway for reduction of CO_2 on Pt. CO_2 reacts with H_{ads} to form $COOH_{ads}$ or CO_{ads}. CO_{ads} can then further react with H_{ads} to form formaldehyde, methanol or methane.

Hori *et al.* [145] classified Pt as a CO_{ads} forming metal concluding that formation of $COOH_{ads}$ due to CO_2 reduction was not important on Pt in contrast to the findings of Brisard *et al.* Presence of linear, bridge and triply bond CO_{ads} on Pt has been found by FTIR spectroscopy [146], and is well established at potentials positive of the RHE. COH_{ads} and $COOH_{ads}$ was also detected by Iwasita *et al.* [146]. Hoshi and Hori [147] found that atomically flat Pt surfaces ((1 1 1) and (1 0 0)) showed poor activity for reduction of CO_2. Stepped, and in particular kinked step Pt surfaces, showed much higher activity for reduction of CO_2.

Studies of carbon supported, Pt based anode catalysts by CV have been reported [143, 148, 149]. These results are in good agreement with observations made using smooth and platinized platinum electrodes discussed above.

Effect of CO_2 in Relation to Fuel cells

The focus of CO_2 poisoning in FC based literature has been on formation of CO_{ads} on Pt based catalysts. Formation of CO can proceed either through the (gas phase) water-gas shift reaction

$$CO_2 + H_2 \rightleftarrows CO + H_2O \tag{5.1}$$

or through the electrochemical equivalent

$$CO_2 + 2H^+ + 2e^- \rightleftarrows CO_{ads} + H_2O \tag{5.2}$$

The equilibrium concentration of CO in Reaction 5.1 is 25–100 ppm at typical PEMFC operating conditions [148, 150]. Less focus has been put on *other* intermediates that may form as a result of CO_2 reduction.

Effects of CO_2 on FC performance have been reported by several groups. Wilson *et al.* [151] found that a Pt based anode catalyst was significantly affected by 25% CO_2 and even more so if a GDL with a Pt catalyst[2] was placed upstream the FC. This showed that the water-gas shift reaction (Reaction 5.1) was promoted by the Pt catalyst on the GDL upstream. Thus, excessive Pt loading, which is not electrochemically active, may reduce tolerance towards CO_2. 2% air/oxygen bleed into the fuel stream almost eliminated the effect of CO_2 as did the use of a carbon supported PtRu catalyst. Other studies [150, 152, 153] have also found CO_2 to have a negative effect on FC performance, in particular when carbon supported Pt is used as anode catalyst. The effect of CO_2 in FCs where carbon supported PtRu is used as anode catalyst is moderate, especially at moderate current densities [151, 152, 154].

In a study of the CO and CO_2 tolerance of Pt, PtRu and PtMo catalysts, Ball *et al.* [149] found that PtMo had better CO tolerance than PtRu at CO levels higher than 50 ppm, but much lower tolerance towards 25% CO_2. Thus, the PtMo catalyst performed significantly worse than the PtRu catalyst operating on synthetic reformate.

5.2.2 Effects of Nitrogen

Nitrogen is present in hydrogen from ATR and POX reforming processes (see Section 2.5.2), but has received less attention than CO_2 and CO poisoning in particular. Available literature seems to indicate that nitrogen only has dilution effects, *i.e.*, that nitrogen is not electrochemically active in FCs [150, 152–154].

[2] *i.e.*, an ETEK GDL with platinum catalyst applied but without ionic nor electronic contact thus not electrochemically active, but capable of promoting Reaction 5.1.

5.2.3 Experimental Determination of Effects of Anode Gas Composition

FC experiments do not normally include an RE. Thus, there is no way to distinguish between contributions from the anode and the cathode to the total overpotential. Even if there was an RE, it would not necessarily be possible to separate the contributions from each electrode, see Chapter 4 for a comprehensive discussion of this. Further, polarization losses of the cathode are large compared to anode losses. Thus, effects of anode gas composition will usually be small when studying a $H_2|O_2$ FC except in the presence of CO. To better assess the effects of gas composition on the anode, a symmetrical cell with H_2 also on the cathode was used. The polarization of the cathode is then comparable to, or smaller than, the polarization of the anode.

5.3 Theory

The observed cell potential for both symmetrical cells ($H_2|H_2$) and for FCs ($H_2|O_2$ or $H_2|$air), is a function of several factors:

$$E = \Phi^c - \Phi^a = E^{rev} - iR_{mem} - \eta^a_{ct} + \eta^c_{ct} - \eta^a_r + \eta^c_r - \eta^a_d + \eta^c_d \tag{5.3}$$

E	Cell potential
Φ^a	Anode Galvani potential
Φ^c	Cathode Galvani potential
E^{rev}	Reversible cell potential
R_{mem}	Ohmic resistance in membrane
i	Current density
η^a_{ct}	Anode activation overpotential due to charge transfer
η^c_{ct}	Cathode activation overpotential due to charge transfer
η^a_r	Anode overpotential due to heterogenous reaction limitations
η^c_r	Cathode overpotential due to heterogenous reaction limitations
η^a_d	Anode overpotential due to mass transfer limitations (diffusion)
η^c_d	Cathode overpotential due to mass transfer limitations (diffusion)

By convention, anodic overpotentials are always positive whereas cathodic overpotentials are always negative, thus the different signs in Equation 5.3. Further, the cell potential is defined as the difference between cathode and

anode potential in accordance with IUPAC conventions[3]. The different overpotentials are discussed in the following.

5.3.1 Concentration Overpotentials

The relationship between current density and steady state mass transfer rate of hydrogen is described by the following equation valid at a constant bulk partial pressure of hydrogen:

$$i = i_d = 2Fk_d(p^b_{H_2} - p^s_{H_2}) = 2Fk_d\Delta p_{H_2}, \qquad k_d = \frac{D_{AB}}{RT\delta}\frac{\epsilon}{\tau} \tag{5.4}$$

k_d is the mass transfer coefficient, $p^b_{H_2}$ and $p^s_{H_2}$ is the partial pressure of hydrogen in the flow channels and at the electrode surface respectively. The relation between k_d and diffusivities is found assuming Fick's 1st law with a GDL with thickness δ assuming that the gas behaves ideally. Corrections for porosity ϵ and tortuosity τ are also required because the mass transfer takes place in a porous GDL. The binary diffusion coefficient D_{AB} can be replaced by an effective diffusion coefficient in cases where there are three or more components present (hydrogen, water and inert). The effective diffusion coefficient for hydrogen may be found from Stefan-Maxwell equation and by the definition of the effective diffusion coefficient analogously to the binary diffusion coefficient, see Bird, Stewart and Lightfoot for details [155]. In the case where all the other $n-1$ components are stagnant, the effective diffusion coefficient of hydrogen (here taken to be component 1) is given by:

$$\frac{1-y_1}{D_{1,m}} = \sum_{j=2}^{n}\frac{y_j}{D_{1j}} \tag{5.5}$$

The limiting current due to mass transfer occurs when $p^s_{H_2} = 0$:

$$i_{d,l} = 2Fk_d p^b_{H_2} \tag{5.6}$$

[3]The FC test station always measures the potential this way ($E = \Phi^c - \Phi^a$). However, when using potentiostats to study the FC anode, the anode was normally connected to the WE and the cathode to the CE. The measured potential in this set-up is then $\Phi^{WE} - \Phi^{RE} = \Phi^{WE} - \Phi^{CE} = -E$. $\Phi^{CE} = \Phi^{RE}$ because we use a two electrode set-up. Our aim with symmetrical cells is to find the overpotential for the anode. It thus makes more sense to measure the potential the way the potentiostat does because $\eta^a = \Phi^{WE} - \Phi^{RE}$. Therefore, all potentials reported for the symmetrical cell uses the latter way of defining the cell potential.

so that the surface concentration of hydrogen may be expressed by:

$$\frac{p^s_{H_2}}{p^b_{H_2}} = 1 - \frac{i}{i_{d,l}} \tag{5.7}$$

This may be introduced into Nernst equation, and the following expression for concentration overpotential may be found:

$$\eta_d = \frac{RT \ln 10}{nF} \log\left[1 - \frac{i}{i_{d,l}}\right] \tag{5.8}$$

The hydrogen content in the bulk gas will change along the flow channel due to conversion of hydrogen. Plug flow is assumed for the gas in the flow channels. In analogy to heat transfer, the appropriate driving force for mass transfer is the log-mean concentration difference [156]. The driving force used in Equation 5.4 is thus modified to account for the change in Δp_{H_2} along the flow channel:

$$i_d = 2Fk_d\Delta p_{H_2,lm} \qquad \Delta p_{H_2,lm} = \frac{\Delta p_{H_2,in} - \Delta p_{H_2,out}}{\ln(\Delta p_{H_2,in}/\Delta p_{H_2,out})} \tag{5.9}$$

5.3.2 Reaction and Charge Transfer Overpotentials for the Hydrogen Oxidation Reaction

The Hydrogen Evolution Reaction (HER) has been studied in much detail the literature, see f. ex. [157] for a review. The Hydrogen Oxidation Reaction (HOR) has been less studied probably because of the low solubility of hydrogen in aqueous solutions. The HOR is a fast reaction resulting in experimental problems with a mass transfer limiting current at a very low overpotential. However, the HOR is a very important reaction in connection with FCs. Mass transfer limitations are much less severe because hydrogen gas is in close proximity of the active sites. Gas diffusion is thus fast enough to support considerable currents. The same mechanistic steps are assumed for HOR as for HER. This gives two possible reaction routes [158, 159]:

The Volmer-Tafel route

$$\mathrm{H_2} + 2\square \leftrightarrows 2\mathrm{H_{ads}} \qquad \text{Tafel step} \tag{5.10}$$

$$\mathrm{H_{ads}} \leftrightarrows \mathrm{H^+} + \mathrm{e^-} + \square \qquad \text{Volmer step} \tag{5.11}$$

and the Volmer-Heyrowsky route

$$\begin{aligned} H_2 + \square &\leftrightarrows H_{ads} + H^+ + e^- \qquad \text{Heyrowsky step} \\ H_{ads} &\leftrightarrows H^+ + e^- + \square \qquad \text{Volmer step} \end{aligned} \tag{5.12}$$

where $\square$ denotes a vacant, active site and H_{ads} is an adsorbed hydrogen atom on the surface. The current densities for the individual steps, assuming Langmuir adsorption, are given by [158]:

$$\begin{aligned} i_V =& F k^0_{a,V} \theta \exp(\alpha_V f(E - E^0)) \\ & - F k^0_{c,V} a^s_{H^+} (1-\theta) \exp(-(1-\alpha_V) f(E - E^0)) \end{aligned} \tag{5.13}$$

$$i_T = 2F k_{T,f} p^s_{H_2} (1-\theta)^2 - 2F k_{T,b} \theta^2 \tag{5.14}$$

$$\begin{aligned} i_H =& F k^0_{a,H} (1-\theta) p^s_{H_2} \exp(\alpha_H f(E - E^0)) \\ & - F k^0_{c,H} a^s_{H^+} \theta \exp(-(1-\alpha_H) f(E - E^0)) \end{aligned} \tag{5.15}$$

where $f = F/RT$. The electrochemical rate constants, $k^0_{i,j}$, are referred to the standard potential of the electrode. In these equations it has also been assumed that $\alpha_a + \alpha_c = 1$. Note that the oxidation rates of both the Tafel and the Heyrowsky step are linear in the concentration of hydrogen on the surface, $p^s_{H_2}$. It is not possible to identify which process that is limiting at high currents if the total reaction rate is limited by either one of these reaction steps or by mass transfer.

The net current of all these reactions at equilibrium is zero making it possible to establish a relationship between the forward and reverse rate constants for the three reactions. At equilibrium, the surface concentrations of hydrogen and protons are the same as the bulk concentrations ($p^s_{H_2} = p^b_{H_2}$ and $a^s_{H^+} = a^b_{H^+}$).

$$k^0_{c,V} = \frac{k^0_{a,V} \theta^{rev}}{a^b_{H^+}(1-\theta^{rev})} \exp(f(E^{rev} - E^0)) \tag{5.16}$$

$$k_{T,b} = \frac{k_{T,f} p^b_{H_2} (1-\theta^{rev})^2}{\theta^{rev\,2}} \tag{5.17}$$

$$k^0_{c,H} = \frac{k^0_{a,H} (1-\theta^{rev}) p^b_{H_2}}{\theta^{rev} a^b_{H^+}} \exp(f(E^{rev} - E^0)) \tag{5.18}$$

The next step is to introduce the exchange current densities for the two electrochemical reactions, $i_{0,V}$, $i_{0,H}$, and the reaction current $i_{r,T}$[4] for the Tafel reaction. The potential difference may be written $E - E^0 = E - E^{rev} + E^{rev} - E^0 = \eta + (E^{rev} - E^0)$ where η is the overpotential. By introducing this as well as Equations 5.16 to 5.18 into Equations 5.13 to 5.15 we obtain:

Volmer step:

$$\frac{i_V}{i_{0,V}} = \frac{\theta}{\theta^{rev}} \exp(\alpha_V f\eta) - \frac{1-\theta}{1-\theta^{rev}} \frac{a^s_{H^+}}{a^b_{H^+}} \exp(-(1-\alpha_V) f\eta) \tag{5.19}$$

$$i_{0,V} = F k^0_{a,V} \theta^{rev} \exp(\alpha_V F(E^{rev} - E^0)) \tag{5.20}$$

Tafel step:

$$\frac{i_T}{i_{r,T}} = \frac{p^s_{H_2}}{p^b_{H_2}} \left(\frac{1-\theta}{1-\theta^{rev}}\right)^2 - \left(\frac{\theta}{\theta^{rev}}\right)^2 \tag{5.21}$$

$$i_{r,T} = 2F k_{T,f} p^b_{H_2} (1-\theta^{rev})^2 \tag{5.22}$$

Heyrowsky step:

$$\frac{i_H}{i_{0,H}} = \frac{1-\theta}{1-\theta^{rev}} \frac{p^s_{H_2}}{p^b_{H_2}} \exp(\alpha_H f\eta) - \frac{\theta}{\theta^{rev}} \frac{a^s_{H^+}}{a^b_{H^+}} \exp(-(1-\alpha_H) f\eta) \tag{5.23}$$

$$i_{0,H} = F k^0_{a,H} (1-\theta^{rev}) p^b_{H_2} \exp(\alpha_H F(E^{rev} - E^0)) \tag{5.24}$$

The mass transfer limitation for protons ($a^s_{H^+}/a^b_{H^+}$) is usually not considered [158, 159] as is the case also in the following. The mass transfer limitation effects for hydrogen $p^s_{H_2}/p^b_{H_2}$ may be expressed by the mass limiting current as shown in Equation 5.7. By introducing Equation 5.7 into Equation 5.21 we get:

$$i_T = \frac{\left(\frac{1-\theta}{1-\theta^{rev}}\right)^2 - \left(\frac{\theta}{\theta^{rev}}\right)^2}{\frac{1}{i_{r,T}} + \frac{1}{i_{d,l}} \left(\frac{1-\theta}{1-\theta^{rev}}\right)^2} \tag{5.25}$$

[4]Even though the Tafel step is not electrochemical, the equilibrium is still dynamic; that is, the forward and reverse reaction proceed at the same rate at equilibrium according to the Guldberg-Waage principle. We can, in analogy to the exchange current density for the Volmer and Heyrowsky reactions, define a reaction rate current $i_{r,T}$ as given in Equation 5.22.

If both the Tafel reaction as well as mass transfer are close to their limiting values, the total observed limiting current is given by [159]:

$$i_s = \frac{i_{d,l} i_{r,T}}{i_{d,l} + i_{r,T}} = \frac{2F k_{T,f} k_d}{k_{T,f} + k_d} p_{H_2}^b \tag{5.26}$$

Relations at Low Coverage

In this limit we set $(1 - \theta^{rev}) = 1$ which leads to a major simplification for the Volmer-Tafel mechanism. The ratio $\frac{\theta}{\theta^{rev}}$ can be eliminated from Equation 5.25:

$$\frac{\theta}{\theta^{rev}} = \sqrt{1 - \frac{i}{i_s}} \tag{5.27}$$

where i_s was defined in Equation 5.26. The total current is the same as the current due to the Volmer reaction ($i = i_V$). Equation 5.27 inserted into Equation 5.19 yields [158]:

$$\frac{i}{i_{0,V}} = \left(\sqrt{1 - \frac{i}{i_s}} - \exp\left(-f\eta\right) \right) \exp\left(\alpha_V f \eta\right) \tag{5.28}$$

$$y = \ln i - \ln \left(\sqrt{1 - \frac{i}{i_s}} - \exp\left(-f\eta\right) \right) = \ln i_{0,V} + \alpha_V f \eta \tag{5.29}$$

Thus, if we plot y as defined above vs. η, $i_{0,V}$ can be determined from the intercept, and the slope yields $\alpha_V f$ at low overpotentials [159].

Dependence of Exchange Current Density on Hydrogen Pressure

The polarization resistance is defined by [158]:

$$R_p = \left. \frac{\partial \eta}{\partial i} \right|_{\eta=0} \tag{5.30}$$

The polarization resistance has different contributions like charge transfer, diffusion and reaction resistances [158]. The exchange current density, i_0, is then related to the charge transfer resistance, R_{ct}, through:

$$i_o = \frac{RT}{zF} \frac{1}{R_{ct}} \tag{5.31}$$

Further, there is a relationship between the exchange current density and the activity of the species involved in the electrochemical reaction as will be shown below. The diffusion overpotential is negligible at low overpotentials.

Volmer Step The exchange current density of the Volmer reaction is given in Equation 5.20. The potential difference in Equation 5.20 can be expressed by the Nernst Equation:

$$E^{rev} = E^0 + \frac{1}{2f} \ln \frac{a_{H^+}^2}{p_{H_2}} \Leftrightarrow \left[\frac{p_{H_2}}{a_{H^+}^2}\right]^{-\frac{\alpha_V}{2}} = \exp(\alpha_V f(E^{rev} - E^0)) \tag{5.32}$$

so that

$$\left(\frac{\partial \ln i_{0,V}}{\partial \ln p_{H_2}}\right)_{a_{H^+}} = \frac{\partial \ln \theta^{rev}}{\partial \ln p_{H_2}} - \frac{\alpha_V}{2} \tag{5.33}$$

We have assumed that the adsorption of hydrogen follows the Langmuir isotherm:

$$K = \frac{\theta^{rev}}{(1-\theta^{rev})\sqrt{p_{H_2}}} \Leftrightarrow \theta^{rev} = \frac{K\sqrt{p_{H_2}}}{1 + K\sqrt{p_{H_2}}} \tag{5.34}$$

Two limiting cases are easily found:

1. $K\sqrt{p_{H_2}} \ll 1$ so that θ^{rev} is small $\Rightarrow \frac{\partial \ln \theta^{rev}}{\partial \ln p_{H_2}} = \frac{1}{2}$
2. $K\sqrt{p_{H_2}} \gg 1$ so that $\theta^{rev} \approx 1 \Rightarrow \frac{\partial \ln \theta^{rev}}{\partial \ln p_{H_2}} = 0$

The slope $\partial \ln i_{0,V} / \partial \ln p_{H_2}$ is thus expected to vary from $(1 - \alpha_V)/2$ at low coverage to $-\alpha_V/2$ at high coverage.

Tafel Step In the case of this heterogenous reaction, a similar relationship between R_p (or rather R_r in this case) and i_r is defined by Vetter [158]. By differentiation of Equation 5.22 we find that:

$$\frac{\partial \ln i_{r,T}}{\partial \ln p_{H_2}} = 1 + 2\,\frac{\partial \ln(1-\theta^{rev})}{\partial \ln p_{H_2}} \tag{5.35}$$

Again we can identify two limiting cased for $(1-\theta^{rev})$ through the Langmuir isotherm. At low coverage the slope tends to unity, and at high coverage the slope tends to zero.

Heyrowsky Step The derivation follows the same scheme as for the Volmer step, and the result is:

$$\left(\frac{\partial \ln i_{0,H}}{\partial \ln p_{H_2}}\right)_{a_{H^+}} = \frac{\partial \ln(1-\theta^{rev})}{\partial \ln p_{H_2}} + (1 - \frac{\alpha_H}{2}) \tag{5.36}$$

At low coverage the slope tends to $1-\alpha_H/2$, and at high coverage the slope tends to $(1-\alpha_H)/2$.

Summary of Relationships between Exchange Current Density and Partial Pressure of Hydrogen The dependency of exchange current density upon the hydrogen partial pressure is given in Table 5.1. The limiting cases have been deduced based on the assumption that one step is much slower than the other in the mechanism. In the case where both steps in the mechanism are important, an average exchange current density may be defined by [159]:

$$i_{0,VT} = \frac{i_{0,V} i_{r,T}}{i_{0,V} + i_{r,T}} \tag{5.37}$$

$$i_{0,VH} = \frac{i_{0,V} i_{0,H}}{i_{0,V} + i_{0,H}} \tag{5.38}$$

Table 5.1: Dependency of exchange current density on partial pressure of hydrogen for the different possible steps in oxidation of hydrogen assuming that only one of the steps involved is limiting.

Reaction step	$\partial \ln i_0 / \partial \ln p_{H_2}$	
	$\theta^{rev} \ll 1$	$\theta^{rev} \approx 1$
Tafel	1	0
Heyrowsky	$1-\alpha_H/2$	$(1-\alpha_H)/2$
Volmer	$(1-\alpha_V)/2$	$-\alpha_V/2$

5.3.3 Ohmic Losses

The ohmic resistance in the cell may be assessed either by current interrupt techniques or by high frequency impedance measurements. The current interrupt technique is easier to implement, and requires less costly equipment.

High frequency impedance measurements on FCs are difficult due to the high currents and low cell impedances involved.

Current interrupt is based on breaking the electronic circuit quickly and then observing the potential relaxation transient. The instantaneous voltage change, ΔE, is related to the ohmic resistance in the cell, R_{cell}, through Ohm's law:

$$R_{cell} = \Delta E / \Delta I \tag{5.39}$$

It is usually assumed that all other ohmic resistances in the FC are small compared to the membrane resistance so that $R_{mem} = R_{cell}$. The major drawback with current interrupt techniques is that the local current in the active layers may not drop to zero immediately. The observed cell resistance is thus not the true cell resistance [160, 161]. This is because there is a potential gradient through the porous electrodes in the FC. The resistance estimated based on Equation 5.39 is too high, that is, some of the overvoltage due to polarization is erroneously attributed to the ohmic resistance of the cell. One should also notice that changes in exchange current density, i_0, of the electrodes is an important parameter; the lower the exchange current density is, the slower the relaxation of the potential gradient in the active layer is [161]. Thus, error in the estimated ohmic resistance increases with decreasing i_0.

5.3.4 Changes in Reversible Cell Potential

The reversible cell potential is affected by the presence of inert gases, and may be estimated using Nernst Equiation. Hydrogen and oxygen is consumed along the flow channels. Therefore, the reversible potential will vary slightly unless the reactant gases are pure hydrogen and oxygen saturated with water vapor throughout the cell. Assuming that the electronic *in-plane* conductivity of the GDL is high, the cell operates at a uniform potential. The overpotential is thus not uniform throughout the cell. For the anode, assuming 25 % inert (on dry basis) and 80 % conversion, the variation in reversible potential over the cell is about 10 mV at 60°C. For a cathode running on air at 40 % conversion, the difference is about 3 mV. In the case of the $H_2|O_2$ cell, variations in reversible voltages are moderate compared to other losses in the system and are thus not corrected for. Both electrodes operate on hydrogen in the symmetrical cell, but inert components may be added in the hydrogen feed to the anode. Again, assuming high *in-plane* electronic conductivity, the appropriate

reversible potential to use must be based on the exhaust conditions. The cathode always operates on pure H_2 in the symmetrical cell so that no corrections for conversion are needed.

5.3.5 Fit of Experimental Data for the $H_2|O_2$ Cell

The total cell reaction is

$$2H_2(g) + O_2(g) \rightarrow 2H_2O(l) \tag{5.40}$$

It is not possible to separate the effect of the anode gas composition from the cathode behavior in the case of the $H_2|O_2$ cell because the polarization of the cathode reaction is large compared to the anode polarization. The activation overpotential for the anode is therefore neglected. The Tafel equation is thus well suited to describe $H_2|O_2$ polarization data:

$$\eta_{ct}^{c} = -\frac{RT\ln 10}{\alpha_c z F}\log i_0 + \frac{RT\ln 10}{\alpha_c z F}\log i = a + b\log i \tag{5.41}$$

The following $E-i$ relationship for the FC is obtained when Tafel kinetics are assumed:

$$E_{cell} = E^{rev} - a - b\log i - iR_{mem} - \frac{RT\ln 10}{nF}\log\left[1 - \frac{i}{i_{d,l}}\right] \tag{5.42}$$

or in terms of fitting parameters:

$$E_{cell} = \beta_0 - \beta_1 i - \beta_2 \log i - \frac{RT\ln 10}{nF}\log\left[1 - \frac{i}{\alpha_1}\right] \tag{5.43}$$

The parameters $\beta_0 \ldots \beta_2$ may easily be obtained using conventional linear algebra methods. However, the nonlinear parameter α_1 is more difficult to estimate because it appears inside a logarithm. Minimization procedures provided by MATLAB® (FMINSEARCH or FMINBND) may be used to optimize this parameter. However, it turned out that the mass transfer limitation at high currents was small so that it was difficult to fit the non-linear term with the required accuracy. It was thus not used in the final fitting procedure.

5.3.6 Bootstrapping

To obtain estimates of the uncertainty of the fitted parameters, the Bootstrapping procedure may be used to assess the variance of the fitting parameters [162, 163]. It is particularly powerful when the uncertainty in non-linear parameters is assessed. The Bootstrap method may be schematically described as:

1. Given a set of n observations
2. Randomly select a sub-set from these n observations *with replacement* containing n_1 observations
3. Perform a least square fit using these n_1 observations and save the regression parameters
4. Repeat Step 2 and 3 m times
5. The average regression parameters along with standard deviations of these parameters may now be calculated directly from the m sets of regression parameters

In our case we let $n_1 = n/2$ and $m = 1000$.

5.4 Experimental Procedure

MEAs from W. L. Gore & Associates (Primea® 5561 with Pt/Ru anode (0.45 mg/cm^2) and a Pt cathode (0.4 mg/cm^2)) were used in all experiments together with backings from E-TEK (ELAT® carbon only). All gases used were 99.999% pure from AGA except the CO_2 and CO that had a purity of 99.9% and 99% respectively, both from AGA.

5.4.1 Experiments with Symmetrical Cells

The test station described in Appendix B was used. The cell and two humidifiers (bubble humidifiers made out of glass) were placed in a heating cabinet to ensure homogeneous temperature and prevent condensation between the humidifiers and the cell. The temperature of the heating cabinet was 38–39 °C whereas the operating temperature of the FC was 40–42 °C depending on the current density. The cell housing was a 6.25 cm^2 graphite housing from

ElectroChem (modified from a 5 cm^2 housing by using larger gaskets). The cell was placed with the cathode down so that the gas flow was in the horizontal plane. The nuts of the cell were tightened to a torque of 120 cNm.

Supply of gases was controlled with Mass Flow Controllers (MFCs) from Bronkhorst. The different gases (N_2, CO_2, Ar and He) have different molar heat capacities. This was automatically corrected for in the set-point signal to the inert gas MFC. The accuracy is then slightly reduced, but because the content of inert components is relatively high, this uncertainty is of minor consequence except for measurements with extremely high contents of inert.

Determination of Limiting Current

The cell potential was controlled by an AutoLab potentiostat with a 10 A booster. Gases were mixed, and contained 90–99% N_2 or He with varying flow rate of hydrogen. The cell was polarized to 0.3–0.5 V where a limiting current was observed. The hydrogen crossover from the cathode running on neat hydrogen was measured by flowing pure He on the anode while measuring the oxidation current at a cell potential of 0.3 V. All potentials were measured against the cathode operating on neat, humidified hydrogen.

Electrochemical Activation of Electrodes

The electrodes were in some cases activated by oxidation using CV scans in inert atmosphere. The electrode was purged with nitrogen or helium for 5-10 minutes while neat hydrogen was fed to the other electrode. A CV of the electrode to be cleaned with limits 0.05 and 0.9 V_{RHE} at 25 mV/s was then recorded using the other electrode as a combined RE and CE.

Experiments at Low Overpotentials

The current and potential were controlled and measured using a Solatron potentiostat (either 1286 or 1287) in these experiments. The ohmic resistance of the cell was measured using current interrupt at a cell current of 2 A performed with the test station setup described in Appendix B before and after each low current experiment. The current was swept at 20 mA/s from 0 to ± 2 A, first anodically, then cathodically. Impedance measurements were also performed (Solartron 1255B or 1260), but a significant inductive and in some cases capacitive contribution to the impedance response was observed. The accuracy of the HFR determined from these experiments was too low to be of

any use in the analysis of the results. The polarization data were corrected for ohmic losses using the average cell resistance measured before and after the polarization scan. *Changes* in the reversible cell potential due to conversion of hydrogen on the anode were corrected for as explained in Sec. 5.3.4.

Experiments over a Wide Range of Overpotentials and Currents

Again the test station described in Appendix B was used. The internal control system in the Agilent 6050A load may run both galvanostatically and potentiostatically. However, the current can not flow in the reverse direction. Further, the load can not run potentiostatically when the cell potential is negative, see footnote on page 93. To circumvent this limitation, a constant voltage signal of 1 V was added to the cell potential by means of a battery powered voltage adder before entering the voltage sense input on the load.

Polarization curves were recorded by first running the cell in galvanostatic mode up to 0.75 A/cm^2 and then in potentiostatic mode to a polarization of 0.4 V. The different loads were kept for 15 seconds, and a current interrupt was made towards the end of each individual load level in order to correct the cell potential for the ohmic drop. Only data from the last 5-10 seconds of each load were used in the analysis. There are several reasons for using much shorter holding times than in the case of the $H_2|O_2$ cell. *1)* The electrode reactions seem to need very short times to reach a (quasi) steady state. *2)* The test station log data at a frequency of 2 Hz whereas the test station used for the $H_2|O_2$ cell experiments logged data only every 15 seconds. *3)* Shorter holding times ensures a more isothermal operation of the FC.

5.4.2 Cyclic Voltammetry in Sulfuric Acid

The cell used for EQCM measurements described in Section 6.3.2 was used. 0.5 M H_2SO_4 was prepared from purified water (18.2 MΩcm, Millipore) and TraceSelect grade sulfuric acid (Fluka). The working electrode was a platinized platinum electrode with a roughness factor of about 25 as determined by integration of the hydrogen adsorption peaks in the second sweep assuming 210 $\mu C/cm^2$. An RHE as described in Section 6.3 was used as RE. CO_2 and CO gas (purity 99.9 and 99% purity from AGA) was bubbled through the solution after which N_2 (99.999%, AGA) was bubbled for about 5 minutes. The WE was held at 0.06 V_{RHE} during the entire procedure with gas bubbling. The potential was then swept at 20 mV/s first down to 0.02 V and then up to 1.25 V twice. The CV was recorded using the setup described in Section 6.3.2.

5.4.3 Fuel Cell Experiments

The FC station described by Vie [164] was used for these tests. Gas flows were automatically regulated according to the cell current if desired, and temperature, voltage and pressure data were logged. Automatic scans were performed at predefined intervals. The active cell area was 4.91 cm^2. The operating pressure was set to 3.5 barg immediately after start up of the cell and maintained at this level. A mechanical clamping pressure on the MEA of 10 barg was used.

The initial current density observed was about 3.40 A/cm^2 at 0.50 V. Decay in cell performance was observed during the first days, probably due to excessive operating temperatures at high current densities which can lead to catalyst agglomeration. Repetitive polarization sweeps were run in order to verify if stable performance was obtained. Five days after the start-up the performance was relatively stable and repeatable after each scan. The current density observed was then about 2.35 - 2.40 A/cm^2 at 0.50 V cell potential.

The conversion on the cathode (fed with pure oxygen) was held at 80% throughout the tests with a minimum flow of 20 mlN/min, that is, the conversion was constant down to a current density of 1.17 A/cm^2 after which the oxygen flow was kept constant.

The scan started at low cell voltages (0.2 V) and was gradually increased to OCV. The holding time at each load was 1.5 minutes below 0.7 V, but only data from the last minute was used in the analysis. At higher potentials the holding time was typically 0.5 minutes and all data were used.

5.5 Results and Discussion

5.5.1 Experiments with Symmetrical Cells

Limiting Current

Several combinations of low inlet hydrogen concentration and high conversion was measured by polarizing the symmetric cell, see Figure 5.1(a). There is a clear limiting current in all these experiments. The potential at open circuit depends on the content of inert through Nernst law. This potential was used to accurately determine the actual composition of the hydrogen mixture. The flow rate of inert was controlled well by the MFCs. However, it was found that in the case of He, the flow rate was about 12% higher than the desired value. The hydrogen crossover from the cathode was measured to be 20-21 mA. The observed limiting current in Figure 5.1(a) was corrected for this.

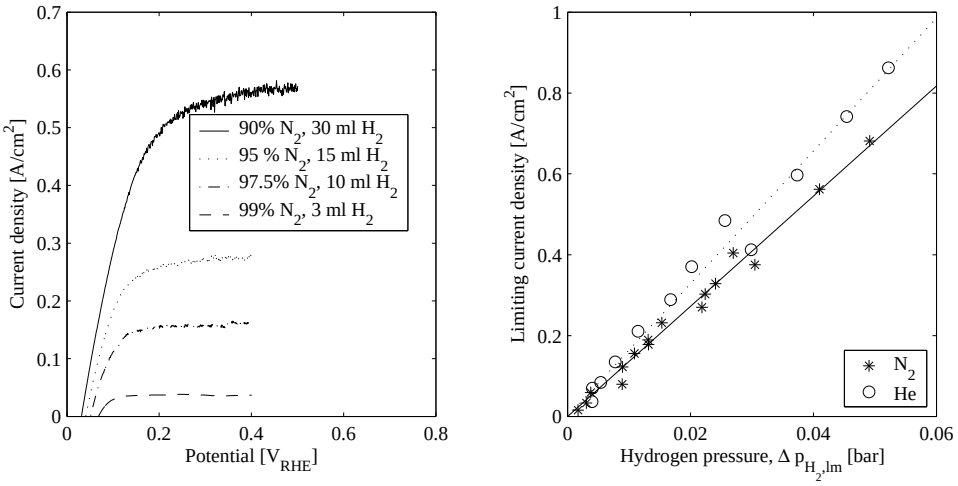

(a) (b)

Figure 5.1: a) Polarization curves obtained operating on different hydrogen inlet concentrations and flow rates of hydrogen (mlN/min) and b) limiting current as function of log-mean partial pressure of hydrogen in the FC.

The outlet composition was calculated based on a mass balance for hydrogen. The log-mean partial pressure of hydrogen was then calculated according to Equation 5.9. The hydrogen partial pressure was also corrected for the water vapor pressure assuming that the hydrogen was fully humidified. The slopes of the lines shown in Figure 5.1(b) were used to estimate the total mass transfer coefficient in the FC assuming that the limiting current is due to mass transfer limitations alone. In the case of nitrogen as the inert, $2Fk^{tot}_{d,N_2}$ was 13.7±0.2 A/(cm^2 bar), and in the case of helium 16.1±0.4 A/(cm^2 bar). Error estimates are given as the standard deviation of the fitted slope.

A replication of the experiment described above was made. In addition, the effect of CO_2 was measured. The hydrogen crossover was about 12 mA in this cell and the observed limiting currents are plotted in Figure 5.2(a). For this cell $2Fk_d$ was 10.0±0.3, 11.6±0.4 and 5.86±0.20 A/(cm^2 bar) for N_2, He and CO_2 respectively. There is a quite substantial difference in these data compared to the observations in the other cell. Also a polarization scan was performed to high potentials operating the cell on a mixture of 95% CO_2 with

a hydrogen flow of 19 mlN/min. The observed polarization curve is shown in Figure 5.2(b).

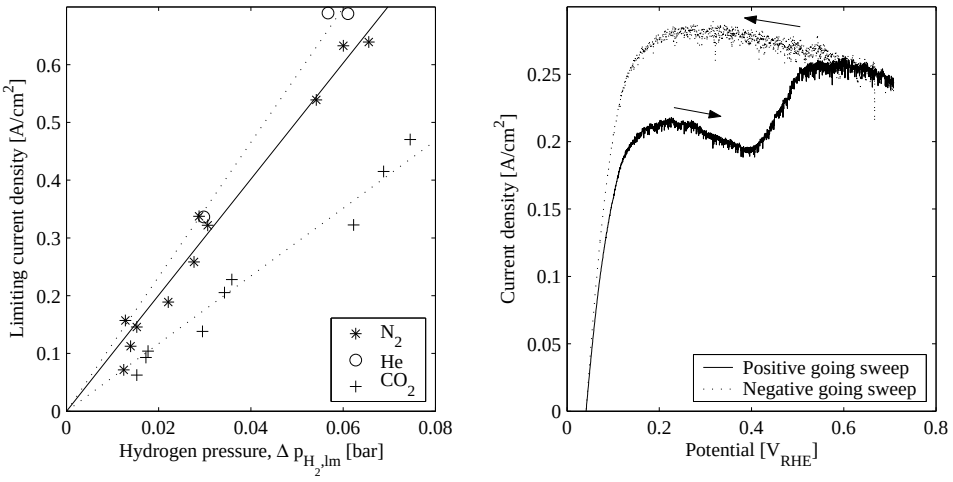

(a) (b)

Figure 5.2: a) Limiting current as function of log-mean partial pressure of hydrogen in the FC and b) polarization curve observed operating on CO_2 containing gas mixture.

Both diffusion and reaction limitations may lead to limiting currents that are linearly dependent on the bulk concentration of hydrogen [158, 159], see Equations 5.9 and 5.22. As is seen in Figure 5.2(a), a lower limiting current is observed in the presence of CO_2 than in the presence of nitrogen and helium. There might be several explanations for this: *1)* Different diffusivity of hydrogen in the different diluting gases *2)* Mass transfer limitations in the ionomer film in the electrode *3)* Presence of a reaction limitation.

Difference in gas diffusivites The diffusivity of hydrogen in helium is 1.93 times higher than in nitrogen, see Table 5.2. If all mass transfer resistance was in the GDL, one would expect k_d^{tot} for He to be a factor 1.93 higher than for N_2. This is seen from Equation 5.4 which leads to Equation 5.46 assuming that no other limitations occurs. However, the ratio is only 1.16 - 1.18 as seen from Figure 5.2(a) and 5.1(b) respectively.

Table 5.2: Binary diffusion coefficients at 1 atm and 293.15 K [165, 166].

Components	D_{ij} cm^2/s
H_2–Ar	0.749
H_2–CO_2	0.412
H_2–He	1.490
H_2–H_2O	0.850
H_2–N_2	0.772

Limiting Current due to Mass Transfer in Ionomer Film Mass transfer limitation through an ionomer film in the active layer before the hydrogen can react electrochemically is another possible explanation for the small observed effect of the nature of the inert component. The mass transport (diffusion) through the ionomer is not influenced by the inert gas component. The mass transfer resistances in the GDL and in the active layer are resistances in series. The different mass transfer coefficients may be estimated from the following set of equations:

$$1/k_{d,N_2}^{tot} = 1/k_{d,N_2}^{GDL} + 1/k_d^{ionomer} \tag{5.44}$$

$$1/k_{d,He}^{tot} = 1/k_{d,He}^{GDL} + 1/k_d^{ionomer} \tag{5.45}$$

$$k_{d,N_2}^{GDL} = D_{H_2,N_2}/D_{H_2,He}\ \ k_{d,He}^{GDL} \tag{5.46}$$

Based on data extracted from Figure 5.1(b), it is estimated that $2Fk_{d,N_2}^{GDL}$ is 44.3, $2Fk_{d,He}^{GDL}$ is 85.5, and $2Fk_d^{ionomer}$ is 19.8 A/(cm^2bar) respectively. Based on the data shown in Figure 5.2(a) the same coefficients are 34.9, 67.4 and 14.0 A/cm^2bar. If we use these latter data to estimate the total mass transfer coefficient in the presence of CO_2 with relations similar to Equations 5.44 and 5.46, including resistance in both GDL and ionomer, we estimate it to be 7.99 A/cm^2bar. The experimental value is 5.86 A/cm^2bar, *i.e.* significantly lower. The effect of the different diluent gases can thus not be explained by difference in mass transfer in the GDL alone.

Limiting Current due to Reaction Limitations Based on the observations described above, it is likely that not only a mass transfer limiting current

is present, but also a reaction limiting current. A reaction limiting current must be due to a step in the oxidation mechanism that is not electrochemical in nature [159]. Only the Tafel-Volmer mechanism contains a step that is not electrochemical, the Tafel step, and we therefore conclude that HOR seems to follow the the Tafel-Volmer mechanism on the anode. This is in line with the findings of Vermeijlen *et al.* for a Pt based catalyst [159]. In an earlier study, Vogel *et al.* [167] studied how CO poisoned HOR on Pt in acidic media. They found that the HOR rate was dependent on the square of the number of unblocked Pt sites consistent with the Tafel-Volmer mechanism, see Equation 5.14.

A further evidence for the presence of a chemical step in the mechanism is shown in Figure 5.2(b). When the potential is increased, a limiting current is reached, but at even higher potentials a new increase in current is observed. This second increase starts at about 0.4 V which is consistent with the voltage at which an adsorbed species (contaminant) is oxidized when electrochemically cleaning the electrode. This is discussed further later, see Figure 5.10(a). The limiting current is higher in the negative going sweep than in the positive going sweep.

We suggest that the reason is that organic contaminants are removed by oxidation at high potentials freeing more active sites for the chemical Tafel reaction (hydrogen adsorption) to take place. We also see that the rate of HOR is higher at 0.2 V_{RHE} than at 0.5–0.6 V_{RHE}. The reason for this is not clear, but could be due to formation of oxides on the catalyst at high potentials which also can block active sites for HOR.

Observations Applying Low Currents

Corrections for ohmic resistance as well as changes in the reversible potential were made to the measured data as described above. The IR corrected data along with the IR and Nerstian corrected data are shown for three experiments in Figure 5.3(a). The plots of current density *vs.* corrected cell potential are linear as seen from Figure 5.3(a). However, at higher contents of inerts, the lines are curved because the influence of mass transfer limitations then becomes important. The polarization resistance, defined in Equation 5.30, was found by fitting a second order polynomial to the experimental data. The slope of this curve at $\eta = 0$ gives R_p, see Equation 5.30. The intercept of the line is the reversible cell potential E^{rev} of the gas mixture in question.

In Figure 5.3(b) it is shown that N_2 behaves like the noble gases Ar and He

within experimental accuracy. A summary of the fitted parameters (E_{rev}, R^a_{ct} and i_0) for the different curves is given in Table 5.3. In the symmetrical cell we assume that $R^a_{ct} = R^c_{ct} = 1/2R^{tot}_{ct}$. It was observed that the performance of this cell decreased with time, see Figure 5.4. To find R^a_{ct} when running the anode on inert containing hydrogen, R^c_{ct} was estimated from the line shown in Figure 5.4, and subtracted from R^{tot}_{ct} to find R^a_{ct}.

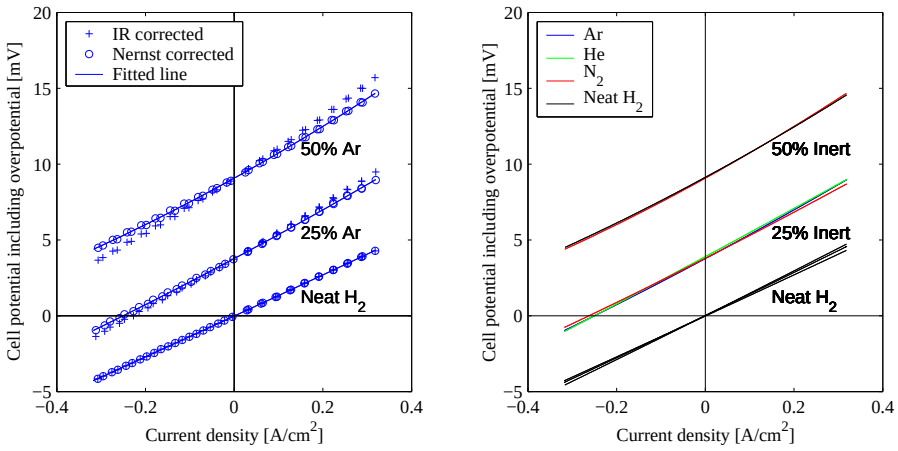

(a) (b)

Figure 5.3: a) Polarization data of symmetrical cell showing the effect of IR, Nernstian correction for conversion and the fitted second order polynomial. b) IR corrected polarization data for the symmetrical cell with neat hydrogen and different additions of N_2, Ar and He.

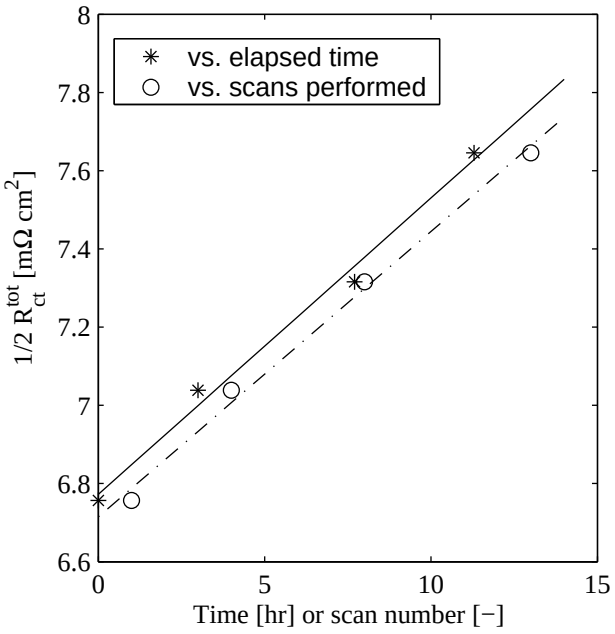

Figure 5.4: Increase in R_{ct}^{c} for $H_2|H_2$ cell with time.

Table 5.3: Calculated parameters for polarization of the symmetrical cell at low currents. The data appear in the order they were measured.

Anode gas	R_{ct} [mΩ cm^2]	i_0[1] [A/cm^2]	E^{rev} [mV] Exp.	Nernst	Comments
Neat H_2	6.74	4.02	-0.011	0	
25% N_2	8.03	3.37	3.843	3.892	
50% N_2	8.91	3.04	9.258	9.377	
Neat H_2	7.08	3.82	0.037	0	
25% He	8.68	3.12	3.921	3.892	
25% Ar	8.46	3.20	3.843	3.892	
50% Ar	8.90	3.04	9.220	9.377	
Neat H_2	7.28	3.72	0.028	0	
25% CO_2	11.9	2.28	3.870	3.892	30 minutes
	13.5	2.00	3.886	3.892	60 minutes
	15.1	1.79	3.889	3.892	90 minutes
Neat H_2	15.6	1.73	0.099	0	After CO_2
	7.66	3.53	-0.003	0	Anode CV
	4.60[2]	5.91	0.012	0	Cathode CV

[1] i_0 is based on the geometric area, not the true catalyst area.
[2] 1/2 of R_{ct}^{tot} observed after CV scan on cathode

From Table 5.3 it is clear that CO_2 has a large effect on R_{ct} and that this effect increases with increasing exposure time. CO_2 further appears to have an effect on the anode which is difficult to reverse by operation on pure hydrogen alone. Electrochemical activation by oxidation of the anode seems to clean the anode efficiently so that the cell performance on neat H_2 is back to the original level, see Table 5.3. Electrochemical cleaning of the cathode enhances the performance even more.

Regression analysis gave very good fit to the experimental data for determination of polarization resistance. The estimated standard deviation for R_p is typically 0.01–0.04 mΩ cm^2. However, the total uncertainty is much larger than the standard deviation of the fit because the ohmic resistance (90–100 mΩ cm^2) is subtracted from the data. The ohmic resistance had a standard deviation of 0.2–0.5 mΩ cm^2, and also changed by 1-3 mΩ cm^2 during each

individual polarization scan as measured by current interrupt, see Figure 5.6.

The observed reversible potential at open circuit is in very good agreement with the one calculated based on Nernst Equation (within 50 μV for 25% inert and 150 μV for 50% inert, see Table 5.3). This means that the actual inert content is within 0.5 percentage point of the set value showing that the MFCs are able to very accurately control the flow of the different gases in these experiments. A slightly lower accuracy was observed when using other gases than di-atomic (noble gases and CO_2), but appropriate corrections were made in cases where this was of importance, in particular in experiments with very high inert contents.

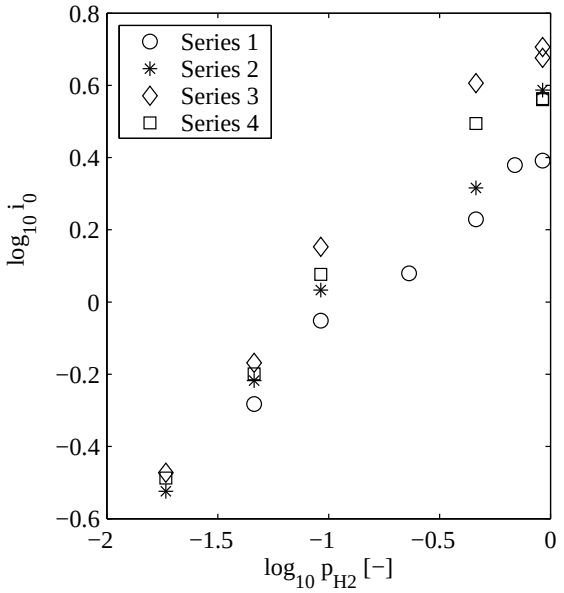

Figure 5.5: Plot of log i_0 vs. log p_{H_2}, see also Table 5.1 for a summary of the theoretical slopes for the different possible reaction steps (Tafel, Volmer and Heyrowsky). Series 1 and 3 were measured after cleaning the electrode electrochemically by CV scans, see Section 5.4.1. Data labelled Series 2 and 4 were measured after operating the FC for about 24 hours after cleaning the electrodes electrochemically.

The dependence of i_0 on the hydrogen concentration was also determined from experiments at low overpotentials, see Figure 5.5. The hydrogen content (on dry basis) was varied from 100% to 2% by dilution with helium. The temperature was 41°C corresponding to a water vapor pressure of 7.78 kPa [168] used to correct the dry mole fraction of hydrogen.

As seen from Figure 5.5, the slope log i_0 *vs.* log p_{H_2} changes with log p_{H_2} because the coverage θ changes with p_{H_2}. The slope observed in pure H_2 is about 0.3–0.4, and it is about 0.75 at low hydrogen content (2% on dry basis). It can be concluded from this that the Volmer step cannot be the sole *rds*, see Table 5.1. At low hydrogen contents, α_V would have to be 1.5 to give the observed slope of log i_0 vs. log p_{H_2}. However, it is not possible to distinguish between the Heyrowsky and Tafel steps based on these data.

Observations at High Currents

Polarization scans The cell was run on neat H_2 and mixtures of H_2 and N_2, He, Ar and CO_2 for shorter periods of time (typically 1-2 hours on each gas mixture). Automated polarization scans were performed on a regular basis. The cell resistance was monitored by frequent current interrupt, see Figure 5.6 for a typical set of resistance values. Note that the resistance increases with increasing current density, probably due to increased water flux away from the anode resulting in a drier and thus less conductive membrane. The measured cell voltage was corrected for Nernstian effects due to dilution as well as ohmic losses to obtain the total overpotential (both anodic and cathodic) as function of current density. Due to the large proportion of the ohmic voltage loss compared to the total cell voltage, the corrected overpotential curves are somewhat noisy.

In Figure 5.8(a) and 5.8(b) it is seen that the effect of N_2 on the total overpotential for the anode and cathode is the same as for the noble gases He and Ar. The effect of CO_2 is larger than for any of the other gases and also increases with time. Large improvements in performance were observed after the electrodes were activated by CV scans. In fact, performance of the cell was even better than when the test started after cleaning the cathode by CV. This is further discussed in Section 5.4.1.

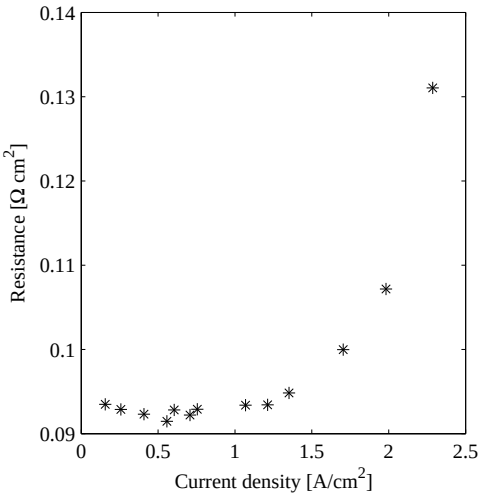

Figure 5.6: Ohmic resistance measured by current interrupt as function of current density for a symmetrical $H_2|H_2$ cell operating at approximately 41 °C.

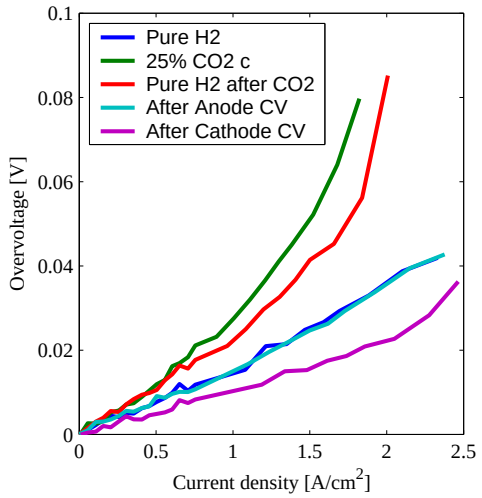

Figure 5.7: Polarization scans showing poisoning and recovery of $H_2|H_2$ cell exposed to CO_2.

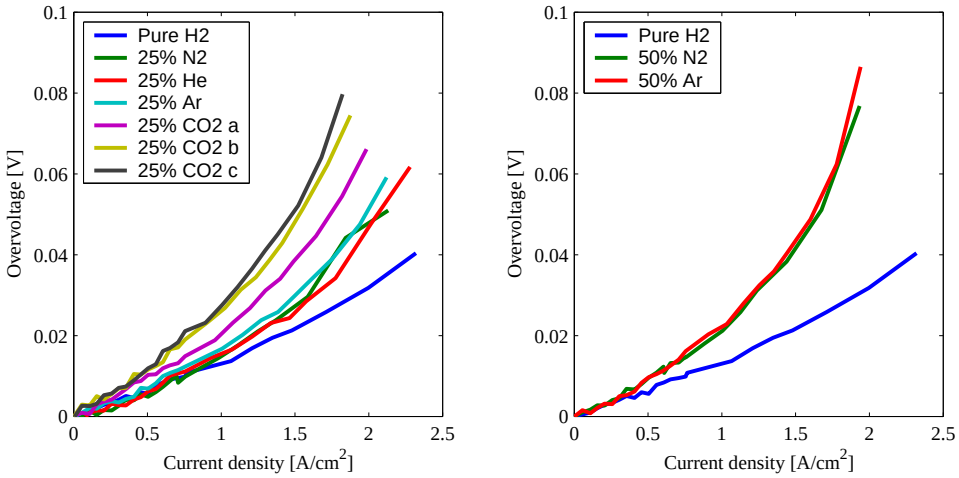

(a) (b)

Figure 5.8: a) IR and Nernstian corrected polarization scans for cell operating on neat H_2 and 25 vol% of different diluents. Scans labelled "CO2 a", "CO2 b", and "CO2 c" were recorded after approximately 30, 60 and 90 minutes of CO_2 exposure respectively b) the same cell operating on hydrogen with 50 vol% of diluents. Operational conditions: 41°C, atmospheric pressure, 30% conversion but minimum 30 mlN/min H_2 on anode, 50 mlN/min H_2 on cathode, both gases fully humidified.

Long-term Effects of Nitrogen and Carbon Dioxide Data for an FC operating with neat hydrogen on the cathode and neat hydrogen or hydrogen containing either 25 mol% N_2 or CO_2 on the anode, are shown in Figure 5.9. As is seen in Figure 5.9, and even more clearly in Figure 5.11, the ohmic resistance increases at regular intervals and then slowly falls. This is because polarization scans were run every other hour. The resistance temporarily increased during each polarization scan experiment as clearly seen in Figure 5.6. The measured cell voltage was corrected for ohmic losses which were measured by current interrupt.

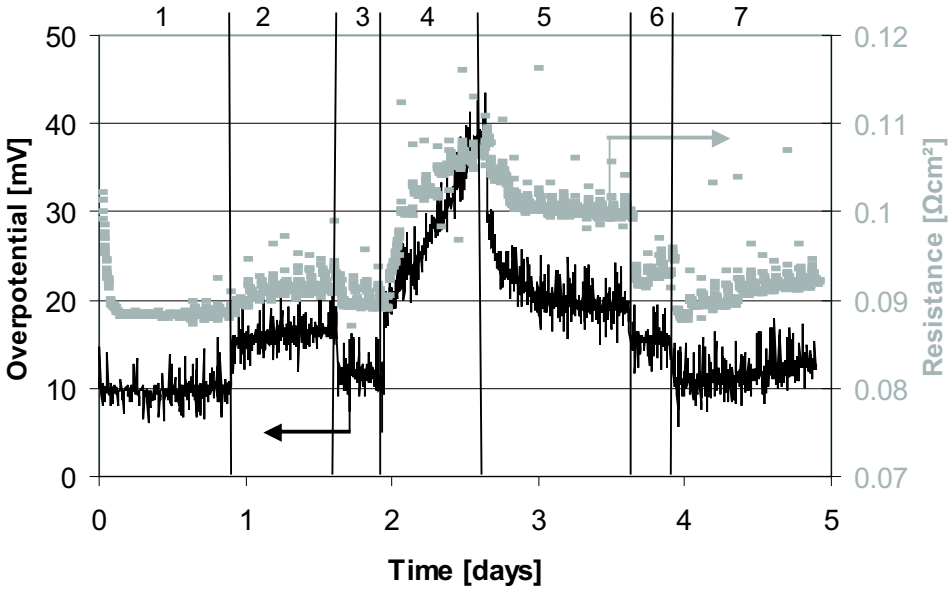

Figure 5.9: Total overpotential at 0.5 A/cm^2 and cell resistance for FC operating on neat hydrogen as well as with additions of N_2 and CO_2. Operational parameters: 41°C, atmospheric pressure, 100 mlN/min H_2 on anode, 50 mlN/min H_2 on cathode, both gases humidified at 39–40°C, see text for further details.

The different regions shown in Figure 5.9 are explained below:

1. Initial operation on neat H_2
2. Operation on H_2 with 25 vol% N_2. There is an increase in cell resistance possibly due to a lower degree of humidification because more gas is flowing to the anode. A slight increase (+2.5 mV/day) in overpotential with time is observed
3. Neat H_2 again. The overpotential is about 2.1 mV higher than before operation with N_2 diluted H_2 started
4. 25 vol% CO_2. The overpotential increases sharply (+31.4 mV/day). Note that the cell resistance also increases sharply

5. Neat H_2. The overpotential falls with time, but stabilizes 7.5 mV higher than before CO_2 was introduced

6. CV, *i.e.*, electrochemical cleaning of the anode, gives a marked improvement in performance with 3.9 mV lower overpotential

7. CV of the cathode further improves FC performance by 4.7 mV. When operating on neat H_2 after this last cleaning, the overpotential increases faster than at the very start, 2.6 mV/day. This is comparable with the increase observed when operating with N_2 .

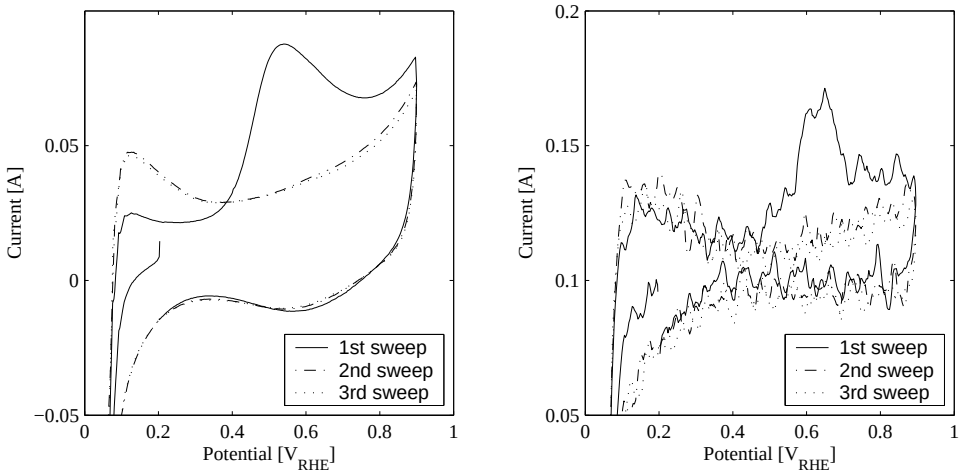

Figure 5.10: a) CV of a) FC anode and b) cathode after exposure to CO_2.

After exposure to CO_2 and subsequent operation on neat hydrogen for 1.5 days, the anode was purged with nitrogen, and a CV of the anode recorded using the cathode, operating on neat hydrogen, as a combined RE and CE. The CV is shown in Figure 5.10(a). After 6 hours the same procedure was performed on the FC cathode. The CVs are shown in Figure 5.10(b). It is clear that some species are being oxidized in the first positive going sweep both on the anode and cathode. The potential range in which this occurs is typical for organic contaminants. Notice that there has also been a substantial

loss of active sites on the catalyst which is recovered by electrode activation with CV scans as evidenced by the change in charge in the adsorbed hydrogen region upon cleaning.

Long-term Stability with Neat Hydrogen The same cell as used above was tested further to study the stability when operating on neat hydrogen. The results are shown in Figure 5.11 below. The overpotential increased with time after the cell had been electrochemically cleaned by CV after CO_2 exposure. The increase in overpotential is about 2.8 mV/day. The anode was electrochemically activated in the start of region 2 in Figure 5.11, see Figure 5.12(a) for CV. Then the cathode was electrochemically activated at the end of region 2 in Figure 5.11, see Figure 5.12(b) for CV. The cleaning procedure again successfully improved the cell performance. The cleaning of the anode recovered 1.6 mV whereas cleaning of the cathode recovered 2.6 mV. Both the anode and cathode CV show oxidation of a contaminant.

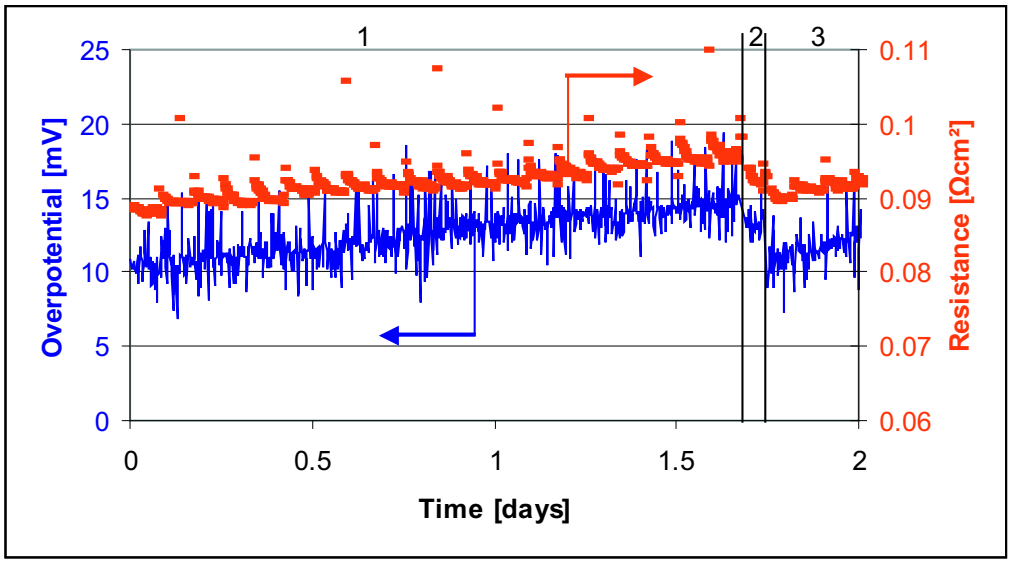

Figure 5.11: Total overpotential at 0.5 A/cm^2 and cell resistance of an FC operating on neat hydrogen. See Figure 5.9 for operational details and text for further details.

After this cleaning procedure the decay in performance was 7.2 mV/day. However, this was only observed for a few hours before CO_2 again was introduced into the cell. The differences in calculated charge between the first and the second scan in the hydrogen desorption region, as well as contamination oxidation charges, are given in Table 5.4. We see that both the loss of H_{ads} charge and oxidation of the contaminant species are smaller by a factor of more than three when operating on pure hydrogen compared to operating on CO_2 mixture. The ratio of the hydrogen adsorption and contamination charges gives approximately how many electrons that are needed to free one active catalyst site, n_{e^-}. The uncertainty in this determination is large. However, the data indicate that somewhat more charge is required to remove the contaminant species due to the slow contamination process in the presence of pure hydrogen compared to the contaminants resulting from CO_2.

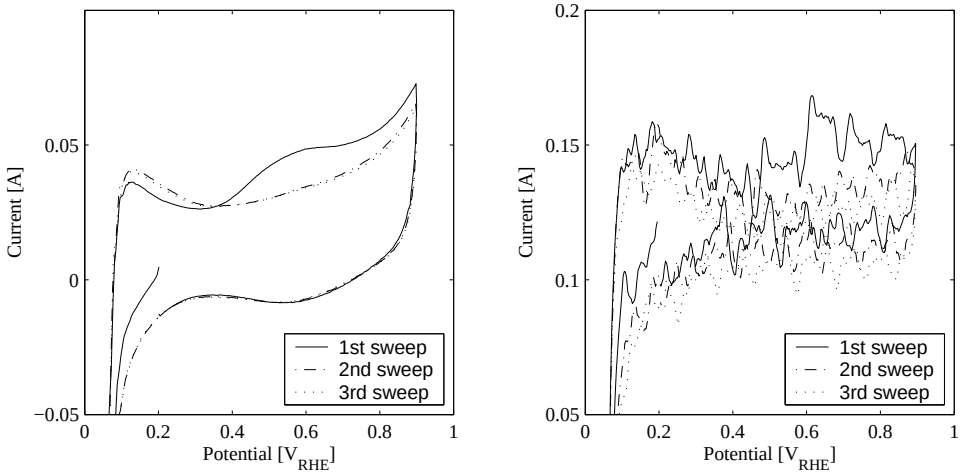

Figure 5.12: a) CV of FC anode after operating on neat H_2 for two days after CO_2 poisoning b) CV for the cathode in the same cell. The cathode CV was filtered using a 15 point Savitzky algorithm [169]. 25 mV/s sweep rate was used in both cases.

Table 5.4: Calculated difference in charge between first and second scan for CVs recorded after exposure to CO_2 (see Figure 5.9) and neat H_2 (see Figure 5.11) in the hydrogen region and at potentials above 0.4 V. The actual CVs are given in Figures 5.10(a), 5.10(b), 5.12(a), and 5.12(b) respectively.

	$\Delta Q_{H_{ads}}$ [mC/cm^2]	ΔQ_{Contam} [mC/cm^2]	$n_{e^-} = \frac{\Delta Q_{Contam}}{\Delta Q_{H_{ads}}}$ [-]
CO_2 exposed	28.1	90.5	3.2
Neat H_2	6.4	31.5	4.9

Ohmic Resistance

The current interrupt method gave stable resistance measurements. However, it was observed that the measured resistance tended to increase as cell performance decreased due to addition of CO_2, see Figure 5.9. This was probably related to the effects discussed in Section 5.3.3, namely that parts of the electrode polarization resistance is erroneously attributed to the ohmic resistance in the analysis of current interrupt results. The reported poisoning effect of CO_2 is therefore somewhat too low.

5.5.2 Cyclic Voltammetry of Platinum in Sulfuric Acid

Platinized Pt was studied in sulfuric acid to more closely assess differences in CO_2 and CO poisoning. The platinized electrode was exposed to CO_2 and CO for different periods of time: *i)* CO_2 for 20 minutes, *ii)* CO for 5 minutes *iii)* CO_2 for 5 minutes followed by 5 minutes of CO. All solutions were bubbled with nitrogen for 5 minutes thereafter before the CVs were recorded. The voltammograms are given in Figure 5.13, and the charges under the different peaks are given in Table 5.5. The charge associated with the different features of the CV, see Figure 5.13, was established by integration in the first and second scan. The coverage of contaminants and hydrogen is then found by [143]:

$$\theta_{contam} = \frac{Q_1^{2nd} - Q_1^{1st}}{Q_1^{2nd}} \tag{5.47}$$

$$\theta_{H_{ads}} = 1 - \theta_{contam} \tag{5.48}$$

The number of electrons required to oxidize the adsorbed contaminants in peak 2 and 3 in Figure 5.13, n_{e^-}, is also estimated:

$$n_{e^-} = \frac{Q_{2+3}^{1st} - Q_{2+3}^{2nd}}{Q_1^{2nd} - Q_1^{1st}} \tag{5.49}$$

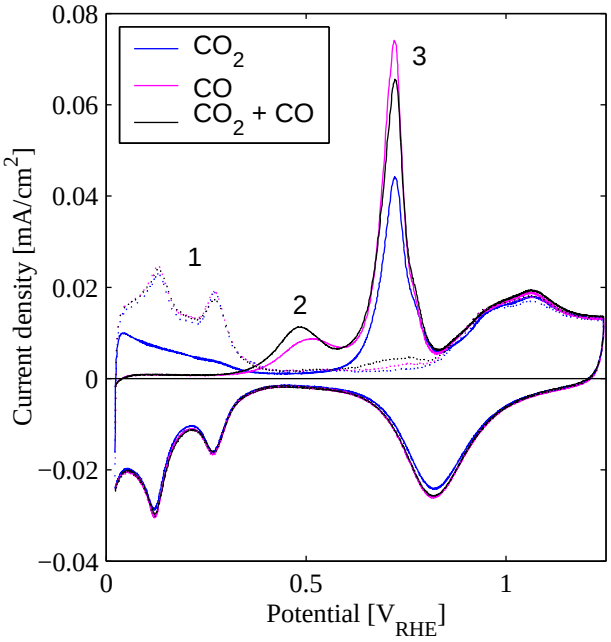

Figure 5.13: CVs recorded in 0.5 M H_2SO_4 after exposure to CO_2 (20 minutes), CO (5 minutes) and CO_2+CO (5+5 minutes) at 0.06 V_{RHE} adsorption potential. First sweep shown as solid lines, second sweep as dotted lines. CVs performed at 20 mV/s.

Table 5.5: Peak potentials, charges and coverages observed when exposing the platinized electrode to CO_2 and CO, see also Figure 5.13.

Parameter	CO_2	CO	CO_2 + CO
E_p^2 [mV_{RHE}]	N/A	512	489
E_p^3 [mV_{RHE}]	721	721	722
θ_{contam} [-]	0.60	0.94	0.93
$\theta_{H_{ads}}$ [-]	0.40	0.06	0.07
n_{e^-} [-]	1.19	1.33	1.37

As was discussed in the Introduction (Section 5.2.1), one possible poisoning mechanism of the FC is that CO_2 reacts with hydrogen to form CO that poisons the cell. However, in sulfuric acid it has been showed that CO_2 also produces other (adsorbed) species than CO_{ads} such as $COOH_{ads}$ and COH_{ads}, see Section 5.2.1. In Figure 5.13 we see that exposure of platinized Pt to CO and CO_2 containing sulfuric acid results in qualitative different cleaning CVs. Only one oxidation peak (3) is observed when exposed to CO_2, but two peaks are observed (2 and 3) when exposed to CO. The charge under peak 3 is larger when exposed to CO than CO_2. Hydrogen adsorption is less affected by exposure to CO_2 than to CO even though there is a significant decrease in hydrogen adsorption peaks in the first sweep also after CO_2 exposure. As seen in Table 5.13, the coverage of the adsorbed contaminant is much higher for CO than CO_2. Also, there is relatively more charge involved in the electrochemical oxidation of contaminants, n_{e^-}, in the case of CO than CO_2.

Papageorgopoulos and de Brujin [143] found higher contamination coverages than reported here, $\theta_{contam} = 0.98$ and 0.78 for CO and CO_2 respectively. The number of electrons required to remove the contaminants from one site, $n_{e^-} = 2$ and 1.4 for CO and CO_2 respectively, was also higher than in our study. The reasons for the discrepancies between our data and the data presented by Papageorgopoulos and de Brujin are not clear.

If the electrode was first exposed to CO_2 and then CO, the CV became very similar to the CV recoded when only exposing the electrode to CO. This suggests that products formed during exposure to CO displaces at least some of the products resulting from CO_2 exposure. The CVs recoded in the FC experiments are more difficult to interpret due to a much more capacitive behavior which is typical for carbon supported catalysts.

5.5.3 $H_2|O_2$ Cell Results

Polarization Data

Polarization data were measured for the FC with and without additions of inert components to the hydrogen fuel. The polarization scans are shown in Figure 5.14. A more marked effect of especially CO_2 is noted when looking at the power density shown in Figure 5.15(a). Also the efficiency at a given power density of the FC shown in Figure 5.15(b) is noticeably affected by additions of CO_2. Notice also that the performance of the FC operating on hydrogen/nitrogen mixtures is not different from the performance observed when running on hydrogen mixtures with the noble gases He and Ar.

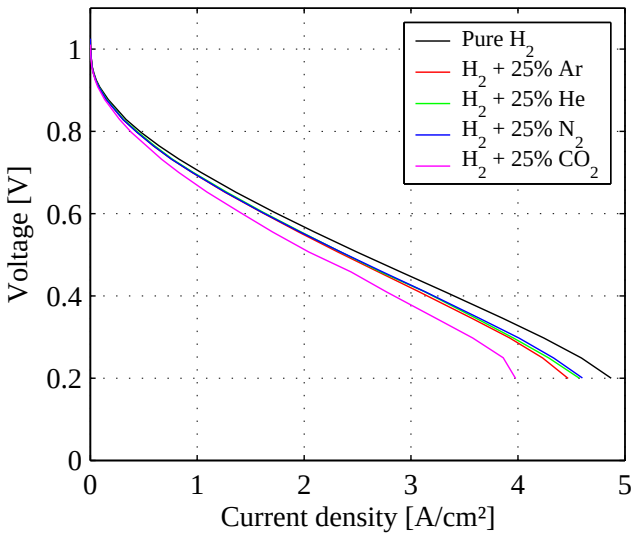

Figure 5.14: Polarization curves obtained with neat hydrogen and hydrogen with 25 vol% of N_2, He, Ar or CO_2. The data are *not* corrected for ohmic drop in the cell. The nominal operating temperature was 75 °C and gases humidified at 60 °C (cathode) and 80 °C (anode). Anode and cathode conversion 80% (pure oxygen) minimum flow of 20 mlN/min.

From Figure 5.17(b) we see that the cell voltage at 1.0 A/cm^2 is 12-14 mV lower for the cell operating on hydrogen containing 25 vol% N_2, He, or Ar.

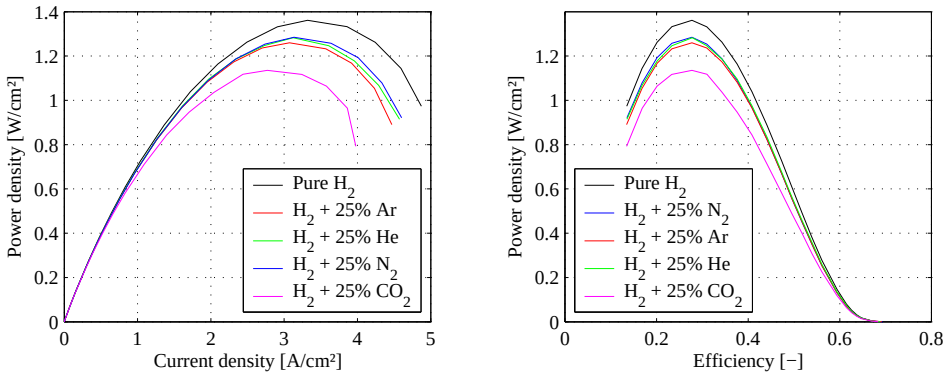

(a) (b)

Figure 5.15: a) Power density of FC operating on neat hydrogen and hydrogen mixtures with 25 vol% of N_2, He, Ar or CO_2. b) FC efficiency *vs.* power density neglecting efficiency losses due to un-reacted hydrogen. Operating conditions as given in Figure 5.14

By using Nernst equation based on the inlet conditions (75 vol% H_2 on dry basis), we estimate the the voltage should be 4.2 mV lower. However, taking into consideration that the conversion is 80%, the exhaust gas contains only 37.5 vol% H_2 corresponding to a loss in reversible cell voltage of about 14.2 mV compared to neat hydrogen, in good agreement with our experimental findings. When the cell operates on hydrogen containing CO_2, the voltage difference is about 33 mV lower than with neat hydrogen.

The maximum observed current density when operating the cell at 0.20 V is given in Table 5.6. Agian N_2, He and Ar mixtures behave very similarly whereas the CO_2 containing mixtures behaves differently.

Changes in Cell Temperature During Polarization Scanning

The FC temperature was strongly dependent on the current density as shown in Figure 5.16. It should be noted that the FC temperature was measured directly in the exhaust gas channel of the FC. This temperature measurement was thus much more direct and sensitive than usual cell designs where the temperature is measured further away from the active layers like in the cell used for the $H_2|H_2$ measurements. No corrections for non-isothermal conditions were made in the analysis.

Table 5.6: Observed current at 0.2 V cell voltage for different mixes of hydrogen.

Anode gas mixture	Number of observations	Average current at 0.2 V [A/cm^2]	95% interval for current at 0.2 V
Pure hydrogen	24	4.87	<4.78, 4.96>
25% nitrogen	8	4.60	<4.56, 4.64>
25% argon	8	4.47	<4.44, 4.50>
25% helium	4	4.57	<4.53, 4.61>
25% carbon dioxide	4	3.98	<3.96, 4.00>

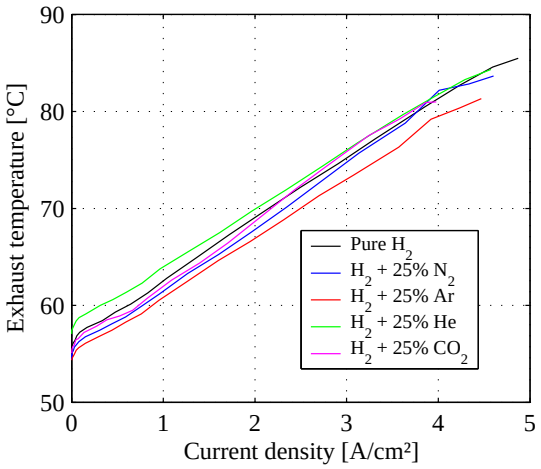

Figure 5.16: Temperature variation in the flow channel during polarization scans. Operating conditions as in Figure 5.14.

Model Fitting

The polarization model in Equation 5.43 was fitted to the measured polarization data using linear regression methods. The mass transfer limitations were rather small as is clear from Figure 5.14. This was also observed during the fitting procedure, and it was difficult to find the limiting current used in Equation 5.42. The regression analysis was thus made neglecting mass transfer limitations. The results obtained from linear regression are presented in Table 5.7.

Table 5.7: Fitted model parameters for the different fuel gas mixtures tested in the $H_2|O_2$ cell.

Anode gas mixture	$\widehat{\beta_0}$	SD($\widehat{\beta_0}$)	$\widehat{\beta_1}$	SD($\widehat{\beta_1}$)	$\widehat{\beta_2}$	SD($\widehat{\beta_2}$)
Pure hydrogen	0.830	0.003	-0.117	0.001	-0.071	0.004
25% nitrogen	0.819	0.002	-0.120	0.001	-0.079	0.003
25% argon	0.823	0.002	-0.124	0.001	-0.078	0.003
25% helium	0.827	0.004	-0.125	0.002	-0.072	0.005
25% carbon dioxide	0.818	0.006	-0.138	0.004	-0.073	0.007

$-\widehat{\beta_1}$ in Table 5.7 is an estimate of the cell resistance (the sum of electronic resistance in backings and electrodes plus ionic resistance in electrodes and membrane). We see that it is quite similar for the different gases, but the estimated resistance in the case of CO_2 is slightly higher. The estimates of the ohmic resistance is in good agreement with data obtained with the current interrupt method (0.096 – 0.117 Ω cm^2 with the majority of the observations at about 0.10 – 0.11 Ω cm^2).

The results from the Bootstrap procedure are shown in Figure 5.17(a) and 5.17(b) and indicate the uncertainty of the fitted parameters. The model does not contain any non-linear terms. The Bootstrap method is therefore not strictly required, but gives a good graphical presentation of the uncertainty of the parameters in the model. We see that there is a marked difference between the three groups *1)* neat hydrogen, *2)* hydrogen mixed with N_2, Ar or He and *3)* hydrogen mixed with CO_2..

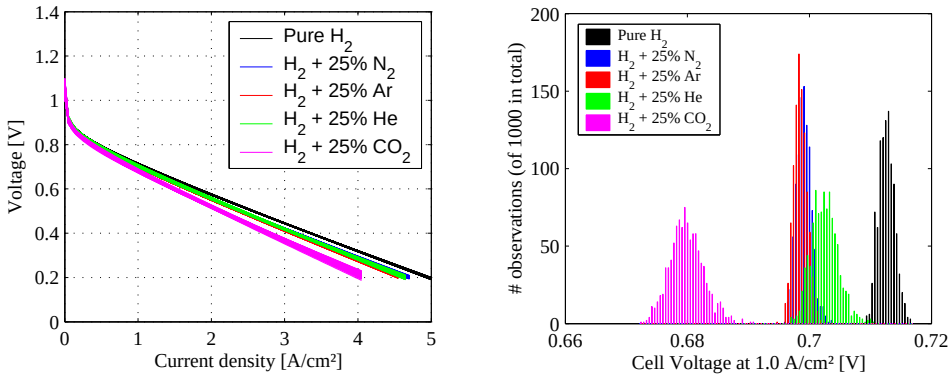

(a) (b)

Figure 5.17: Fitting results obtained using the Bootstrap method a) showing all the different polarization curves fitted to the experimental data and b) the estimated cell voltage at 1.0 A/cm^2 from these fitted curves.

5.5.4 Variations in Temperature

All kinetic constants like a and b in equation 5.41, R_{ct} and thus i_0 as well as the rate constants in the Tafel, Volmer and Heyrowsky steps are dependent on temperature. The mass transfer limiting current is also dependent on temperature through diffusivity and possibly solubility of gases in the ionomer phase. Temperature variations also affect the conductivity of the membrane and thus the ohmic losses. As a secondary effect, humidification and water balances are also affected by the temperature further influencing the conductivity.

Temperature variations were neglected in the analysis. The variation in temperature was large for the $H_2|O_2$ cell experiments at high pressure and temperature (about 10% variation in the absolute temperature (55 – 85 °C)). Temperature variations were also present in the experiments involving the symmetrical cell. Typical variations recorded were ±1 °C.

The temperature sensors in the $H_2|O_2$ cell were placed in the flow channels very close to the active layer and thus sensed a temperature closer to the true temperature in the active layer. The temperature sensors in the $H_2|H_2$ cell were in the graphite block so that heat conduction and thermal capacity of the graphite tended to even out temperature transients during measurement of polarization data. Also, the current densities in the $H_2|O_2$ cell were much

higher than in the $H_2|H_2$ cell thereby producing more heat. Further, the cathode overvoltage in the case of the $H_2|O_2$ cell is substantial, also contributing to heating of the cell.

Vie [170] observed that the temperature in the electrode may be substantially higher than the temperature observed in the gas channel. This difference is dependent upon current density and may be as high as 10 °C at 1 A/cm^2. This temperature variation is not reflected in our measurements because we sensed the temperature in the flow channel. The local temperature of the FC catalyst during polarization scans can thus be substantially higher than indicated by the measurements, especially if the temperature is measured f. ex. in the graphite block as in the case of the symmetrical cell.

5.5.5 Effects of Nitrogen, Noble Gases and Carbon Dioxide

In all experiments reported here, the behavior of all the cells split into three groups:

1. Pure hydrogen
2. Additions of nitrogen, helium and argon
3. Additions of carbon dioxide

This suggests that the effect of nitrogen is limited to being an inert diluent with no further short term effects to the cell performance than dilution of the fuel gas. A slight decrease in performance when operating the $H_2|H_2$ cell with 25% N_2 on one side for linger times was observed, but this decline or contamination was similar to what was observed for a cell operated on pure H_2. The source of this contamination was not identified. Both the anode and cathode in the symmetrical cell were affected by contaminations, see Figure 5.12(a) and 5.12(b). The cathode seemed to be slightly more affected than the anode. It is expected that the contaminant is some form of organic species. It would therefore be expected that the PtRu based anode catalyst is somewhat more tolerant to these contaminants than the Pt based cathode.

The performance of cells exposed to H_2 containing CO_2 showed a steady decrease in performance which was much higher than what was observed for pure hydrogen or N_2 mixtures, see Figure 5.9. Ball *et al.* [149] observed the effect of CO_2 in a $H_2|O_2$ cell for a period of about two hours. Others have also operated PEMFC on synthetic reformate gas mixtures for several

thousand hours observing stable performance [150, 171] with a decay rate of 3-10 mV/1000 hrs.

It should be noted that when running an FC with oxygen or air on the cathode, contamination effects due to diffusion of CO_2 related species through the membrane will be avoided because the potential of the cathode will promote oxidation of such species. Further, some oxygen will diffuse through the membrane to the anode where it can partially oxidize adsorbed species on the anode catalyst. It is well known that introducing a small air bleed on the anode increases the anode performance [151, 153, 154, 172]. Also, recovery of the symmetrical $H_2|H_2$ cell was not complete unless the electrodes were cleaned electrochemically. Recovery of an $H_2|O_2$ cell exposed to CO_2 was complete without such interventions. This also supports the notion that diffusion of oxygen through the membrane helps to remove adsorbed contaminants on the anode. Alternatively, dissolved contaminants formed on the anode may diffuse to the cathode where they may be oxidized.

A PEMFC was tested in FC modus, *i.e.,* an $H_2|O_2$ cell, in the same hardware as used for the symmetrical cells with all operational parameters being the same as for the symmetric cell. The data are not shown here, but showed higher stability. The cell also showed good stability when operating on pure hydrogen. The reason for the large effect of CO_2 on cell performance in our study compared to other available literature is not clear, but is not associated with the test station hardware. It could be that the CO_2 gas, which was only 99.9% pure, contain other contaminants.

5.6 Conclusions

Hydrogen Oxidation Reduction (HOR) on the PtRu anode catalyst follows the Tafel-Volmer mechanism based on observation of limiting currents that were not due to mass transfer. The conclusion is also supported by the observation of higher HOR rates after the electrodes had been electrochemically cleaned by oxidation. The mass transfer limiting currents in the GDL was found to be very high based on the observation of a very small difference in limiting current forH_2 diluted with N_2 or He. Mass transfer through the ionomer in the catalyst layer covering the active catalyst also contributed to the limiting current. It was not possible to accurately estimate the relative importance of mass transfer through the ionomer compared to the reaction limiting current due to the Tafel step.

We further found that the influence of CO_2 on the performance of the

PtRu anode was significant, especially in cells with hydrogen on either electrode (symmetrical cells). Nitrogen did not seem to have any effect on anode performance other than dilution. Dilution of hydrogen with the noble gases Ar and He gave very similar results as dilution with nitrogen.

Contamination species formed on the anode and on platinized Pt by CO_2 and CO respectively were different. The contamination coverage of the catalyst when exposed to CO was higher than for CO_2. The adsorbed contaminants formed from CO also displaced the contaminants formed by CO_2. The poisoning mechanism for CO_2 can not be explained by formation of CO through the reverse water-gas shift reaction alone. Other species, such as $COOH_{ads}$ and COH_{ads}, may be involved.

Recovery of the symmetrical $H_2|H_2$ cell after exposure to CO_2 was quite slow and not complete. To achieve complete recovery it was required to scan the potential of both the anode and cathode thus electrochemically activating them by oxidation of the contaminants.

Chapter 6

Oxidation of Ammonium on Platinum in Acidic Solutions

6.1 Summary

Oxidation of ammonia on platinum in alkaline solutions has been studied in some detail in the literature. However, oxidation of ammonium in acidic solution has not been studied in detailpreviously, but may be important for example in relation to PEMFC poisoning.

We have found that ammonium is electrochemically active in acidic solutions at room temperature. Oxidation of ammonium to form nitrogen or nitric oxide species is slow at room temperature. Formation of N_2 was observed using Differential Electrochemical Mass Spectroscopy (DEMS). Also formation of NO was detected at electrode potentials higher than 1.2 V_{RHE}. Nevertheless, this moderate activity for ammonium oxidation can be critical in order to understand steady state tolerance of PEMFCs towards ammonia poisoning. Recovery after contamination will also be influenced by the rate of ammonium oxidation.

Cyclic Voltammetry (CV) and Electrochemical Quartz Crystal Microbalance (EQCM) data have shown that presence of ammonium affects the formation and reduction of Pt oxides formed at high potentials. This seems to involve the formation of very stable nitrogen or nitrogen-oxygen species on the surface of the electrode. Some of these species seem to be removed from the electrode only at very low potentials in the hydrogen adsorption region.

The hydrogen adsorption region is also strongly affected by presence of

ammonium, in particular the most strongly bond hydrogen which is shifted to lower potentials. Both species formed at very high potentials as well as an interaction between ammonium and hydrogen sulfate in the electrolyte seem to be responsible for this effect on hydrogen adsorption. The impact of these factors on the Hydrogen Oxidation Reaction is not clear. The hydrogen desorption region is not affected by ammonium.

6.2 Introduction

Oxidation of ammonia in alkaline solutions was studied as early as 1905 by Müller and Spitzer [51] by galvanostatic experiments. The reaction has later been studied in more detail. Different reaction mechanisms have been suggested [22, 23, 56] which will be reviewed below. There has been no reports in the literature on the reaction mechanism for oxidation of ammonium in acidic systems. The oxidation in acidic solution has been found to be extremely slow [22].

The reaction mechanism is not fully understood in the alkaline system. Nitrogen has a very complex chemistry with many different possible oxidation states in (adsorbed) intermediates and reaction products. Oxidation numbers of nitrogen may vary from -III (NH_3/NH_4^+) to +VII (HNO_4, pernitric acid) [173]. Many intermediates and final products, and thus different reaction steps, are conceivable in the oxidation mechanism. Therefore, it is a difficult task to clearly identify the reaction mechanism.

6.2.1 Oxidation of Ammonia in Alkaline Solutions

Nitrogen Evolution from N_{ads} Species

Oswin and Salomon [22] proposed the following mechanism :

$$NH_3 + OH^- \rightarrow NH_{2,ads} + H_2O + e^- \tag{6.1}$$
$$NH_{2,ads} + OH^- \rightarrow NH_{ads} + H_2O + e^- \tag{6.2}$$
$$NH_{ads} + OH^- \rightarrow N_{ads} + H_2O + e^- \tag{6.3}$$
$$2N_{ads} \rightarrow N_2 \tag{6.4}$$

Oswin and Salomon found step 6.2 to be the rate-determining step (*rds*) at low c.d. where the Tafel slope was found to be 39 mV/dec. Step 6.4

was the*rds* at high c.d. based on the observation of an infinite Tafel slope indicating that a chemical reaction, like Equation 6.4, is limiting. Despić *et al.* [174] noted that Oswin and Salomon used transient current data, obtained after 30 s equilibration, in the Tafel analysis. The reported $E - i$ relationship and Tafel slopes were thus not measured at true steady state.

Spahrbier and Wolf [56] proposed basically the same mechanism seemingly independent of Oswin and Salomon. However, a preceding step where NH_3 is adsorbed from the solution was added, see Equation 6.6, as well as a succeeding step where adsorbed N_2 desorbs, see Equation 6.14. Spahrbier and Wolf measured the transient c.d., and found a Tafel slope of 120 mV/dec. at times shorter than 100 ms. A substantial decrease in current was observed at longer times. Formation of a Pt oxide or hydroxide layer blocking the surface was proposed to be the cause of the observed decrease in current. Despić *et al.* [174] found even more complicated current transients. They suggested that also the chemical equivalent reactions of Equation 6.1 to 6.4 (*i.e.* $NH_3 \rightarrow NH_{2,ads} + H_{ads}$ etc.) followed by electrochemical oxidation of H_{ads} should be included as possible steps in the mechanism.

Nitrogen Evolution from $NH_{x,ads}$ Species

Gerischer and Mauerer [23] suggested a different reaction scheme with a different mechanism for nitrogen production. The mechanism is rather complex partly because the nature of the intermediate species is not known.

$$OH^- \rightleftarrows OH_{ads} + e^- \tag{6.5}$$

$$NH_{3,aq} \rightleftarrows NH_{3,ads} \tag{6.6}$$

$$NH_{3,ads} + OH_{ads} \rightarrow NH_{2,ads} + H_2O + e^- \tag{6.7}$$

$$NH_{2,ads} + OH_{ads} \rightarrow NH_{ads} + H_2O + e^- \tag{6.8}$$

$$NH_{2,ads} + NH_{2,ads} \rightarrow N_2H_{4,ads} \tag{6.9}$$

$$NH_{2,ads} + NH_{ads} \rightarrow N_2H_{3,ads} \tag{6.10}$$

$$NH_{ads} + NH_{ads} \rightarrow N_2H_{2,ads} \tag{6.11}$$

$$NH_{ads} + NH_{3,ads\ or\ aq} \rightarrow N_2H_{4,ads} \tag{6.12}$$

$$N_2H_{n,ads} + nOH_{ads} \rightarrow N_{2,ads} + nH_2O + ne^- \tag{6.13}$$

$$N_{2,ads} \rightarrow N_{2,aq} \tag{6.14}$$

$$NH_{ads} + OH_{ads} \rightarrow N_{ads} + H_2O + e^- \tag{6.15}$$

Step 6.13 is a simplified mechanistic step. Most likely the de-hydrogenation of $N_2H_{n,ads}$ proceeds through n one-electron steps. García *et al.* [175] found the de-hydrogenation $N_2H_{3,ads} \rightarrow N_2H_{2,ads} + H^+ + e^-$ to be the *rds* in the oxidation of hydrazine in acidic solution.

Although the proposed reaction mechanism is very complex, one should note the key role played by adsorbed NH_2 and NH in forming the N-N bond *before* the remaining hydrogen atoms react. Reaction 6.15 is considered to be a poisoning reaction for the electrode, see below for further discussion.

Applying a potential step from OCV to typically 630 mV_{RHE}, Gerischer and Mauerer [23] observed that the current fell markedly with time. If the potential pulse was turned off within a few minutes, the cell potential fell back to the original OCV after some time. The same oxidation current transient was again observed when re-applying the same potential. They suggested that this initial, reversible poisoning was due to OH_{ads} blocking the surface for adsorption of NH_3 from the solution. On the other hand, OH_{ads} was also assumed to be vital for the reaction mechanism explaining the low oxidation currents observed at low potentials. If the electrode was operated for longer times, Gerischer and Mauerer observed an irreversible poisoning of the electrode that was not recoverable by letting the cell rest nor by electrochemical reduction. Gerischer and Mauerer found the species poisoning the electrode to be nitrogen by *ex situ* thermal desorption of the species adsorbed on the Working Electrode (WE) and analysis of those species.

de Vooys *et al.* [176] also found a marked deactivation of the electrode at potentials above 0.57 V_{RHE}, especially at potentials above 0.60 V_{RHE}. There was a very distinct onset of the poisoning mechanism. They also found a Tafel slope of 40 mV/dec. in the potential range from 0.40–0.55 V_{RHE} in agreement with the findings of Oswin and Salomon [22].

Gootzen *et al.* [177] found, using DEMS, that the rate of nitrogen evolution was stable for at least ten minutes at an electrode potential of 0.65 V_{RHE}. They observed that the *total* cell current fell quickly in this time period. This indicated that two species were produced by oxidation of ammonia; nitrogen and an adsorbed species which gradually saturated the electrode surface. This was also supported by the observation that the current transient in the potential step experiments showed two time constants. Wasmus *et al.* [24] found that the adsorption process of species originating from NH_3 at 0.4 V_{RHE} was complete in about 5 minutes. The adsorption was associated with an oxidation current.

Experimental Confirmation of Reaction Mechanism. Both Wasmus *et al.* [24] and Gootzen *et al.* [177] found experimental evidence for the Gerischer and Mauerer mechanism, *i.e.*, that nitrogen was formed from an adsorbed species with negative oxidation number. Wasmus *et al.* [24] performed adsorbate experiments where the electrode potential was kept constant for five minutes in 0.5 M KOH/0.05M NH_3, typically at 0.4 V_{RHE}. The electrolyte was then replaced with the base electrolyte (0.5 M KOH) while the electrode was still under potentiostatic control. A positive going sweep was then applied and current and DEMS signals were recorded. Nitrogen was detected in the positive going sweeps, and was associated with an oxidation current peak. This means that the source of nitrogen evolution is a species with oxidation number less than 0, *e.g.* $NH_{2,ads}$ or NH_{ads}. If the intermediate adsorbed species leading to nitrogen evolution was N_{ads}, the nitrogen evolution would occur with no net faradic current due to this process.

Gootzen *et al.* [177] also concluded, based on adsorption experiments and a similar analysis as Wasmus *et al.*, that $NH_{x,ads}$ species were responsible for nitrogen evolution. A further evidence for the Gerischer-Mauerer mechanism was also found. After adsorption at 0.75 V_{RHE} followed by electrolyte exchange, a negative going sweep was started, but halted at 0.55 V_{RHE}. The current changed from reductive to oxidative with time. Gootzen *et al.* explained this by assuming that two reactions took place at the same time. The first reaction was assumed to be the *reductive* formation of $NH_{x,ads}$ from N_{ads}. The second reaction was assumed to be the *oxidative* formation of nitrogen from $NH_{x,ads}$ via $N_2H_{n,ads}$.

de Vooys *et al.* [176] found the Gerischer-Mauerer mechanism to be the most likely mechanism also for the precious metals Ru, Rh, Pd, and Ir, but not for the coinage metals Au, Ag and Cu. In a Surface Enhanced Raman Spectroscopy (SERS) study [178] they demonstrated the presence of N_{ads} on Pd, but it was not active in the formation of N_2. They found gold to be inactive for ammonia oxidation except at high potentials where oxides were present on the surface. Using EQCM measurements they also found that the coinage metals were dissolved as ammonia forms very stable complexes with these ions. Zeng and Bruckenstein [179] found that ammonia was oxidized on gold according to the Oswin-Salomon mechanism accompanied by dissolution of ammonia-gold complexes.

The Gerischer-Mauerer mechanism has much more experimental support than the Oswin-Salomon mechanism for oxidation of ammonia on Pt in alkaline solution. Reaction 6.15 may thus be regarded as a poisoning side reaction to

the main reaction path via $N_2H_{n,ads}$ which leads to formation of molecular nitrogen.

Nature of Adsorbed $NH_{x,ads}$ Species. Gerischer and Mauerer [23] found the Tafel slope for the ammonia oxidation from slow CV scans. The Tafel slope found was strongly dependent on temperature, decreasing from 80–110 mV/dec. at 0 °C to 35 mV/dec. at 80 °C. A high Tafel slope is indicative of the *rds* occurring early in the reaction sequence. Gerischer and Mauerer found Equation 6.9 or 6.12 to be consistent with the lower Tafel slope. Based on analogy to photolysis of ammonia, where NH_2 was the favoured product over NH, Gerischer and Mauerer suggested that Step 6.9 was more likely than 6.12. Gootzen *et al.* [177] reached the opposite conclusion. They found that the dominant adsorbed species at 0.35 V_{RHE} was $NH_{2,ads}$ based on the oxidation charge attributed to adsorption. However, no nitrogen evolution was detected at this potential. The adsorbed species was further oxidized and nitrogen evolution observed when the potential was increased to 0.75 V. This led the authors to conclude that NH_{ads} was the active species in the process leading to nitrogen evolution.

Reduction of Adsorbates Formed at High Potentials

Several authors have reported that strongly adsorbed nitrogen species can be reduced by operating the electrode at potentials in or close to the hydrogen adsorption region [24, 177] as opposed to the findings of Gerischer and Mauerer [23]. In negative going sweeps, Wasmus *et al.* [24] observed a significant formation of NH_3, detected as m/e=15, at potentials below 0.50 V_{RHE}. They also observed an m/e=30 signal at potentials below 0.15 V_{RHE} when the upper reversal limit in the CV was at least 1.20 V_{RHE}. The m/e=30 signal was much stronger with 1.6 V_{RHE} as the reversal limit for the CV.

Gootzen *et al.* [177] suggested that N_{ads} is reduced to $NH_{x,ads}$ and NH_3 in the negative going sweep. They found that after adsorption at 0.75 V_{RHE} with subsequent electrolyte exchange, the reduction charge observed in the negative going sweep compared to the blank electrolyte was dependent on the sweep rate. A relatively higher reduction charge was observed at 5 mV/s than at 1 mV/s. N_{ads} is hydrogenated to yield $NH_{x,ads}$ that can recombine and yield nitrogen at slow sweep rates, see Steps 6.9 to 6.12. The net reaction would have a zero net faradic current because the nitrogen source is N_{ads}. At higher sweep rates the formation of $N_2H_{n,ads}$ is too slow to keep up with the formation

of $NH_{x,ads}$. NH_x may then fully hydrogenate to produce NH_3, in this case with a net reductive current.

Gootzen *et al.* also found that the total charge associated with reduction in the negative going sweep depended strongly on how long the adsorption at 0.75 V_{RHE} was allowed to proceed. However, adsorption times larger than 15 minutes did not increase the reduction charge observed.

Formation of Nitrous Components

There has been some discussion in the literature if the oxidation of ammonia to nitrogen is the only reaction taking place in alkaline solutions. Müller and Spitzer [51] found that there was several oxidation products being formed (N_2, NO_2^- and NO_3^-). In addition, about 23 % of the total current passed could not be accounted for. Data regarding the potential at which the anode was operated at during these experiments were not given. Katan and Galiotto [52] also performed galvanostatic experiments, and found that only N_2 was being formed by oxidation of ammonia in alkaline solution. The anode was operated at 0.3 to 0.7 V_{RHE} in these experiments.

The formation of NO and N_2O has been observed also by Wasmus *et al.* [24]. They found that formation of nitrous oxides commenced at approximately 0.8 V_{RHE} with a plateau of maximum rate at potentials above 1.0 V_{RHE}. However, the intensity of the mass signals were smaller by a factor 20–40 compared to the mass signal observed for nitrogen at the same potential[1]. The maximum nitrogen signal was about 100–250 times higher than the maximum NO and N_2O signals. The observation that formation of nitrous oxides are formed at high electrode potentials suggests that presence of adsorbed oxygen species on the electrode is required in the oxidation of ammonia to nitrous oxides. This is supported by observations in the gas phase both on Pt(1 0 0) [180] and Pt(1 1 1) [181].

6.2.2 Problem Statement

Numerous studies are available on oxidation of ammonia in alkaline solutions. Our interest in oxidation of ammonium in acidic solutions stems from the observation that ammonium affects PEMFC performance. Both partial and full recovery has been observed when operating the PEMFC on neat hydrogen after

[1] We have not corrected for differences in ionization probability and detector sensitivity between the species, but have accounted for differences in fragmentation patterns

exposure to ammonia [20, 21]. It is of interest to identify if the recovery mechanism may be electrochemical oxidation of ammonium. Our aim is to study the extent of this net oxidation reaction. Furhter, presence of adsorbed species on the Pt surfaces in the FC catalyst layer may also impede the desired Fuel Cell (FC) reactions. Through this study of oxidation of ammonium in acidic solutions, the aim is to better understand possible poisoning mechanisms in PEMFC. Differential Electrochemical Mass Spectroscopy (DEMS) data will be used to identify oxidation products. Cyclic Voltammetry (CV), Rotating Disk Electrode (RDE) and Electrochemical Quartz Crystal Microbalance (EQCM) data will be used to asses the formation of (adsorbed) species not necessarily leading to the formation of stable, volatile oxidation products.

6.3 Experimental

All glassware used was thoroughly washed and then cleaned in a hot solution of 5–10 wt% H_2O_2 in 0.5 M sulfuric acid to remove contaminants. The equipment was then rinsed with purified water. The water was first purified in a Barnstead NANOpure II system, then through a MilliPore Milli-Q UV Plus system. The Reference Electrode (RE) used in all experiments was a Reversible Hydrogen Electrode (RHE) consisting of a platinized platinum gauze in a glass tube sealed in one end and filled with the same electrolyte as the WE was exposed to. A hydrogen bubble was electrochemically evolved in the top of the glass tube before the experiments were started. A pipette drawn to a fine tip was used as a Luggin capillary.

Chemicals used were TraceMetal grade acids and NH_4OH (Fisher) as well as $NaOH{\cdot}H_2O$ (Alfa Æsar, 99.996% pure on metal basis). EQCM data for perchloric acid were measured using TraceSelect chemicals (Fluka). Continuous nitrogen purge was used to remove oxygen from the solutions (Ultra High Purity (UHP) 5.0 quality from Praxair and AGA). UHP helium from Praxair was used for the DEMS experiments because N_2 was one of the volatile reaction products of interest. The approximate pH and ionic strength of the different solutions used here is given in Appendix C.

6.3.1 Differential Electrochemical Mass Spectrometry

A comprehensive description of the DEMS system employed is given by Wasmus *et al.* [182]. A brief description of the system is given below, see also Figure 6.1. The electrochemical cell was controlled using a computer con-

trolled PAR 273 potentiostat. The WE, which was painted on a porous Teflon sheet, was mounted in the cell applying high vacuum to the other side of the microporous Teflon membrane. Species which were formed at the WE during potential sweeping and not adsorbed, were sucked continuously into the first vacuum chamber. A high capacity Turbo Molecular Pump (TMP, Osaka Vacuum, Model TH162) evacuated this chamber down to an operating pressure of about 10^{-2} Pa. A rotary vane pump (Welch, Model 1402) was used as a backing pump for the TMP. A small fraction of the sample sucked into chamber 1, shown in Figure 6.1, was further sucked into chamber 2. The vacuum in chamber 2 was about 10^{-5} Pa, and was maintained with a combination of a Balzer TMP, model TPU 062, and a Hovac oil-less diaphragm pump. Due to malfunction of the latter pump, the Welch backing pump also served the Balzer TMP in most experiments reported here.

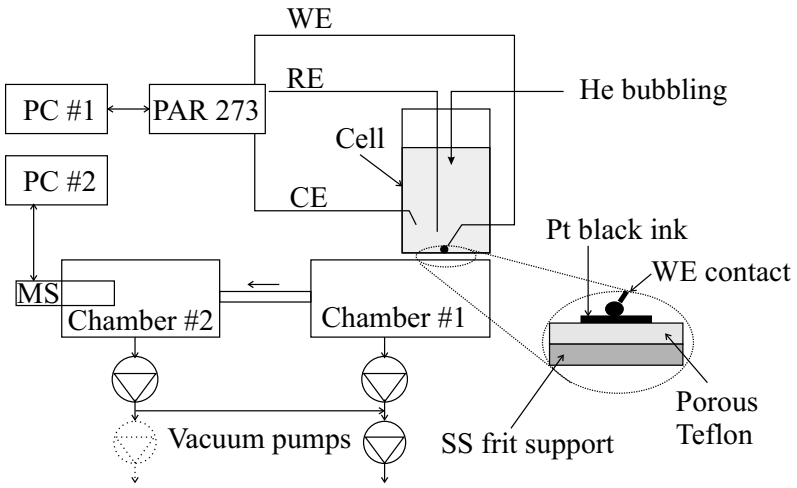

Figure 6.1: Cell design used for DEMS experiments, see text for further details.

The actual mass detector was located in chamber 2. The gas species were ionized in an ion chamber by electrons emitted from a filament and then accelerated into a quadrupole mass filter. A combination of dc and ac voltage was applied between two pairs of electrode rods running in parallel, typically 20–50 cm long, in this mass filter. Ions with the appropriate mass are able to move down the filter because the trajectory of these ions is stable. Ions with different masses collide either with a positive or a negative rod [183]. Wolfgang Paul, together with Norman F. Ramsey and Hans G. Dehmelt, received the

Nobel Prize in Physics in 1989 for the discovery of ion trapping, the principle behind the quadrupole mass filter. The ions that passed through the filter were detected by a Faraday cup detector where the ions were discharged thus creating a current proportional to the rate of ions hitting the detector. To enhance the detection limit and sampling speed, a Secondary Electron Multiplier (SEM) with a voltage of approximately 1.8 kV was used. When an ion hit the SEM surface, a cascade of electrons was released thus increasing the measurable current. The SEM voltage was automatically adjusted to have the same total pressure reading from the SEM and the Faraday cup sensors.

The major difference compared to Wasmus *et al.* [182] was how the WE was prepared. A solution of 2.2 wt% BN-18 in 97.8 wt% Diacetone alcohol was thoroughly mixed 2:1 by weight with Pt black (HiSPEC^{TM} 1000, Alfa Æsar) and then painted by hand onto the microporous Teflon substrate to form a thin, even layer. The ink was allowed to dry for at least one day before it was mounted in the DEMS cell. Electric contact to the active layer was achieved with a Pt wire with a bead on the end, see Figure 6.1. The *in-plane* electronic resistance of the active layer was relatively high resulting in slightly distorted CVs. 5 mV/s sweep rate was used to avoid excessive distortion of the CVs. The thickness of the active layer was a tradeoff between the desire to get more current and hence better MS signals, and the limitation in *in-plane* conductivity leading to more distorted CVs if the current was too high. The electrode was cleaned by stepping the potential between 0.03 and 1.6 V_{RHE}. The cleanliness of the WE was checked by monitoring the m/e=28 (CO) and 44 (CO_2) signals [24].

6.3.2 Electrochemical Quartz Crystal Microbalance

Equipment Used

An experimental set-up from Elchema (EQCN-701 and PS-305 potentiostat) was used for EQCM measurements. IR compensation was used at sweep rates higher than 50 mV/s. The cell resistance (HFR) was measured using a Solartron 1280B. An EG&G 175 sweep generator was used to generate the desired sweeps, and the data were logged using an oscilloscope (Tektronix TDS 420A) or a 16-bit AD card (DaqBoard, IOtech).

The crystals used were Pt sputtered, AT-cut, unpolished 10 MHz crystals from International Crystal Manufacturing Co., Inc. with no adhesion layer like Cr or Ti between the quartz and the platinum. The crystals were glued onto glass fittings using a silicone adhesive (DOW CORNING® 3140 RTV coating).

The mass sensitive area and the electrochemical active area are not equal. The mass sensitive area on the crystal is the disk in the center of the crystal shown in Figure 6.2. The electrochemically active area also includes the part of the current collector exposed to the electrolyte. The ratio of the two areas was about 1.05–1.08 for the different crystals used.

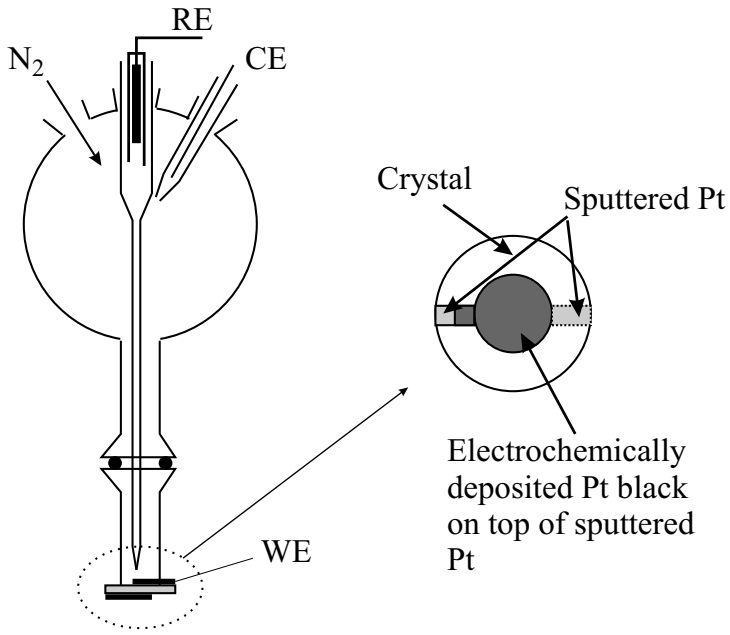

Figure 6.2: Cell design used for EQCM experiments, see text for further details.

Effect of Potential Cycling and Platinization of Crystals

A complication of the EQCM method is that the mass response changes dramatically if the crystal is cycled for a long time [184, 185]. Raudonis *et al.* [184] observed that the entire mass response changed sign after undergoing 10 000 CV cycles; that is, instead of measuring a mass *increase* in the positive going sweep, a mass *decrease* was observed. Wilde *et al.* [185] did not find the mass response in the oxide region to change sign. However, a large effect of potential cycling was found on the hydrogen adsorption region and also partly in the double layer region. They found that the effect of cycling was more pronounced in acidic solutions. Simultaneously there is a change in area of the

electrode as determined by hydrogen adsorption, but the features of the CV are not affected by cycling. The loss of surface area alone can thus not explain the change in mass response. The reasons for these observations are not well understood.

The crystals were platinized by pulse deposition in a solution of platinic acid in hydrochloric acid adding a total of 5 μg platinum to the WE each time to reduce the problem with changes in the mass responses due to potential cycling. The platinum black was rinsed well with purified water followed by exposure to a 50/50 vol% mixture of concentrated nitric and sulfuric acid for about 30 s to remove contaminants [186]. This was followed by thorough rinsing with purified water before the glass tube with the crystal on one end was clamped onto the main compartment of the cell using a silicone O-ring for sealing. The cell used is shown in Figure 6.2.

Solutions Used and Experimental Details

The solutions were made directly in the cell to minimize contamination. Based on the amount of purified water and the specified concentration of the pure acids, concentrated acid was added by weight to the cell to produce 0.500 M solutions. The RE was filled with electrolyte after thorough mixing and charged with a hydrogen bubble. If the WE had just been platinized, 20-30 cyclic sweeps were allowed prior to any measurements to stabilize the Pt surface because the surface decreased quite rapidly with potential cyclic just after platinization.

The WE was regularly cleaned by sweeping the potential between 0.04 and 1.25 V_{RHE} at 50 mV/s. To verify the cleanliness of the system, the WE was kept at typically 0.5 V_{RHE} for 5 minutes. Then three initially negative going cyclic sweeps were performed, and the differences in hydrogen adsorption peaks and oxide formation peaks between the first and subsequent sweeps were noted. Changes in these features were taken as an indication of the contamination level in the cell.

The standard sweep rate used was 50 mV/s with potential limits 0.025–1.25 V_{RHE} (both parameters were varied). The real surface area of the electrode was found by assuming that the charge of hydrogen adsorption is 210 $\mu C/cm^2$. The roughness factor was typically 15–25. The cyclic sweeps were run in a continuous mode because the main purpose was to study adsorption processes. If needed, NH_4OH was added to the cell by weighing the cell while adding NH_4OH solution. The RE was always filled with the same electrolyte as in the cell to ensure that the RE was a true RHE. The pH and ionic strength of the

different electrolytes used here are given in Appendix C.

To verify that the cell design was appropriate for CV measurements, tests were made with a solution of 5 mM of both $K_4Fe(CN)_6$ and $K_3Fe(CN)_6$ in 0.5 M KNO_3 with addition of 0.025 M NaOH. The Fe^{2+}/Fe^{3+} redox couple is well known to behave reversibly on Pt [187]. CV scans with different sweep rates, ν, were performed. The observed peak currents scaled with $\sqrt{\nu}$, and the peak potential was not dependent on sweep rate as expected for a reversible process. It was therefore conclude that the cell design, with proper IR compensation, was suited for CV measurements.

The Sauerbrey Equation

The frequency response of the quartz crystal is proportional to the mass change of the active area of the crystal according to the Sauerbrey equation [188, 189]:

$$\frac{\Delta f}{\Delta m} = -\frac{2f_0^2 n}{A\sqrt{\rho\mu}} \tag{6.16}$$

where f_0 is the fundamental harmonic frequency of the quartz crystal, n is the n^{th} overtone, ρ is the density of quartz, μ is the shear modulus of quartz, and A is the area of the mass sensitive portion of the crystal.

The presumption for the Sauerbrey equation is that the deposited mass behaves as a rigid film. Further, linearity is only found for moderate changes in mass. Thus, Δf should be within a few % of f_0 [190]. It is important that the mass is deposited or dissolved homogeneously [190]. Other complications in the interpretation of EQCM data are possible such as slippage between the adsorbed layer and the electrolyte and changes in viscosity close to the electrode surface due to the electrode process [191, 192].

The theoretical sensitivity of the crystal used in this work with a fundamental resonance frequency of 10 MHz, which is determined by the thickness of the crystal [188], is -0.8673 ng/Hz. The mass sensitivity was calibrated by bulk deposition of Cu from a 5 mM solution of cupric sulfate in 0.5 M H_2SO_4 at 0.06 V_{RHE}. The applied c.d. was typically 350 $\mu A/cm^2$. The Sauerbrey coefficient was found to be -1.24±0.10 ng/Hz from the slope of Q vs. Δf. The calibrated value is significantly higher than the theoretical value. The reason for this could be less than 100% current efficiency, or that the mass sensitive area is slightly larger than quoted. However, Gabrielli *et al.* [190] found that the Sauerbrey coefficient for their 6 MHz crystal was dependent on the size of the electrode. The 5 mm diameter electrode, the same size as our electrode,

had a Sauerbrey coefficient that was about 55% higher than the theoretical value. This is in good agreement with our calibration data. The reason for the difference is that the Sauerbrey coefficient in Equation 6.16 is calculated assuming infinite dimensions of the crystal [190].

The regular platinization procedure used in this work implies that the mass of the crystal increases. The fundamental resonance frequency will then also change so that the Sauerbrey coefficient increases with time. However, the change, which would be of the order 1% in the "life-time" of a crystal, has not been corrected for.

It should be noted that the relative effects of ammonium is not affected by the calibration, and since we focus mostly on relative effects, the absolute values are not strictly needed. The relatively large uncertainty we found when calibrating the crystal does thus not affect most of our conclusions.

6.3.3 Rotating Disk Electrode

A rotating disk[2] set-up from Pine Instruments was used (AFMSRX rotator and an AFRDE5 bipotentiostat). Data were collected with a 12 bit AD card (Measurement Computing Inc.) controlled by LabVIEW. Measurements were performed in a standard electrochemical cell with three separate compartments for the RE, CE and WE. The WE had a geometric area of 0.164 cm^2, and was polished with 0.05 μm alumina powder in the last polishing step. The real surface area of the electrode was established from hydrogen adsorption measured in pure acid assuming a monolayer charge of 210 $\mu C/cm^2$. The roughness factor was 1.55. A Pt sheet was used as CE.

6.4 Results

6.4.1 Response Time of the DEMS System

To verify that a suitable sweep rate was used and that the response time of the DEMS system was adequate, CO_2 was adsorbed on the WE by saturating the solution with CO_2 while keeping the electrode at 0.2 V_{RHE} for five minutes. CO_2 was then removed from the solution by He bubbling for ten minutes. The WE potential was swept at 5 mV/s, initially positive going, and both the CV and the m/e=44 signals were recorded in two subsequent cycles. The

[2] In reality a Rotating Ring-Disk Electrode was used, but only the disk was used in these experiments.

differences between the signals in the first and second cycle are shown in Figure 6.3. The curves show that at this sweep rate there is no noticeable time lag between the current and the MS signal, and there is very good agreement between the two measurements.

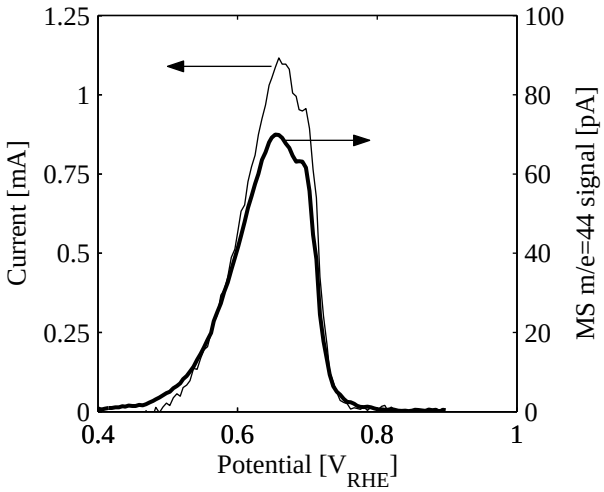

Figure 6.3: Difference in current and m/e=44 MS signal between first and second positive going sweep at 5 mV/s after the WE was poisoned with CO_2 for five minutes with ten minutes subsequent He bubbling. The thinner line is the current, the thicker line is the MS signal.

6.4.2 Volatile Oxidation Species of Ammonium in Acidic Solution

Potentiodynamic measurements with simultaneous measurements of MS spectra in acidic sulfate and perchlorate solutions were performed. The results are shown in Figures 6.4 and 6.5. There were substantial background levels in the MS system for the species of interest. The background of m/e=28 and 14 is probably due to ingress of atmospheric nitrogen. The reasons for the high background at m/e=44 is not clear, but believed to be CO_2. To enhance the signal-to-noise ratio, averaging was used while collecting the data (16 points were measured for each saved). A drift in background signal was observed in some of the data sets. The magnitude of the drift was determined by fitting a

base line to the MS signals measured at potentials below 0.40 V_{RHE} before and after each scan to high potentials. There were no significant MS signals at low potentials. The MS data series were then corrected for the drift using the fitted line. Data from 5-8 different sweeps were then averaged while post-processing the data to further reduce noise.

As seen from Figure 6.4 and 6.5, there is a stronger m/e=28 signal in the positive going sweep in the solution containing perchlorate than in the sulfate solution, notice the different scales used in the two Figures. The peak of the m/e=28 signal occurs at about 0.79 V_{RHE} in both solutions. The negative going sweep shows a signal of similar magnitude in both solutions at about 0.68 V_{RHE}. The m/e=14 signal was also monitored in the perchloric solution, see Figure 6.5 (d), and follows the m/e=28 signal closely. Further, no m/e=28 signal was found in the pure acid, showing that no CO was formed on the WE at high potentials. We thus conclude that the m/e=28 signal is due to formation of nitrogen on the WE.

There is also an m/e=30 signal in both solutions, but somewhat stronger in the sulfate than the perchlorate solution. This signal is attributed to formation of NO on the WE at potentials higher than 1.25 V_{RHE}. There might be a broad signal peak of m/e=30 at lower potentials in the perchloride solution (Figure 6.5 (c)), but the noise level is too large to draw any firm conclusions. In alkaline solutions it was found that nitric oxides (NO and N_2O) were formed at potentials higher than 0.80 V_{RHE} [24]. The maximum NO and N_2O signals in alkaline solution were detected at potentials higher than 1.2 V_{RHE} in alkaline solutions compared to at about 1.4 V_{RHE} found here in acidic solutions.

There is no sign of m/e=44 (N_2O) in either solutions studied in this work (data are only shown for the sulfate solution in Figure 6.4(d)). The NO and N_2O signals in alkaline solution are of the same magnitude. The background level for m/e=44 signal is about eight times higher than for m/e=30 in our DEMS system. The high background level could thus make the detection of N_2O difficult.

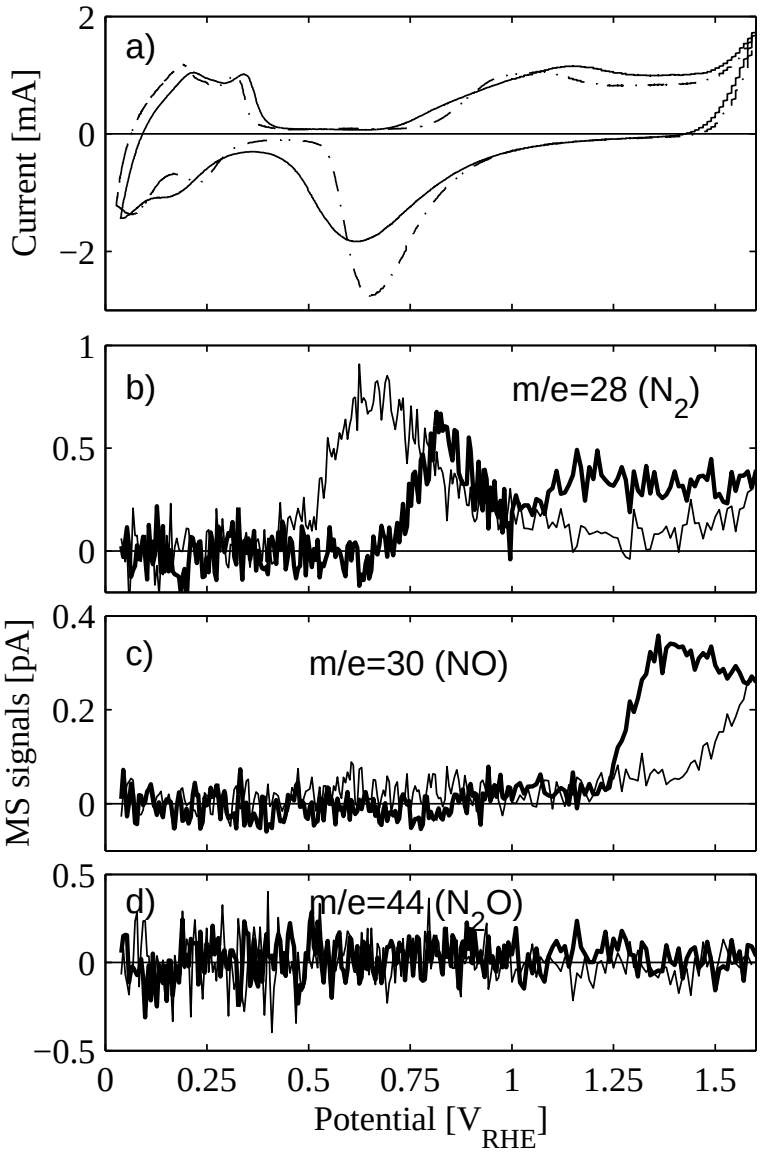

Figure 6.4: (a) CVs at 5 mV/s for pure 0.1 M H_2SO_4 (– · –) as well as in 0.1 M H_2SO_4 + 0.1 M NH_3 (—) and mass signals (b) m/e=28 (c) 30 and (d) 44, recorded in the ammonium containing electrolyte. Thick lines for positive going sweep, thin lines for negative going sweep.

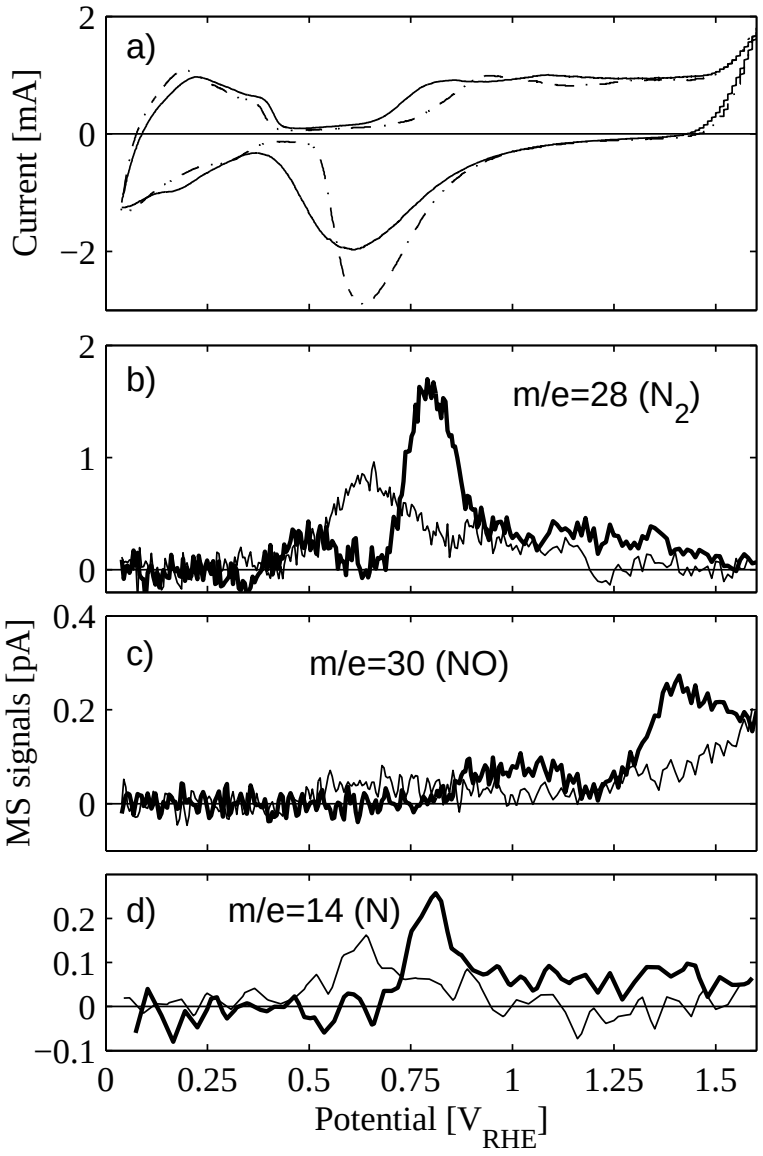

Figure 6.5: (a)CVs at 5 mV/s for pure 0.1 M $HClO_4$ (– · –) as well as in 0.1 M $HClO_4$+0.05 M NH_3 (—) and mass signals (b) m/e=28 (c) 30 and (d) 14, recorded in the ammonium containing electrolyte. Thick lines for positive going sweep, thin lines for negative going sweep.

The current that was passed during a CV in the EQCM measurements was integrated to obtain a relationship between total charge passed as function of potential, see Figure 6.6. The net oxidation charge passed during one complete CV cycle was calculated both for the pure 0.5 M sulfuric acid, Q_{ox}^{acid}, and for the acid containing 0.5 M ammonium for different sweep rates $Q_{ox}^{NH_4^+}$. The two net oxidation charges were subtracted to find the net oxidation of ammonium species during one complete cycle, $\Delta Q_{ox} = Q_{ox}^{NH_4^+} - Q_{ox}^{acid}$, see Figure 6.7(a). The net oxidation charge increases with decreasing sweep rate. The upper reversal potential was 1.25 V_{RHE} in the pure sulfuric acid and 1.30 V_{RHE} in the ammonium containing electrolyte.

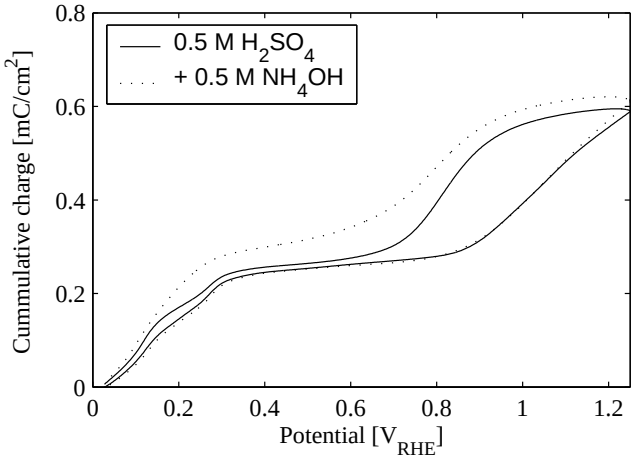

Figure 6.6: Cumulative charge passed during one CV cycle on platinized Pt in pure 0.5 M H_2SO_4 and with addition of 0.5 M NH_4OH at 50 mV/s starting at low potentials.

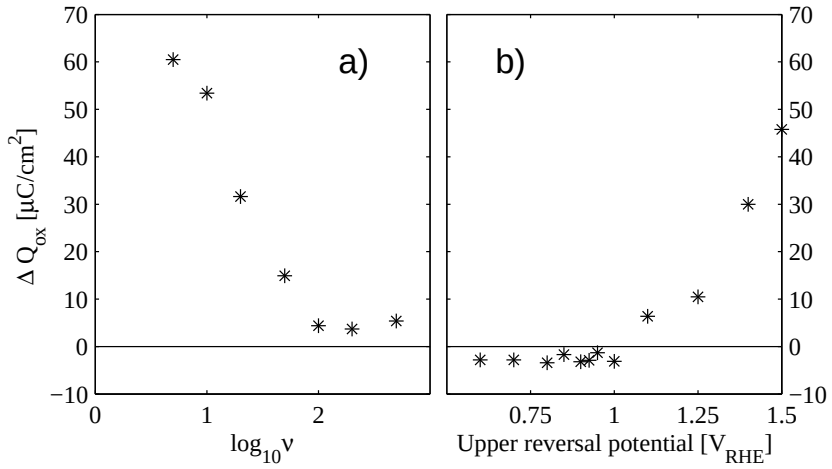

Figure 6.7: (a) Difference in net oxidation charge between acid with addition of NH_4OH and pure sulfuric acid during one complete CV cycle at different sweep rates. (b) The same oxidation charge difference but with varying upper reversal limits. The sweep rate was 50 mV/s.

The influence of the upper reversal potential on the net oxidation charge was also investigated as shown in Figure 6.7(b). The net charge passed in ammonium containing electrolyte is positive, *i.e.*, a net oxidation process is taking place, for upper reversal potentials above 1.0 V_{RHE}. When lower upper reversal potentials are used, there seems to be a small net *reductive* charge. This could be due to hydrogen escaping from the electrode in very small quantities at low potentials even though the lower reversal limit is higher than the RHE potential. A similar problem is encountered at very low sweep rates because there is a tendency that one gets a very high reductive current at low potentials at low sweep rates.

However, the main observation is that there is a net oxidation current at high potentials, and that the net oxidation increases with decreasing sweep rate, *i.e.*, longer times at high potentials. This is consistent with the observation of NO evolution in the DEMS experiments, but we do not see any significant net oxidation current due to the N_2 evolution which occurs at lower potentials. One should keep in mind that the variation in upper reversal limit was performed at a higher sweep rate (50 mV/s) than in the DEMS esperi-

ments (5 mV/s). Based on the findings in Figure 6.7(b) we would expect a higher net oxidation charge, consistent with the DEMS data, if a lower sweep rate was used in the experiments with different upper reversal limits.

6.4.3 Effect of Ammonium Concentration

Observations in the DEMS System

The concentration of ammonium in the perchloric acid was also varied, and the effects on the *m/e* 28 and 30 signals were observed, see Figure 6.8 and 6.9. Both mass signals are dependent on the concentration of ammonium in the solution. The N_2 signal (m/e=28) can be detected in a 0.1 M $HClO_4$ solution containing 0.025 M NH_3. The NO signal (m/e=30) is detectable in the solution containing 0.01 M NH_3. The apparent reaction order of ammonium is about 1.5 for N_2 evolution and 0.5 for NO evolution. It should be stressed that these reaction orders are very uncertain because very few points in a very narrow concentration range are available. It should also be kept in mind that both pH and ionic strengths of the solutions are affected by the additions of NH_3 to the solution, see Appendix C. This is discussed in more detail in Section 6.4.6.

Observations in the EQCM System

The observed CVs and corresponding mass responses for different concentrations of ammonium in 0.5 M H_2SO_4 are shown in Figures 6.10(a) and 6.10(b) respectively. There are noticeable effects of additions of NH_4OH to sulfuric acid. A shoulder appears at approximately 0.8 V_{RHE} in the CV in the positive going scan. The Pt oxide formation region is affected so that the onset of oxide formation is less marked with ammonium present. There is also a slightly higher oxidation current at potentials above 1.0 V_{RHE} with ammonium present in the solution. In the negative going scan, we see that the Pt oxide reduction peak at 0.80 V_{RHE} decrease with increasing concentration of ammonium, but there is a broad reduction shoulder following from 0.70 V_{RHE} to 0.50 V_{RHE}. The reduction peak for adsorption of strongly bond hydrogen at 0.25 V_{RHE} is affected, and a shoulder appears at about 0.18 V_{RHE}. There is also a slightly higher reductive current at potentials below 0.10 V_{RHE}. Note that the hydrogen desorption peaks are not affected by ammonium.

There is an increasing hysteresis in the mass response with increasing ammonium concentration which is especially noticeable at potentials below 0.90 V_{RHE}. At approximately 0.92 V_{RHE} in the positive going sweep there is a

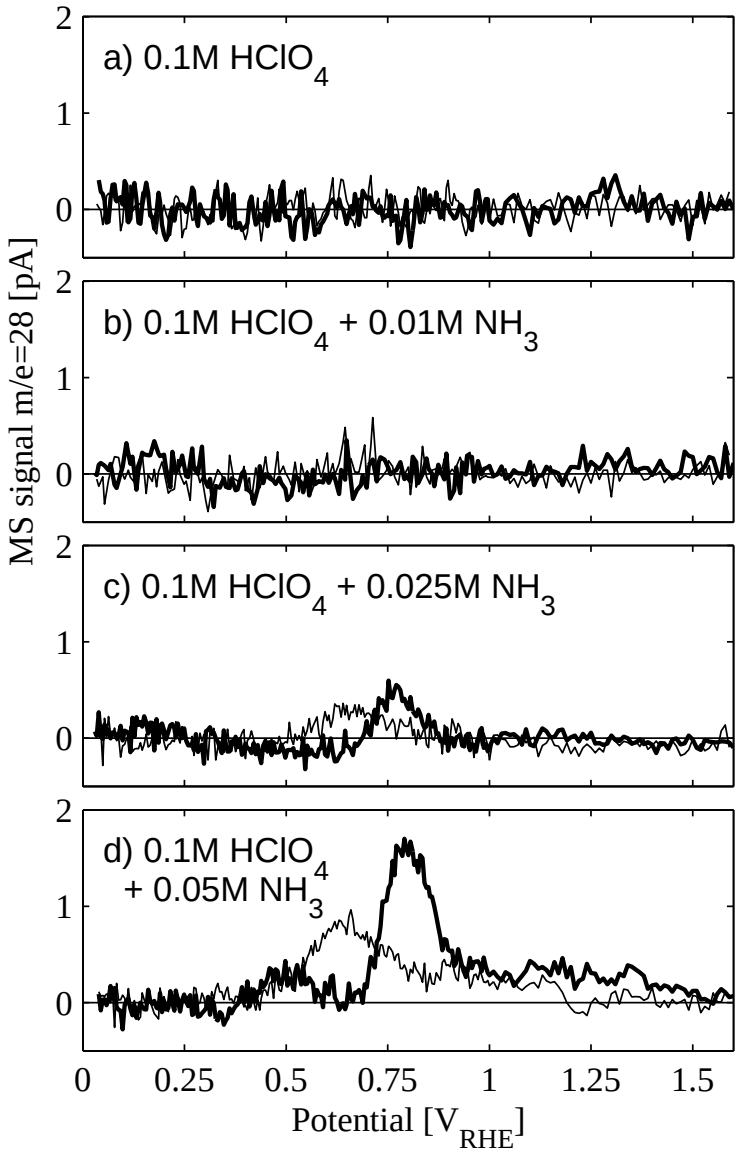

Figure 6.8: m/e=28 signal (N_2) for (a) pure 0.1 M $HClO_4$, (b) acid + 0.01 M NH_3, (c) acid + 0.025 M NH_3, (d) acid + 0.05 M NH_3. Sweep rate 5 mV/s.

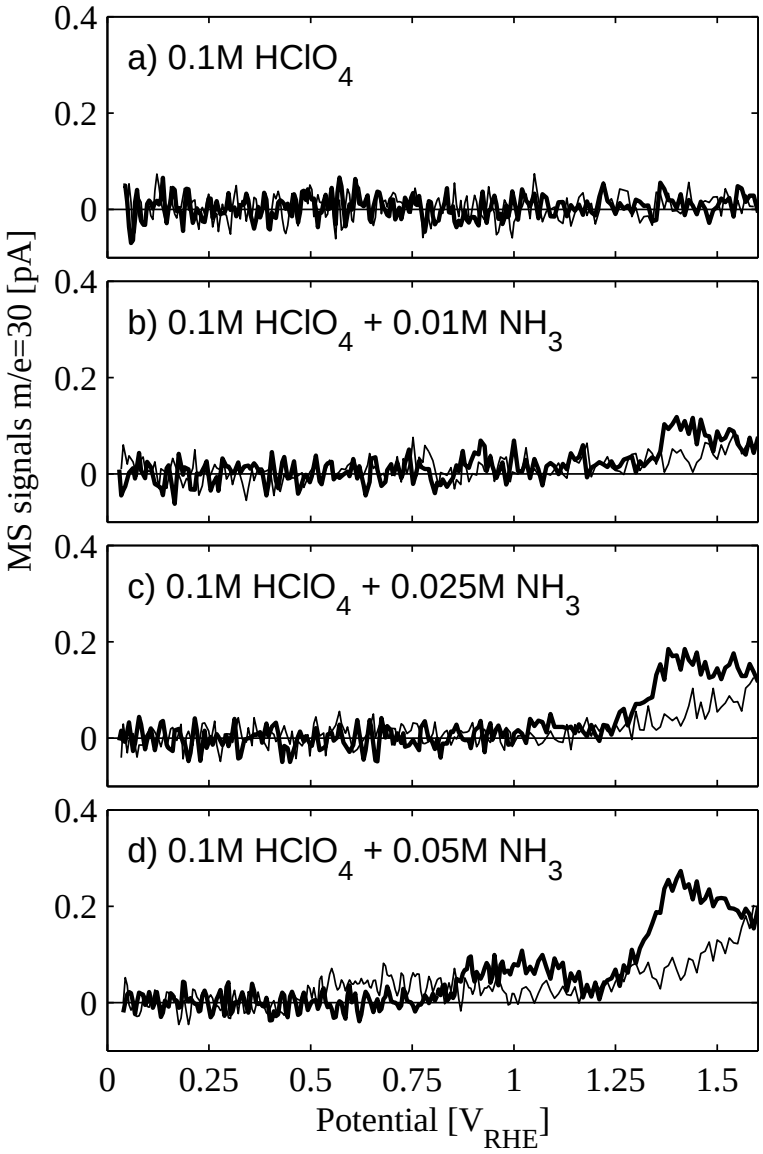

Figure 6.9: m/e=30 signal (NO) for (a) pure 0.1 M $HClO_4$, (b) acid + 0.01 M NH_3, (c) acid + 0.025 M NH_3, (d) acid + 0.05 M NH_3. Sweep rate 5 mV/s.

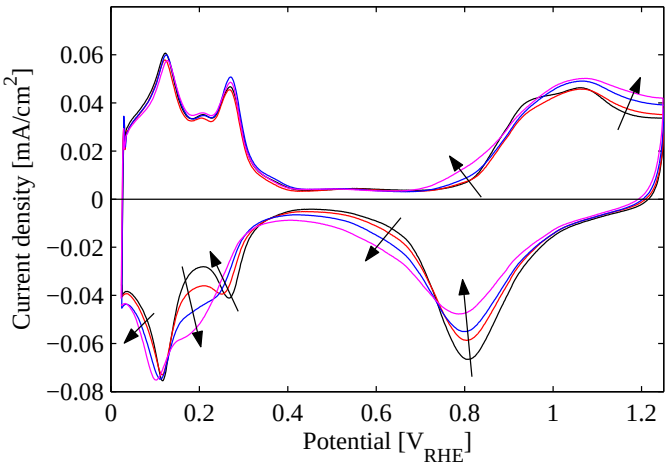

(a)

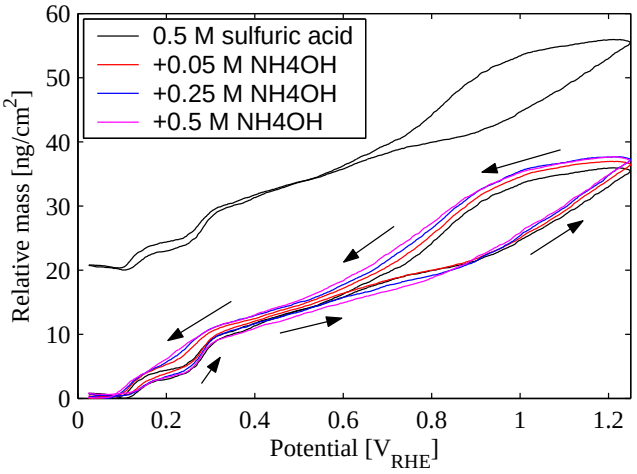

(b)

Figure 6.10: (a) CV and (b) corresponding mass response measured on platinized Pt at 50 mV/s in electrolyte containing 0.5 M H_2SO_4 base electrolyte. The mass response for pure acid is also shown with an offset of 20 ng/cm^2. Legend applies to both plots. Arrows in (a) indicates effect of increasing ammonium concentration, arrows in (b) indicate the path followed by the mass response through one CV cycle.

crossover where the mass in ammonium containing electrolytes becomes larger than in the pure acid. The mass at high potentials, where Pt is oxidized, is higher the higher the ammonium concentration is. The mass is also higher in the negative going sweep, but coincides with pure acid below 0.10 V_{RHE}.

The mass determination in EQCM is relative, that is, only *changes* in mass are detected, ref. Equation 6.16. The mass signals tend to drift somewhat with time making it necessary to adjust the offset of the mass signal. In order to compare results from different experiments, where different offsets were used, all mass responses were shifted so that the minimum mass, typically found at 0.10 V_{RHE}, is set to zero. This makes it difficult to conclude with absolute certainty that for example the mass in the positive going sweep is smaller in the presence of ammonium than in pure acid. However, it does seem that by fixing the minimum mass at zero, reasonable trends with increasing ammonium concentrations are observed. In our opinion, the approach used here is reasonable.

6.4.4 Interpretation of Mass Responses of EQCM in Pure Acids in the Literature

In the hydrogen adsorption region, it is observed that the mass *increases* as hydrogen desorbs. The proposed explanation for this is that as hydrogen desorbs, water can adsorb [193, 194]. At potentials higher than the *pzc*, *e.g.* 0.30-0.35 V_{SHE} for Pt in sulfuric acid [195], it has been established by different methods (radiotracer, FTIR) that hydrogen sulfate adsorbs on the electrode [196, 197] and thus contributes to the mass increase seen in the double layer region [193, 198]. Watanabe *et al.* [198] suggested that adsorption of hydrogen sulfate was solely responsible for the observed mass increase in the double layer region.

However, a significant mass increase in the double layer region has also been observed in studies of perchloric acid by Shimazu and Kita [199], although the mass gain was larger in the case of sulfuric acid. Since the usual view is that perchlorate ions adsorb only to a very small degree, the mass change in perchloric acid must mainly be due to water or species originating from water. Visscher *et al.* [191] also found a mass increase in the double layer region in perchloric acid although lower than in sulfuric acid. Lim and Hwang [193] found that the effective mass of the species adsorbed in the double layer region was about 17 g/mol e^-. They also found from their low-noise derivative mass change data that there was a broad peak in the region 0.45-0.65 V_{SHE}

independent of sulfuric acid concentration which they interpreted as specific adsorption of hydrogen sulfate. The broad peak was not found in perchloric acid. It seems most reasonable to assume that *both* water *and* hydrogen sulfate affect the measured responses of the EQCM in the double layer region, but the relative importance is less clear.

The mass in the oxide region is continuously increasing. The consequence of this is that the formation of Pt oxides does not involve initial formation of a monolayer of Pt-OH that is subsequently oxidized to Pt-O. If the initial species was Pt-OH, the second process would have a negative mass change associated with it [200–202] in conflict with experimental observations. Rather, Pt-O is formed up to a potential of about 1.1 V_{RHE} with a coverage of 50% followed by formation of a full monolayer of Pt-O up to 1.4 V_{RHE}. This monolayer formation is coupled with place exchange between Pt and O [201–203][3].

6.4.5 Comparison of Pure Acid EQCM Data to Available Literature Data

The mass responses of the electrodes used in our study are similar to reported responses by other researchers [184, 185, 191, 198, 200]. Minor differences are mainly observed in the hydrogen adsorption region whereas the mass gain in the oxide region is similar in all cases. Also within our own data we observe more scatter in the data in the hydrogen adsorption region (all data are not shown here).

On the other hand, several other authors have observed larger mass changes [193, 194, 199, 205]. Again, the differences are more noticeable in the hydrogen adsorption and double layer regions of the CVs.

6.4.6 Effect of pH on Oxidation of Ammonium

It could be argued that the effects observed in Section 6.4.3 could be due to pH effects in the solution. As NH_4OH is added to the solution, the pH will in-

[3] In the paper by Zolfaghari *et al.* [201], the mass change in the oxide region was significantly larger than what was later reported by members from the same research group (Jerkiewicz *et al.* [202]). In the first paper, they concluded that the mass increase from on-set of Pt oxide formation to one monolayer (at 1.4 V in their case) was equivalent to 16 g/mol Pt, but in the second paper they argued that the total mass change from *pztc* (0.27 V_{RHE}) to 1.4 V_{RHE} had to be included to get a change of 15.8 g/mol Pt. The discrepancy between the two papers is probably due to the calibration which was not performed in the first paper [204].

crease because H_2SO_4 is partially neutralized by ammonia forming ammonium. Further, the ionic strength and also the concentration of sulfate and hydrogen sulfate increases, see Appendix C. Two sets of experiments were made to verify the effect of pH. First, NaOH was added to the sulfuric acid instead of NH_4OH. The CVs and corresponding mass responses, not shown here, were very similar to the observations in pure acid. This indicates that the effect of pH, ionic strength and increased concentration of (hydrogen)sulfate *alone* is small.

We also increased the concentration of sulfuric acid to keep the pH constant. Simultaneously the ionic strength of the electrolyte will increase. Measurements on pure 0.5 M sulfuric acid electrolyte were made first before NH_4OH equivalent to 0.5 M was added and new experiments made. In the last step, an additional amount of sulfuric acid equivalent to 0.5 M was added to the solution and yet another set of measurements performed. The data are shown in Figure 6.11.

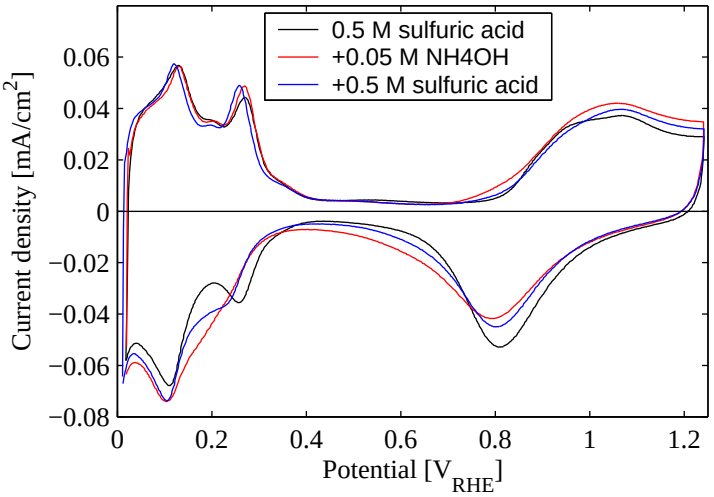

Figure 6.11: CV recorded at 50 mV/s on platinized Pt in electrolytes with different ammonium and acid concentration to assess the combined effect of pH and ammonium concentration.

We see that the effect of ammonia is partially reversed by addition of more acid to the 0.5 M H_2SO_4 + 0.5 M NH_4OH solution. However, there is still

a significant influence of ammonium compared to the pure acid. We thus conclude that there is a combined effect of ammonium concentration and pH of the solution. The change in pH is accompanied by changes in ionic strength and concentration of (hydrogen)sulfate. We are not able to distinguish between these effects based on these experiments. However, we would expect the pH effect to be more important because it is know from studies of oxidation in alkaline solutions that the oxidation of ammonia is significantly higher at high pH and also pH dependent [48, 49].

6.4.7 Effect of Sweep Rate

The effect of sweep rate was also determined. The observed current was scaled by the inverse of the sweep rate, ν. By applying this scaling, all curves will collapse into one curve if the underlying process is a reversible adsorption process [187]. In pure acid there is an effect of sweep rate on the Pt oxidation and reduction features, see Figure 6.12. The higher the sweep rate, the less oxide species are formed on the surface at high potentials. This is reasonable because the formation of Pt oxide species is relatively slow [206]. When the electrode is exposed to high potentials for longer times, *i.e.*, the slower the sweep rate, the more Pt oxide species will form. The peak potential of the Pt oxide reduction shifts to lower potentials. The Pt oxide formation peak shifts to higher potentials at higher sweep rates, *i.e.*, an increased peak separation. This is an usual observation for irreversibly adsorbed species on an electrode. The charges associated with hydrogen adsorption and desorption are not affected by the sweep rate. The mass responses (data not shown here) are consistent with the CV observations; the lower the sweep rate, the higher the maximum relative mass of the electrode.

A significant effect of sweep rate was observed in the ammonium containing solution, see Figure 6.13 (a). The hydrogen desorption peaks are not noticeably affected by sweep rate as also observed in the pure acid. A shoulder is observed in the positive going sweep at 0.83 V_{RHE} which increases relatively with decreasing sweep rate.

The charge associated with Pt oxidation decreases with increasing sweep rate as for the pure acid. The charge associated with Pt oxide reduction is almost independent of sweep rate. The Pt oxide reduction peak potential decreases slightly with sweep rate as in pure acid. Further, there is a shoulder to the Pt oxide reduction peak at about 0.60 V_{RHE} which also increases relatively with decreasing ν.

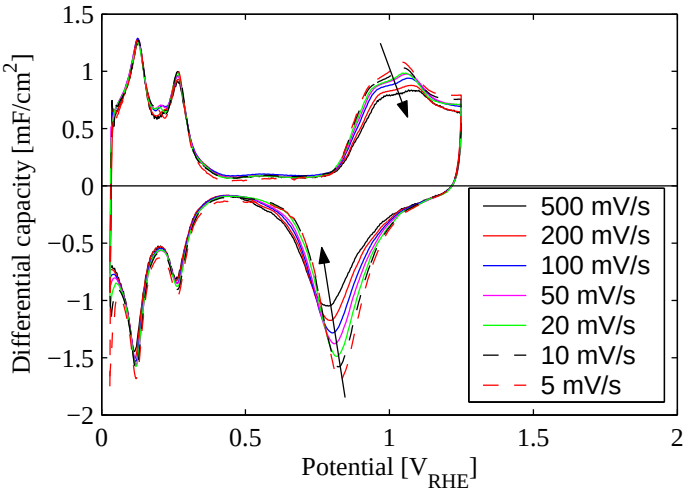

Figure 6.12: CVs of platinized Pt recorded at various sweep rates in pure 0.5 M H_2SO_4. Arrows indicate the direction of *increasing* scan rate.

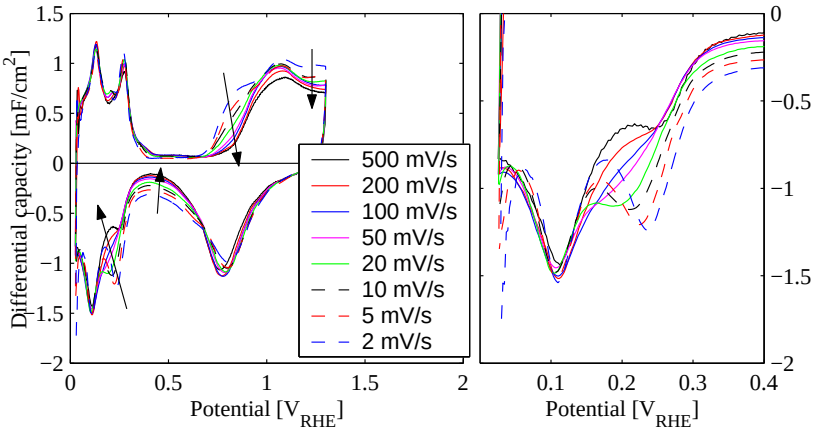

Figure 6.13: (a) CVs of platinized Pt recorded at various sweep rates in 0.5 M H_2SO_4 + 0.5 M NH_4OH. Arrows indicate the direction of *increasing* scan rate, (b) shows details in the hydrogen adsorption region.

The charge passed in the double layer region is dependent on the sweep rate. The hydrogen adsorption peak occurring at about 0.25 V_{RHE} is also strongly affected by sweep rate. This is shown more clearly in Figure 6.13 (b). The peak for the most strongly bond hydrogen is clear at sweep rates below 20 mV/s. The peak decreases and shifts to lower potentials with increasing sweep rate.

Variation of sweep rate was also performed in 0.5 M $HClO_4$, both with pure acid and with additions of 0.25 M NH_4OH. The data are shown in Figure 6.14. The same observations are made in this case as in the case of sulfuric acid

- Positive going scan
  - Peak in front of Pt oxide formation
  - More charge at high potential at low scan rates
- Negative going scan
  - Nearly constant charge under the reduction peak for Pt oxides
  - Shoulder on the Pt oxide reduction peak
  - More charge passed in the negative going sweep in the double layer region the slower the sweep
  - An effect on the most strongly adsorbed hydrogen peak.

However, the charge associated with the peak in front of the Pt oxidation region is higher and more marked in the perchloric acid as compared to the sulfuric acid as shown in Figure 6.15 (a) and (b).

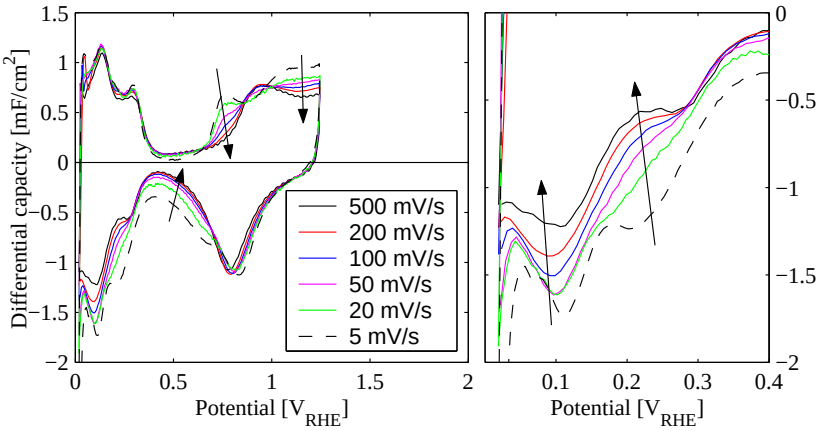

Figure 6.14: (a) CVs of platinized Pt recorded at various sweep rates in 0.5 M $HClO_4$ + 0.25 M NH_4OH. Arrows indicate the direction of *increasing* scan rate, (b) shows details in the hydrogen adsorption region.

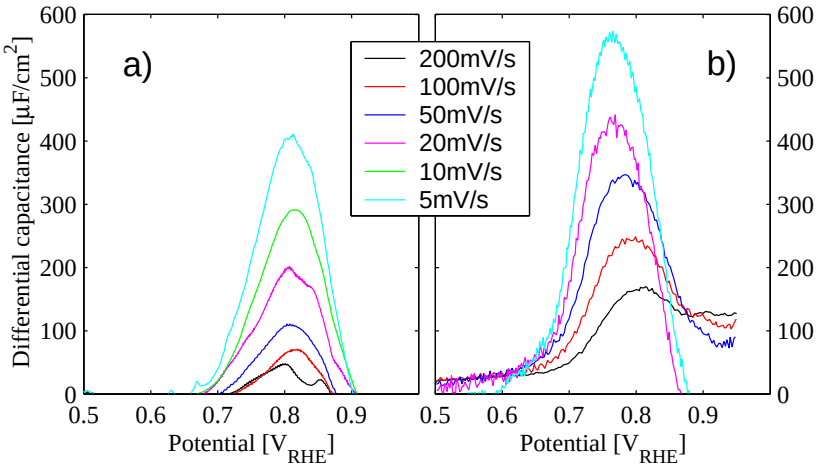

Figure 6.15: Detail of oxidation peak occurring just before Pt oxidation in positive going sweep at different sweep rates, (a) 0.5 M H_2SO_4 + 0.5 M NH_4OH (b) 0.5 M $HClO_4$ + 0.25 M NH_4OH. The CVs recorded in the pure acids have been subtracted.

6.4.8 Effect of Reversal Potential

Perchloric Acid

The reversal potential was also found to be an important parameter for the measured CV and mass response. Measurements performed in pure perchloric acid are shown in Figure 6.16. Figure 6.17 shows the effect of ammonia addition to the solution. The CV in the positive going scan is not affected. This indicates that the surface of the electrode is fully restored during the negative going scan to low potentials.

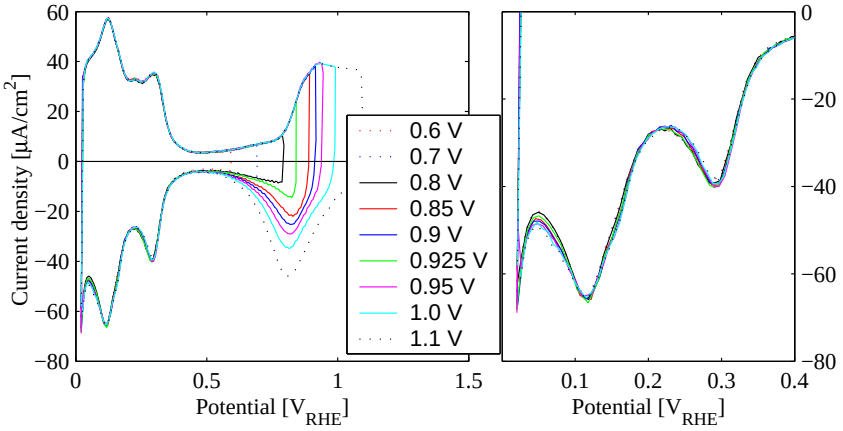

Figure 6.16: a) CVs of Pt in pure 0.5 M $HClO_4$ at 50 mV/s with different upper reversal potentials. (b) Details of the CVs in the hydrogen adsorption region.

The influence of concentration and sweep rate on the peak indicated by "1" in Figure 6.17 (a) was shown in Figure 6.10(a) and 6.15 (b). The peak potential in the positive going scan occurs at a slightly higher potential in the sulfuric acid system (810 mV_{RHE}) compared to perchloric acid (760–800 mV). From Figure 6.15 we see that the peak potential is slightly dependent on sweep rate especially in the perchloric acid system (+30 mV shift in the positive direction when increasing the sweep rate one decade).

In the reverse scan there are two reduction peaks visible at high potentials ("2" and "3" in Figure 6.17(a)). We argue that peak 3 is associated with the reduction of Pt oxides, occurring at 0.80–0.81 V_{RHE} consistent with our

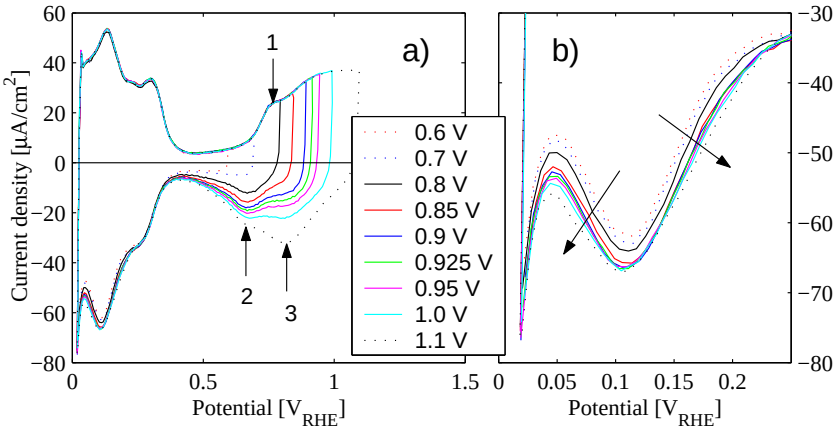

Figure 6.17: a) CVs of Pt in 0.5 M $HClO_4$ + 0.25 M NH_4OH at 50 mV/s with different upper reversal potentials. Refer to text for explanation of arrows and numbers. (b) Details of the CVs in the hydrogen adsorption region, arrows indicates direction of increasing reversal potential.

observations for different reversal potentials in pure perchloric acid shown in Figure 6.16. Note that the Pt oxide reduction peak is much more rounded and also smaller in the presence of ammonium. Further, we argue that peak 2 is associated with peak 1 forming a red-ox couple in the system. Peak 2 occurs at 0.66-0.67 V_{RHE}, the same potential where N_2 formation was observed in the DEMS measurements, see Figures 6.4 and 6.5. The peak separation fo 1 and 2 is thus about 0.11 V. The peak current, i_p, does not scale with ν as seen in Figure 6.15, but scales much better with $\sqrt{\nu}$. However, there is a slight decrease in $i_p/\sqrt{\nu}$ with increasing sweep rate in the sulfuric acid system.

Sulfuric Acid

Different reversal potentials were also tried in pure sulfuric acid (Figure 6.18) and ammonium containing sulfuric acid shown in Figure 6.19. The peak in front of the Pt oxide formation region in the ammonium containing electrolyte is less clearly identified as is the separation of two peaks in the reverse scan. A small, broad peak is seen for reversal at 0.9 V_{RHE}. There is a clear effect of ammonium on the hydrogen adsorption region as shown in Figure 6.19(b), much

more so than in the pure acid shown in Figure 6.18(b). More reduction charge is passed at potentials below 0.2 V_{RHE} as the reversal potential increases. This was also observed for the perchloric acid system. However, increasing the reversal potentials further than 1.25 V does not affect the observed CV at low potentials in the hydrogen adsorption region. The dependence on reversal potential indicates that some of the influence in the hydrogen adsorption region stems from processes taking place at very high potentials. This effect seems to be fully reversed in the negative going scan because the hydrogen desorption peaks are identical for all reversal potentials.

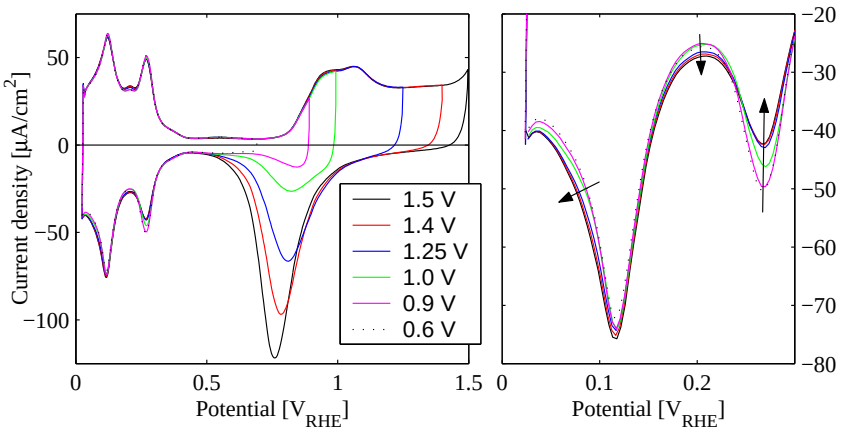

Figure 6.18: (a) CVs of platinized Pt in pure 0.5 M H_2SO_4 at 50 mV/s. (b) Details of the CVs in the hydrogen adsorption region, arrows indicates effect of increasing reversal potential.

Mass responses were also recorded with different upper reversal potentials as shown in Figure 6.20. The mass gain at high potentials decreases with decreasing reversal potential because less Pt oxides are formed. Further, there is a hysteresis between the positive going and negative going sweeps. This hysteresis is observed even when the upper reversal potential is as low as 0.30 V_{RHE} although not as noticeable as with higher reversal potentials. In Figure 6.20 (b) the mass response observed in pure acid is shown for comparison and does not show any hysteresis. The mass response in positive going sweeps is not dependent on the upper reversal potential used as was also observed in the CVs shown in Figures 6.17 and 6.19.

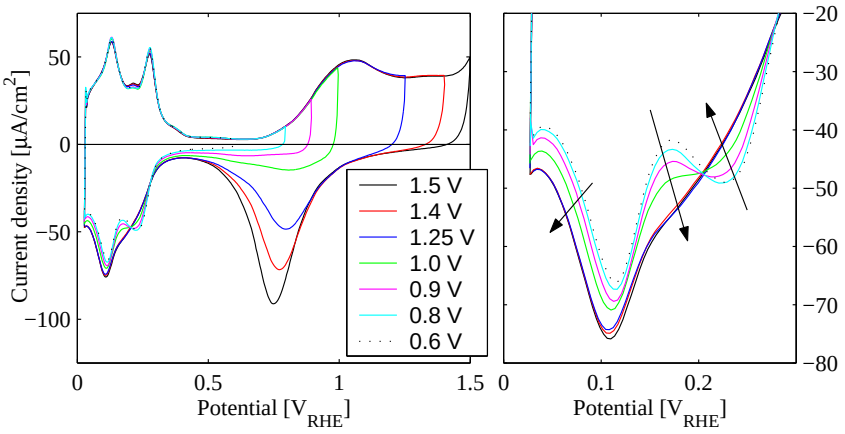

Figure 6.19: (a) CVs of platinized Pt in 0.5 M H_2SO_4 + 0.5 M NH_4OH at 50 mV/s. (b) Details of the CVs in the hydrogen adsorption region, arrows indicates effect of increasing reversal potential.

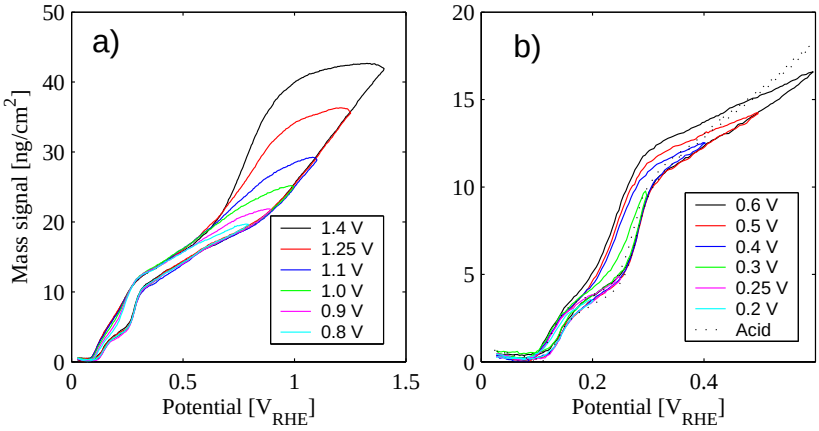

Figure 6.20: a) Mass response during CV of Pt in 0.5 M H_2SO_4 + 0.5 M NH_4OH at 50 mV/s at relatively high reversal potentials. b) Details of mass response at lower reversal potentials, response in pure acid also shown.

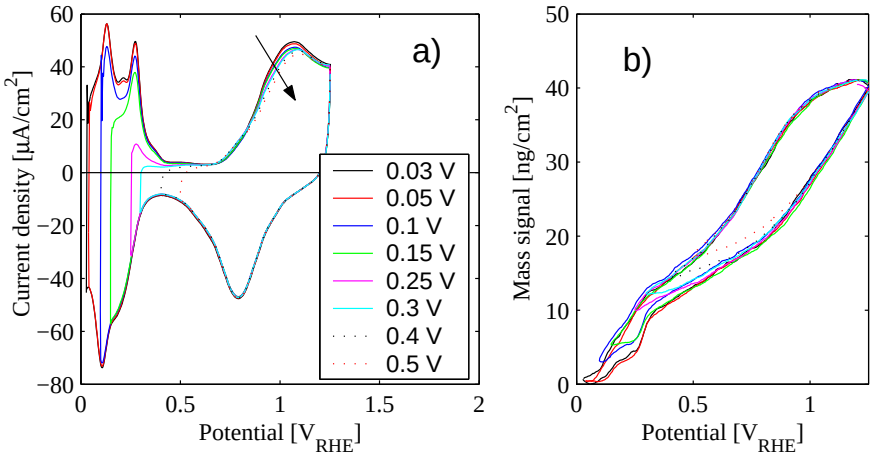

Figure 6.21: a) CVs of Pt in 0.5 M H_2SO_4 + 0.5 M NH_4OH at 50 mV/s with different lower reversal potentials for the sweep. The arrow indicates the change in the direction of increasing lower reversal potential. Plot b) shows the corresponding mass response.

The *lower* reversal limit was also varied, see Figure 6.21. The mass responses were adjusted so that they all have the same relative maximum mass at the *upper* reversal potential. Two things should be noticed in Figure 6.21: *1)* The Pt oxide formation peak decreases slightly with increasing lower reversal potential. *2)* There is still a hysteresis, and the mass responses all tend to follow the same curve in the positive going sweep. The removal of the mass associated with the hysteresis is thus not dependent on very low electrode potential, *e.g.*, in the hydrogen adsorption region.

6.4.9 Differential Analysis of Mass Responses

Time Derivative of Mass Response

The time-derivative of the mass changes for 0.5 M H_2SO_4 and the same acid with 0.5 M NH_4OH added is shown in Figure 6.22. The curves shown are the average of five different measurements to reduce the noise. The data were also filtered using a 9-point Savitzky-Golay filter [169]. Lim and Hwang [193] reported data with a much lower noise level, but they used an EQCM system that had been designed to have especially low noise. The mass gain rate

in the positive going double layer region seems to be slightly lower for the ammonium containing electrolyte. Another interesting thing to note is that there is a slightly higher rate of mass increase in the region 0.8–1.0 V_{RHE} in the positive going sweep in teh ammonium containing electrolyte. Also, there is a slightly lower rate of loss of mass in the oxide reduction peak in the negative going scan. Further, we see that the mass loss rate associated with the adsorption of the most strongly adsorbed hydrogen is lower in the ammonium containing solution. However, there is a significantly higher loss rate in the region between the two hydrogen adsorption peaks. The mass loss rate in ammonium containing electrolyte is also higher in the range 0.12–0.08 V_{RHE}.

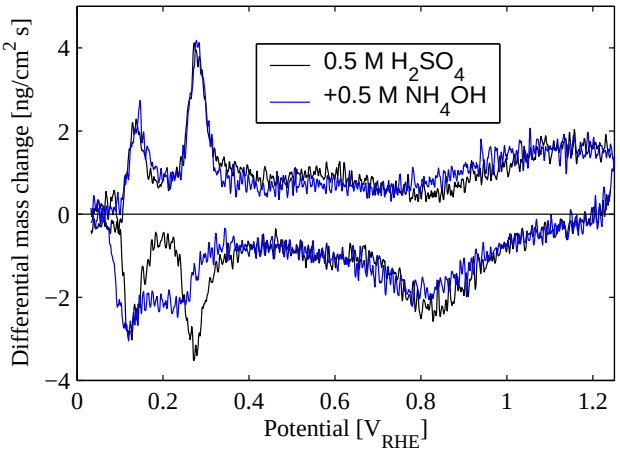

Figure 6.22: Time derivative of mass response for pure 0.5 M H_2SO_4 and with additions of 0.5 M NH_4OH recorded at 50 mV/s. The data shown are the average of five data sets for each solution followed by a 9-point numeric Savitzky-Golay filter [169].

Charge Derivative of Mass Response

The mass change is plotted against the accumulated charge passed through the cell in Figure 6.23. The derivative of the mass change with respect to charge yields the net equivalent weight of the species involved in the process, $M = F \cdot \partial\Delta m/\partial Q$ [179]. It should be emphasized that the results from this analysis are uncertain because of uncertainties in the determination of the

Sauerbrey coefficient of the crystal. Further, since only the change in mass is detected, the equivalent weight is also affected by which species that are desorbing.

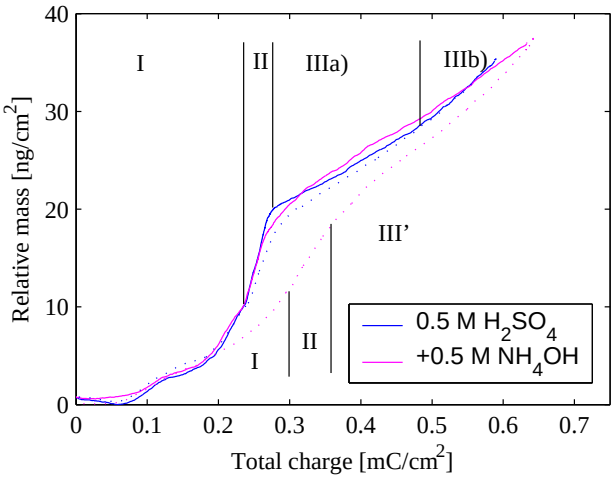

Figure 6.23: Mass response as function of total charge passed through the cell for pure 0.5 MH_2SO_4 and with additions of 0.5 M NH_4OH recorded at 50 mV/s. (—) positive going sweep, $(\cdot\ \cdot\ \cdot)$ negative going sweep.

The behavior of the pure acid is very similar in the positive and negative going scan. Region I is the hydrogen desorption/adsorption region, Region II is the double layer region and Region III is the Pt oxide region. Region I and III can be divided into sub-regions. In the hydrogen adsorption/desorption this subdivision is questionable due to the experimental difficulties and uncertainties associated with mass changes in this region, see Section 6.4.5. However, the subdivision of Region III is more reliable, and has also been observed by Shimatzu and Kita [199]. They found equivalent weights of 5.0 and 8.8 g/mol e^- in IIIa and IIIb respectively. We find slopes of about 3.6 and 6.5 g/mol e^- respectively. The ratio of the slopes is very similar to Shimatzu and Kita's data; the absolute difference can be due to uncertainties in calibration etc. The transition from IIIa to IIIb occurs after passing about 200 $\mu C/cm^2$ in the IIIa region, or about 1 electron per Pt surface atom. Shimatzu and Kita suggested that this marked the transition from formation of Pt-OH to Pt-O. However, as discussed in Section 6.4.4, the Pt oxidation mechanism whereby Pt is first covered by a monolayer of Pt-OH before further oxidized to Pt-O,

has been rejected by other researchers [200, 202]. However, it is interesting to observe this change in slope which seems to be of a fundamental nature.

In the case of ammonia addition, the positive going scan is very similar in the hydrogen desorption and double layer region. The slope is similar to the slope observed in pure acid in Region IIIa, but does not change significantly in Region IIIb. We may speculate that this indicates that the Pt oxide formation mechanism is different in the presence of ammonium as discussed further below. It should also be noted that there is a net total oxidation charge passed in the presence of ammonium compared to pure acid, see Figure 6.7. Therefore, the absence of the second slope could also partly be explained by oxidation of ammonium to volatile species that do not lead to mass increase on the electrode but do contribute to a higher charge.

In the negative going sweep there is a marked difference compared to the acid. The transition between the regions is much more gradual. The extent of Region II' (double layer) is not well defined, but the charge corresponding to a cell potential of 0.60 V is taken as the upper limit.

6.4.10 Rotating Disk Electrode Results

RDE experiments were run to assess the influence of mass transfer on the peak appearing in front of the oxide region (1) and its corresponding reduction peak (2), see Figures 6.17 and 6.24. The scan reversal potential was set at 1.0 V_{RHE} to more clearly see the reduction peak. We see that both peak 1 and 2 tend to decrease equally with increasing rotation rate, ω.

Further, we note that also peak 3 and the hydrogen desorption peaks tend to decrease. These features are definitely associated with adsorption processes. One would therefore expect these features to be *independent* on ω [187]. The fact that they *are* dependent on ω is probably due to a slight contamination in the system even though the cell was cleaned carefully. The RDE is more sensitive to contaminants than f. ex. the EQCM WE because the mass transfer is much higher. Also the roughness factor for the RDE WE is very low, only 1.55, compared to the EQCM WE with a roughness factor of 15-25.

When letting the electrode rest at a fixed potential (0.5–0.7 V_{RHE}) for several minutes, a large oxidation current was observed in the positive going scan at potentials higher than 1.0 V_{RHE} (not shown here). The oxidation current on top of the Pt oxide oxidation current was nearly absent in the subsequent scan. The hydrogen adsorption peaks were also larger after this initial cleaning scan to high potentials. These are all typical observations in

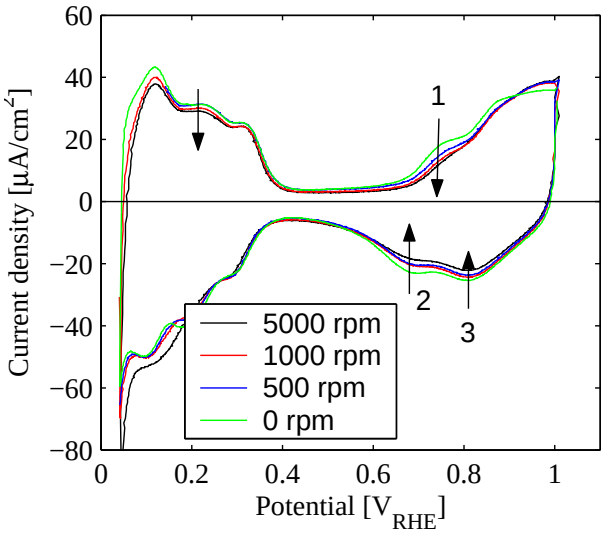

Figure 6.24: CVs of Pt in 0.5 M $HClO_4$ + 0.25 M NH_4OH at 50 mV/s with different rotation rates. The arrow indicates the change in the direction of increasing rotation rate. The numbering of the peaks is the same as in Figure 6.17

contaminated electrolytes where the contaminants are normally some form of organic component. However, the important difference we observe, is that there is no oxidation peak in the range 0.5–0.9 V_{RHE} which is typically seen when the contaminant is of organic origin. It *could* therefore be that the contaminant in this solution is linked to the presence of ammonium, but no firm conclusion on this matter has been reached in this work.

However, presence of the contaminant, if any, does not affect the main finding here: peak 1 and 2 are affected to the same extent by rotation rate. This indicates that an adsorbed species is formed oxidatively in peak 1. The same species, or a product from it, is reduced in peak 2, see Section 6.5.2 for futher discussion.

6.5 Discussion

6.5.1 Effects On Hydrogen Desorption and Positive Going Double Layer Region

The hydrogen desorption peaks were not affected by the presence of ammonium. This suggests that all adsorbed species are more or less completely removed in the negative going scan so that the effect of ammonium in the positive going scan is not noticeable. This was also observed by de Vooys *et al.* [176] in alkaline solution. The double layer region in the positive going sweep is also unaffected by the presence of ammonium.

6.5.2 Presence of a Red-Ox Couple

Peak 1 and 2 in Figure 6.17 coincides with the N_2 peaks observed in the DEMS measurements, see Figure 6.4 (b) and 6.5 (b) both in the positive and negative going scans. Based on measurements we made of ammonia oxidation in alkaline solution (data not shown here), we find that the ratio between the MS signal and the observed current is about $4{\cdot}10^{-8}$. We here assume a 100% current efficiency with respect to N_2 formation [24]. We can thus estimate that the observed N_2 signal in the positive going scan only accounts for about 8% of the observed current signal in the perchloric system and about 6% of the current in the sulfuric system. It should be added that these calculations are uncertain. However, it clearly shows that the charge associated with peak 1 is mainly due to a different reaction than N_2 evolution.

Peak 2 in the negative going sweep is due to a *reduction* process so that N_2 evolved by oxidation of ammonium would actually reduce the height of this peak. It is likely that this peak represents reduction of the species formed in peak 1 in the positive going sweep. The fact that i_p for peak 1 clearly does not scale with $1/\nu$ but much better with $1/\sqrt{\nu}$ would normally lead us to the conclusion that the species associated with peak 1 and 2 is not an adsorbed species, but a species that is soluble.

RDE data indicate that the species is adsorbed. If it was soluble, peak 2 would decrease rapidly with increasing ω. If the oxidation process in peak 1 was limited by mass transfer, it should increase with ω. The concentration of ammonium is so high that one would not expect mass transfer limitations in this case. If peak 1 is associated with an adsorbed species, it is normally observed that the peak is not affected by ω.

A further indication that the species is adsorbed, is that the separation of peak 1 and 2 is high, about 110 mV. A separation of less than 60 mV is normally found in reaction mechanisms involving dissolved species [187]. For adsorbed species that adsorb and desorb reversibly, the peak separation is very small; one example is hydrogen adsorption/desorption. Large peak separations are observed for irreversibly adsorbed species. One example is formation of Pt oxide and subsequent desorption that takes place at substantially lower potentials than formation. The peak separation in the case of irreversibly adsorbed species should increase with increasing sweep rate. This is the case here, see Figure 6.15, but the increase in peak separation is not very large. A closer inspection of the mass response in Figure 6.10(b) show that the mass of the WE increases stronger compared to pure acid in the positive going sweep in the range 0.75–0.95 V_{RHE} possibly caused by adsorption of the species involved in peak 1.

We have contradicting observations as to if the species associated with peak 1 and 2 is adsorbed or not. We are not able to firmly resolve this issue with the data we have available, but tend to believe that the species is adsorbed. Neither the nature of the species has not been identified nor what chemical reaction that yields the species responsible for peak 1 and 2. The observation of N_2 evolution at the same potentials as peak 1 and 2 indicates that the species is related to the mechanism leading to N_2 evolution. Based on the Gerischer and Mauerer mechanism [23] it seems natural to assume that the adsorbed species could be N_{ads} formed from $NH_{x,ads}$ in the positive going sweep in addition to nitrogen. In the reverse sweep, N_{ads} may be reduced forming either nitrogen *via* $NH_{x,ads}$ or ammonium as observed by Gootsen *et al.* [177] in alkaline solution.

It is interesting to note that the detected N_2 signal in the DEMS in the negative going sweep is very similar both in perchloric and sulfuric acid electrolytes, see Figure 6.4 and 6.5. This could indicate the the source of N_2 formation in the negative going sweep is an adsorbed species with equal surface coverage in both ammonium containing sulfuric and perchloric acids. The relative intensity of the N_2 signal in the negative going sweep compared to the positive going sweep is about 0.8 and 2.0 in sulfuric respectively perchloric acid. In alkaline solution, the same ratio is about 0.1 [24]. A further observation is that there is no difference between the pure acids and ammonium containing acids in the double layer in the positive going scan. Thus, the formation of adsorbed species does not take place at potentials below 0.65 V_{RHE}. In alkaline solutions a significant oxidation current is observed at potentials as low as 0.45 V_{RHE} [24, 177].

6.5.3 Effects on Platinum Oxides

The platinum oxide formation and reduction is also significantly affected by the presence of ammonium. The on-set of Pt oxide formation is less sharp compared to pure acid, see f. ex. Figure 6.10(a). There is also a significantly higher oxidation current at potentials above 1.0 V_{RHE} in the presence of ammonium. We have observed formation of NO, at least at potentials above 1.2 V_{RHE}, see Figures 6.4(c), 6.5(c), and 6.9. However, the charge associated with oxidation of NO from ammonium is too low to explain this additional charge.

The Pt oxide reduction peak appearing at about 0.8 V_{RHE} is shifted slightly negatively in the presence of ammonium, see Figure 6.11. However, the most noticeable effect of ammonium is that the charge associated with this Pt oxide peak is almost independent on sweep rate (Figure 6.13) and also much smaller than in the pure acid. Similar observations were made by Wasmus *et al.* [24] and Gootzen *et al.* [177] in alkaline electrolytes. The charge associated with Pt oxide reduction in pure sulfuric acid at 50 mV/s and 1.30 V_{RHE} upper reversal is about 360 $\mu C/cm^2$ or 0.86 monolayers of Pt-O. The reduction charge in the ammonium containing electrolyte is approximately 280 $\mu C/cm^2$ at 0.67 V_{RHE} where the shoulder associated with peak 2 is observed in the sulfate system (50 mV/s, 1.30 V_{RHE} reversal, see Figure 6.13). The reduction charge in pure acid at the same potential was about 92% of the total reduction charge. If we assume the same coverage of oxygen in the ammonium containing electrolyte as on pure acid, only 78% of the Pt oxide reduction charge was passed at 0.67 V_{RHE}. This is compensated by a larger reduction current in the double layer region presumably partly due to reduction of Pt oxides that are more stable in the presence of ammonium, see Section 6.5.4.

Other species could also be present like N-O species. de Vooys *et al.* [176] suggest that metal oxynitrides are present on the Pt surface in alkaline solutions at high potentials. Detection of NO in the DEMS data at high potentials also supports the possibility of N–O species present at high potentials. de Vooys *et al.* also found NO and N_2O formation when ammonia was in the solution, but in adsorbate experiments with adsorbates formed at 0.9 V_{RHE} no evolution of nitrous oxides at high potentials was detected. This led them to conclude that the oxynitride species were very stable and inactive in the formation of NO and N_2O.

6.5.4 Effects in the Negative Going Double Layer Region

A substantially higher reduction current is observed in the negative going sweep in the presence of ammonium than in pure acids. The reduction current increased with concentration (Figures 6.10(a)) and upper reversal potential (Figures 6.16, 6.17, 6.18, and 6.19). The reduction current decreased with increasing sweep rate (Figure 6.13). We belive that part of this higher current can be explained by a more stable Pt oxide layer in the presence of ammonium, see above, but also due to reduction of the species formed at 0.7–0.9 V_{RHE} in the positive going sweep. The reduction charge in the double layer is also much higher in alkaline solutions containing ammonia [24, 177]. Parts of this reduction leads to formation of N_2, but also NH_3 has been detected [24].

6.5.5 Effects on Hydrogen Adsorption

Strongly Adsorbed Hydrogen

As has been shown above, there is a significant effect on the hydrogen adsorption peaks when there is ammonium present in the solution. The most marked effect is that the peak at 0.25 V_{RHE} associated with the most strongly adsorbed hydrogen is depressed and shifted to lower potentials. This effect has been shown to become more pronounced with increasing ammonia concentration (Figure 6.10(a)) and increasing upper reversal potential for the CVs in the hydrogen sulfate system, see Figure 6.19. There was no effect on the most strongly bond hydrogen in the perchloric system, see Figure 6.17. The effect of the sweep rate was more complex, see Section 6.4.7.

In a study on the effect of co-adsorption of ammonia and hydrogen sulfate on Pt (1 1 1), Shingaya *et al.* [207] found, using Infra-Red Reflection Spectroscopy (IRAS), that ammonium and hydrogen sulfate co-adsorbes on Pt. Ammonium stablizes the hydrogen sulfate species so that it desorbs at lower potentials than in pure acid. It is also known that the peak associated with the most strongly bond hydrogen is strongly affected by adsorption of hydrogen sulfate [208]. The findings of Shingaya *et al.* is very similar to our findings; the effect on the H_{ads} peak is noticeable even at quite low upper reversal potentials, and the effect was more pronounced at 50 than at 5 mV/s sweep rate. Shingaya *et al.* observed a small effect also on the hydrogen desorption peak in contrast to our findings. In 0.1 M HF containing 0.01 M ammonium there was very small effects on the hydrogen adsorption features. This is in line with our observations in perchloric acid. Both fluoride and perchlorate are known

to adsorb to a very low extent on Pt.

de Vooys *et al.* [176] also found that ammonia had an effect on the hydrogen adsorption peaks in 1 M KOH applying reversal potentials in the range 0.35–0.4 V_{RHE} with no passage of net charge. They suggested that this indicated adsorption of NH_3 on the surface.

We believe that the delayed desorption of hydrogen sulfate is also the reason why we see a shift in the differential mass change shown in Figure 6.22. The mass loss normally associated with the strongly bond hydrogen peak is shifted to lower potentials.

Reduction Currents at Very Low Potentials

At very low potentials we observe a reduction current that increases with increasing reversal potential both in sulfuric and perchloric acid solutions containing ammonium, see Figures 6.19 and 6.17. There is a similar effect in the pure acid too as shown in Figure 6.18, but the effect is much smaller. We also observe a loss of mass on the EQCM not present in pure acid in the potential region 0.12–0.08 V_{RHE} in the negative going scan, see Figure 6.22. Wasmus *et al.* observed formation of N_2, NO and N_2O at similar potentials in their alkaline electrolyte. We therefore suggest that a similar reaction occurs in our system where a highly oxidized nitrogen species is reduced to form nitrous oxides, N_2 and possibly also ammonium. No mass signals associated with this process were detected in our DEMS experiments. However, we belive that this is explained by the fact that these mass signals are very weak. The background level was very high compared to the strength of our signals in all DEMS measurements reported here.

6.6 Conclusions

We have found that ammonium is electrochemically active in acidic solutions at room temperature. Oxidation of ammonium to form nitrogen or nitric oxide species is slow at room temperature. Formation of N_2 was demonstrated using DEMS, and also NO was detected at electrode potentials higher than 1.2 V_{RHE}. Nevertheless, this moderate activity for oxidation of ammonium can be critical to understand state state tolerance of ammonia poisoning in PEMFCs. Recovery after contamination will also be influenced by the rate of ammonium oxidation.

CV and EQCM data have shown that presence of ammonium affects the formation and reduction of Pt oxide at high potentials. This seems to involve the formation of very stable nitrogen or nitrogen-oxygen species on the surface of the electrode. Some of these species seem to be removed from the electrode only at very low potentials in the hydrogen adsorption region.

The hydrogen adsorption region is also strongly affected by presence of ammonium, in particular the most strongly bond hydrogen which is shifted to lower potentials. Both species formed at very high potentials as well as an interaction between ammonium and hydrogen sulfate in the electrolyte seem to be responsible for this effect on hydrogen adsorption. The impact of these factors on the Hydrogen Oxidation Reaction is not clear. The hydrogen desorption region is not affected by ammonium poisoning.

Chapter 7

Oxygen Reduction on Platinum in the Presence of Ammonium

7.1 Summary

The Oxygen Reduction Reaction (ORR) rate was studied using a Rotating Disk Electrode (RDE). The effect of ammonium on the ORR in a sulfuric acid electrolyte is significant. There is also a slight effect of potassium on the rate of the ORR, but much smaller than the effect of ammonium. ORR on oxide-free Pt surfaces is more affected by ammonium than ORR on oxide covered Pt. The Tafel slope at low current density (c.d.) on oxide-free Pt is about 90 mV/dec. in the presence of ammonium compared to about 60 mV/dec. in pure acid. The Tafel slopes of ORR on oxide-free Pt at high c.d. are the same in pure acid and with ammonium present. The exchange c.d. is lower in the presence of ammonium. The Tafel slope of ORR on oxidized Pt surface in the low c.d. region is not significantly affected by ammonium. The Tafel slope of ORR at high c.d. was 150 to 160 mV/dec. on oxidized Pt, somewhat higher than on oxide-free Pt (about 120 mV/dec.). The exhange c.d. is lower for the ammonium containing electrolyte also in this case. The apparent reaction order of ammonium in ORR is -0.4 to -0.5 on the oxide-free Pt and -0.15 to -0.2 on the oxide covered Pt. The origin of the loss of ORR activity has not been established.

7.2 Introduction

The Oxygen Reduction Reaction (ORR) and its counterpart, the Oxygen Evolution Reaction (OER), are important electrochemical reactions in corrosion, Fuel Cells (FCs), electrowinning of metals etc. The oxygen electrode has thus been investigated by numerous researchers. Several review articles are available, f. ex. by Tarasevich, Sadkowski and Yeager [209] and Damjanovic [210]. The ORR is especially important in relation to FCs, because the overpotential required to drive the ORR at a satisfactory speed is very high. This overvoltage represents the single most important contribution to loss of efficiency in the low-temperature, acidic Polymer Electrolyte Membrane FCs (PEMFCs). Of particular interest is the fact that the observed Open Circuit Voltage (OCV) for the ORR is typically 1.0 V vs. the Reversible Hydrogen Electrode (RHE). The expected voltage based on the Gibb's energy of the ORR at room temperature is 1.229 V. However, applying extreme cleaning and pre-oxidation procedures, several research groups have been able to attain OCVs very close to the theoretical values, see Tarasevich *et al.* [209] for further details.

Several explanations have been proposed to explain the large discrepancy between the OCV usually observed and the theoretical potential. In particular, several researchers have proposed that an oxidation reaction occurs simultaneously at the electrode [209]. This could be oxidation of organic impurities, but the OCV is usually independent on stirring. Therefore, this possibility is less likely [209]. Reduction of oxygen may form hydrogen peroxide that can influence the potential. Oxidation and slow dissolution of platinum has been observed in acidic solutions [211–213] and suggested to be the side reaction responsible for the low OCV [209, 212].

7.2.1 ORR Mechanism on Oxide Free Platinum

The reaction mechanism of the ORR has been thoroughly investigated. There is a large difference in reaction rates on oxide covered and oxide-free platinum surfaces. The oxide-free metal is much more active for ORR than the oxide covered [210]. The reaction mechanism suggested by Damjanovic and others for bare platinum, as summarized in [210], is applicable to ORR in acidic FCs. The cathode in an FC under load is typically oxide-free [210] although effects of a Pt-oxide layer accumulating over time have been observed [214]. Damjanovic and Brusic [215] assumed that the first electron transfer is the rate determining step (*rds*):

$$O_{2,ads} + H^+ + e^- \rightarrow (O_2H)_{ads} \tag{7.1}$$

Damjanovic and co-workers have determined that the surface coverage of oxide species is a function of pH and potential [210]. The Temkin isotherm was shown to be suitable for describing the surface coverage at low current densities (c.d.). The resulting theoretical rate equation described the experimental data well:

$$i = k_l n F p_{O_2} c_{H^+}^{3/2} \exp\left(\frac{-FE}{RT}\right) \tag{7.2}$$

where it has been assumed that $\alpha_a + \alpha_c = 1$. Note that the reaction order with respect to protons is 1.5, and that the Tafel slope is -60 mV/dec. despite the first step being the *rds* (one would then normally expect this to be -120 mV/dec.). At high c.d. the adsorption isotherm for oxygen species was found to be better described by the Langmuir isotherm resulting in the following rate equation consistent with experimental data:

$$i = k_h n F p_{O_2} c_{H^+} \exp\left(\frac{-\alpha_c FE}{RT}\right) \tag{7.3}$$

The reaction order of protons at high c.d. is 1, and the Tafel slope is -120 mV/dec.

7.2.2 ORR Mechanism on Oxide Covered Platinum

Also on oxide covered Pt two Tafel slopes are found; -60 mV/dec. at low c.d. and -120 mV/dec. at high c.d. The reaction order of protons is 1 in both cases in contrast to what is observed on oxide free Pt [210]. Birss and Damjanovic [216] found the ORR mechanism to be the same as that on iridium. One important difference compared to iridium is that the ORR rate on oxide covered Pt is strongly dependent on the thickness of the oxide because it is an insulator and electrons have to tunnel through the Pt oxides. Iridium oxides have much better electronic conductivity [210].

7.2.3 ORR in PEMFC

Only a few papers dealing with ORR in (PEM)FC are discussed here. Direct measurements of ORR in FCs are difficult because many factors can influence the results. However, combinations of experimental Electrochemical Im-

pedeance Spectroscopy (EIS) data and modelling efforts have provided useful insight into the cathode processes like charge transfer reactions, proton conductivity in the active layer, gas diffusion in the Gas Diffusion Layer (GDL) and importance of humidity and water transport in the membrane [123, 217].

One alternative measurement technique that has gained popularity is to cover a Rotating Disk Electrode (RDE) with a thin film of recast ionomer [218–223]. The advantage with these filmed electrodes is that it is easier to have control over the parameters in the system. Pt behaves similarly to the catalyst in an FC because it is in contact with the ionomer and not the bulk electrolyte. However, there are many complications with this method such as:

- Pin-holes in the ionomer film
- Uneven film thickness. This is minimized by spin coating the ionomer film on the electrode [219–223].
- Sorption of electrolyte anions in the membrane. It has been shown that f. ex. chloride ions affect the ORR severly in even very small concentrations [224]. The rate of the ORR is also lower in sulfuric acid compared to ORR in perchloric acid. However, the effect of (hydrogen) sulfate is much less than that of chlorides [224]. Anions are probably present at the electrode surface because the CVs obtained from these filmed electrodes share the same characteristics as the bare electrode exposed to the same acid [219]. In particular, the very characteristic hydrogen adsorption/desorption peaks at approximately 0.25 V_{RHE} on poly-crystalline Pt in sulfuric acid, related to co-adsorption of hydrogen sulfate [208], is also noticed on the Nafion® filmed electrodes exposed to sulfuric acid [219–223]. The CV of Pt in the hydrogen adsorption/desorption region when exposed to a Nafion® membrane with no external electrolyte, is less sharp and lacks the peak mentioned above [225].
- Surface roughness of Pt electrode. To enhance adhesion of the Nafion® film to the electrode, some researchers have polished their electrodes with relatively coarse #400–#600 emery paper [218, 220–223]. The abrasive particles are typically 15-20 μm so the surface roughness of the electrode is significant compared to the thickness of the typically 10 μm Nafion® film used. The assumption of a planar diffusion field in the ionomer film is thus not fulfilled.

- Complications in the analysis of the data because both the liquid electrolyte as well as the film impedes mass transfer [226, 227]. The simplified treatment of diffusion in the Nafion® film as semi-infinite has been shown to be inaccurate by Diard *et al.* [226, 227], at least for thin films/slow sweep rates.

- The kinetic current may not be extracted from the current data by extrapolation of RDE data to infinite rotation speed using the Koutechy-Levic relation. For a bare electrode the kinetic current may be found from the intercept of $1/i$ vs. $1/\sqrt{\omega}$. The mass transfer inside the ionomer is unaffected by rotation rate and only indirectly affected through the effect of rotation rate on the oxygen concentration on the electrolyte|ionomer interface. Thus, only the difference in kinetic current between a contaminated film and a pure film can be measured at high c.d. [220–223]. The difference can also be measured at very low overpotentials where the effect of diffusion is negligible [220–223].

Alternatively to a thin film of ionomer covering a Pt electrode, a thin layer of catalyst ink (mixture of carbon supported catalyst with ionomer and solvents like water and alcohol, see Section 8.3.1) can be deposited on a carbon electrode [224, 228–230]. In this case, one can use carbon supported Pt catalysts more similar to the real FC catalyst. However, the catalyst layer is directly exposed to the electrolyte so that influence of anions in the solution is even more likely than in the filmed RDEs. Use of f. ex. perchloric acid would reduce the problem because perchlorate adsorbs poorly on Pt surfaces [224].

Microelectrodes contacting a Nafion® membrane have been used to overcome potential problems with pin-holes and anion adsorption associated with filmed electrodes [105, 225, 231]. Humidity control can be a problem in these experiments [105]. The Reference Electrode (RE) used in these experiments is usually the Dynamic Hydrogen Electrode (DHE) where a small current is passed between two Pt electrodes so that water electrolysis is achieved. The hydrogen evolving electrode is taken as the reference, and it usually has 10–20 mV lower potential than the RHE. The DHE has been observed to shift slightly with the partial pressure of oxygen in the cell [105].

7.2.4 Influence of Cations on PEMFC Performance

Okada and co-workers have studied the influence of cations on membrane properties (water content conductivity, water diffusion etc.) [107, 111, 115]. The

influence of various cations on ORR on filmed Pt electrodes has also been studied [220–223]. They found that cations such as sodium, potassium, calcium, iron, nickel, and copper affected ORR on Nafion® filmed electrodes at low concentrations (0.1% of the sulfuric acid concentration in the external electrolyte). The different ions had different effects on ORR; higher valency ions had a more pronounced effect than the alkali metals ions. The poisoning effect gradually increased over several days before a steady state was reached.

Antoine *et al.* [229] used a half cell with a GDL and a cathode catalyst layer on one side of a Nafion® membrane with the other side of the membrane exposed to a liquid electrolyte. The electrolyte was then contaminated with sodium so that the concentration of protons in Nafion® was 1/3 of the pure proton form. At low c.d., the rate of ORR was 1/4 of that in pure acid in line with the Damjanovic mechanism; Equation 7.2 predicts a reaction order of 1.5 for protons. At high c.d., the ORR rate was 1/2 of that the pure acid. A rate of 1/3 was expected from Equation 7.3 where the reaction order of protons is unity.

7.2.5 Objectives with this Study

Our aim is to determine if ammonium influences the ORR in acidic solutions. Two different studies have been published where it is clearly demonstrated that ammonia has a negative effect on PEMFC performance [20, 21]. Both these studies concluded that the major poisoning effect of ammonia was on the anode. However, studies of PAFCs have revealed that there is a significant effect of ammonium on ORR [25].

A standard RDE with no ionomer film was used in this study. This allows us to study the specific effect of ammonium on pure platinum in a sulfuric acid solution where we have good control over all experimental parameters. The main conclusions of these studies should be applicable to the PEMFC, although the effect may be somewhat different in real PEMFCs operation where the anion is obviously different.

7.3 Experimental

An RDE set-up from Pine Instruments (AFMSRX rotator) was used. The cell was controlled by a Solartron 1287/1255B set-up which in turn was controlled by a PC. Measurements were performed in a standard electrochemical cell with

three separate compartments for the RE, Counter electrode (CE) and Working Electrode (WE). The WE had a geometric area of 0.164 cm^2, and was polished with 0.05 μm alumina abrasive powder. The real surface area of the electrode was established from hydrogen adsorption measured in pure acid assuming a monolayer charge of 210 $\mu C/cm^2$. The roughness factor was 1.55.

All glassware used was thoroughly washed and then treated in a hot solution of 5–10 wt% H_2O_2 in 0.5 M sulfuric acid to further clean the glassware. The equipment was then rinsed with purified water from a MilliPore Academique system (18.2 MΩcm). The WE was cleaned by repeatedly sweeping the potential between 0.02 and 1.5 V_{RHE} at 200 mV/s. The RE used in all experiments was a Reversible Hydrogen Electrode (RHE) as described in Section 6.3. The High Frequency Resistance (HFR) was measured, and the polarization data were corrected for the ohmic drop.

Sulfuric acid solutions (Trace Select, Fluka) were used as the base electrolyte. The solutions were made directly in the cell to minimize contamination. Based on the amount of purified water and the specified concentration of the pure concentrated acid, acid was added by weight to the cell to give 0.100 M solutions. The pure acid solution was then used for a set of experiments including ORR measurements to check for reproducibility. NH_4OH or KOH (both TraceSelect from Fluka) was then added by weight as needed. Usually pure sulfuric acid was also added to the solution at the same time to keep the pH constant. The pH and ionic strengths of the different solutions are estimated in Appendix C. The electrolyte was deaerated with N_2 (99.999%, AGA) bubbling for about 20 minutes. 50 mV/s cyclic voltametry scans at 300 rpm were performed with each solution to check for purity. All measurements were performed at room temperature, about 22 °C.

Measurements with deaerated solution were then made for use in subsequent data analysis. It is assumed that the double layer and Pt oxidation/reduction behavior is the same in O_2 and N_2 saturated solutions. Thus, the current associated with ORR can be found by subtracting the blank nitrogen CV from the Linear Sweep Voltammetry (LSV) measured in the presence of oxygen. It has been observed that Pt oxide formation is higher in the presence of oxygen than in deaerated electrolyte [232, 233]. However, in our case we have an additional effect of ammonium oxidation and adsorption in deaerated solution, see Chapter 6, which makes it more important to correct for the background.

After the measurements in blank solution were completed, the solution

was saturated with O_2 (99.999%, AGA) and the ORR experiments performed. The electrode was first cleaned by repeated potential cycling between 0.02 and 1.5 V_{RHE}. The potential was held for 20 s at 0.2 V or 1.1 V_{RHE} to study ORR on oxide free or oxide covered surfaces respectively. LSV at various rotation and sweep speeds was used to establish the Tafel slope. Positive going scans were recorded at different sweep rates (5–200 mV/s); negative going sweeps only at 50 mV/s. In the latter case, the Pt surface is (partially) covered by oxides according to Damjanovic [210]. Oxygen reduction on oxide covered Pt surfaces is slower than on metallic Pt. The only way to obtain the kinetic Tafel parameters when working with oxide covered Pt, is by using fast sweep rates.

The mass transfer limiting current on an RDE is given by the Levich equation [187]:

$$i_d = 0.62nFD^{2/3}\nu^{-1/6}c^b\omega^{1/2} \tag{7.4}$$

where i_d is the mass transfer limiting current, n is the total number of electrons transferred, F is Faraday's constant, D is the diffusivity of the electroactive species, ν is the kinematic viscosity of the solution, c^b is the bulk concentration of the electroactive species, and ω is the angular rotation rate. In the following the rotation rate ω_{rpm} is given in rpm; the relation between the two is $\omega=(2\pi/60)\cdot\omega_{rpm}$.

Corrections for mass transfer limitations were applied as given in Equation 7.5 to find the kinetic current, i_k. This equation is easily derived by assuming that i_k and i_d operates in series ($1/i=1/i_k+1/i_d$) [158].

$$i_k = \frac{ii_d}{i_d - i} \tag{7.5}$$

The reported c.d. is based on the real surface area unless otherwise stated. At low c.d. this is the appropriate surface area to use. As mass transfer limitations become more pronounced, the geometric surface area is actually the area that should be used because the diffusion layer is planar (the roughness of the surface is small compared to the thickness of the diffusion layer at the electrode). In the determination of Tafel parameters, the real surface is used because the current then is corrected for mass transfer limitations as per Equation 7.5.

It is well known that the c.d. is homogeneous for an RDE in the mass transfer limiting case [187]. When the current is lower than the mass transfer

limiting current, but still appreciable, the c.d. is not homogeneous. This has implications on the kinetic parameters determined from RDE experiments [234, 235]. We have not corrected our data for these effects. However, the RE was placed relatively far away from the WE so that less distortion of the kinetic parameters is expected [235].

7.4 Results and Discussion

7.4.1 Verification of Mass Transfer Controll

The limiting current at 0.25 V_{RHE} was measured for different rotation rates and plotted according to the Levich equation (Equation 7.4) in Figure 7.1. The c.d. was found using the geometric area. As seen from this Figure, the measurements follow the Levich equation well although there is a small non-zero intercept. However, the conclusion is that the reaction rate is mass transfer controlled at low potentials. The difference in the slope of the lines indicates that there is a difference in either D_{O_2}, $c^b_{O_2}$ or both between the two solutions as discussed below.

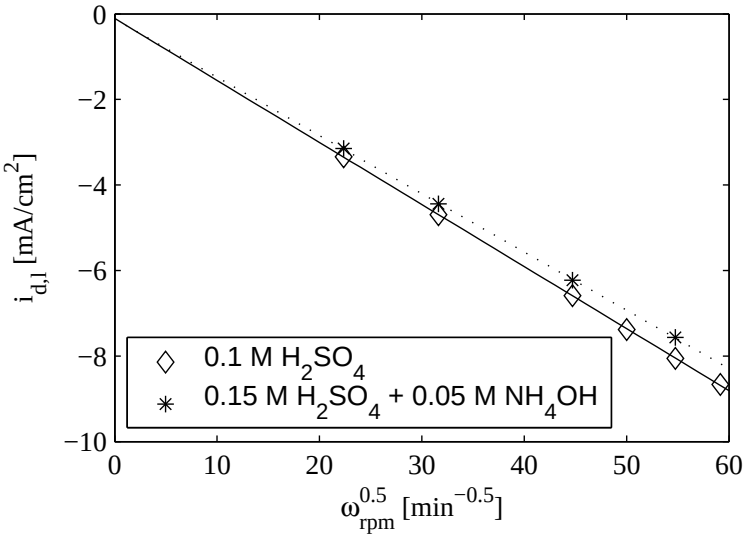

Figure 7.1: Mass transfer limiting current for the ORR as function of rotation rate.

7.4.2 Effect of Ammonium on ORR

The $E - i$ relations for different electrolytes containing ammonium and potassium as well as pure acid are shown in Figure 7.2. The data were measured in a positive going scan from high to low c.d., *i.e.* at oxide free Pt. The acid concentration was increased as more ammonia solution was added to keep the pH essentially unchanged. We note that there is a large effect of ammonium on the ORR rate at a given potential. There is also an effect of additions of KOH to the solution in contrast to the data reported by Okada *et al.* [220]. They found that potassium did not affect ORR on Pt in acidic solution, but there was a significant effect of potassium on Pt electrodes covered with a Nafion® film.

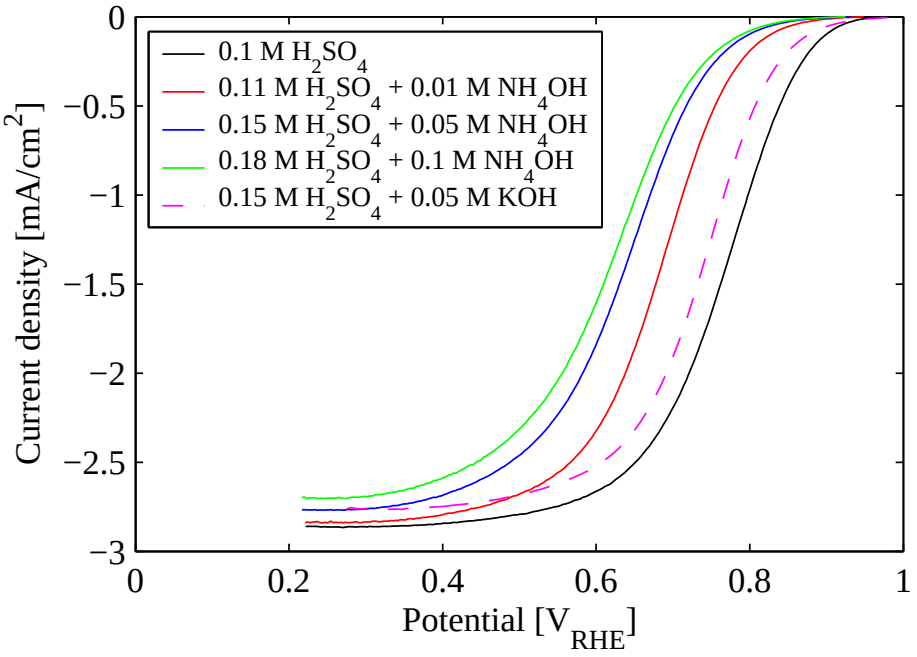

Figure 7.2: Relationship between cell potential and ORR current for different concentrations of ammonium in the solution. The pH was kept constant at 1.0, and data were measured at a sweep rate of 5 mV/s and a rotation rate of 1000 rpm.

The second thing to notice is that the limiting current is dependent on the electrolyte composition. This means that the diffusivity or concentration of oxygen changes with electrolyte composition as was also noted in the Levich plot in Figure 7.1. We computed the ionic strength, $I = 1/2 \sum_i c_i z_i^2$, of the solutions based on the following simplifications: *1)* The first dissociation step of sulfuric acid is complete. *2)* Only ammonium is present in the solution (pK_a of NH_4^+ is 9.24 [78]). *3)* The pK_a of hydrogen sulfate is 1.99 [78]. The logarithm of the ratio between the observed current and the current in pure acid is a linear function of the ionic strength of the solution as seen in Figure 7.3. According to Harned and Owen [236], the logarithm of the solubility of gases is expected to be linearly dependent on the ionic strength. The mass transfer limiting current is linear in the concentration of oxygen in the bulk solution, see Equation 7.4. The observed effect of composition on the limiting current is thus more likely due to differences in bulk concentration of oxygen than diffusivity.

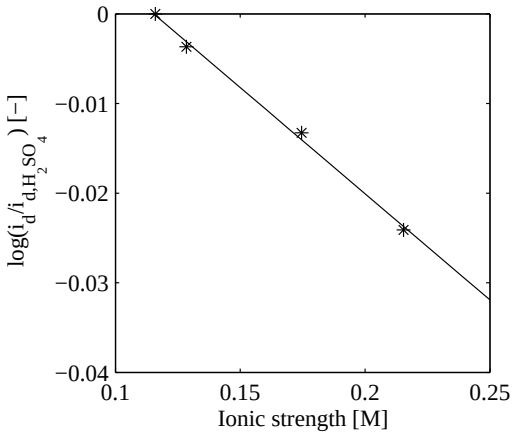

Figure 7.3: Relative limiting c.d. as function of ionic strength of the electrolyte.

7.4.3 Differences between Oxidized and Reduced Pt

The difference between oxidized and reduced Pt is shown in Figure 7.4, and is especially noticeable in the presence of ammonium. There are minor differences also in pure acid. These differences are most noticeable at potentials above

0.75 V_{RHE}. The differences in the pure acid are clearer in the Tafel slope analysis given in the following section.

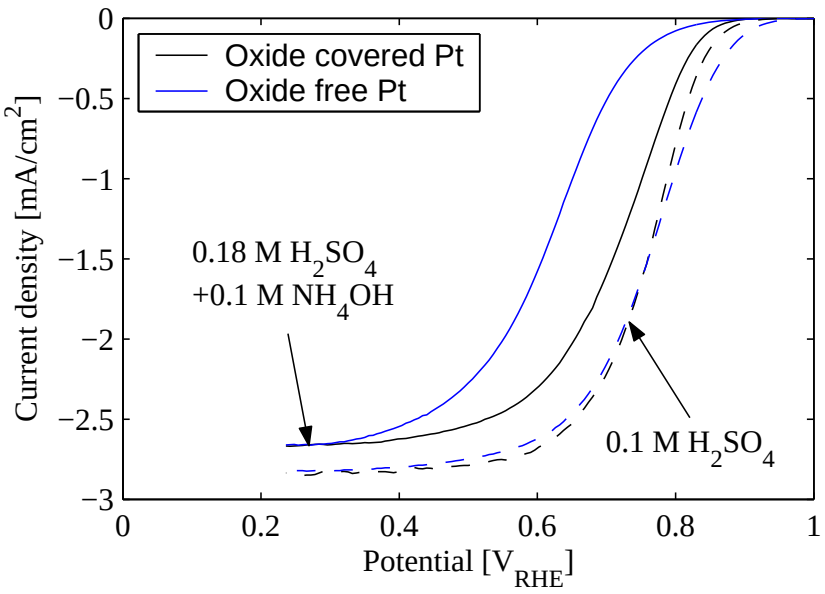

Figure 7.4: LSV scans of oxide covered Pt (negative going sweep at 50 mV/s) and oxide free Pt (positive going sweep at 5 mV/s) in pure acid (- -) and acid containing 0.1 M NH_4OH (—).

7.4.4 Tafel Analysis

The ORR data shown in Figure 7.2 were corrected for the mass transfer limitations according to Equation 7.5. The current measured in the deaerated solution was subtracted from the current measured in the oxygen saturated solution. Measurements were performed on both oxide free and oxidized Pt electrodes. The Tafel plots are shown in Figures 7.5 and 7.6 respectively.Only a few of the measurement points are shown for clarity.

From Figure 7.5 and Table 7.1 we note that the Tafel slope on oxide free Pt is essentially the same at high c.d. At low c.d., the Tafel slope in the presence of ammonium is about 90 mV/dec. compared to about 60 mV/dec. in pure acid.

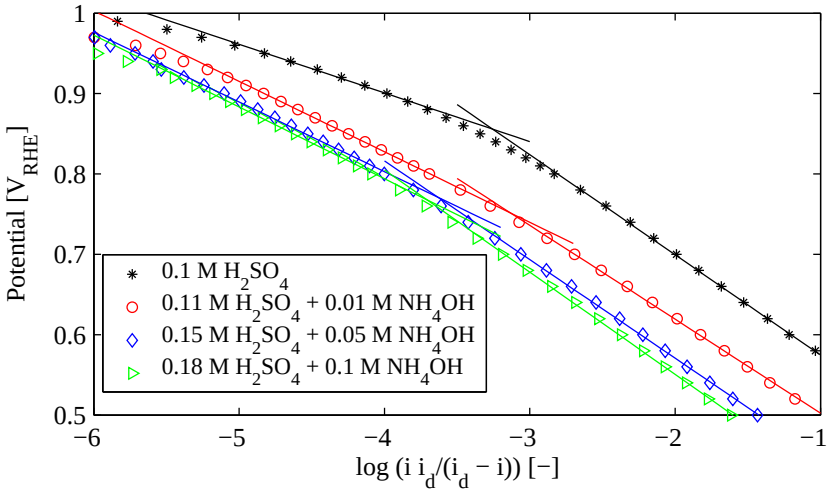

Figure 7.5: Tafel plot of ORR on oxide free Pt corrected for mass transfer limitations and IR corrected cell potential for electrolytes with different ammonium content but constant pH. Oxide free Pt surface, 20 s at 0.2 V_{RHE} before sweeping at 5 mV/s positive going, room temperature.

Table 7.1: Tafel slopes for ORR on Pt in sulfuric acid electrolytes containing various concentrations of ammonium.

Electrolyte	low c.d. mV/dec.	high c.d. mV/dec.
Oxide free Pt		
0.1 M H_2SO_4	-61	-125
0.11 M H_2SO_4 + 0.01 M NH_4OH	-88	-117
0.15 M H_2SO_4 + 0.05 M NH_4OH	-87	-123
0.18 M H_2SO_4 + 0.1 M NH_4OH	-89	-127
Oxide covered Pt		
0.1 M H_2SO_4	-57	-147
0.11 M H_2SO_4 + 0.01 M NH_4OH	-56	-151
0.15 M H_2SO_4 + 0.05 M NH_4OH	-54	-162
0.18 M H_2SO_4 + 0.1 M NH_4OH	-54	-165

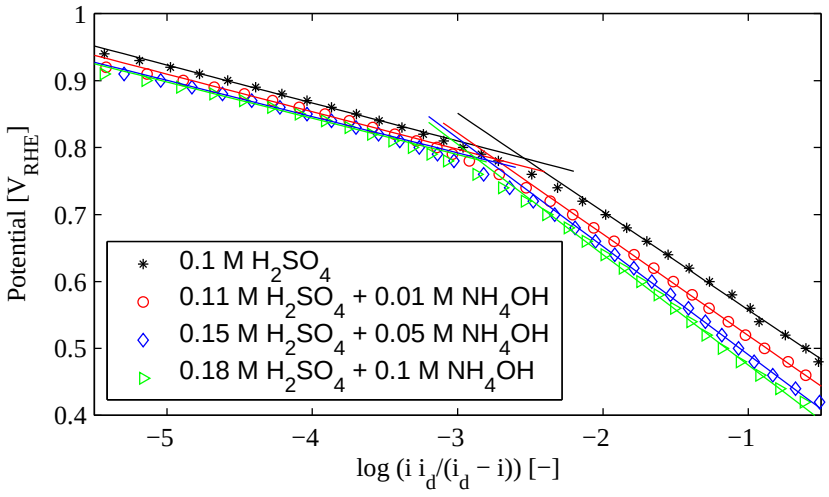

Figure 7.6: Tafel plot of ORR on oxide covered Pt corrected for mass transfer limitations and IR corrected cell potential for electrolytes with different ammonium content but constant pH. Oxide covered Pt surface, 20 s at 1.1 V_{RHE} before sweeping in the negative going at 50 mV/s, room temperature.

The Tafel slope at low c.d. for oxide covered Pt is approximately the same, 55 mV/dec., for all the electrolytes studied. On pre-oxidized Pt at high c.d. there is a slightly higher Tafel slope in the ammonium containing electrolytes, but the differences between the different electrolytes are not significant taking the uncertainty of the Tafel slope fitting procedure into account. At 0.5 V_{RHE} the current is about 98% of the limiting current for the pure acid which makes the calculated kinetic current, i_k, which is based on the correction given in Equation 7.5, very sensitive to i_d. The uncertainty of the Tafel slopes at high c.d. is therefore larger than can be inferred from the Tafel plots in Figures 7.5 and 7.6 alone.

There is a difference in Tafel slope at high c.d. between oxide covered, or rather pre-oxidized Pt, and oxide free Pt or pre-reduced Pt. Zecevic *et al.* [219] observed a Tafel slope of -135 mV/dec in 0.1 M $HClO_4$ on pre-oxidized Pt. In contrast to this and our findings, Birss and Damjanovic [216] found a Tafel slope of -120 mV/dec. in 2 N H_2SO_4.

The exchange c.d., i_0, was found by extrapolation of the Tafel curve to the

reversible potential of the ORR (1.229 V_{RHE}). i_0 was about 10^{-9} A/cm^2 on oxide free Pt and 10^{-11} A/cm^2 on oxide covered Pt in the low c.d. region. i_0 was lower for higher ammonium concentrations on both surfaces. However, the determination of i_0 is very uncertain because the Tafel slope must be extrapolated several hundreds of mVs. A small error in the slope thus has a large impact on the calculated i_0. In the high c.d. region, i_0, a pure fitting parameter in this case, was dependent on ammonium concentration for oxide free Pt but essentially independent of ammonium concentration on oxide covered Pt.

The reaction order of ammonium in the ORR is defined by:

$$p_{NH_4^+} = \left. \frac{\partial \log i_k}{\partial \log c_{NH_4^+}} \right|_{E,c_i} \tag{7.6}$$

The *apparent* reaction order of ammonium was found to be -0.4 to -0.5 for oxide free Pt and about -0.15 to -0.2 for oxide covered Pt varying slightly with the cell potential. However, not only the ammonium concentration varies in these experiments, but also the concentration of (hydrogen) sulfate. These reaction orders are thus only approximate.

Positive going scans of an oxide free Pt electrodes were performed at several sweep rates both in pure acid and with ammonium present. The results are given in Figure 7.7. There is a small effect in the pure acid solution which is possibly due to a slight contamination of the electrode from the electrolyte. Conditioning of the electrode at 0.2 V followed by a sweep at 5 mV/s takes about 3 minutes compared to only 30 seconds when sweeping at 100 mV/s. There is a much larger effect of sweep rate on the ORR kinetics in the ammonium containing electrolyte. This indicates the the process responsible for the reduced ORR kinetics in the ammonium containing electrolyte is relatively slow.

7.4.5 Effect of Ammonium on ORR

We have observed a very large effect of ammonium on the rate of ORR, especially for oxide-free Pt, *i.e.*, in positive going sweeps. The effect of ammonium on ORR on oxide covered Pt was much smaller. In Chapter 6 we observed that ammonium also affects Pt in deaerated solution. The effects in the hydrogen desorption and the double layer region on oxide free Pt in positive going sweeps in deaerated solution were small, but noticeable when oxide started to form and also in the negative going sweep. It is not clear why the effect of

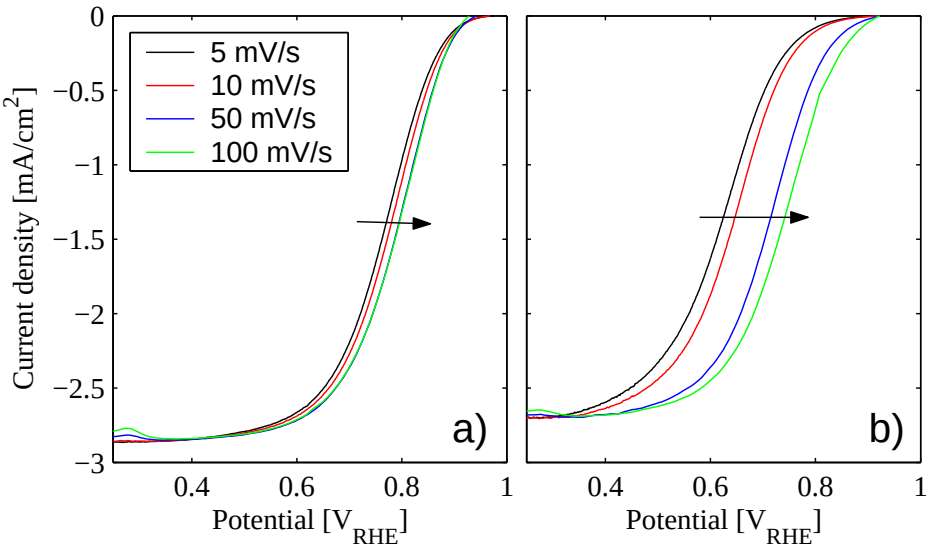

Figure 7.7: ORR c.d. as function of sweep rate at a rotation rate of 1000 rpm. (a) pure 0.1 M sulfuric acid, (b) 0.18 M H_2SO_4 + 0.1 M NH_4OH. Data were IR corrected, but not corrected for background in deaerated solutions.

ammonium in oxygen saturated and the deaerated solutions are seemingly so different. Nor is it clear which species that are responsible for the reduced ORR rate. It could be that presence of oxygen changes the potential at which the different species are formed and removed. Paik *et al.* [233] found that the rate of formation of Pt oxides was dependent on oxygen concentration, and that nearly a full monolayer could be formed even at 0.85 V_{RHE} in pure oxygen. However, further studies are needed to clarify the effect of oxygen in the solution on formation of contaminant species from ammonium.

The effect of ammonium and quarternary ammonium salts (NR_4^+ where R=C_nH_{2n+1}, n=1–4) on ORR on Nafion® covered Pt electrodes in sulfuric acid was studied by Okada *et al.* [223]. Okada *et al.* found that salts with $n \leq 2$ behaved differently from salts with $n \geq 3$. The effect of the heavier cations was more immediate and also more severe. The solubility and diffusivity of oxygen was also affected. For $n \leq 2$, the solubility was affected more than the diffusivity and *vice versa* for $n \geq 3$. The effect of ammonium on the kinetic

ORR current [223] was *smaller* than the effect of Na^+ and K^+ [220] in contrast to our findings on the bare Pt electrode.

Okada and co-workers reported that there was no effect of ammonium salts or other cations on ORR on electrodes not covered with ionomer [220–223]. This lead them to the conclusion that the observed reduction in ORR activity was due to an interaction between the cations and the ionomer on the Pt|ionomer interface. Lower proton concentration, which according to Equations 7.2 and 7.3 would lead to lower ORR rate, was not found to be sufficient to explain the experimental observations. Oxygen solubility and diffusivity was smaller in the presence of the contaminants. Okada and co-workers argue that the reduction in solubility and diffusivity can not explain the lower kinetic current. This argument seems strange since the effect of solubility and diffusivity is supposedly factored out in the analysis yielding the kinetic current.

Okada and co-workers [220–223] also observed that it took a long time to reach a steadystate for the rate of ORR after additions of a contaminant. This was taken as an indication that a reorientation of the ionomer was involved. The anionic sites in the ionomer has limited flexibility because they are fixed on a polymer backbone. Therefore, effects of impurity ions on the thickness of the diffuse electric double layer may be different in the ionomer than in solution, referred to as "restricted double layer" [237]. Okada *et al.* [222] suggest that the monovalent contaminant ions are more strongly bond to the sulfonic acid group thus increasing the thickness of the diffuse double layer. This in turn decreases the electric field gradient close to the electrode so that the rate of ORR would decrease (the Frumkin effect [189]). However, with multivalent ions, the thickness of the double layer would decrease increasing the electric field gradient. This should then, applying the same arguments, lead to an *increased* ORR rate in the presence of multivalent ions in contradiction to experimental observations. Okada *et al.* do not discuss this matter, and the proposed model seems to be deficient. Further, the argument that the slow response in ORR rate to contamination must be due to a reorientation of the ionmer phase is not necessarily valid. It is know that water content is dependent on the ionic form and structure of Nafion®. If we take the rate of water sorption/desorption to be an indication of reorientation of the ionomer, it is known that water sorption into a dry membrane from liquid water is complete within a few minutes [106]. Also water sorption/desorption from thin, recast Nafion® films is complete within minutes [238]. Water exchange caused by change in ionic composition is also complete within a few minutes [239], as is the actual ion exchange process itself [240].

7.5 Conclusions

The effect of ammonium, even in moderate quantities, on ORR is significant. There is also a slight effect of potassium on the rate of ORR, but much smaller than the effect of ammonium. ORR on the oxide-free Pt surface is more affected by ammonium than ORR on oxide covered Pt. The Tafel slope at low c.d. on oxide-free Pt is about 90 mV/dec. in the presence of ammonium compared to about 60 mV/dec. in pure acid. The Tafel slope of ORR on oxide-free Pt at high c.d. is the same in pure acid and with ammonium present. The exchange c.d. is also lower in the presence of ammonium. The Tafel slope of ORR on oxidized Pt surface in the low c.d. region is not significantly affected by ammonium. The Tafel slope of ORR at high c.d. was 150 to 160 mV/dec. on oxidized Pt, somewhat higher than on oxide-free Pt (about 120 mV/dec.). The exhange c.d. is lower for the ammonium containing electrolyte also in this case. The apparent reaction order of ammonium in the ORR is -0.4 to -0.5 on the oxide-free Pt and -0.15 to -0.2 on the oxide covered Pt. The origin of the loss of ORR activity has not been established.

Chapter 8

Effect of Ammonia on PEMFC Performance

8.1 Summary

The effect of ammonia on Polymer Electrolyte Membrane Fuel Cells (PEMFC) was tested by addition of 10 ppm NH_3 to the hydrogen feed to PEMFCs based on GORE™ PRIMEA® Membrane Electrode Assemblies (MEAs). There was a significant loss in performance of the FCs. The poisoning process was slow taking 24 hours or more to reach a steady state. In some cases no steady state was reached during the experiment. The performance loss was in most cases reversible, but only after operation on neat hydrogen for several days. Additions of 1 ppm NH_3 for one week also resulted in significant performance losses. An MEA based on carbon supported Pt catalyst did not differ from the GORE™ MEA which uses a PtRu based anode catalyst. The performance losses were higher than could be explained by the observed increase in ohmic resistance in the cell. There was also a significant decay in performance in a symmetrical $H_2|H_2$ cell, especially at high current density (c.d.) where a reaction limiting current was observed. The reaction limiting current is consistent with the Tafel step in a Tafel-Volmer HOR mechanism. There is also a significant effect of ammonium on the Oxygen Reduction Reaction (ORR) on the cathode. This effect is dominant at lower c.d., but at higher c.d., the reaction limiting current of the HOR becomes the most important limitation of the cell.

8.2 Introduction

Ammonia can be used as a hydrogen carrier for PEMFC, see Chapter 2 for more details. In order to use ammonia in PEMFC, it has to be split to nitrogen and hydrogen. Traces of ammonia will be present in the hydrogen rich fuel stream [18]. Further, ammonia as such is an interesting contaminant in PEMFC even if ammonia is not used as a hydrogen carrier. Ammonia may be formed in fuel reforming processes at levels up to 150 ppm [15] especially if the reforming involves homogeneous precombustion with air, or if the fuel itself contains nitrogen containing species [16]. Ammonia may also be present in ambient air as such. There has also been reports that AB_5 metal hydride alloys used for hydrogen storage has a catalytic effect on the formation of ammonia from mixtures of hydrogen and nitrogen [17]. Ammonia may thus be present also in hydrogen from metal hydride storages if there is nitrogen in the hydrogen used to fill the metal hydride storage.

To our knowledge, only two different research groups have published papers regarding ammonia in PEMFC [19–21]. The focus of Uribe *et al.* [19, 20] and Soto *et al.* [21] was to study poisoning of cells in operation and recovery after exposure to ammonia. The poisoning mechanism has only partly been identified.

Uribe *et al.* found that the cell resistance, as measured by HFR, more than doubled when the cell was exposed to 30 ppm ammonia for 15 hours. They used MEAs containing 0.15–0.20 mg Pt/cm^2 catalyst on either electrode. The cell resistance started to increase when the cell had been exposed to ammonia for more than 1 hour. Exposure to 30 ppm ammonia for about 1 hour resulted in performance[1] losses which were recoverable in about 18 hours. Extended exposure to 30 ppm NH_3 for 17 hours was not fully recoverable within 4 days of operation on neat hydrogen. Cyclic Voltammetry (CV) did not indicate any adsorbed contaminants, that were electrochemically detectable, to be present neither on the anode nor the cathode. The increase in ohmic cell resistance was not by itself sufficient to explain the performance loss observed. Uribe *et al.* thus suggested that the observed losses were due to loss of proton conductivity in the anode.

Soto *et al.* used a Gore™ PRIMEA® series 5621 MEA with 0.45 mg PtRu/cm^2 anode catalyst and 0.6 mg Pt/cm^2 cathode catalyst. The cell resis-

[1] By *performance* we shall mean either the current density or the cell potential depending on if the cell is operating in potentiostatic or galvanostatic mode respectively.

tance was monitored by an automated current interrupt technique. Exposure to 200 ppm NH_3 for 10 hours increased the measured cell resistance by about 35%, much less than observed by Uribe *et al.* who used lower concentration of ammonia. The increase in resistance observed by Soto *et al.* [21] could only explain about 10% of the performance loss. CVs recorded on the anode did not reveal any electrochemically active species. During poisoning of the cell, Soto *et al.* observed that the cell resistance increased immediately when NH_3 was added and also showed apparently two regions of increase corresponding to two processes with different time constants. The performance decreased apparently as a first order process. When operating on neat hydrogen, the performance showed two regions of recovery whereas the resistance followed a first order response, *i.e.*, the opposite of what was observed during poisoning of the cell. Soto *et al.*, similarly to Uribe *et al.*, suggested that ammonium interfered primarily with the anode. No detailed hypothesis regarding poisoning mechanism was suggested.

Another relevant study of the effect of ammonia on acidic FCs was made by Szymanski *et al.* [25]. Their study concerned how Phosphoric Acid Fuel Cells (PAFC), operating at 191 °C, were affected by ammonia. They found that the ORR occurring at the cathode was the process that was most noticeably affected by ammonia. At 1% conversion of the phosphoric acid to $(NH_4)H_2PO_4$, 84 % of the cathode activity was lost. They also found a significant ability of the cell to oxidize ammonium, presumably to nitrogen, especially at high cathode potentials.

In this Thesis, different aspects of how ammonia and ammonium may affect PEMFC performance was discussed in the Introduction of the Thesis, see Chapter 1.3. So far effects of ammonia on single components (in particular the membrane, Chapter 3) and processes (ORR in Chapter 7 and oxidation of ammonium in acidic solution in Chapter 6) has been discussed in this Thesis. Results of FC testing with additions of ammonia to the cell are given in the present Chapter and interpreted in the light of the findings of previous Chapters.

8.3 Experimental

8.3.1 Preparation of Membrane Electrode Assemblies

MEAs from W. L. Gore & Associates (PRIMEA® 5561 with Pt/Ru anode (0.45 mg/cm^2) and a Pt cathode (0.4 mg/cm^2)) were used in most experiments. The commercial MEAs were used as received.

Nafion® based inks were prepared using a commercial 20% Pt on carbon catalyst from Alfa Æsar following a recipe described by Wilson *et al.* [241] with minor modifications as described below. Five parts of supported catalyst was sonicated for two minutes with two parts by solids Nafion® in form of a 5 wt% solution of Nafion® (Ion Power Inc.). Di-ethyleneglycol (DEG) (Merck *p.a.*), about 50% of the Nafion® solution weight, was added, and the ink further sonicated for two minutes. 1.3 times the stoichiometrically required quantity of Tetrabutylammoniumhydroxide (TBA-OH) solution in water (Merck) was added to convert the Nafion® in proton form to a more thermoplastic TBA form [241]. The ink was then stirred for several hours before isopropanol (Arcus, approximately the same volume as DEG) was added followed by further sonication.

Spraying of the ink onto Teflon® decals was done using an air-brush (Badger). After each spraying, the ink was dried in air in a forced convection oven at 150 °C. It was necessary to spray 3–4 times to obtain the required loading (0.35 mg Pt/cm^2). A Nafion® membrane, prepared as described in Section 3.3.1, but converted to the sodium form by immersion in 6 wt% NaOH solution over-night, was dried in a convection oven for two hours at 50 °C. The membrane was then sandwiched between two Teflon decals, and hot-pressed using a stainless steel die. The MEA was first pressed at 100 °C and 10 MPa for five minutes. The temperature and pressure was then ramped up to 200 °C and 20 MPa respectively applying these conditions for three minutes. The MEA was then cooled down and converted to proton form by immersion in 90 °C 1 M H_2SO_4 for four hours. The acid solution was replaced once. The MEA was then rinsed with purified water and stored in purified water until used.

8.3.2 Testing of Fuel Cells

All gases used were 99.999% pure from AGA including synthetic air (79/21 N_2/O_2 mix). A special gas mix containing 104 ppm NH_3 (99.95%) by volume in 99.999% hydrogen was used for additions of ammonia to the system.

Gas Diffusion Layers (GDLs) from E-TEK Inc. (ELAT®, carbon only) were pressed gently onto the active layer of the MEA before it was mounted in the FC housing and tested. Two different cell housings were used in these experiments; one was 6.25 cm^2 (ElectroChem Inc.), and the other 10 cm^2 (in-house design). The 10 cm^2 cell was used in most experiments except were otherwise noted. The applied mechanical pressure on the MEA in the 10 cm^2 housing was controlled using a pneumatic piston and set to 1 MPa. The mechanical pressure applied in the 6.25 cm^2 cell housing can only be indirectly controlled by the torque when assembling the housing. A 120 cNm torque was used in this study. The cell housings and test stations are described in more detail in Appendix B. All experiments reported here were conducted at atmospheric pressure and with a cell temperature of approximately 40 °C. The gas humidifiers, described in more detail in Appendix B.2.1, were operated either at room temperature or at about 40 °C. Ammonia containing hydrogen was mixed with pure hydrogen downstream of the humidifiers to avoid absorption of ammonia in the water-filled humidifiers. The FC performance increased gradually during the first 2–4 days of operation, and all further experiments were only made after this initial period. Frequent polarization scans shortened the required time to reach stable performance. The performance of symmetrical cells typically stabilized in a few hours.

The cells were controlled using an Agilent 6050A load that may run both galvanostatically and potentiostatically. In order to achieve low cell voltages, a HP 6032A power supply was connected in series with the cell. A solid state relay was also connected in series to facilitate current interrupt measurements, see Sections B.2.3 and B.4 in Appendix B.

Most experiments were conducted in normal FC mode, that is, with a cell operating on hydrogen and synthetic air. In addition, some experiments with symmetrical cells with hydrogen on either side was performed to isolate the effect of ammonium on the anode performance (Hydrogen Oxidation Reaction, HOR).

Polarization curves were recorded automatically at preset intervals. The polarization curves were measured by first running the cell potentiostatically from a cell voltage of 0.2 V to open circuit. Longer holding times were used at high than at lower currents (2 minutes to 15 seconds). Current interrupt measurements were made simultaneously in order to correct the polarization curves for ohmic losses. The polarization scan design used for symmetrical cells was the same as described in Section 5.4.1.

8.4 Results

8.4.1 Stability of Fuel Cells

Relatively large problems with long-term stability of the FCs were encountered. Several possible reasons for these problems were identified:

- Much higher performance was observed if the stainless steel flow-fields were polished prior to use. This was believed to be due to passivation of the stainless steel, and a gold layer (3–5 μm) was applied to the flow-field. Ihonen *et al.* [242] also found that the contact resistance between stainless steel and the GDL could be substantial. However, pin-holes in the gold layer applied to the custom designed cell could increase corrosion of the stainless steel substrate. The gold layer was removed after some time.

- Another possible source of contaminants could be the humidifiers. The stainless steel humidifiers were thus heated to 400 °C, and then cleaned with a concentrated solution of KOH to remove organic and inorganic contaminants [243]. Also, humidifiers made out of glass were used in some of the tests.

- The air quality was also considered. Compressed air from an oil-less compressor approved for food industry was replaced with bottled air and later high-purity synthetic air.

- The operating temperature was also critical in order to get more stable performance. Cell temperatures higher than 40 °C usually gave problems with stability as did higher temperatures in the humidifiers. The operation temperature of the cell was thus kept at 40 °C even though this is low compared to normal operating temperatures used for PEMFC.

The reasons for the low stability were not clearly identified. However, all the above measures seemed to result in a satisfactory stability of the cell. It is not believed that the most severe stability problems were due to the MEA itself as testing in another, very similar test station described by Vie [164], gave better stability. Further, regular polarization scans seemed to help stability of the cell, see below for a further discussion of this.

8.4.2 Exposure of PEMFC to NH_3

A typical cell response to exposure to hydrogen containing 10 ppm NH_3 is showed in Figure 8.1. The cell was operated galvanostatically at 0.7 A/cm^2 and allowed to stabilize before 10 ppm NH_3 was added to the fuel gas for 24 hours. The ammonia addition was then turned off allowing the cell to recover. Three days after the addition of ammonia was stopped, the gas supply to the cell was stopped for a few hours letting the cell potential fall to 0 V. One day after this, several polarization scans with two hours interval were performed.

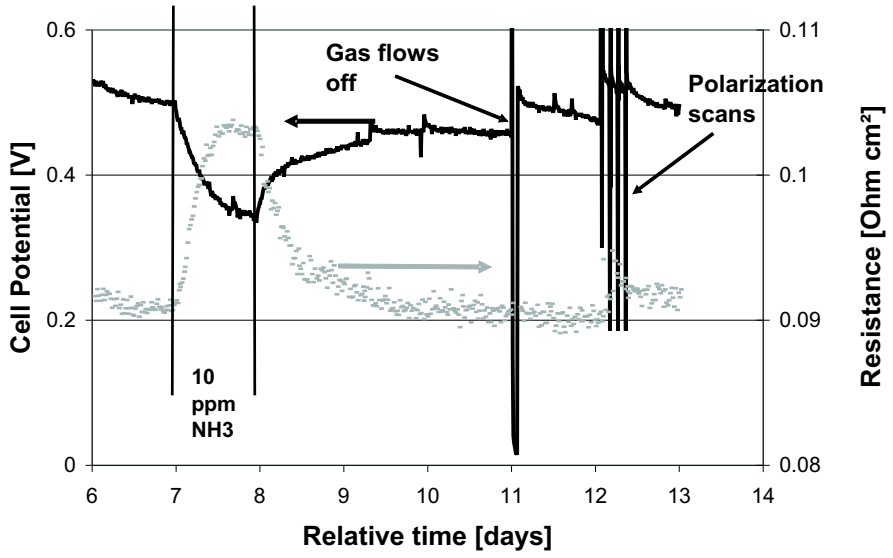

Figure 8.1: Performance of 10 cm^2 GORE™ MEA with addition of 10 ppm NH_3 for 24 hours. The cell was running galvanostatically at 0.7 A/cm^2 at 40 °C with humidification at 30 °C, 80% conversion on anode, 40% on cathode, 30 and 20 mlN/min minimum flow respectively. The data are not corrected for ohmic losses.

The first thing to notice in Figure 8.1, where the cell was run galvanostatically, is that the cell resistance increases when ammonia is added. The performance of the cell decreases, but it takes almost one day to reach a seemingly steady state for cell resistance and performance. The increase in cell resistance is only approximately 0.012 Ωcm^2 corresponding to an increase in ohmic losses

of about 8 mV. The observed drop in cell potential is about 160 mV so the increase in ohmic resistance can only explain about 5% of the total potential loss.

Measurements were also performed with other cells running potentistatically with regular scanning applied also during NH_3 poisoning. Typical transients observed during NH_3 poisoning are shown in Figure 8.2. The different regions shown in Figure 8.2 are:

1. Operation on pure hydrogen
2. Poisoning with 10 ppm NH_3 for four hours
3. Recovery period operating on pure hydrogen recording polarization curves every four hours
4. Poisoning with 10 ppm NH_3 for 26 hours
5. Recovery period operating on pure hydrogen recording polarization curves every four hours
6. Power failure. First a short power failure after which the cell was restarted followed by a longer power failure. Gas supply to the cell was interrupted in this period so that the cell potential dropped to 0 V. Note the significant recovery in performance after these events.
7. Operation on pure hydrogen after power failure

The increase in resistance shown in Figure 8.2, where the cell was run potentiostatically, is larger than the increase observed running in galvanostatic mode, see Figure 8.1. This was also observed in the cell with an MEA based on carbon supported Pt (not PtRu as in the Gore™ MEA), see Figure 8.4 which we shall revert to in more detail later. Further, the resistance does not seem to reach a steady state within the period NH_3 was added. The c.d. at 500 mV cell potential after 26 hours of contamination was 0.25 A/cm^2. The cell potential at the same c.d. in the cell before contamination was 0.731 mV, all potentials not corrected for ohmic losses. The increased ohmic resistance can explain about 36 mV of the total of 231 mV losses, or about 15 %. During the first poisoning, shown as region 2 in Figure 8.2, ohmic effects could explain 6 out of 74 mV change, or about 9%. The relative importance of increase in ohmic resistance is consistent with data reported by Soto *et al.* [21].

The performance of the cell shown in Figure 8.2 was higher after the second contamination than before the first NH_3 poisoning. There might be several

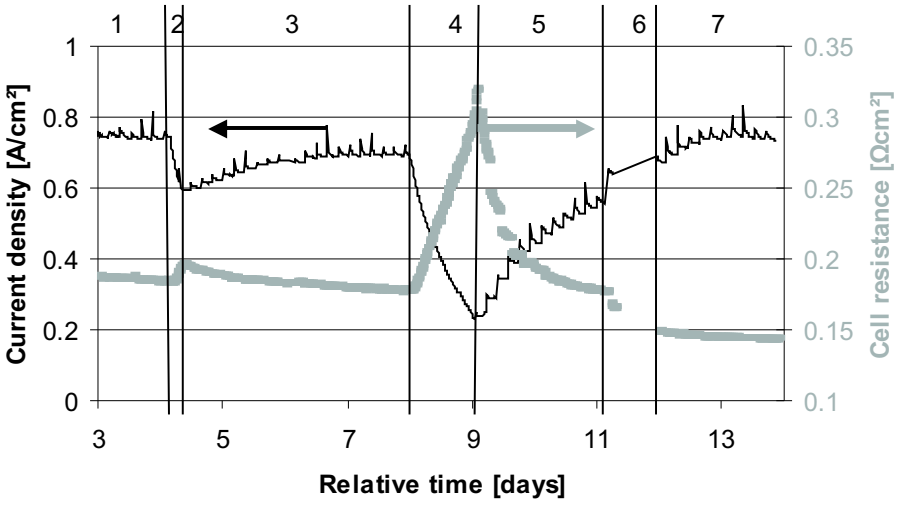

Figure 8.2: Performance of 10 cm^2 GORE™ MEA with addition of 10 ppm NH_3 for 4 and 26 hours (region 2 and 4 in the graph). The cell was running potentiostically at 0.50 V at 40 °C cell temperature, room temperature humidifiers, atmospheric pressure, 80% conversion of H_2, 40% conversion of O_2 in air, 50 mlN/min minimum flow on either side. The data are not corrected for ohmic losses. See the text for explanation of the different regions.

explanations for this. *1)* The cell resistance dropped markedly after the interruption of gas supply to a level much lower than before contamination started. The reason for this is not clarified. *2)* The cell had been running for more than a week before the second addition of ammonia was made. Thus, the cell had probably lost some performance before the ammonia addition that could have been recovered by interrupting the gases *before* additions of ammonia were made. *3)* Also, there might be a residual effect of the first addition of ammonia that was reversed when the gas supply was stopped.

Polarization curves were obtained both before and after poisoning of the FC, and after gas supply was temporarily stopped. Typical polarization curves are shown in Figure 8.3.

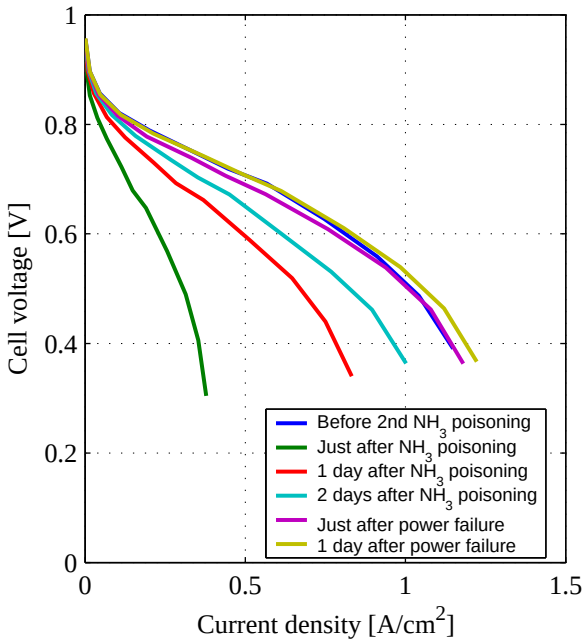

Figure 8.3: IR corrected polarization curves obtained before and after addition of 10 ppm NH_3 for 26 hours, see Figure 8.2. Conditions as in Figure 8.2. Potential scans were performed on a regular basis every four hours.

8.4.3 Effect of Anode Catalyst

An MEA with Pt as anode catalyst was also tested. The results of the testing are shown in Figure 8.4. The different regions of the graph are explained below:

1. Operation on pure hydrogen
2. Addition of 10 ppm NH_3
3. Operation on pure hydrogen
4. Swithced from potentiostatic to galvanostatic operation on pure hydrogen
5. Addition of 10 ppm NH_3

6. Operation on pure hydrogen

7. Operation on pure hydrogen after gases had been temporarily stopped

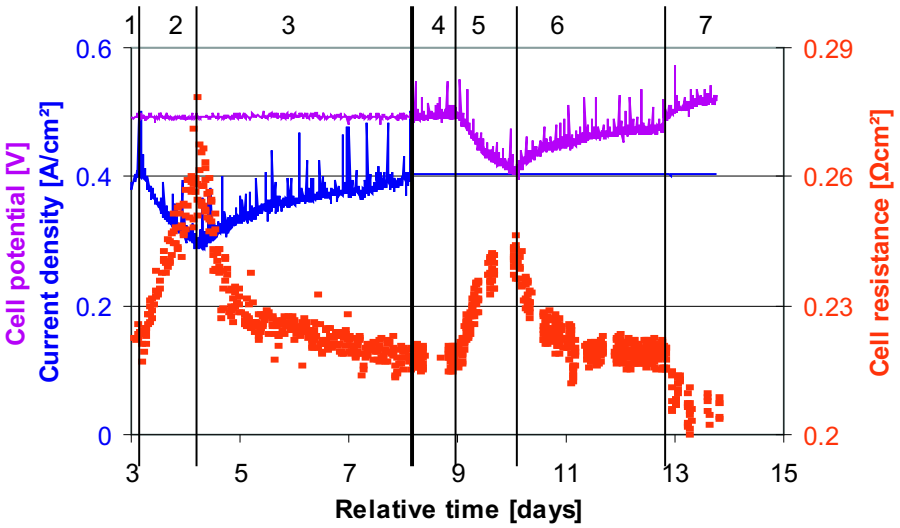

Figure 8.4: Performance of a 10 cm^2 *in-house* prepared MEA with Pt on either electrode with addition of 10 ppm NH_3 for about 26 hours (region 2 and 4 in the graph). The cell was first run potentiostically at 0.50 V then galvanostatically at 0.40 A/cm^2. Operational parameters are the same as given in Figure 8.2 except minimum flow of hydrogen was 30 mlN/min. The data are not corrected for ohmic losses. See the text for explanation of the different regions.

The cell was run in both potentiostatic and galvanostatic mode (the switch marked with a thick line in Figure 8.4). No large differences between the two modes were observed. The ohmic resistance increased more in potentiostatic mode than in galvanostatic mode. Recovery is complete after shutting the gas supply off for a while. Interrption of gas supply was not done after running in potentiostatic mode, so we can not assess if there is a different effect of interruption of gas supply in galvanostatic and potentiostatic mode. The effect of ammonia seems to be very similar for both Pt and PtRu based anode catalysts. The loss of cell performance is larger than the effect of the increased

cell resistance also in this case where carbon supported Pt is used rather than PtRu.

8.4.4 Different Contamination Levels

Uribe *et al.* [20] and Soto *et al.* [21] studied the effect of relatively high contamination levels (13–130 ppm and 200–1000 ppm respectively). The FCs studied in this work were contaminated with different levels of NH_3 in the hydrogen (1–20 ppm). In Figure 8.5 the result of contaminating a cell for one week with 1 ppm NH_3 in the fuel is shown. The influence of even quite low concentrations of ammonia is significant over time. Recovery of performance is only partial, but the gas supply was not interrupted in this case.

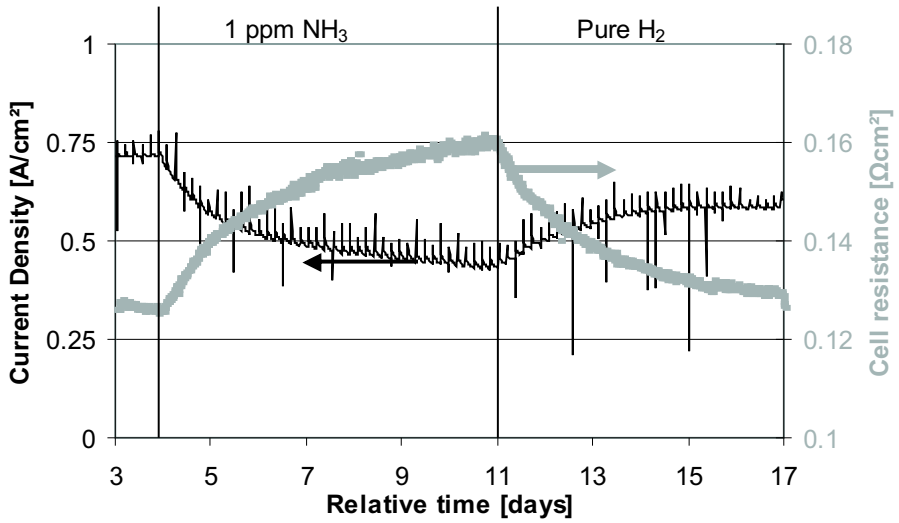

Figure 8.5: Performance of 10 cm^2 Gore™ MEA with addition of 1 ppm NH_3 for one week. The cell was running potentiostically at 0.50 V at 40 °C cell temperature, room temperature humidifiers, atmospheric pressure, 80% conversion of H_2, 40% conversion of O_2 in air, 10 and 20 mlN/min minimum flow on anode and cathode respectively. The data are not corrected for ohmic losses.

8.4.5 Symmetric $H_2|H_2$ Cell

An MEA was tested with hydrogen on either side to better isolate the effect of ammonium on the anode reaction (HOR). The different regions indicated in the graph are explained below:

1. Initial operation on pure hydrogen
2. Addition of 10 ppm NH_3
3. Operation on pure hydrogen with polarization scans recorded every day
4. Operation on pure hydrogen with polarization scans every 2.5 hours
5. Operation on pure hydrogen after gases had been temporarily stopped

Ammonia containing hydrogen has to be added downstream of the humidifiers so the anode feed gas is not fully humidified. Hence, when ammonia was not added to the cell, the same flow rate of pure, dry hydrogen was added downstream of the anode humidifier.

We notice from Figure 8.6 that the cell resistance does not fall when operating on pure hydrogen after exposure to ammonia in contrast to the $H_2|O_2$ cells presented above. Futher, potential scanning and interruption of gas supply to the cell does not affect the cell resistance. There is a slight recovery of the FC when ammonia addition is stopped.

Polarization curves were recorded before and just after ammonia exposure. Such curves were also recorded with regular intervals thereafter. The polarization curves are shown in Figure 8.7. There is a very marked effect of ammonium, especially at high c.d. A slight recovery after stopping ammonia additions is also observed in the polarization scans. However, the most striking observation is that there seems to be a limiting current in the system. In Section 5.5.1 we found that the mass transfer limiting current of the HOR is very high, especially in this case where there is pure hydrogen feed to the cell. The limiting behavior is thus caused by a reaction limitation. In Section 5.5.1 we found that the HOR followed the Tafel-Volmer mechanism, and that the Tafel step may explain reaction limitations.

It should also be noted that both the overpotential of the HOR and HER are measured in this cell because there is no reference electrode. It is possible that ammonia affects both reactions, and that the effect on HOR alone is smaller than indicated by these results.

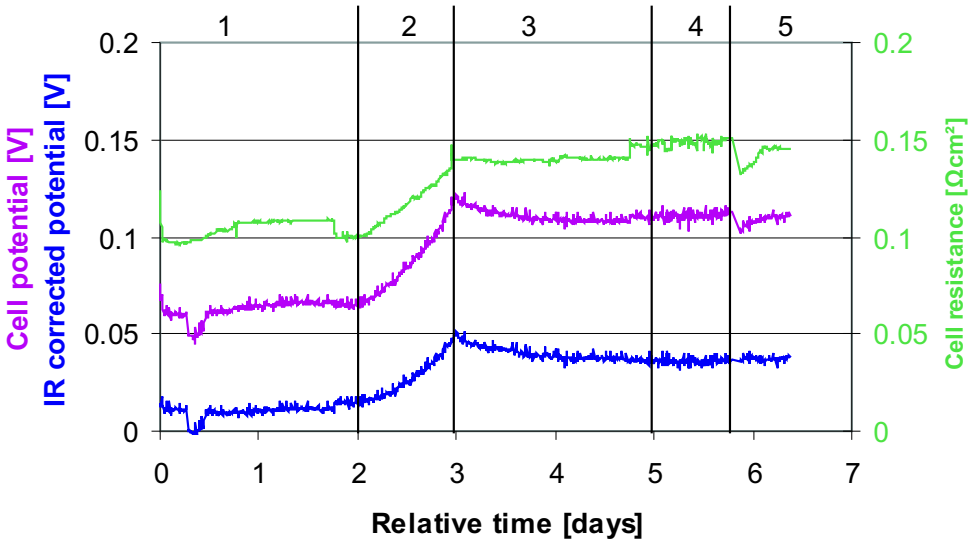

Figure 8.6: Performance of 6.25 cm^2 Gore™ MEA running in symmetric mode with addition of 10 ppm NH_3 for one day. The cell was running galvanostatically at 0.50 A/cm^2 at 41 °C cell temperature, humidifiers at 39 °C, atmospheric pressure, 50 mlN/min humidified hydrogen on each side with addition of 5.3 mlN/min dry hydrogen or ammonia containing hydrogen downstream of the humidifiers on the anode side.

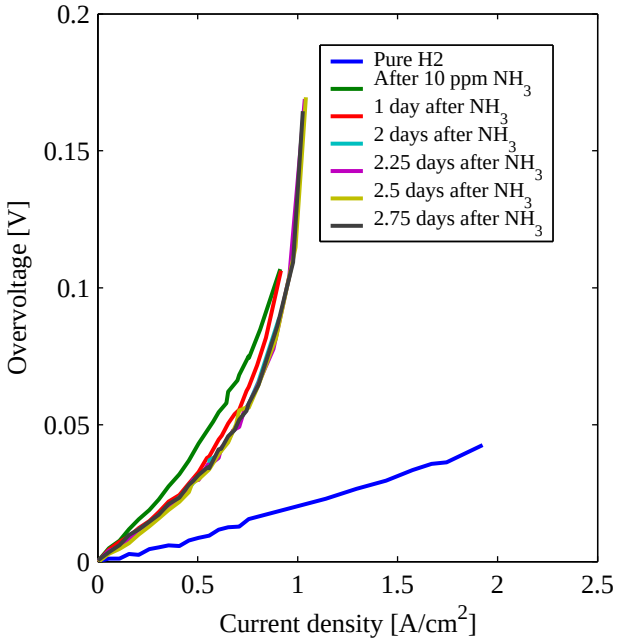

Figure 8.7: Polarization curves for 6.25 cm^2 GORE™ MEA running in symmetric mode with addition of 10 ppm NH_3 for one day. Operating conditions as in Figure 8.6.

8.5 Discussion

8.5.1 Poisoning of the Fuel Cell by NH_3

The loss in cell performance was larger in all the experiments than could be explained by increase in cell resistance alone. From the results from the symmetrical cell shown in Figure 8.6, we see that the increase in ohmic resistance is responsible for about 20 mV of the total increase in overpotential of the cell of 55 mV. The total losses in the symmetric cell are moderate at relatively low currents. However, as was seen in the polarization curves shown in Figure 8.7, the effect of ammonium on the anode is much more noticeable at higher c.d. where a limiting current occurs.

The second poisoning shown in Figure 8.2 was more severe than observed in the most cases presented here. The increase in resistance does not level off which is different from most of the other cases. A similar behavior could be observed when operating the cell with a carbon supported Pt based MEA potentiostatically, see the first addition of ammonia in Figure 8.4. The resistance increase in the symmetric cell was also larger, and did not seem to level off. This larger increase in resistance is more similar to that observed by Uribe *et al.* [20]. The more moderate increase in resistance observed in the other cells is more similar to the data reported by Soto *et al.* [21].

Performance degradation of the cells seems to follow a first order response as does recovery. This indicates that there is no significant adsorption of ammonia on carbon in the GDLs. If that had been the case, one would expect a second order response because the carbon material would only gradually be saturated with ammonia. The change in ammonia concentration at the surface of the active electrode would thus not be instantaneous. Soto *et al.* [21] found recovery of performance to follow a second order response, but this can not be explained by adsorption effects because the initial degradation followed a first order response.

8.5.2 Adsorption of NH_3 in the Membrane

Typically the increase in cell resistance when exposed to ammonia is about 20% in most cases presented here. In Section 3.4.1 we found that there is a linear relationship between membrane ammonium content and conductivity of Nafion® 117 in aqueous solutions. Further, the conductivity of proton form Nafion® is about 3.8–4.2 times higher than ammonium form (Section 3.4.2 and

Uribe *et al.* [20]). Based on this, and assuming that the physical properties of the ionomer in the GORE™ PRIMEA® are the same as for Nafion® 117, the ammonium content in the membrane phase is estimated from the observed resistance in pure proton form and after poisoing as shown below and presented in Table 8.1.

$$y_{NH_4^+} = \frac{R_{contam} - R_{H^+}}{R_{NH_4^+} - R_{H^+}} = 1/3(R_{contam}/R_{H^+} - 1)$$

The amount of sulfonic acid groups in the membrane can also be estimated, but several assumptions must be made: *1)* The dry thickness l of the membrane in the GORE™ MEA is about 25 μm [244] and that of Nafion® 112 about 50 μm. *2)* The active cell area A is 10 cm^2, but the total area of the membrane, which is assumed to be accessible to ammonium, is approximately twice as large. *3)* The density of dry Nafion® ρ is 2.05 g/cm^3 [96]. *4)* The equivalent weight of the ionomer M is 1100 g/mol. *5)* The membrane used in the GORE™ MEA is reinforced with inert ePTFE (expanded PolyTetraFluoroEtylene) fabric, but the volume of this phase is not subtracted from the total membrane volume. The number of sulfonic acid groups can then be estimated:

$$n_{SO_3^-} = \frac{2Al\rho}{M}$$

The results of the calculations are given in Table 8.1 below:

Table 8.1: Mass balance for NH_3 added to the fuel cell through the fuel gas. The data given are moles of sulfonic acid groups in the membrane, mole fraction of ammonium in the membrane estimated from cell resistance, mols of NH_3 added through the fuel gas and how much of this NH_3 that was absorbed. All MEAs were based on carbon supported PtRu anode catalyst except as noted.

Experiment	Figure	Mols SO_3^- [μmol]	$y_{NH_4^+}$ [-]	Mols NH_3 [μmol]	Adsorbed %
Galv. Stat., 10 ppm	8.1	93	0.05	39	12
Pot. Stat., 10 ppm	8.2[1]	93	0.28	39	67
Pt catalyst, 10 ppm	8.4[2]	186	0.07	24	54
	8.4[3]	186	0.03	25	22
1 ppm NH_3	8.5	93	0.07	24	27
Symmetric Cell	8.6	93	0.12	35	32

[1] Data for second addition of NH_3
[2] Operating in potentiostatic mode (first part of the graph)
[3] Operating in galvanostatic mode (second part of the graph)

The mass balance for ammonia as given in Table 8.1 shows that a substantial part of the ammonia entering the cell is not accumulated in the membrane. There could be several reasons for this: *1)* There is a small equilibrium vapor pressure of ammonia over the membrane *2)* Mass transfer of ammonia through the GDL is limiting *3)* Ammonium is oxidized in the FC to other (volatile) components that do not affect the conductivity of the membrane. *4)* Some of our assumptions used to calculate $y_{NH_4^+}$ and the fraction of ammonia adsorbed in the membrane are not valid.

Volatility of Ammonia over PFSA Membranes

The equilibrium between ammonium in the membrane and ammonia in the gas phase can be described by the two reactions:

$$NH_4^+ \rightleftarrows NH_3(\text{mem}) + H^+ \tag{8.1}$$

$$NH_3(\text{mem}) \rightleftarrows NH_3(\text{g}) \tag{8.2}$$

Based on Le Châteliers principle, one would expect Equation 8.1 to be shifted to the left because the strong acid found in PerFluoroSulfonic Acid (PFSA) ionomers stabilizes the ammonium ion in the membrane phase. Further, the Henry's law constant, $k_{H,NH_3} = p_{NH_3}/c_{NH_3}$ ref. Equation 8.2, for ammonia dissolved in water is very small so that the solubility of ammonia in water is high. Since the PFSA ionomer contains a large fraction of water, see Section 3.4.1, it would be expected that also the PFSA ionomer has a high solubility for ammonia. In summary, we would expect both Equation 8.1 and 8.2 to be shifted to the left so that the vapor pressure of ammonia over an PFSA membrane would be very low indeed.

Data from the symmetrical cell in Figure 8.6 show that the cell resistance does not fall after the addition of ammonia ends. This demonstrates that the ammonium stays in the membrane phase confirming the low volatility of ammonium over PFSA ionomers.

Mass Transfer Limitations in the GDL

The diffusion rate of NH_3 through the mainly hydrogen filled GDL can be estimated to find if there are any mass transfer limitations that may explain the relatively low percentage of ammonia that is absorbed in teh membrane. We assume that there is virtually no vapor pressure of NH_3 over the PFSA ionomer. The mass transfer coefficient for hydrogen in nitrogen was estimated in Section 5.5.1. D_{H_2,NH_3} is higher than D_{H_2,N_2} by a factor 1.09 [245]. Strictly speaking, since the hydrogen is not stagnant, in contrast to nitrogen in the case of hydrogen diffusion in nitrogen, the full Stefan-Maxwell equation should be used. However, for this rough estimate the effect of the total bulk flow is neglected (assumed to be stagnant). The mass transfer coefficient is very high, but the concentrations of ammonia is relatively low. We estimate the concentration in the exhaust gas to be about 0.01 ppm NH_3 given an inlet concentration of 10 ppm. If the Stefan-Maxwell equation had been used, the exhaust concentration would have been lower. Szymanski *et al.* [25] assumed that all NH_3 entering the cell was absorbed in the electrolyte.

Oxidation of Ammonium

As shown in Chapter 6, oxidation of ammonium on platinum in acidic solutions to form nitrogen and/or nitric oxides can take place. The oxidation rate is modest and much lower than in alkaline solutions. The potential at which

this electrochemical oxidation occurs is relatively high, typically >700 mV_{RHE}. We have detected nitrogen as one of the oxidation products of this process. Converting ammonium to nitrogen may be one way that ammonium is removed from the cell by. Szymanski *et al.* [25] assumed that this was the primary "sink" of ammonium in their PAFC study. We have also detected nitric oxide as a possible oxidation product, but at higher potentials.

Further, a study of platinum in acidic solutions containing ammonium by CV has shown that several species are formed at potentials higher than about 700 mV_{RHE} in deaerated solutions, see Section 6.4.2. The chemical nature of these species has not been identified.

All these processes have been found to occur at high potentials. The polarization of the FC anode is small, see Chapter 5. Therefore, it is not likely that oxidation of ammonium to nitrogen and other volatile species takes place on the anode. This is also supported by the observation that the cell resistance of the symmetrical cell, typically operating at low potentials, did not fall after exposure to ammonia. The cathode of an FC typically operates at potentials in a range where we have observed oxidation of ammonium to form nitrogen. One should also note that the oxidation current from these processes will normally not be detectable in an FC because of the large reduction current due to ORR.

Oxygen is present at the cathode in contrast to the electrochemical experiments made with electrolyte from which oxygen had been removed by purging with an inert gas. The presence of oxygen could possibly promote chemical oxidation of adsorbed intermediate species of ammonium discussed in Chapter 6 to nitric oxides like N_2O and NO. Nitric oxides may leave the cell with the exhaust gases, or react with water to form nitrite and nitrate.

Validity of Assumptions

Table 8.1 shows that a significant fraction of the ammonia supplied to the cell is not absorbed in the membrane even in the symmetrical cell where we do not expect oxidation of ammonium to occur. Also, the mass transfer limitations for ammonia in the GDL are so small that they can not explain the low fraction of ammonia absorbed.. It could therefore be that some of the other assumptions, or the control system for addition of ammonia, are not correct.

8.5.3 Recovery after Exposure to NH_3

Recoverable Performance Losses by Interruption of Gas Supply

Recovery of the FC after exposure to NH_3 seems to be improved by turning off the gas supply to the cell letting the cell voltage drop to 0 V, see Figure 8.1 and 8.2. Increased cell performance after shutting off the cell for a while has also been observed by Jarvi *et al.* [214]. They found this to be caused by removal of a relatively stable oxide layer that had formed on the Pt catalyst over time, especially at high cathode potentials. Uribe and Zawodzinski [246] found that operation of the FC at low potentials at regular intervals improved stability. Applying CV they showed that a stable oxide was formed on the cathode over time. Paik *et al.* [233] found that Pt oxide formation on the cathode was proportional to the oxygen concentration.

As shown in Figure 8.1 and 8.2, the observed recovery was complete in some cases and in others not. Both complete and incomplete recovery have been observed in both galvanostatic and potentiostatic mode in this work. The effect of operational mode, if any, is not clarified. It is interesting to note that Uribe *et al.* [20], who ran the cell potentiostatically, observed incomplete recovery whereas Soto *et al.*, running the cell galvanostatically, observed complete recovery.

In our experiment with a symmetrical cell, there was only a temporary decrease in cell resistance after interrupting the gases. The IR corrected overpotential of the cell was not affected by the interruption.

Potential Scanning of the Fuel Cell

Potential scanning of the cell also seems in some cases to at least speed up recovery if not also make recovery more complete, see Figure 8.1 where potential scanning seemingly has a positive effect on cell performance. However, it was also observed that the stability of cells running on pure hydrogen seemed to be better if regular potential scanning was applied, see the discussion in Section 8.4.1 and in the next paragraph. It is thus not clear if potential scanning has a positive effect on recovery from NH_3 exposure. It is conceivable that changing the potential of primarily the cathode through a potential scan may be beneficial because (adsorbed) species on the cathode then may be reduced or oxidized. Szymanski *et al.* found that the oxidation of ammonium in phosphoric acid was higher at high potentials [25]. The same could be the case for PEMFC, but more work has to be done to verify this.

Performance Loss not Induced by Ammonia

Loss of performance over time can also be due to contamination of the cell by other species as discussed in Section 8.4.1. In the case of testing symmetrical cells in Chapter 5, it was observed that performance could be recovered by sweeping the potential of the two electrodes, in inert atmosphere, to relatively high potentials where a presumably organic contaminant was oxidized. The same poisoning processes may occur also in the cells studied in this Chapter, but probably to a lesser extent. On the cathode, presence of oxygen as well as high operating potential, makes contamination by organic components less likely. Likewise, diffusion of oxygen through the MEA may help to chemically oxidize organic contaminants on the anode. The potential of the anode is not high enough to oxidize these contaminants electrochemically. It is therefore expected that contamination of organic components is less severe for FCs than for symmetrical cells.

Timescale of Performance Recovery

Both poisoning and recovery after ammonia exposure are slow processes taking hours if not days. This is very different from f. ex. CO poisoning. One reason for this may be that processes contributing to "sinks" in the mass balance for ammonia in the cell are slow like the oxidation of ammonium. Furhter, there is a significant volume of ionomer not contained between the active electrodes because the membrane must be cut to a larger diameter to enable sealing of the gas compartments using gaskets. This membrane volume may act as a buffer volume for ammonium in the MEA. During poisoning, ammonium diffuses *in-plane* along the membrane out to the electrochemically inactive part of the membrane. During recovery this ammonium can diffuse back to the active MEA reducing the recovery rate.

Effect of Operating Temperature

Soto *et al.* [21] observed a quicker recovery of the cell after exposure to 200 and 1000 ppm NH_3 than we do. In only 10 hours they had complete recovery after exposure to 200 ppm NH_3 for 10 hours. Our experiments, with 10 ppm NH_3, typically required 3–4 days for complete recovery. One possible explanation may be that Soto *et al.* ran their experiments at 70 °C whereas 40 °C was used in our experiments. Higher temperature may increase the rate of oxidation of

ammonium, and also increase the volatility of ammonia possibly explaining the large difference in recovery rates.

On the other hand, Uribe *et al.*, operated their cell at 80 °C [20]. When the cell was exposed to 30 ppm NH_3 for 1 hour, complete recovery was only found after 12 hours of operation on pure hydrogen. This is more in line with our findings. However, at longer exposure times, Uribe *et al.* found recovery to be incomplete in contrast to our findings.

It is thus not possible to make firm conclusions as to the effect of temperature on recovery rate, but we would expect generally higher recovery rates at higher temperatures.

8.5.4 Tolerance towards Ammonia

As was shown in Section 8.4.4, the poisoning effect of ammonia is severe even in the case where the cell is exposed to only 1 ppm NH_3 for one week. The performance loss observed is not acceptable for practical applications of FCs. This has several implications: *1)* If ammonia is to be used as hydrogen carrier for PEMFC, virtually all traces of ammonia must be removed. This can be accomplished by absorption of ammonia in an acid trap before entering the FC [20, 71]. *2)* Traces of ammonia in hydrogen fuel based on reforming of liquid fuels may be detrimental to FC performance. *3)* Hydrogen from seemingly ammonia-free sources can also be associated with problems, f. ex. because formation of ammonia is catalyzed by metal-hydride alloys [17]. The content of nitrogen in the hydrogen may have to be closely monitored in such cases. *4)* It is not clear what the effect of ammonia in the oxidant (air) stream is. If ammonia can be absorbed on the cathode as well, equally large problems with ammonia poisoning may be experienced. Recovery after exposure to ammonia is relatively slow, therefore, even short exposure of PEMFC to high levels of ammonia may be detrimental to performance. Clearly, more work is needed in order to understand the mechanism of ammonia poisoning, and the consequence of this potential problem for PEMFC performance and durability. Tolerance levels towards ammonia need to be more firmly established.

There may also be ways to improve the tolerance of PEMFC to ammonia trough design and choice of materials. Different cathode catalyst materials is one option. The purpose of these catalysts would be either to enhance the oxidation rate of ammonium on the cathode so that the "sink" of ammonia in the cell would be larger. Alternatively, the catalyst could possibly be formulated, by using other noble metals in combinations with Pt, so that the ORR is less

affected by the presence of ammonium on the cathode. In alkaline systems, iridium and Pt-Ir alloys have been found to have a reasonably good activity for oxidation of ammonia [54]. Recently, Endo *et al.* [247] also found that a binary alloy of Pt and Ir (80:20 on atom basis) showed somewhat higher activity for oxidation of ammonia in alkaline solutions. Onset of oxidation at a slightly lower electrode potential compared to pure Pt is of particular interest. These catalysts could have a potential for increased oxidation of ammonium also in PEMFC making the PEMFC more tolerant to ammonia. Okada *et al.* demonstrated that the ORR kinetics of a Nafion® covered Pt disk in sulfuric acid can be recovered by addition of D-α-alanine when exposed to Na^+ or Ca^{2+} ions [223]. Other additives were also tried, but no details were reported. Durability and stability of these additives would have to be assessed.

Also the anode seems to be affected by ammonium. At high c.d. a limiting current is observed which is not due to mass transfer limitations. It is most probably a reaction limiting current due to the Tafel step in the Tafel-Volmer mechanism for HOR also established in Section 5.5.1. Active sites on the anode are blocked by a species rendering them inaccessible to HOR. The nature of these species has not been identified. It is not clear if it is possible to reduce the effect of ammonium on HOR directly by choosing other catalyst materials.

8.6 Conclusions

The poisoning process of the PEMFC by ammonia was slow taking 24 hours or more to reach a steady state. In some cases no steady state was reached during the experiment. The performance loss was in most cases reversible, but only after operation on neat hydrogen for several days. Additions of 1 ppm NH_3 for one week also resulted in significant performance losses. An MEA based on carbon supported Pt catalyst did not differ from the Gore™ MEA which uses a PtRu based anode catalyst. The performance losses were higher than could be explained by the observed increase in ohmic resistance in the cell. There was also a significant decay in performance in a symmetrical $H_2|H_2$ cell, especially at high c.d. where a reaction limiting current was observed. The limiting current is consistent with the Tafel step in a Tafel-Volmer HOR mechanism being the rate determining step. There is also a significant effect of ammonium on the Oxygen Reduction Reaction (ORR) on the cathode. The effect on the ORR is dominant at lower c.d., but at higher c.d. the reaction limiting current of the HOR becomes the most important limitation of the cell.

Chapter 9

Conclusions

Ammonia has several intriguing properties as a hydrogen carrier as discussed in Chapter 2. Ammonia has a relatively high energy density, it is a well known chemical commodity product, and the energy efficiency of the production process is the same as f. ex. for methanol. The major drawback is the toxicity.

Several factors may be important in order to understand poisoning of Polymer Electrolyte Membrane Fuel Cells (PEMFC) by ammonia as discussed in the Introduction of this Thesis. The main effects are: *1)* Effect of ammonium on the Hydrogen Oxidation Reaction (HOR) *2)* Effect of ammonium on conductivity and other membrane properties and *3)* Effect of ammonium on the Oxygen Reduction Reaction (ORR). These effects are discussed below. In addition, hydrogen is diluted by nitrogen. It is difficult to separate the polarization of each electrode in the Fuel Cell (FC) because a reference electrode is not necessarily reliable due to geometric artifacts as discussed in Chapter 4.

9.1 Effect of Dilution of Hydrogen

Nitrogen is present in the hydrogen fuel if based on splitting of ammonia, or if other fuels are reformed using air in auto-thermal reforming or partial oxidation processes. We found that the effect of nitrogen was limited to dilution of the fuel similar to the effect of noble gases. The mass transfer rate in the Gas Diffusion Layer is high so that mass transfer is normally not limiting. Losses in FC voltage associated with dilution are therefore marginal as long at the conversion of hydrogen is not too high. The utilization of the fuel, and thus

loss of fuel efficiency, is significant if the remaining fuel in the exhaust gas from the FC is not used. This is the same for other chemical hydrogen carriers like methanol etc.

CO_2 originating from reformation of carboneous fuels had a much more negative impact on FC performance than nitrogen. Our observations showed that CO_2 poisoned the FC catalyst by blocking active sites on the catalyst. This, together with the observation of a reaction limiting current, lead us to the conclusion that HOR on the fuel cell anode followed the Tafel-Volmer mechanism. The contamination species formed by CO_2 were not identified, but they are probably different from contamination species formed by CO.

9.2 Effect of Ammonia/Ammonium on HOR

Both polarization curves and galvanostatic performance data were collected before and after the FC was exposed to ammonia. The effect of ammonia on a symmetrical $H_2|H_2$ cell was to increase the ohmic resistance of the cell. The HOR was also affected, especially at high current density (c.d.). The performance loss of the $H_2|O_2$ cells was higher than what could be explained by the combined effect of ammonia on conductivity and HOR, especially at moderate c.d.

This finding is in contrast to the conclusions of Uribe *et al.* [20] and Soto *et al.* [21] who found that effects of ammonium on conductivity or complexation of the ionomer by ammonium in the anode catalyst layer were the primary reason for loss of performance. These conclusions were based on the fact that ammonia enters the FC on the anode side, and that CVs of the cathode did not show any signs of electrochemically active species (nor did the anode). The membrane in a PEMFC is typically 10-100 μm thick, and the time constant for diffusion of ammonium from the anode to the cathode is of the order a few minutes. This was verified experimentally by using pH and Ion Selective Eletrodes for ammonium to monitor the exchange of protons and ammonium between the membrane phase and an aqueous phase. The exchange process was complete within minutes (data not included in this Thesis). Fast ion exchange for alkali metal ions has also been observed by Samec *et al.* [240]. The argument that the anode is necessarily more affected because ammonia enters on the anode side is thus not valid. Diffusion is fast enough for the cathode to be significantly affected by ammonium in the time frame typically used in these experiments (hours or days).

9.3 Effect of Ammonium on Conductivity and Other Membrane Properties

The effect of ammonium on conductivity, water content and composition has been discussed in Chaper 3. Conductivity effects could only explain 5-15% of the observed poisoning effect of ammonia in PEMFC as has been discussed in Chapter 8. The effect of reduced water content and lower proton concentration on FC performance, and probably ORR in particular, was not quantified.

9.4 Effect of Ammonium on ORR

The effect of ammonium on ORR in acidic solution was quite large as shown in Chapter 7. The mol fraction of ammonium in the ionomer was relatively low, but even at quite low concentrations of ammonium in sulfuric acid (about 10% NH_4^+), we observed a significant increase in overpotential required to drive the ORR at a given c.d. The effect of ammonium on the ORR seemed to be the most important effect at moderate c.d. At high c.d., close to 1 A/cm^2, the reaction limiting current of the HOR became more important so that the ammonium effect on the anode was the most important effect.

The mechanism by which ammonium affects ORR is not clear. This has been discussed in some detail in Chapter 7, but more work is required to get a better understanding of the poisoning mechanism.

9.5 Tolerance of PEMFC towards NH_3

The poisoning effect of ammonia was severe even in the case where the cell was exposed to only 1 ppm NH_3 for one week, see Chapter 8. The performance losses observed were not acceptable for practical applications of FCs. This has several implications: *1)* If ammonia is to be used as hydrogen carrier for PEMFC, virtually all traces of ammonia must be removed to a sub-ppm level. *2)* Traces of ammonia in hydrogen fuels based on reforming of other liquid fuels may be detrimental to FC performance. *3)* Hydrogen from seemingly ammonia-free sources can also be associated with problems, f. ex. because formation of ammonia is catalyzed by metal-hydride alloys [17]. The content of nitrogen in the hydrogen may have to be closely monitored in such cases. *4)* It is not clear what the effect of ammonia in the oxidant (air) stream is.

If ammonia is absorbed on the cathode as well, equally large problems with ammonia poisoning may be experienced.

Recovery after exposure to ammonia was relatively slow. Therefore, even short exposure of PEMFC to high levels of ammonia contamination may be detrimental to performance. Clearly, more work is needed in order to understand the mechanism of ammonia poisoning, and the consequence of this potential problem on PEMFC performance and durability. Tolerance levels towards ammonia need to be more firmly established.

Chapter 10

Further work

It seems that more questions have been raised than have been answered throughout the work with this Thesis as is often the case with research work. The nature and extent of further work with ammonia as a poison for PEMFC naturally depends on the objective of the work. Although there is no sharp distinction between technological development and more fundamental research, I divide my suggestions for further work into these categories.

10.1 Technological Development

From a practical point of view it is important to establish more carefully the tolerance level of PEMFC towards ammonia contamination. It is also important to see if ammonia contamination of the inlet air has a poisoning effect on the PEMFC. Half-cell studies would enable assessment of the performance of each electrode. Suggestions for how such a cell should be designed have been given in Chapter 4. Measurement techniques suitable for this cell could be Cyclic Voltammetry (CV), polarization curves to determine kinetic parameters, and impedance measurements. A liquid electrolyte makes it easier to study the effect of ammonium concentration on ORR/HOR as well as oxidation of ammonium itself. Further, experiments on ordinary FCs incorporating techniques like EIS and CV should also provide useful information.

The second issue would be to evaluate if other catalysts may be better suited for operation in the presence of ammonium. PtIr alloys have showed promising results in alkaline solution [54, 247] and should also be tested in acidic media. Also other catalysts may also be better suited than carbon

supported Pt. Both the anode and cathode catalysts could be of importance. Additives to the active layer have been suggested by Okada *et al.* [223] to suppress the effect of cation contamination, and could be tested both with respect to efficiency and durability.

It would probably also be useful to incorporate the findings in this Thesis, supplemented with findings from other studies, into a PEMFC model. The model should allow for transient effects, and it must include a mass balance for ammonium in the membrane.

The use of ammonia as hydrogen carrier is intriguing. Several aspects of technological/scientific nature have to be resolved like efficient storage, splitting and cleaning of the produced hydrogen. However, the most important issues are probably how toxicity should be handled and how to gain public acceptance for ammonia.

10.2 More Fundamental, Mechanistic Research

The poisoning mechanisms of both the anode and the cathode (HOR and ORR respectively) are not well understood. Use of spectroscopic techniques like FTIR could give valuable insight into which species that are involved in what seems to be surface poisoning. Also, comparison of effects caused by ammonia to the effects of alkali and alkali earth cations should be of interest to study if there are effects of changes in the double layer structure or proton concentration. Poisoning effects of these cations are also interesting in its own right because this will give useful data regarding the required cleanliness of water to be used in connection with PEMFC.

Adsorption experiments, *i.e.*, where the WE is exposed to ammonium containing electrolytes, which are then replaced by a clean electrolyte keeping the electrode continuously under potential control, could also provide useful information on the nature of the adsorbed species. Adsorption experiments would be powerful, especially in combination with EQCM, DEMS and other techniques, to study the nature of adsorbed intermediate products.

Bibliography

[1] U. Bossel. *The Birth of the Fuel Cell 1835–1845.* European Fuel Cell Forum, CH-5452 Oberrohrdorf, Switzerland, 2000.

[2] E. Chen. History. In G. Hoogers, editor, *Fuel Cell Technology Handbook*, chapter 2, pages 2–1. CRC Press LLC, 2003.

[3] J. A. A. Ketelaar. History. In L. J. M. J. Blomen and M. N. Mugerwa, editors, *Fuel Cell Systems*, chapter 1, page 19. Plenum Press, New York, 1993.

[4] U.S. Department of Energy. Energy Secretary Abraham Launches FreedomCAR, Replaces PNGV. `http://www.energy.gov/HQPress/releases02/janpr/pr02001.htm`, 2002. Press Release, visited June 2003.

[5] M. A. Weiss, J. B. Heywood, A. Schafer, and V. K. Natarajan. Comparative Assessment of Fuel Cell Cars. `http://lfee.mit.edu/publications/PDF/LFEE_2003-001_RP.pdf`, February 2003. Visited June 2003.

[6] L-B-Systemtechnik and General Motors. GM Well-To-Wheel Analysis of Energy Use and Greenhouse Gas Emissions of Advanced Fuel Cell/Vehicle Systems – An European Study. `http://www.lbst.de/gm-wtw`, 2002. Visited July 2003.

[7] J. M. Ogden. Alternative Fuels and Prospects – Overview. In W. Vielstich, A. Lamm, and H. A. Gasteiger, editors, *Fuel Cell Technology and Applications: Part 1*, Handbook of Fuel Cells – Fundamentals, Technology and Applications, chapter 1, page 3. John Wiley & Sons Ltd., Chichester, West Sussex, England, 2003.

[8] Naval Technology. U212/U214 Attack Submarine, Germany. http://www.naval-technology.com/projects/type_212/, 2003. Visited June 2003.

[9] The California Hydrogen Business Council. Hydrogen Ships & Subs. http://www.ch2bc.org/index16.htm, 2003. Visited June 2003.

[10] J. A. Johnson. Micro Fuel Cells: Oppertunities for Urban Electric Utilities. In M. Nurdin, editor, *The Fuel Cell Home*, page 261, CH-5452 Oberrohrdorf, Switzerland, 2001. European Fuel Cell Forum.

[11] S. Kimijima and N. Kasagi. Performance Evaluation of Gas Turbine-Fuel Cell Hybrid Micro Generation System. In *Proceedings of ASME TURBO EXPO 2002*. ASME Paper GT-2002-30111, 2002.

[12] National Fuel Cell Research Center. "HYBRID" - 220 kW Hybrid Solid Oxide Fuel Cell / Micro Turbine Generator System. http://www.nfcrc.uci.edu/RESEARCH/projects/hybrid.htm, 2002. Visited June 2003.

[13] E. Barendrecht. Electrochemistry of Fuel Cells. In L. J. M. J. Blomen and M. N. Mugerwa, editors, *Fuel Cell Systems*, chapter 1, page 73. Plenum Press, New York, 1993.

[14] J. Larminie and A. Dicks. *Fuel Cell Systems Explained*. Wiley, Chichester, England, 2nd edition, 2003.

[15] Arthur D. Little Inc. Cost Analysis of Fuel Cell System for Transportation – Baseline System Cost Estimate. http://www.ott.doe.gov/pdfs/baseline_cost_model.pdf, March 2000. Visited Aug. 2002.

[16] R. Borup, M. Inbody, J. Tafoya, T. Semelsberger, and L. Perry. Durability Studies: Gasoline/Reformate Durability. http://www.eren.doe.gov/hydrogen/pdfs/nn0123ba.pdf, 2002. Visited Aug. 2002.

[17] H. Y. Zhu. Room Temperature Catalytic Ammonia Synthesis over an AB_5-type Intermetallic Hydride. *J. Alloy. Compd.*, 240:L1, 1996.

[18] A. S. Chellappa, C. M. Fischer, and W. J. Thomson. Ammonia Decomposition Kinetics over Ni-Pt/Al_2O_3 for PEM Fuel Cell Applications. *Appl. Catal. A–Gen.*, 227:231, 2002.

[19] F. A. Uribe, T. A. Zawodzinski, Jr., and S. Gottesfeld. Effect of Ammonia as Possible Fuel Impurity on PEM Fuel Cell Performance. In S. Gottesfeld, T.F. Fuller, and G Halpert, editors, *Proceedings of the 2nd International Symposium on Proton Conducting Membrane Fuel Cells II*, volume 98-27 of *Electrochemical Society Proceedings*, page 229, Pennington, NJ, 1998. Electrochemical Society Inc.

[20] F. A. Uribe, T. A. Zawodzinski, Jr., and S. Gottesfeld. Effect of Ammonia as Potential Fuel Impurity on PEM Fuel Cell Performance. *J. Electrochem. Soc.*, 149:A293, 2002.

[21] H. J. Soto, W-K. Lee, J. W. Van Zee, and M. Murthy. Effect of Transient Ammonia Concentrations on the PEMFC Performance. *Electrochem. Solid-State Lett.*, 6:A133, 2003.

[22] H. G. Oswin and M. Salomon. The Anodic Oxidation of Ammonia at Platinum Black Electrodes in Aqueous KOH Electrolyte. *Can. J. Chem.*, 41:1686, 1963.

[23] H. Gerischer and A. Mauerer. Untersuchungen zur Anodischen Oxidation von Ammoniak an Platin-Elektroden. *J. Electroanal. Chem.*, 25:421, 1970.

[24] S. Wasmus, E. J. Vasini, M. Krausa, H. T. Mishima, and W. Vielstich. DEMS-Cyclic Voltammetry Investigation of the Electrochemistry of Nitrogen-Compounds in 0.5 M potassium hydroxide. *Electrochim. Acta*, 39:23, 1994.

[25] S. T. Szymanski, G. A. Gruver, M. Katz, and H. R. Kunz. The Effect of Ammonia on Hydrogen-Air Phosphoric Acid Fuel Cell Performance. *J. Electrochem. Soc.*, 127:1440, 1980.

[26] R. Halseid, P. J. S. Vie, and R. Tunold. Influence of Ammonium on Conductivity and Water Content of Nafion 117 Membranes. *J. Electrochem. Soc.*, 151:A381, 2004.

[27] R. Halseid, P. J. S. Vie, R. J. Aaberg, and R. Tunold. Influence of Cell Geometry on ac Impedance Measurements as Applied to PEFCs. In F. Büchi, G. G. Scherer, and A. Wokaun, editors, *Proceedings of the First European PEFC Forum*, page 119. European Fuel Cell Forum, 2001.

[28] H. Bakemeier, T. Humerich, R. Krabetz, W. Liebe, M. Schunk, D. Mayer, and C. L. Becker. Ammonia. In W.Gerhartz, Y. S. Yamamoto, F. T. Campbell, R. Pfefferkorn, and J. F. Rounsaville, editors, *Ullmann's Encyclopedia of Industrial Chemistry*, volume A2, page 143. VCH Verlagsgesellschaft, 5 edition, 1985.

[29] M. Appl. *Ammonia – Principles and Industrial Practice.* Wiley-VCH, 1999.

[30] K. G. Andersen and G. Yttri. *Et forsøk verdt – Forskning og Utvikling i Norsk Hydro gjennom 90 år.* Universitetsforlaget, Oslo, Norway, 1997.

[31] J. Rothstein. Hydrogen and Fossile Fuels. *Int. J. Hydrogen Energy*, 20:283, 1993.

[32] R. Metkemeijer and P. Achard. Ammonia as a Feedstock for a Hydrogen Fuel Cell; Reformer and Fuel Cell Behaviour. *J. Power Sources*, 49:271, 1994.

[33] R. Metkemeijer and P. Achard. Comparison of Ammonia and Methanol Applied Indirectly in a Hydrogen Fuel Cell. *Int. J. Hydrogen Energy*, 19:535, 1994.

[34] K. Kordesch, V. Hacker, J. Gsellmann, Cifrain M., G. Faleschini, P. Enzinger, R. Fankhauser, M. Ortner, M. Muhr, and R. R. Aronson. Alkaline Fuel Cell Applications. *J. Power Sources*, 86:162, 2000.

[35] R. B. Steele. A proposal for an ammonia economy. *Chemtech*, 29:28, 1999.

[36] A. Nielsen. Ammonia Storage and Transportation-Safety. In A. Nielsen, editor, *Ammonia – Catalysis and Manufacture*, chapter 7, page 329. Springer-Verlag, 1995.

[37] T. A. Czuppon, S. A. Knez, and J. M. Rovner. Ammonia. In R. E. Kirk, D. F. Othmer, J. I. Kroschwitz, and M. Howe-Grant, editors, *Encyclopedia of Chemical Technology*, volume 2, page 638. Wiley, 4 edition, 1991.

[38] G. Astarita, D. W. Savage, and A. Bisio. *Gas Treating with Chemical Solvents.* John Wiley & Sons, 1983.

[39] European Fertilizer Manufacturers' Association. Production of Ammonia – Best Available Techniques for Pollution Prevention and Control in the European Fertilizer Industry. `http://www.efma.org/Publications/BAT%202000/Bat01/booklet1.pdf`, 2000. Visited May 2003.

[40] T. Murakami, T. Nishikiori, T. Nohira, and Y. Ito. Electrolytic Synthesis of Ammonia in Molten Salts under Atmospheric Pressure. *J. Am. Chem. Soc.*, 125:334, 2003.

[41] S. E. Gay and M. Ehsani. Ammonia Hydrogen Carrier for Fuel Cell Based Transportation. pages 2003–01–2251. Society of Automotive Engineers, 2003.

[42] S. Issley and E. Lang. Toxicity, Ammonia. `http://www.emedicine.com/emerg/topic846.htm`, 2001. Visited July 2003.

[43] T. Kurvits and T. Marta. Agricultural NH_x and NO_x emissions in Canada. *Environ. Pollut.*, 102:187, 1998.

[44] P. M. Vitousek, J. D. Aber, R. W. Howarth, G. E. Likens, P. A. Matson, D. W. Schindler, W. H. Schlesinger, and D .G. Tilman. Human Alteration of the Global Nitrogen Cycle: Sources and Consequences. *Ecol. Appl.*, 7:737, 1997.

[45] R. L. Graves, J. W. Hodgson, and J. S. Tennant. Ammonia as a Hydrogen Carrier and its Application in a Vehicle. In T.N. Veziroğlu, editor, *Hydrogen Energy, Proceedings of Hydrogen Economy Miamy Energy Conference*, page 755, 1974.

[46] W. H. Avery. A Role for Ammonia in the Hydrogen Economy. *Int. J. Hydrogen Energy*, 13:761, 1988.

[47] C. Boffito and J. D. Baker. Getter Materials for Cracking Ammonia. US Patent 5 976 723, November 1999.

[48] G. Frick, W. J. Sucasky, and M. Shaw. Chronopotentiometric Study of Ammonia Oxidation. Electrochemical Society Proceedings, page 107, Pennington, NJ, 1963. The Electrochemical Society.

[49] W. Vielstich. *Fuel Cells – Modern Processes for the Electrochemical Production of Energy.* Wiley-Interscience, 1970. Translated by Ives, D. J. G.

[50] F. J. Vidal-Iglesias, N. García-Aráez, V. Montiel, J. M. Feliu, and A. Aldaz. Selective Electrocatalysis of Ammonia Oxidation on Pt(100) Sites in Alkaline Medium. *Electrochem. Commun.*, 5:22, 2003.

[51] E. Müller and F. Spitzer. Über die Elektrolytische Oxydation des Ammoniaks und Ihre Abhängigkeit vom Anodenmaterial. *Z. Elektrochemie*, 11:917, 1905.

[52] T. Katan and R. J. Galiotto. Current Efficiencies for the Anodic Oxidation of Ammonia in Potassium Hydroxide Solution. *J. Electrochem. Soc.*, 110:1022, 1963.

[53] R. A. Wynveen. The Ammonia Fuel Cell. *Am. Chem. Soc., Div. Petrol. Chem., Preprints*, 6:49, 1961.

[54] D. W. McKee, A. J. Scarpellino Jr., I. F. Danzig, and M. S. Pak. Improved Electrocatalysts for Ammonia Fuel Cell Anodes. *J. Electrochem. Soc.*, 116:562, 1969.

[55] E. L. Simons, E. J. Cairns, and D. J. Surd. The Performance of Direct Ammonica Fuel Cells. *J. Electrochem. Soc.*, 116:556, 1969.

[56] D. Spahrbier and G. Wolf. Zur Anodischen Oxydation von Ammoniak an Platiniertem Platin. *Z. Naturforsch.*, 19A:614, 1964.

[57] R. D. Farr and C. G Vayenas. Ammonia High Temperature Solid Electrolyte Fuel Cell. *J. Electrochem. Soc.*, 127:1278, 1980.

[58] N. M. Gamanovich and G. I. Novikov. Electrochemical Oxidation of Ammonia in High- Temperature Fuel Cells. *Russ. J. Appl. Chem.*, 70:1136, 1997.

[59] G. I. Novikov and N. M. Gamanovich. Electrochemical Oxidation of Ethanol-Ammonia Mixture in High-Temperature Fuel Cell. *Russ. J. Appl. Chem.*, 71:2032, 1998.

[60] N. M. Gamanovich, V. A. Gorbunova, and G. I. Novikov. Oxidation of Alcohol-Ammonia Mixtures in High- Temperature Fuel Cell with Various Electrodes. *Russ. J. Appl. Chem.*, 74:746, 2001.

[61] S. C. Singhal. Advances in Solid Oxide Fuel Cell Technology. *Solid State Ionics*, 135:305, 2000.

[62] A. Wojcik, H. Middleton, I. Damopoulos, and J. Van herle. Ammonia as a Fuel in Solid Oxide Fuel Cells. *J. of Power Sources*, 118:342, 2003.

[63] European Integrated Hydrogen Project. Ammonia Cracking for Clean Electric Power Technology. `http://www.eihp.org/public/documents/fuero/ACCEPT.pdf`, 2001. Visited June 2003.

[64] K. Yamada, K. Asazawa, K. Yasuda, T. Ioroi, H. Tanaka, Y. Miyazaki, and T. Kobayashi. Investigation of PEM Type Direct Hydrazine Fuel Cell. *J. of Power Sources*, 115:236, 2003.

[65] L. J. Christiansen. Thermodynamics Properties of Ammonia Synthesis. In A. Nielsen, editor, *Ammonia – Catalysis and Manufacture*, chapter 1, page 1. Springer-Verlag, 1995.

[66] P. N. Ross Jr. Characteristics of an NH_3 - Air Fuel Cell System for Vehicular Applications. In *Proceedings of the 16th Intersociety Energy Conversion Engineering Conference*, page 726, 1981.

[67] G. Faleschini, V. Hacker, M. Muhr, K. Kordesch, and R. R. Aronsson. Ammonia for High Density Hydrogen Storage. In *2000 Fuel Cell Seminar - Abstracts*, page 336, 2000.

[68] T. V. Coudhary, A. K. Sivadinarayana, and D. W. Goodman. Catalytic Ammonia Decomposition: CO_x- Free Hydrogen Production for Fuel Cell Applications. *Catal. Lett.*, 72:197, 2001.

[69] J. P. Collins and J. D. Way. Caralytic Decomposition of Ammonia in a Membrane Reactor. *J. Membr. Sci*, 96:259, 1994.

[70] F. Sakamoto, Y. Kinari, F. L. Chen, and Y. Sakamoto. Hydrogen Permeation through Palladium Alloy Membranes in Mixture Gases of 10% Nitrogen and Ammonia in the Hydrogen. *Int. J. Hydrogen Energy*, 22:369, 1997.

[71] M. F. Collins, R. Michalek, and W. Brink. Design Parameters of a 300 Watt Ammonia-Air Fuel Cell System. In *Proceedings of the 7th Intersociety Energy conversion engineering conference*, page 32, 1972.

[72] O. J. Adlhart and P. L. Terry. Ammonia-Air Fuel Cell System. *Engelhard-Industries-Technical-Bulletin*, 10:80, 1969.

[73] M. Kawase, Y. Mugikura, T. Watanabe, Y. Hiraga, and T. Ujihara. Effects of NH_3 and NO_x on the Performance of MCFCs. *J. Power Sources*, 104:265, 2002.

[74] M. Kawase, Y. Mugikura, T. Watanabe, Y. Hiraga, and T. Ujihara. Erratum to "Effects of NH_3 and NO $_x$ on the Performance of MCFCs" [J. Power Sources 104 (2002) 265–271]. *J. Power Sources*, 109:239, 2002.

[75] K. J. Laidler and J. H. Meiser. *Physical Chemistry of Electrolytic Solutions*. Benjamin/Cummings Publishing Co. Inc., 1982.

[76] A. E. Lutz, R. S. Larson, and J. O. Keller. Thermodynamic Comparison of Fuel Cells to the Carnot Cycle. *Int. J. Hydrog. Energy*, 27:1103, 2002.

[77] A. J. Appleby and F. R. Foulkes. *Fuel Cell Handbook*. Van Nordstrand Reinhold, New York, NY, 1989.

[78] G. H. Aylward and T. J. V. Findlay. *SI Chemical Data*. John Wiley & Sons, 2 edition, 1974.

[79] E. Chen. Thermodynamics and Electrochemical Kinetics. In G. Hoogers, editor, *Fuel Cell Technology Handbook*, chapter 3, pages 3–1. CRC Press LLC, 2003.

[80] A. English, J. Rovner, and S. Davies. Methanol. In R.E. Kirk, D.F. Othmer, J.I. Kroschwitz, and M. Howe-Grant, editors, *Encyclopedia of Chemical Technology*, volume 16, page 537. Wiley, 4 edition, 1991.

[81] G. Strickland. Hydrogen Derived from Ammonia: Small Scale Costs. *Int. J. Hydrogen Energy*, 9:759, 1984.

[82] R. E. Billings. Hydrogen Energy. In R. E. Kirk, D. F. Othmer, J. I. Kroschwitz, and M. Howe-Grant, editors, *Encyclopedia of Chemical Technology*, volume 13, page 927. Wiley, 4 edition, 1991.

[83] J. J. Fontanella, M. G. McLin, M. C. Wintersgill, J. P. Calame, and S. G. Greenbaum. Electrical-Impedance Studies of Acid Form Nafion® Membranes. *Solid State Ion.*, 66:1, 1993.

[84] B. D. Cahan and J. S. Wainright. AC-Impedance Investigations of Proton Conduction in Nafion®. *J. Electrochem. Soc.*, 140:L185, 1993.

[85] H. B. George and R. A Courant. Conductance and Water Transfer in a Leached Cation-Exchange Membrane. *J. Phys. Chem.*, 71:246, 1967.

[86] S. D'Alessandro and A. Tantillo. Electrostatic Phenomena in Ion Exchange Membranes. *Desalination*, 9:225, 1971.

[87] M. W. Verbrugge and R. F. Hill. Analysis of Promising Perfluorosulfonic Acid Membranes for Fuel-Cell Electrolytes. *J. Electrochem. Soc.*, 137:3770, 1990.

[88] M. W. Verbrugge, E. W. Schneider, R. S. Conell, and R. F. Hill. The Effect of Temperature on the Equilibrium and Transport Properties of Saturated poly(perfluorosulfonic acid) Membranes. *J. Electrochem. Soc.*, 139:3421, 1992.

[89] H. Strahtmann. Ion-Exchange Membranes. In W.S. Winston Ho and K.K. Sirkar, editors, *Membrane Handbook*, chapter 18, page 230. Van Nostrand Reinhold, 1992.

[90] M. Yoshitake, M. Tamura, N. Yoshida, and T. Ishisaki. Studies of Perfluorinated Ion Exchange Membranes for Polymer Electrolyte Fuel Cells. *Denki Kagaku*, 64:727, 1996.

[91] S. Slade, S. A. Campbell, T. R. Ralph, and F. C. Walsh. Ionic Conductivity of an Extruded Nafion 1100 EW Series of Membranes. *J. Electrochem. Soc.*, 149:A1556, 2002.

[92] S. Nouri, L. Dammak, G. Bulvestre, and B. Auclair. Comparison of Three Methods for the Determination of the Electrical Conductivity of Ion-Exchange Polymers. *Eur. Polym. J.*, 38:1907, 2002.

[93] C. Gavach, G. Pamboutzoglou, M. Nedyalkov, and G. Pourcelly. Ac Impedance Investigation of the Kinetics of Ion Transport in Nafion Perfluorosulfonic Membranes. *J. Membr. Sci.*, 45:37, 1989.

[94] G. Pourcelly, P. Sistat, A. Chapotot, C. Gavach, and V. Nikonenko. Self Diffusion and Conductivity in Nafion^{TM}Membranes in Contact with NaCl+$CaCl_2$ Solutions. *J. Membrane Sci.*, 110:69, 1996.

[95] V. Subrahmanyan and N. Lakshiminarayanaiah. A Rapid Method for the Determination of Electrical Conductance of Ion–Exchange Membranes. *J. Phys. Chem.*, 72:4314, 1968.

[96] D. R. Morris and X. D. Sun. Water-Sorption and Transport Properties of Nafion 117 H. *J. Appl. Polym. Sci.*, 50:1445, 1993.

[97] M. Cappadonia, J. W. Erning, S. M. Saberi Niaki, and U. Stimming. Conductance of Nafion 117 Membranes as a Function of Temperature and Water Content. *Solid State Ion.*, 77:65, 1995.

[98] P. Dimitrova, K. A. Friedrich, B. Vogt, and U. Stimming. Transport Properties of Ionomer Composite Membranes for Direct Methanol Fuel Cells. *J. Electroanal. Chem.*, 532:75, 2002.

[99] P. Dimitrova, K. A. Friedrich, U. Stimming, and B. Vogt. Modified Nafion®-based Membranes for Use in Direct Methanol Fuel Cells. *Solid State Ion.*, 150:115, 2002.

[100] J. Halim, F. N. Büchi, O. Haas, M. Stamm, and G. G. Scherer. Characterization of Perfluorosulfonic Acid Membranes by Conductivity Measurements and Small-Angle X-Ray Scattering. *Electrochim. Acta*, 39:1303, 1994.

[101] M. Ottøy. *Mass and Heat Transfer in Ion-Exchange Membranes – Applicable to Solid Polymer Fuel Cells.* PhD thesis, Norwegian University of Science and Technology, 1996.

[102] C. L. Gardner and A. V. Anantaraman. Measurement of Membrane Conductivities using an Open-Ended Coaxial Probe. *J. Electroanal. Chem.*, 395:67, 1995.

[103] C. L. Gardner and A. V. Anantaraman. Studies on Ion-Exchange Membranes. II. Measurement of the Anisotropic Conductance of Nafion®. *J. Electroanal. Chem.*, 449:209, 1998.

[104] W. B. Johnson and W. Liu. Ionic Conductivities of Perfluorosulfonic Acid Membranes as a Function of Temperature, Humidity and Equivalent Weight. In S.C. Singhal, editor, *High Temperature Materials*, volume PV 2002-5, page 132, Pennington, NJ, 2002. The Electrochemical Society Proceedings Series.

[105] A. Parthasarathy, S. Srinivasan, A. J. Appleby, and C. R. Martin. Temperature Dependence of the Electrode Kinetics of Oxygen Reduction at

the Platinum Nafion® Interface — A Microelectrode Investigation. *J. Electrochem. Soc.*, 139:2530, 1992.

[106] T. A. Zawodzinski, Jr., C. Derouin, S. Radzinski, R. J. Sherman, V. T. Smith, T. E. Springer, and S. Gottesfeld. Water Uptake by and Transport Through Nafion® 117 Membranes. *J. Electrochem. Soc.*, 140:1041, 1993.

[107] G. Xie and T. Okada. The State of Water in Nafion 117 of Various Cation Forms. *Denki Kagaku*, 64:718, 1996.

[108] Y. Sone, P. Ekdunge, and D. Simonsson. Proton Conductivity of Nafion 117 as Measured by a Four-Electrode AC Impedance Method. *J. Electrochem. Soc.*, 143:1254, 1996.

[109] V. Tricoli, N. Carretta, and M. Bartolozzi. A Comparative Investigation of Proton and Methanol Transport in Fluorinated Ionomeric Membranes. *J. Electrochem. Soc.*, 147:1286, 2000.

[110] L. Jones, P. N. Pintauro, and H. Tang. Coion Exclusion Properties of Polyphosphazene Ion-Exchange Membranes. *J. Membrane Sci.*, 162:135, 1999.

[111] T. Okada, Y. Ayato, M. Yuasa, and I. Sekine. The Effect of Impurity Cations on the Transport Characteristics of Perfluorosulfonated Ionomer Membranes. *J. Phys. Chem. B*, 103:3315, 1999.

[112] C. M. Gates and J. Newman. Equilibrium and Diffusion of Methanol and Water in a Nafion 117 Membrane. *AIChE J.*, 46:2076, 2000.

[113] E. I. du Pont de Nemours and Company. Product information: Nafion® M embranes N-112, NE-1135, N-115, N-117, NE-1110. `http://www.dupont.com/fuelcells/pdf/extrusion_cast.pdf`, November 2002. Visited March 2003.

[114] S. Logette, C. Eysseric, A. Pourcelly, and C. Gavach. Selective Permeability of a Perfluorosulphonic Membrane to Different Valency Cations. Ion-Exchange Isotherms and Kinetic Aspects. *J. Membrane Sci.*, 144:259, 1998.

[115] T. Okada, N. Nakamura, M. Yuasa, and I. Sekine. Ion and Water Transport Characteristics in Membranes for Polymer Electrolyte Fuel Cells Containing H^+ and Ca^{2+} Cations. *J. Electrochem. Soc.*, 144:2744, 1997.

[116] M. Rankothge, J. Hook, L. vanGorkom, and G. Moran. ^{14}N NMR Spectroscopy of Nitrate Co-ions in Ionomer Membranes. *Macromolecules*, 30:4357, 1997.

[117] R. Lteif, L. Dammak, C. Larchet, and B. Auclair. Conductivité Électrique Membranaire: Étude de l'Effect de la Concentration, de la Nature de l'Électrolyte et de la Structure Membranaire. *Eur. Polym. J.*, 35:1187, 1999.

[118] J. A. Kolde, B. Bahar, M. S. Wilson, T. A. Zawodzinski, and S. Gottesfeld. Advanced Composite Polymer Electrolyte Fuel Cell Membranes. In S. Gottesfeld, G. Halpert, and A. Landgrebe, editors, *Proton Conducting Membrane Fuel Cells I*, volume PV 95-23, page 193, Pennington, NJ, 1995. The Electrochemical Society Proceedings Series.

[119] N. Yoshida, T. Ishisaki, A. Watakabe, and M. Yoshitake. Characterization of Flemion® Membranes for PEFC. *Electrochim. Acta*, 43:3749, 1998.

[120] T. E. Springer, T. A. Zawodzinski, and S. Gottesfeld. Polymer Electrolyte Fuel-Cell Model. *J. Electrochem. Soc.*, 138:2334, 1991.

[121] T. Thampan, S. Malhotra, H. Tang, and R. Datta. Modeling of Conductive Transport in Proton-Exchange Membranes for Fuel Cells. *J. Electrochem. Soc.*, 147:3242, 2000.

[122] A. S. Nowick and W.-K Lee. The Conductivity Pre-Exponential of Solid Electrolytes. In A.L. Laskar and S. Chandra, editors, *Superionic Solids and Solid Electrolytes: Recent Trends*, page 381. Academic Press Inc., Boston, MA, 1989.

[123] T. E. Springer, T. A. Zawodzinski, M. S. Wilson, and S. Gottesfeld. Characterization of Polymer Electrolyte Fuel Cells Using AC Impedance Spectroscopy. *J. Electrochem. Soc.*, 143:587, 1996.

[124] S. J. Lee, S. Mukerjee, J. McBreen, Y. W. Rho, Y. T. Kho, and T. H. Lee. Effects of Nafion Impregnation on Performances of PEMFC Electrodes. *Electrochim. Acta*, 43:3693, 1998.

[125] M. Ciureanu and H. Wang. Electrochemical Impedance Study of Electrode-Membrane Assemblies in PEM Fuel Cells I. Electro-Oxidation

of H_2 and H_2 / CO Mixtures on Pt-Based Gas-Diffusion Electrodes. *J. Electrochem. Soc.*, 146:4031, 1999.

[126] M. Ciureanu and H. Wang. Electrochemical Impedance Study of Anode CO-Poisoning in PEM Fuel Cells. *J. New Mat. Electrochem. Systems*, 3:107, 2000.

[127] G. Hsieh, T. O. Mason, E. J. Garboczi, and L. R. Pederson. Experimental Limitations in Impedance Spectroscopy. 3. Effect of Reference Electrode Geometry/Position. *Solid State Ionics*, 96:153, 1997.

[128] J. Winkler, P. V. Hendriksen, N. Bonanos, and M. Mogensen. Geometric Requirements of Solid Electrolyte Cells with a Reference Electrode. *J. Electrochem. Soc.*, 145:1184, 1998.

[129] M. Nagata, Y. Itoh, and H. Iwahara. Dependence of Observed Overvoltages on the Positioning of the Reference Electrode on the Solid-Electrolyte. *Solid State Ion.*, 67:215, 1994.

[130] S. B. Adler, B. T. Henderson, M. A. Wilson, D. M. Taylor, and R. E. Richards. Reference Electrode Placement and Seals in Electrochemical Oxygen Generators. *Solid State Ionics*, 134:35, 2000.

[131] S. B. Adler. Reference Electrode Placement in Thin Solid Electrolytes. *J. Electrochem. Soc.*, 149:E166, 2002.

[132] Z. Y. Liu, J. S. Wainright, W. W. Huang, and R. F. Savinell. Positioning the Reference Electrode in Proton Exchange Membrane Fuel Cells: Calculations of Primary and Secondary Current Distribution. *Electrochim. Acta*, 49:923, 2004.

[133] W. H. He and T. V. Nguyen. Edge Effects on Reference Electrode Measurements in PEM Fuel Cells. *J. Electrochem. Soc.*, 151:A185, 2004.

[134] A. M. Svensson and K. Nişancioğlu. Interpretation of Measured Polarization Resistance at a Solid Electrode/Electrolyte Interface. *J. Electrochem. Soc.*, 146:1840, 1999.

[135] N. Wagner, W. Schnurnberger, B. Muller, and M. Lang. Electrochemical Impedance Spectra of Solid-Oxide Fuel Cells and Polymer Membrane Fuel Cells. *Electrochim. Acta*, 43:3785, 1998.

[136] S. Kjelstrup, P. Pugazhendi, and D. Bedeaux. Impedance of the Hydrogen Polymer Fuel Cell Electrode. Theory and Experiments. *Z. Phys. Chem.*, 214:895, 2000.

[137] P. Millet. Water Electrolysis Using EME Technology – Electric- Potential Distribution inside a Nafion Membrane During Electrolysis. *Electrochim. Acta*, 39:2501, 1994.

[138] E. Rasten. *Electrocatalysis in Water Electrolysis with Solid Polymer Electrolyte*. PhD thesis, Norwegian University of Science and Technology, 2001.

[139] J. N. Han, G. G. Park, Y. G. Yoon, T. H. Yang, W. Y. Lee, and C. S. Kim. A New Evaluation Method of Anode/Cathode Used for Polymer Electrolyte Membrane Fuel Cell. *Int. J. Hydrog. Energy*, 28:609, 2003.

[140] S. K. Ratkje, M. Ottøy, R. Halseid, and M. Strømgård. Thermoelectric Power Relevant for the Solid-Polymer-Electrolyte Fuel Cell. *J. Membrane Sci.*, 107:219, 1995.

[141] J. Giner. Electrochemical Reduction of CO_2 on Platinum Electrodes in Acid Solutions. *Electrochim. Acta*, 8:857, 1963.

[142] Y. B. Vassiliev, V. S. Bagotzky, N. V. Osetrova, and A. A. Mikhailova. Electroreduction of Carbon Dioxide. Part III. Adsorption and Reduction of CO_2 on Platinum Metals. *J. Electroanal. Chem.*, 189:311, 1985.

[143] D. C. Papageorgopoulos and F. A. de Bruijn. Examining a Potential Fuel Cell Poison – A Voltammetry Study of the Hydrogen Oxidation Capabilities of Carbon- Supported Pt and PtRu Anodes. *J. Electrochem. Soc.*, 149:A140, 2002.

[144] G. M. Brisard, A. P. M. Camrgo, F. C. Nart, and T. Iwasita. On-line Mass Spectrometry Investigation of the Reduction of Carbon Dioxide in Acidic Media on Polycrystalline Pt. *Electrochem. Comm.*, 3:603, 2001.

[145] Y. Hori, T. Wakebe, T. Tsukamoto, and O. Koga. Electrocatalytic Process of CO Selectivity in Electrochemical Reduction of CO_2 at Metal Electrodes in Aqueous Media. *Electrochim. Acta*, 39:1833, 1994.

[146] T. Iwasita, F. C. Nart, and W. Vielstich. On the Study of Adsorbed Species at Platinum from Methanol, Formic Acid and Reduced Carbon Dioxide *Via In Situ* FT-*ir* Spectroscopy. *Electrochim. Acta*, 37:2361, 1992.

[147] N. Hoshi and Y. Hori. Electrochemical Reduction of Carbon Dioxide at a Series of Platinum Single Crystal Electrodes. *Electrochim. Acta*, 45:4263, 2000.

[148] F. A. de Bruijn, D. C. Papgeorgopoulos, E. F. Sitters, and G. J. M. Janssen. The Influence og Carbon Dioxide on PEM Fuel Cell Anodes. *J. Power Sources*, 110:117, 2002.

[149] S. Ball, A. Hodgkinson, G. Hoogers, S. Maniguet, D. Thompsett, and B. Wong. The Proton Exchange Membrane Fuel Cell Performance of a Carbon Supported PtMo Catalyst Operating on Reformate. *Electrochem. Solid-State Lett.*, 5:A31, 2002.

[150] C. Sishtla, G. Koncar, R. Platon, S. Gamburzev, A. J. Appleby, and O. A. Velev. Performance and Endurance of a PEMFC Operated with Synthetic Reformate Fuel Feed. *J. Power Sources*, 71:249, 1998.

[151] M. S. Wilson, C. R. Derouin, J. A. Valerio, and S. Gottesfeld. Electrocatalysis Issues in Polymer Electrolyte Fuel Cells. In *Proceedings of the 28th Intersociety Energy Conversion Engineering Conference: IECEC-93, August 8–13, 1993, Atlanta, Georgia.*, volume 1, page 1203. IEEE, 1993.

[152] K. R. Weisbrod and N. E. Vanderborgh. Effect of Operating Parameters and Anode Gas Impurities upon Polymer Electrolyte Fuel Cells. In *Proceedings of the 29th Intersociety Energy Conversion Engineering Conference: IECEC-94, August 7–11, 1994, Monterey, California*, page 855. IEEE, 1994.

[153] D. P. Wilkinson and D. Thompsett. Materials and Approaches for CO and CO_2 Tolerance for Polymer Electrolyte Membrane Fuel Cells. In O. Savadogo and P. R. Roberge, editors, *Proceedings of the 2nd International Symposium on New Materials for Fuel Cell and Modern Battery Systems*, page 266, Montreal, Canada, 1997.

[154] T. A. Zawodzinski, T. Springer, J. Bauman, T. Rockward, F. Uribe, and S. Gottesfeld. Performance of PEM Fuel Cells Operating on Synthetic Reformate: Experimental and Modeling Studies. In S. Gottesfeld, T. F. Fuller, and G Halpert, editors, *Proceedings of the 2nd International Symposium on Proton Conducting Membrane Fuel Cells II*, volume 98-27 of *Electrochemical Society Proceedings*, page 127, Pennington, NJ, 1998. Electrochemical Society Inc.

[155] R. B. Bird, W. E. Stewart, and E. N. Lightfoot. *Transport Phenomena.* John Wiley & Sons, 1960.

[156] Geankoplis C. J. *Transport Processes and Unit Operations.* Prentice Hall, 2 edition, 1983.

[157] M. Enyo. Hydrogen Electrode Reaction on Electrocatalytically Active Metals. In B. E. Conway, J. O'M Bockris, E. Yeager, S. U. M. Khan, and R. E. White, editors, *Kinetics and Mechanisms of Electrode Processes*, volume 7 of *Comprehensive Treatise of Electrochemistry*, chapter 5, page 241. Plenum Press, New York, 1983.

[158] K. J. Vetter. *Elektrochemische Kinetik.* Springer Verlag, 2 edition, 1961.

[159] J. J. T. T. Vermeijlen, L. J. J. Janssen, and G. J. Visser. Mechanism of Hydrogen Oxidation on a Platinum-Loaded Gas Diffusion Electrode. *J. Appl. Electrochem.*, 27:497, 1997.

[160] J. S. Newman. *Electrochemical Systems.* Prentice Hall, 2 edition, 1991.

[161] C. Lagergren, G. Lindbergh, and D. Simonsson. Investigation of Porous-Electrodes by Current Interruption — Application to Molten-Carbonate Fuel-Cell Cathodes. *J. Electrochem. Soc.*, 142:787, 1995.

[162] P. A. Garthwaite, I. T. Jolliffe, and B. Jones. *Statistical Interference.* Prentice Hall, 1995.

[163] B. Efron and R. J. Tibshirani. *An Introduction to the Bootstrap.* Chapman&Hall, 1998.

[164] P. J. S. Vie. *Characterisation and Optimisation of the Polymer Electrolyte Fuel Cell.* PhD thesis, Norwegian University of Science and Technology, 2002.

[165] D. R. Lide, editor. *CRC Handbook of Chemistry and Physics : A Ready-Reference Book of Chemical and Physical data.* CRC Press, 83 edition, 2002.

[166] J. R. Welty, C. E. Wicks, and R. E. Wilson. *Fundamentals of Momentum, Heat and Mass Transport.* John Wiley & Sons, 3 edition, 1984.

[167] P. Vogel, W.and Lundquist, P. Ross, and P. Stonehart. Reaction Pathways and Poisons – II The Rate Controlling Step for Electrochemical Oxidaition of Pt in Acid and Poisoning of the Reaction by CO. *Electrochim. Acta*, 20:79, 1975.

[168] D. R. Lide, editor. *CRC Handbook of Chemistry and Physics : A Ready-Reference Book of Chemical and Physical data.* CRC Press, 71 edition, 1990.

[169] A. Savitzky and M. J. E. Golay. Smoothing and Differentiation of Data by Simplified Least Square Procedures. *Anal. Chem.*, 36:1627, 1964.

[170] P. J. S. Vie and S. Kjelstrup. Thermal Condutivities from Temperature Profiles in the Polymer Electrolyte Fuel Cell. *Electrochim. Acta*, 49:1069, 2004.

[171] X. Cheng, L. Chen, C. Peng, Z. Chen, Y. Zhang, and Q. Fan. Catalyst Microstructure Examination of PEMFC Membrane Electrode Assemblies *vs.* Time. *J. Electrochem. Soc.*, 151:A48, 2004.

[172] T. E. Springer, T. Rockward, T. A. Zawodzinski, and S. Gottesfeld. Model for Polymer Electrolyte Fuel Cell Operation on Reformate feed – Effects of CO, H_2 Dilution, and High Fuel Utilization. *J. Electrochem. Soc.*, 148:A11, 2001.

[173] M. Pourbaix. *Atlas of Electrochemical Equilibria in Aqueous Solutions.* National Association of Corrosion Engineers, 2 edition, 1974.

[174] A. R. Despić, D. M. Dražić, and P. M. Rakin. Kinetics fo Electrochemical Oxidation of Ammonia in Alkaline Solution. *Electrochim. Acta*, 11:997, 1966.

[175] M. D. García, M. L. Marcos, and J. G. Velasco. On the Mechanism of Electrooxidation of Hydrazine on Platinum Electrodes in Acidic Solutions. *Electroanalysis*, 8:267, 1996.

[176] A. C. A. de Vooys, M. T. M. Koper, R A. van Santen, and J. A. R. van Veen. The Role of Adsorbates in the Electrochemical Oxidation of Ammonia on Noble and Transition Metal Electrodes. *J. Electroanal. Chem.*, 506:127, 2001.

[177] J. F. E. Gootzen, A. H. Wonders, W. Visscher, R. A. van Santen, and J. A. R. van Veen. A DEMS and Cyclic Voltammetry Study of NH_3 Oxidation on Platinized Platinum. *Electrochim. Acta*, 43:1851, 1998.

[178] A. C. A. de Vooys, M. F. Mrozek, M. T. M. Koper, R. A. van Santen, J. A. R. van Veen, and M. J. Weaver. The Nature of Chemisorbates Formed from Ammonia on Gold and Palladium Electrodes as Discerned from Surface-Enhanced Raman Spectroscopy. *Electrochem. Commun.*, 3:293, 2001.

[179] X. Q. Zeng and S. Bruckenstein. Polycrystalline Gold Electrode Redox Behavior in an Ammoniacal Electrolyte – Part I. A Parallel RRDE, EQCM, XPS and TOF- SIMS Study of Supporting Electrolyte Phenomena. *J. Electroanal. Chem.*, 461:131, 1999.

[180] J. M. Bradley, A. Hopkinson, and D. A. King. Control of a Biphasic Surface Reaction by Oxygen Coverage: The Catalytic Oxidation of Ammonia over Pt(1 0 0). *J. Phys. Chem.*, 99:17032, 1995.

[181] W. D. Mierher and W. Ho. Thermally Activated Oxidation of NH_3 on Pt(1 1 1): Intermediate Species and Reaction Mechanisms. *Surf. Sci.*, 322:151, 1995.

[182] S. Wasmus, S. R. Samms, and R. F. Savinell. Multipurpose Electrochemical Mass Spectrometry – A New Powerful Extension of Differential Electrochemical Mass Spectrometry. *J. Electrochem. Soc.*, 142:1183, 1995.

[183] W. Paul. Electromagnetic Traps for Charged and Neutral Particles – Nobel Lecture, December 8, 1989. `http://www.nobel.se/physics/laureates/1989/paul-lecture.pdf`, 1989. Visited January 2004.

[184] R. Raudonis, D. Plaušinaitis, and V. Daujotis. On the Frequency Response of a Quartz Supported Platinum Electrode: Dependence on Pretreatment. *J. Electroanal. Chem.*, 358:351, 1993.

[185] C. P. Wilde, S. V. De Cliff, K. C. Hui, and D. J. L. Brett. The Influence of Adsorbed Hydrogen and Extended Cycling on the EQCM Response of Electrodeposited Pt Electrodes. *Electrochim. Acta*, 45:3649, 2000.

[186] Z. Jusys and S. Bruckenstein. Electrochemical Quartz Crystal Microgravimetry of Gold in Perchloric and Sulfuric Acid Solutions. *Electrochem. Solid State Lett.*, 1:74, 1998.

[187] D. Pletcher, R. Greff, R. Peat, L. M. Peter, and J. Robinson. *Instrumental Methods in Electrochemistry.* Horwood Publishing Ltd., 2001.

[188] G. Sauerbrey. Verwendung von Schwingquarzen zur Wägung Dünner Schichten und zur Mikrowägung. *Z. Phys.*, 155:206, 1959.

[189] A. J. Bard and L. R. Faulkner. *Electrochemical Methods – Fundamentals and Applications.* John Wieley & Sons, Inc., 2 edition, 2001.

[190] C. Gabrielli, M. Keddam, and R. Torresi. Calibration of the Electrochemical Quartz Crystal Microbalance. *J. Electrochem. Soc.*, 138:2657, 1991.

[191] W. Visscher, J. F. Gootzen, A. P. Cox, and J. A. van Veen. Electrochemical Quartz Crystal Microbalance Measurements of CO Adsorption and Oxidation on Pt in Various Electrolytes. *Electrochim. Acta*, 43:533, 1998.

[192] L. Daikhin, E. Gileadi, V. Tsionsky, M. Urbakh, and G. Zilberman. Slippage at Adsorbate-Electrolyte Interface. Response of Electrochemical Quartz Crystal Microbalance to Adsorption. *Electrochim. Acta*, 45:3615, 2000.

[193] Y. Lim and E. Hwang. An Electrochemical Quartz Crystal Microbalance Study of Adsorption on a Platinum Electrode in Sulfuric Acid. *Bull. Korean Chem. Soc.*, 18:6, 1997.

[194] Z. Jusys, H. Massong, and H. Baltruschat. A New Approach for Simultaneous DEMS and EQCM: Electro-oxidation of Adsorbed CO on Pt and Pt-Ru. *J. Electrochem. Soc.*, 146:1093, 1999.

[195] J. F. Llopis and F. Colom. Platinum. volume VI of *Encyclopedia of Electrochemistry of the Elements*, chapter VI-4, page 170. Marcel Dekker Inc., New York, USA, 1976.

[196] F. C. Nart and T. Iwasita. On the Adsoption of Sulfate Species on Polycrystalline Platinum – An FTIR Study in Fluoride Base Electrolytes. *J. Electroanal. Chem.*, 308:277, 1991.

[197] A. Wiekowski, P. Zelenay, and K. Varga. A Comprehensive Study of Bisulfate Adsorption on Pt(1 1 1) by Radioactive Labeling and Voltammetry. *J. Chim. Phys.*, 88:1247, 1991.

[198] M. Watanabe, H. Uchida, and N. Ikeda. Electrochemical Quartz Crystal Microbalance Study of Copper ad-atoms on Gold and Platinum Electrodes Part I. Adsorption of Anions in Sulfuric Acid. *J. Electroanal. Chem.*, 380:255, 1995.

[199] K. Shimazu and H. Kita. *In situ* Measurements of Water-Adsorption on a Platinum Electrode by an Electrochemical Quartz Crystal Microbalance. *J. Electroanal. Chem.*, 341:361, 1992.

[200] V. I. Birss, M. Chang, and J. Segal. Platinum Oxide Film Formation-Reduction: An *in- situ* Mass Measurement Study. *J. Electroanal. Chem.*, 355:181, 1993.

[201] A. Zolfaghari, B. E. Conway, and G. Jerkiewicz. Elucidation of the Effects of Competitive Adsorption of Cl^- and Br^- Ions on the Initial Stages of Pt Surface Oxidation by Means of Electrochemical Nanogravimetry. *Electrochim. Acta*, 47:1173, 2002.

[202] G. Jerkiewicz, G. Vatankhah, J. Lessard, M. P. Soriaga, and Y.-S. Park. Surface-Oxide Growth at Platinum Electrodes in Aqueous H_2SO_4 – Reexamination if Its Mechanism through Combined Cyclic-Voltammetry, Electrochemical Quartz-Crystal Nano Balanse, and Auger-Electron Spectroscopy Measurements. *Electrochim. Acta*, 49:1451, 2004.

[203] H. Agerstein-Kozlowska, B. E. Conway, and W. B. A. Sharp. The Real Condition on Electrochemically Oxidized Platinum Surfaces Part I Resolution of Component Processes. *J. Electroanal. Chem.*, 43:9, 1973.

[204] G. Jerkiewicz. Private communication, January 2004.

[205] T. Frelink, W. Visscher, and J. A. van Veen. Measurement of the Ru Surface Content of Electrocodeposited PtRu Electrodes with the Electrochemical Quartz Crystal Microbalance: Implications for Methanol and CO Electrooxidation. *Langmuir*, 12:3702, 1996.

[206] S. G. Roscoe and B. E. Conway. State of Surface Oxide Films at Pt Anodes and " Vulcano" Behaviour in Electrocatalysis for Anodic Cl_2 Evolution. *J. Electroanal. Chem.*, 224:163, 1987.

[207] Y. Shingaya, H. Kubo, and M. Ito. Coadsorption of Ammonia and Electrolyte Anions on a Pt(111) Electrode. *Surf. Sci.*, 428:173, 1999.

[208] J. C. Huang, W. E. O'Grady, and E. Yeager. The Effects of Cations and Anions on Hydrogen Chemisorption at Pt. *J. Electrochem. Soc.*, 124:1732, 1977.

[209] M. R. Tarasevich, A. Sadkoxski, and E. Yeager. Oxygen Electrochemistry. In B. E. Conway, J. O'M Bockris, E. Yeager, S. U. M. Khan, and R. E. White, editors, *Kinetics and Mechanisms of Electrode Processes*, volume 7 of *Comprehensive Treatise of Electrochemistry*, chapter 6, page 301. Plenum Press, New York, 1983.

[210] A. Damjanovic. Progress in the Studies of Oxygen Reduction during the Last Thirty Years. In O. J. Murphy, S. Srinivasan, and B. E. Conway, editors, *Electrochemistry in Transition – From the 20^{th} to the 21^{st} Century*, chapter 9, page 107. Plenum Press, New York, 1992.

[211] K. Kinoshita, J. T. Lundquist, and P. Stonehart. Potential Cycling Effects on Platinum Electrocatalyst Surfaces. *J. Electroanal. Chem.*, 48:157, 1973.

[212] D. B. Sepa, M. V. Vojnovic, and A. Damjanovic. Reaction Intermediates as a Controlling Factor in teh Kinetcs and Mechanism of Oxygen Reduction at Platinum Electrodes. *Electrochim. Acta*, 26:781, 1981.

[213] R. M. Darling and J. P. Meyers. Kinetic Model of Platinum Dissolution in PEMFCs. *J. Electrochem. Soc.*, 150:A1523, 2003.

[214] T. D. Jarvi, T. W. Patterson Jr., N. E. Cipollini, J. B. Hertzberg, and M. L. Perry. Recoverable Performance Losses in PEM Fuel Cells. In *203^{rd} Meeting of The Electrochemical Society – Meeting Abstracts*, 65 South Main Street, Pennington, NJ, USA, 2003. The Electrochemical Society, Inc.

[215] A. Damjanovic and V. Brusic. Electrode Kinetics of Oxygen Reduction on Oxide-Free Platinum Electrodes. *Electrochim. Acta*, 12:615, 1967.

[216] V. I. Birss and A. Damjanovic. A Study of the Anomalous pH Dependence of the Oxygen Evolution Reaction at Platinum in Acid Solutions. *J. Electrochem. Soc.*, 130:1694, 1983.

[217] V. A. Paganin, C. L. F. Oliveira, E. A. Ticianelli, T. E. Springer, and E. R. Gonzalez. Modelistic Interpretation of the Impedance Response of a Polymer Electrolyte Fuel Cell. *Electrochim. Acta*, 43:3761, 1998.

[218] S. Gottesfeld, I. D. Raistrick, and S. Srinivasan. Oxygen Reduction Kinetics on a Platinum RDE Coated with a Recast Nafion Film. *J. Electrochem. Soc.*, 134:1455, 1987.

[219] S. K. Zečević, J. S. Wainright, M. H. Litt, S. Lj. Gojković, and R. F. Savinell. Kinetics of O_2 Reduction on a Pt Electrode Covered with a Thin Film of Solid Polymer Electrolyte. *J. Electrochem. Soc.*, 144:2973, 1997.

[220] T. Okada, J. Dale, Y. Ayato, O. A. Asbjørnsen, M. Yuasa, and I. Sekine. Unprecedented Effect of Impurity Cations on the Oxygen Reduction Kinetics at Platinum Electrodes Covered with Perfluorinated Ionomer. *Langmuir*, 15:8490, 1999.

[221] T. Okada, Y. Ayato, J. Dale, M. Yuasa, I. Dekine, and O. A. Asbjørnsen. Oxygen Reduction Kinetics at Platinum Electrodes Covered with Perfluorinated Ionomer in the Presence of Impurity Cationins Fe^{3+}, Ni^{2+} and Cu $^{2+}$. *Phys. Chem. Chem. Phys.*, 2:3255, 2000.

[222] T. Okada, Y. Ayato, H. Satou, M. Yuasa, and I. Sekine. The Effect of Impurity Cations on the Oxygen Reduction Kinetics at Platinum Electrodes Covered with Perfluorinated Ionomer. *J. Phys. Chem. B*, 105:6980, 2001.

[223] T. Okada, H. Satou, and M. Yuasa. Effects of Additivs on Oxygen Reduction Kinetics at the Interface between Platinum and Perfluorinated Ionomer. *Langmuir*, 19:2325, 2003.

[224] T. J. Schmidt, U. A. Paulus, H. A. Gasteiger, and R. J. Behm. The Oxygen Reduction Reaction on a Pt/Carbon Fuel Cell Catalyst in the Presence of Chloride Anions. *J. Electroanal. Chem.*, 508:41, 2001.

[225] S. Mitsushima, N. Araki, N. Kamiya, and K. Ota. Analysis of Oxygen Reduction on Pt Microelectrode with Polymer Electrolytes of Various Exchange Capacities. *J. Electrochem. Soc.*, 149:A1370, 2002.

[226] J.-P. Diard, B. Le Gorrec, and C. Montella. Comments to "Kinetics of O_2 Reduction on a Pt Electrode Covered with a Thin Film of Solid Polymer Electrolyte" by S. K. Zečević, J. S. Wainright, M. H. Litt, S. Gojković, and R.F. Savinell *J. Electrochem. Soc.*, 144:3308, 1997. *J. Electrochem. Soc.*, 145:3308, 1998.

[227] J. P. Diard, B. Le Gorrec, and C. Montella. O_2 Mass-Transfer Function for Polymer- Filmed Metal Electrodes — Application to the Linear Sweep Voltammetry Method. *J. Electrochem. Soc.*, 147:296, 2000.

[228] S. Lj. Gojković, S. K. Zečević, and R. F. Savinell. O_2 Reduction on an Ink-Type Rotating Disk Electrode using Pt Supported on High-Area Carbons. *J. Electrochem. Soc.*, 145:3713, 1998.

[229] O. Antoine, Y. Bultel, and R. Durand. Oxygen Reduction Reaction Kinetics and Mechanism on Platinum Nanoparticles Inside Nafion®. *J. Electroanal. Chem.*, 499:85, 2001.

[230] U. A. Paulus, T. J. Schmidt, H. A. Gasteiger, and R. J. Behm. Oxygen Reduction on a High-Surface Area Pt/Vulcan Carbon Catalyst: A Thin-Film Rotating Ring-Disk Electrode Study. *J. Electroanal. Chem.*, 495:134, 2001.

[231] A. Parthasarathy, B. Dave, S. Srinivasan, A. J. Appleby, and C. R. Martin. The Platinum Microelectrode Nafion Interface - an Electrochemical Impedance Spectroscopic Analysis of Oxygen Reduction Kinetics and Nafion Characteristics. *J. Electrochem. Soc.*, 139:1634, 1992.

[232] J.-P. Diard, B. Le Gorrec, C. Montella, C. Poinsignon, and G. Vitter. Impedance Measurements of Polymer Electrolyte Membrane Fuel Cells Running on Constant Load. *J. Power Sources*, 74:244, 1998.

[233] C. H. Paik, T. D. Jarvi, and W. E. O'Grady. Extent of PEMFC Cathode Surface Oxidation by Oxygen and Water Measured by CV. *Electrochem. Solid State Lett.*, 7:A82, 2004.

[234] W. H. Tiedemann, J. Newmann, and D. N. Bennion. The Error in Measurements of Electrode Kinetics Caused by Nonuniform Ohmic-Potential Drop to a Disk Electrode. *J. Electrochem. Soc.*, 120:256, 1973.

[235] A. C. West and J. Newman. Corrections to Kinetic Measurements taken on a Disk Electrode. *J. Electrochem. Soc.*, 136:139, 1989.

[236] H. S. Harned and B. B. Owen. *The Physical Chemistry of Electrolytic Solutions*. Reinhold, 3 edition, 1958.

[237] J. X. Wang and R. R. Adžić. Surface Reconstruction at Metal|Solid Polymer Electrolyte Interfaces: Au(111)|Nafion® Interface. *J. Electroanal. Chem.*, 448:205, 1998.

[238] P. Krtil, A. Trojánek, and Z. Samec. Kinetics of Water Sorption in Nafion Thin Films — Quartz Crystal Microbalance Study. *J. Phys. Chem. B*, 105:7979, 2001.

[239] M. L. Shi and F. C. Anson. Dehydration of Protonated Nafion® Coatings Induced by Cation Exchange and Monitored by Quartz Crystal Microgravimetry. *J. Electroanal. Chem.*, 425:117, 1997.

[240] Z. Samec, A. Trojánek, J. Langmaier, and E. Samcová. Diffusion Coefficients of Alkali Metal Cations in Nafion ® from Ion-Exchange Measurements – An Advanced Kinetic Model. *J. Electrochem. Soc.*, 144:4236, 1997.

[241] M. S. Wilson, J. A. Valerio, and S. Gottesfeld. Low Platinum Loading Electrodes for Polymer Electrolyte Fuel-Cells Fabricated Using Thermoplastic Ionomers. *Electrochim. Acta*, 40:355, 1995.

[242] J. Ihonen, F. Jaouen, G. Lindbergh, and G. Sundholm. A Novel Polymer Electrolyte Fuel Cell for Laboratory Investigations and *in-situ* Contact Resistance Measurements. *Electrochim. Acta*, 46:2899, 2001.

[243] J. Ihonen. Private communication, April 2002.

[244] M. Murthy, M. Esayian, W.-k. Lee, and J. W. Van Zee. The Effect of Temperature and Pressure on the Performance of a PEMFC Exposed to Transient CO Concentrations. *J. Electrochem. Soc.*, 150:A29, 2003.

[245] D. W. Green, editor. *Perry's Chemical Enigneers' Handbook*. McGraw-Hill, 7 edition, 1999.

[246] F. A. Uribe and T. A. Zawodzinski. A Study of Polymer Electrolyte Fuel Cell Performance at High Voltages. Dependence on Cathode Catalyst Layer Composition and on Voltage Conditioning. *Electrochim. Acta*, 47:3799, 2002.

[247] K. Endo, Y. Katayama, and T. Miura. Pt-Ir and Pt-Cu Binary Alloys as the Electrocatalyst for Ammonia Oxidation. *Electrochim. Acta*, 49:1635, 2004.

[248] Sluttrapport Miljøsok fase 2, juni 2000. `http://www2.olf.no/art/no_miljosok/2000/0918/162627.html`, 1998. Visited August 2003.

[249] L. Dalen and N. A. Nordlien. Norges offisielle statistikk (NOS C 525) – Olje- og gassvirksomhet 4. kvartal 1998. `http://www.ssb.no/emner/10/06/nos_olje_gass/arkiv/nos_c525/vedl-no.shtml`, 1998. Visited August 2003.

[250] I. Dybkjær. Ammonia Production Processes. In A. Nielsen, editor, *Ammonia – Catalysis and Manufacture*, chapter 7, page 199. Springer-Verlag, 1995.

[251] M. S. Wilson, S. Møller-Holst, and C. Zawodzinski. Efficient Fuel Cell Systems. In S. Chalk, editor, *2000 Annual Progress Report – Transportation Fuel Cell Power Systems*, page 88. US Department of Energy, 2000.

[252] S. Møller-Holst. *Solid Polymer Fuel Cells – Electrode and Membrane Performance Studies.* PhD thesis, Norwegian University of Science and Technology, 1996.

Appendix A

Details Regarding Efficiency of the Ammonia Fuel Chain

A.1 Production of Natural Gas

Available data for specific CO_2 emissions due to natural gas production on the Norwegian Continental Shelf show that about 100 kg CO_2 is produced per ton oil equivalent (toe) natural gas [248]. 1 toe corresponds to 42.3 GJ (HHV) [249]. About 2.3 kg CO_2 is released when burning 1 Sm^3 of natural gas. 1 Sm^3 natural gas corresponds to 40.52 MJ (HHV) [249]. Using these data, we estimate that the energy consumption for production and transport of natural gas to mainland Norway is

$$\frac{100\ kg\ CO_2/toe}{2.3\ kg\ CO_2/Sm^3} * 40.52\ MJ/Sm^3 = 1.8\ GJ/toe$$

or an efficiency of 95.7% (HHV basis).

A.2 Energy Efficiency of Ammonia Synthesis

A.2.1 Synthesis Based on Natural Gas

The energy efficiency of conversion of natural gas to ammonia is given in several sources. The HHV for ammonia vapor at 25 ^oC and atmospheric pressure is 22.543 GJ/t. For liquid ammonia it is 21.377 GJ/t [29]. Several sources for data on synthesis energy consumption have been found and are tabulated

below. The HHV for ammonia vapor is used in efficiency calculations because evaporation of ammonia may easily be achieved by supplying low-quality heat from exhaust etc.

Table A.1: Energy consumption for production of ammonia. Product assumed to be liquid ammonia at ambient temperature. In addition 0.3 GJ/t is required to chill the ammonia to –33 °C [29], and 0.8 GJ/t to dispose CO_2 from the process.

Energy input GJ(HHV)/t NH_3	Efficiency η_{HHV}	Comments	Ref.
32-37	61-70	Low-energy concepts (1974-84)	[29]
< 31	>72	Modern concepts (since 1991)	
30	74	Newest plant concept from M. W. Kellogg	
39.7	56	1970s plant	[37] [1]
32	70	1980s plant	
32-35	64-70	BAT[2] 2000	[39]

[1] Not clearly stated if based on HHV or LHV, assumed to be LHV, converted to HHV assuming pure methane feed stock

[2] Best Available Technique

In the further analysis of the ammonia chain it is assumed that an efficiency of 72% (HHV) is typical for modern ammonia plants. This efficiency is lowered to 70% when taking into account chilling of liquid ammonia from ambient temperature to -33 °C and compression of CO_2.

A.2.2 Compression of CO_2

It may be beneficial to operate the regeneration unit for the chemical solvent, which is used for CO_2 removal, slightly above atmospheric pressure (2-3 barg) if the CO_2 removed from the synthesis gas is to be used or disposed. However, this will then require slightly higher regeneration temperatures (higher quality of heat), and is not reflected in the figures given in Table A.1.

We assume that the CO_2 from the regeneration unit is available at 1.5 atma pressure at 25 °C saturated with water. The production of CO_2 is about 1.15 – 1.30 t CO_2/t NH_3 when based on conventional steam reforming [39], in good agreements with 1.22 t CO_2/t NH_3 given by Astarita *et al.* [38]. In an

AutoThermal Reforming (ATR) process, the CO_2 content in the synthesis gas will be higher because emissions from the fired furnace is avoided. No data have been found, but we assume that about 1.5 t CO_2/t NH_3 is a representative figure. Further, we assume that the final delivery pressure of the CO_2 is 150 barg, that centrifugal compressors used have 70 % polytropic efficiency, 0.5 bar pressure drop in coolers and 0.25 bar pressure drop in scrubbers. The compression energy requirement is thus about 0.7 GJ/t NH_3. Including allowance for cooling water etc., a total energy requirement of 0.8 GJ/t NH_3 is reasonable.

A.2.3 Synthesis Based on Water Electrolysis and Air Separation

If ammonia is to be synthesized based on water electrolysis and air separation, the energy consumption would be higher. The energy consumption was 44.3 GJ/t NH_3 based on 1970's technology [37]. Assuming a similar development in energy efficiency as for other feed stocks, it is likely that the present figure would be about 39-40 GJ/t. The energy requirement was also estimated based on other available data [29, 250], see Table A.2 below.

Table A.2: Energy consumption for production of ammonia from water electrolysis and air separation. Chilling of ammonia not included.

	Energy requirement GJ(HHV)/t NH_3	Ref.
Water electrolysis[1]	32.7	[29]
Air separation	0.3	[29]
Compression	2.5	[29]
Synthesis	1.7	[250]
Others	1.3	[250]
Total	38.5	

[1] Based on stoichiometric H_2 consumption

The energy efficiency (η_{HHV}) for ammonia production from electrolysis of water is thus about 56-58%.

A.3 Transportation and Storage

No data for the energy requirement for storage and transportation of ammonia to the end user have been found. A rough estimate is that about 5% of the energy present in the ammonia is required for transportation and storage, including chilling.

A.4 Splitting of Ammonia

Efficient heat transfer between ammonia gas feed and the product gases is required to minimize energy consumption. The theoretical minimum energy requirement for the splitting reaction is 2.7 GJ/t NH_3 vapor (12% of the HHV of vaporous ammonia). A thermal efficiency of 75–80% based on HHV is assumed to be possible, but this depends on size and load of the splitter [71]. No energy allowance for gas treatment or compression has been included in these figures. It remains to be verified if gas separation is required (removal of traces of ammonia, nitrogen etc.), which would further decrease splitting efficiency.

A.5 Efficiency of the Fuel Cell

It is assumed that the typical operating cell voltage of PEMFC is 0.70 V. The isothermal cell voltage is 1.48 V at standard conditions, thus the efficiency is about 47%. Only design point efficiency is considered here, but it should be noted that FC efficiency under part load is higher than at full load because the cell voltage then is higher. ICEs tend to have a steadily decreasing efficiency with decreasing load.

The content of nitrogen in the fuel gas is high. Therefore, a substantial bleed of fuel gas is required. It is assumed that this bleed is balanced with the energy requirement for ammonia splitting, and thus does not contribute to any further loss of efficiency.

A.6 Auxiliary Equipment

It is assumed that dc current can be used to drive the auxiliaries. The required power to operate the auxiliary equipment is very dependent on system design. Operating the cell under elevated pressure or with substantial pressure drop,

especially for the air stream, will dramatically increase power requirements. Parasitic losses lower than 5% are practical [251], but requires atmospheric FC operation pressure and careful design of the entire system.

A.7 Electrical Motor and Inverter

Once the chemical energy is converted to electrical energy in the FC, this energy has to be converted to mechanical energy in an electric motor. Efficiencies of electric motors are dependent on size and, to some extent, design. A typical efficiency is about 93–95% [14]. In our calculations, we have used an efficiency of 95%.

Appendix B

PEMFC Test Facility

B.1 Introduction

Two Fuel Cell (FC) test stations for testing of single cells were built at Department of Materials Technology as part of the PhD study and the concurrent research project. The various parts of the FC test stations as well as FC housings employed will be discussed. Some of the FC data acquisition program capabilities will also be described. The test facility has been designed by Rune Halseid and Preben J. S. Vie. The design was to a large extent based on test facilities built by Møller-Holst [252] and Vie [164]. Some solutions were also inspired by solutions developed at Case Western Reserve University. The programming was performed by Preben J. S. Vie, and was implemented in LabVIEW (`www.ni.com/labview`).

B.2 Fuel Cell Test Station

A flow diagram showing the most important components and signal transmitters is shown in Figure B.1. A more detailed discussion of the different elements is given below.

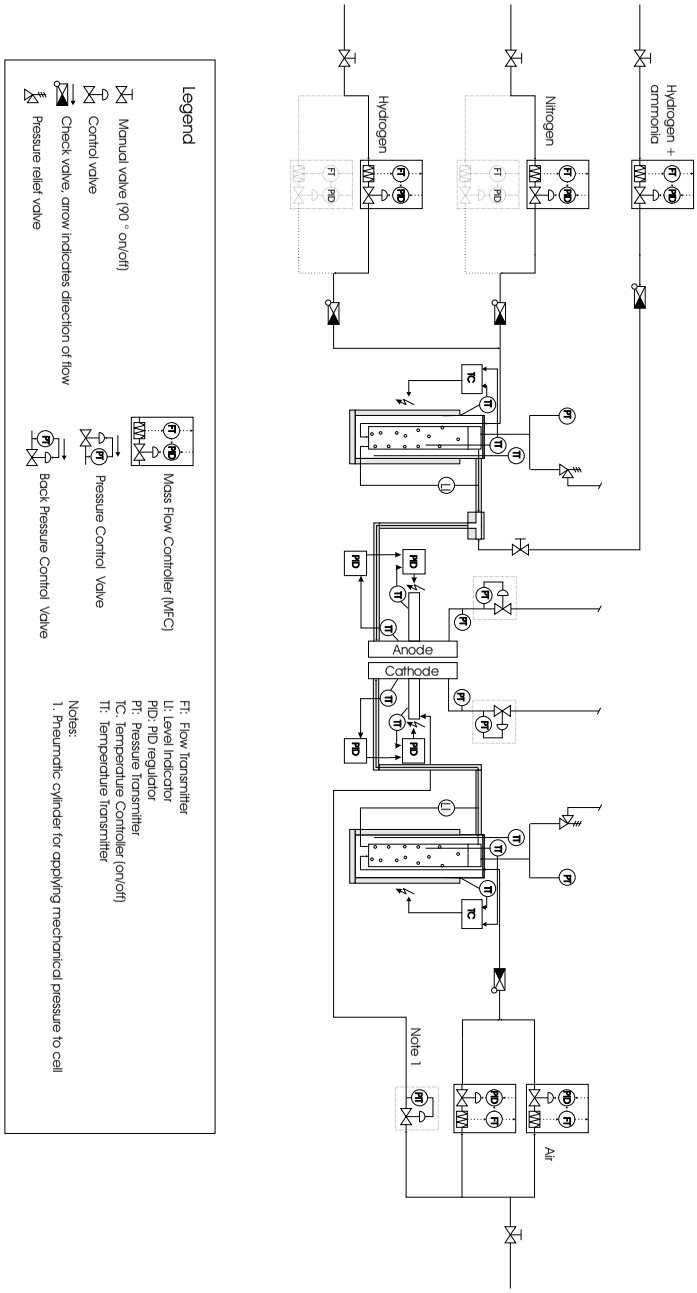

Figure B.1: Simplified flow and instrumentation diagram for the test facility.

B.2.1 Gas Humidifiers

The gas humidifiers used were of the same type as used by Vie [164]. An inner saturation tank (Ø63 mm) is heated by a water-filled outer tank (Ø100 mm) which in turn is heated by an electrical heating tape. The outer tank will ensure a more homogeneous temperature around the inner saturation tank than a saturation tank directly heated by an electrical heating tape, see Figure B.2.

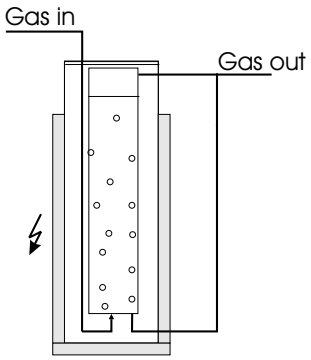

Figure B.2: A simplified sketch of the gas humidifier.

One draw-back with this design is that the humidified gas has to flow about 0.5 m in tubes after humidification before reaching the FC. Condensation is thus a problem. One solution would be to heat-trace the tubes, but it would be very difficult to avoid cold spots all together. Local overheating is also a potential problem, especially if using polymer tubing. As discussed in Section 8.4.1, there were problems with long-term stability of the FC system. Contaminants from the humidifiers could be a problem, both organic residues and corrosion products[1]. Therefore, we also tried to put the cell as well as two waterfilled gas scrubbers inside a heating cabinet. The gas scrubbers can easily be clean and condensation is avoided. The draw back is that it is not possible to pressurize the system, and in the present configuration it is not possible to run with fully or super-saturated reactant gases.

[1]The humidifiers were made in SS-316, but local corrosion was observed due to local heating during welding of the tanks.

B.2.2 Gas Flow Rate and Gas Pressure

The gas flows were controlled with EL-FLOW Mass Flow Controllers (MFCs) from Bronkhorst Hi-Tec with analog set-point and reading signals. Due to the need for large flexibility in the test facility, MFCs were connected in parallel to give a larger flow-range and to facilitate mixing of different gases.

Cathode and anode gas pressures were controlled by manual back pressure regulators from Fairchild, type FC-10262BP. The gas pressures were measured at the back-pressure regulators and upstream the gas humidifiers (Kobold, type SEN8600 pressure transmitters).

B.2.3 Load Circuitry

The current or the cell potential was controlled by an Agilent 6051A load box. To enable characterization of the FC down to very low potentials, a power supply (HP 6032A) running potentiostatically was used to boost the cell voltage. Also, a solid state relay was included for current interrupt measurements. A simplified scheme is given in Figure B.3. Separate potential probes measuring the potential on the backing were connected to the input sense of the load to be able to accurately control the actual potential of the cell avoiding ohmic losses in the external circuit.

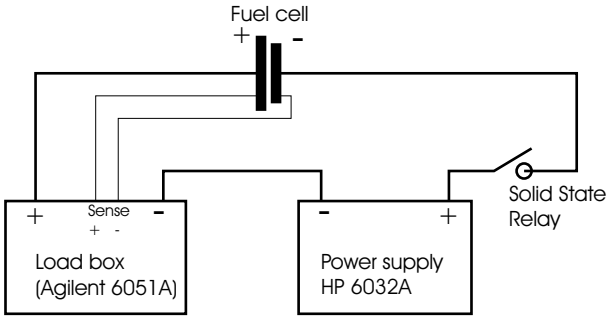

Figure B.3: A simplified diagram of the load circuit.

B.2.4 Data Acquistion and Control System

The data acquisition and control system was implemented with computer boards from Measurement Computing Inc. (`www.measurementcomputing.com`).

CIO-DAS 1602/12 An analog input/output 12-bit board including digital input and output. In our system this board controls the temperature and voltage measurements on the EXP-32 board, in addition to output of digital control signals.

CIO-EXP-32 This board multiplexes voltages on 32 channels to two 12-bit AD converters on the CIO-DAS 1602/12 board. The voltage range can be selected individually for each bank of 16 channels. The cold junction temperature for the thermocouples is also measured by this board.

CIO-DAC 16 Analog output signals, 12-bit resolution DA converter.

In addition to these boards, a GPIB-bus (PCI-GPIB - IEEE 488.2) card was used to control the FC load, an Agilent 6051A (`www.agilent.com`). A 3 MHz digital oscilloscope (Pico Technology Ltd ADC-212/3 - `www.picotech.com`) connected to the parallel port on the PC measured the voltage change in the FC upon current interrupt (see Section B.4).

Data were measured as voltages and collected with the CIO-EXP-32 board. All the transmitters convert gas pressures, gas flow rates and temperatures to voltages. The controlled variables were regulated either by an on/off control loop in the computer (heating tape on humidifiers), PID-loop in the computer (heating elements on the FC pistons[2]) or by internal PID-loops in the MFCs. The digital signals from the CIO-DAS 1602/12 board controlled the on/off regulation loops (heating elements on humidifiers), and the CIO-DAC 16 sent analog signals to various units, either as setpoints (flow meters) or as control signals (thyristors). The gas pressures were controlled by manual mechanical regulators.

B.2.5 The Measurement and Control Program

The measurement and control program was programmed in LabVIEW 6i (`www.ni.com/labview`). The program controls and measures the most important parameters of the FC:

[2]Due to the relatively long delay between applying voltage to the heating element and observing a temperature change in the FC, a cascade controller was used. A temperature transmitter very close to the heating element was used as feedback for the heating element control loop. The set-point of this loop was in turn regulated by a slower PID loop which used the FC temperature as feedback signal.

- Measure temperatures inside the FC (anode gas in/out, cathode gas in/out)
- Measure temperature on the FC heating elements
- Measure three temperatures on each gas humidifier (inner tank, annulus and under the heating tape)
- Measure two temperatures in the gas entering the FC, included to allow for heat tracing, but presently not implemented
- Control anode and cathode FC temperature through the heating element temperature
- Control temperature of anode and cathode
- Control degree of anode and cathode gas humidification through the gas humidifier temperature
- Control and measure gas flow and composition to the anode and cathode
- Measure four gas pressures
- Control the FC load, either galvanostatically, potensiostatically or applying constant resistance (the latter mode was not used in our experiments)
- Measurement of total ohmic FC resistance by automated current interrupt
- Perform and record pre-programmed scan/polarization curves
- Emergency operation:
  - Shut-down of the system in the event of computer error
  - Shut-down when FC voltage drops below a specified limit
  - Shut-down when some temperatures are higher than a specified limit

The program measures and controls all the parameters at a loop frequency of 2 Hz. The main front panel is shown in Figure B.4.

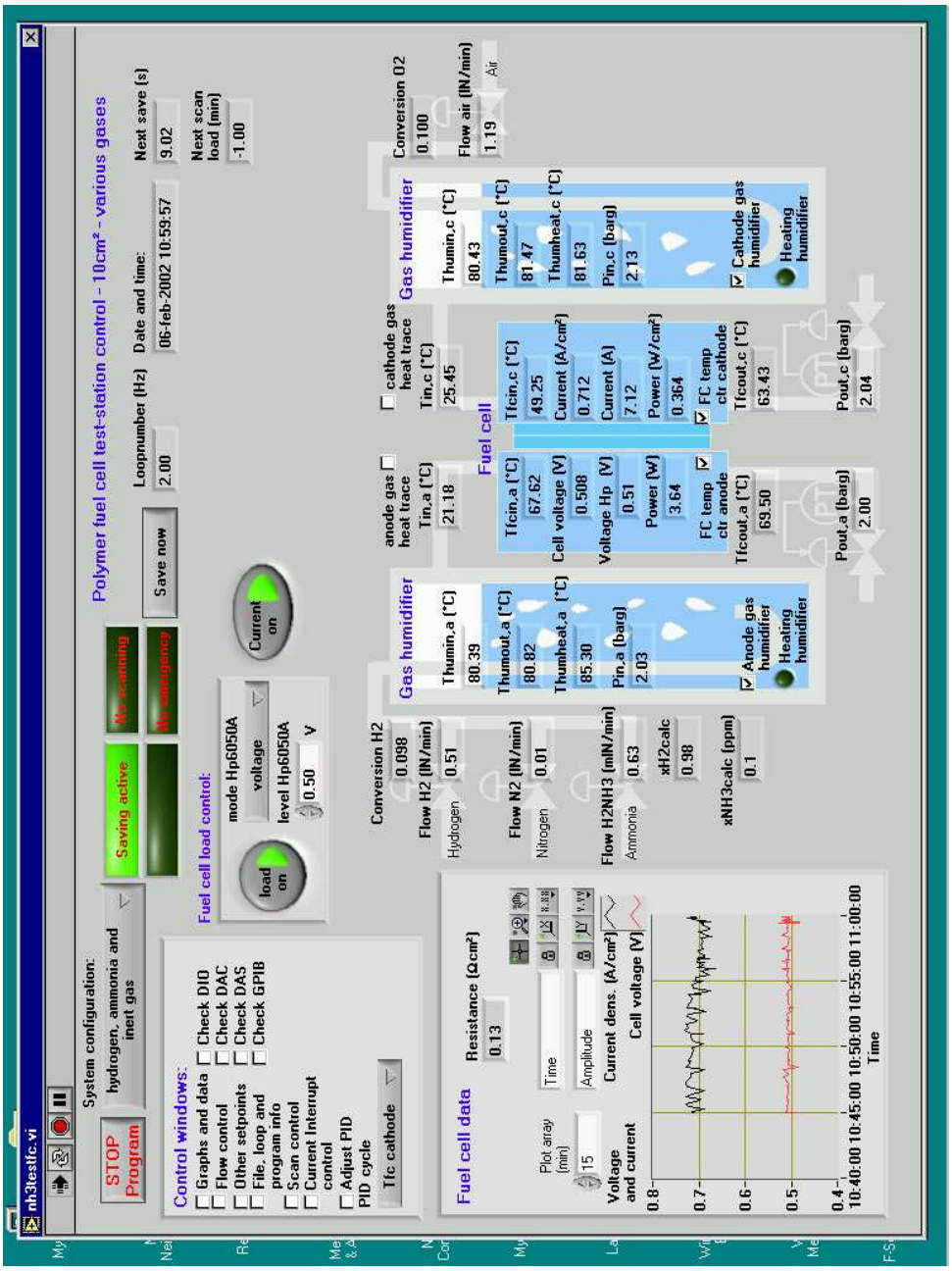

Figure B.4: The main front panel of the control program.

B.3 Fuel Cell Housing

Two different FC housings were used for testing cells in this work. The housings are briefly described below as well as the shortcomings of the two designs.

B.3.1 ElectroChem Housing

One housing used was a 5 cm^2 housing from ElectroChem made from graphite blocks with a somewhat special flow pattern where three serpentines run in parallel. However, these serpentines are connected with a common header after each crossing of the active area. We have observed that this design is prone to flooding since the pressure drop over each segment is small with two other channels in parallel thus preventing efficient transport of liquid water by pressure build-up. The cell is also intended to be mounted so that the flow fields run vertically up and down so that also gravity further impedes transport of liquid water. This problem was partially overcome by placing the cell on its side, but it was observed that large amounts of liquid water accumulated becoming an operational problem after a couple of weeks. It was noted that the performance was much more stable when running symmetrical $H_2|H_2$ cells probably since no water is formed in these cells. Sealing of the cell was made with silicone rubber gaskets with a thin Teflon gasket on top to reduce the possibility of contamination of the Membrane Electrode Assembly (MEA) from the silicone. To prevent short-circuiting of gas flows, the active area was increased to 6.25 cm^2 (25x25 mm) by cutting the gaskets a little wider (original dimensions were 5 cm^2, 22x23 mm). The graphite blocks are fitted with two thermocouple wells each located relatively far away from the MEA. There are also separate connections for potential measurements in the graphite blocks.

The cell was also equipped with a reference electrode placed next to the main active area and actively supplied with gas from the main part of the cell. As discussed in Chapter 4, the validity of reference potentials measured with this kind of electrodes is questionable. The potential was always logged, but not used for analysis.

B.3.2 In-house Fuel Cell Housing

This FC housing is similar to the FC housings developed by Møller-Holst [252] and Vie [164]. The material is mainly stainless steel (SS-316 and SS-316L),

except for the non-conducting "inert" polymer material (PEEK) used on the top of the housing. This material prevents short-circuits over the MEA. The flow fields were initially gold-plated (5 μm) to prevent corrosion and to reduce the contact resistance between the Gas Diffusion Layer (GDL) and the flow field. However, over time the gold layer started to chip off so that galvanic corrosion of the stainless steel base could occur at a high rate. The gold plating was therefore removed. The parallel flow field also turned out to perform worse than expected. Very high flow rates were required to ensure flow in all channels making the cell prone to drying out as well as high consumption of gases. A flow field with a double serpentine was thus constructed. A pneumatic piston controled the mechanical pressure applied on the MEA. Gas sealing of the cell was achieved with O-rings and specially moulded silicone gaskets (Loctite® 5926) which were dried at >100 °C and then boiled in purified water to remove contaminants.

A cut-through drawing of the in-house FC housing is shown in Figure B.5. The design incorporates temperature probes in the gas channels very close the MEA so that the temperature is more accurately measured with faster response than in f. ex. the ElectroChem cell. The temperature sensors can be seen in Figure B.6. Also, there are separate potential probes with contact directly on the GDL so that ohmic voltage drops in the external circuit are not included in the measured cell potential.

B.4 Ohmic Resistance by Current Interrupt Measurements

The total ohmic resistance in the FC was measured by a current interrupt technique. The principle is that the voltage drop due to ohmic resistance instantaneously drops to zero when the current is cut[3]. Overpotentials due to electrochemical processes decay exponentially with time, and may thus be separated from the ohmic resistance. The changes in cell voltage is measured with an oscilloscope.

A typical current interrupt voltage curve is given in Figure B.7(a). We observe a distinct change in the voltage around 1.5 ms. This change represents the IR loss in the FC and the start of the current interrupt measurement. After 1.5 ms there is an exponential decay, corresponding to electrochemical

[3]The local current in the electrodes is not necessarily zero; this introduces an error in the measured ohmic resistance, see Section 5.3.3

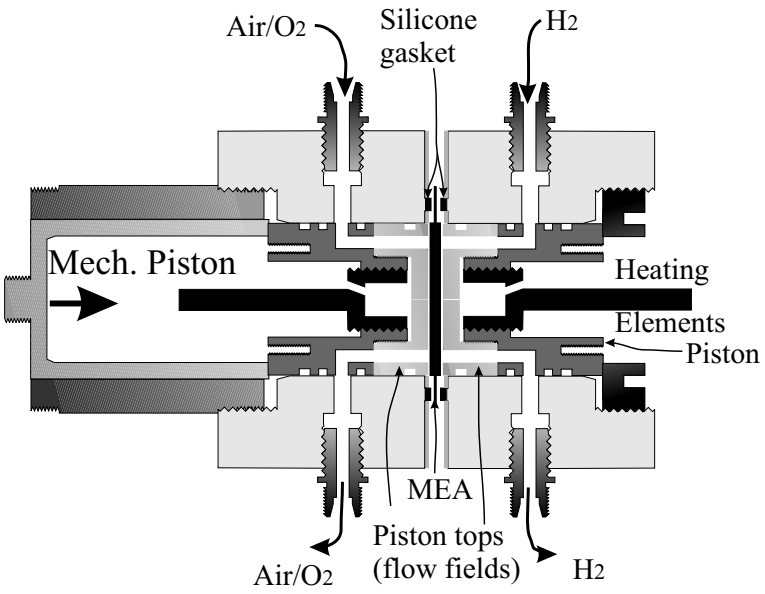

Figure B.5: In-house FC housing used for testing.

processes, where the voltage eventually will reach the Open Circuit Voltage (OCV) for the FC system. The ohmic resistance can be calculated by a thorough analysis of the voltage behavior around the current interrupt. This is shown in Figure B.7(b). As can be seen in Figure B.7(a), there is some ringing in the potential signal right after interrupt of the current making it impossible to pick one single representative value for the cell potential right after interruption. Instead, the voltage change at current interrupt can be calculated by extrapolating a linear fit to data observed some time after the interrupt back to $t = 0$. The same procedure is used to establish the cell potential just before the interrupt. The ohmic resistance is then calculated from Ohm's law. The estimated potential change at interrupt is to a small extent (2–5%) affected by how the data points used for fitting are selected. However, the method is quite robust, and was able to accurately follow changes in cell resistance. Comparison to impedance measurements with a Solartron 1287/1255B set-up on a low-impedance dummy circuit showed good agreement between the two methods.

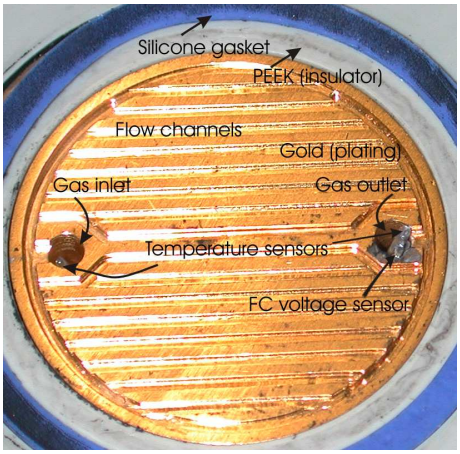

Figure B.6: Details of the piston top and flow field. The gold plated parallel flow field is shown on this picture.

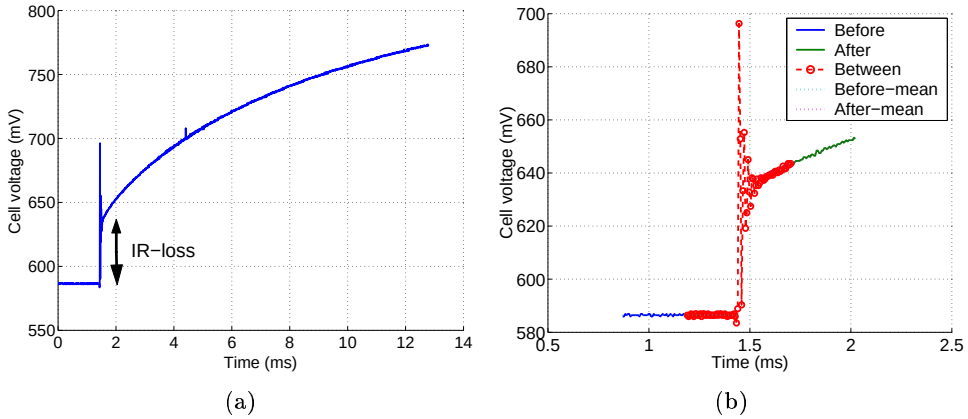

(a) (b)

Figure B.7: a) A typical voltage transient observed after current interrupt. The current was interrupted at approximately 1.5 ms and b) the analysis of the current interrupt data.

Appendix C

Estimation of pH and Ionic Strength of Electrolytes Used

The pH and ionic strengths of the different electrolytes used in various experiments are estimated. The pKa value of perchloric acid is 1.77 [168], and for hydrogen sulfate the pKa is 1.99 [78]. The first dissociation step of sulfuric acid is assumed to be complete. Further, all ammonia added to the solution is assumed to be present as ammonium (pK_a=9.24 [78]). Based on the equilibrium constants, the pH and ionic strength was estimated and is given in Table C.1

Table C.1: Estimated pH and ionic strength I of different electroytes used in the experiments.

c^0_{acid} [M]	$c^0_{NH_3}$ [M]	Sulfuric acid pH [-]	Sulfuric acid I[M]	Perchloric acid pH [-]	Perchloric acid I[M]	Comment
0.100	0.000	0.96	0.117	1.47	0.034	
0.100	0.010	1.00	0.119	1.55	0.038	DEMS
0.100	0.025	1.07	0.121	1.69	0.045	RDE
0.100	0.050	1.20	0.128	1.96	0.061	
0.100	0.100	1.56	0.155	-	-	
0.100	0.000	0.96	0.117	1.47	0.034	
0.110	0.010	0.96	0.129	1.52	0.040	ORR
0.150	0.050	0.95	0.175	1.71	0.070	
0.180	0.100	1.01	0.214	1.97	0.111	
0.500	0.000	0.29	0.520	1.08	0.084	
0.500	0.050	0.34	0.522	1.22	0.110	EQCM
0.500	0.250	0.57	0.537	1.82	0.265	
0.500	0.500	1.18	0.633	-	-	
1.000	0.500	0.28	1.039	1.80	0.516	